



HAL
open science

Selected aspects of central heavy-ion collisions around Fermi energies studied over 25 years with INDRA

J.D. Frankland

► **To cite this version:**

J.D. Frankland. Selected aspects of central heavy-ion collisions around Fermi energies studied over 25 years with INDRA. Nuclear Experiment [nucl-ex]. Université Caen Normandie, 2020. tel-03064998

HAL Id: tel-03064998

<https://theses.hal.science/tel-03064998>

Submitted on 14 Dec 2020

HAL is a multi-disciplinary open access archive for the deposit and dissemination of scientific research documents, whether they are published or not. The documents may come from teaching and research institutions in France or abroad, or from public or private research centers.

L'archive ouverte pluridisciplinaire **HAL**, est destinée au dépôt et à la diffusion de documents scientifiques de niveau recherche, publiés ou non, émanant des établissements d'enseignement et de recherche français ou étrangers, des laboratoires publics ou privés.



Normandie Université

HDR

Pour obtenir le diplôme d'habilitation à diriger des recherches

Spécialité Physique

Préparée au sein de l'Université de Caen-Normandie

Selected aspects of central heavy-ion collisions around Fermi energies studied over 25 years with INDRA

**Présentée et soutenue par
John David FRANKLAND**

**Thèse soutenue publiquement le 4 décembre 2020
devant le jury composé de**

Mme Francesca GULMINELLI	Professeur de l'Université de Caen, LPC Caen	Garant
M Denis LACROIX*	Directeur de recherches CNRS, IJCLab Orsay	Rapporteur
Mme Yvonne LEIFELS*	Deputy research director, GSI Darmstadt, Allemagne	Rapporteur
Mme Sherry YENNELLO*	Director of the Cyclotron Institute, A&M University, College Station, Texas, USA	Rapporteur
M Abdelouahad CHBIHI	Directeur de recherches CNRS, GANIL, Caen	Examineur, Président
M Bernard BORDERIE*	Directeur de recherches émérite CNRS, IJCLab Orsay	Examineur

*** en visioconférence**



Preface

This manuscript has been prepared with the aim of obtaining the degree of “Habilitation à Diriger des Recherches” (Authorization to Supervise Research) or “HDR”. The HDR sanctions recognition of a candidate’s high scientific level, the original nature of their approach in a field of science, their ability to master a research strategy in a sufficiently broad scientific or technological field and their ability to supervise young researchers.¹

As such, this manuscript is divided into two parts. The first part is a detailed summary of my research activities since my Ph.D thesis, with many references to the various publications which resulted from these works. As a large proportion of my activity has also been dedicated to software development and maintenance for the INDRA and FAZIA collaborations, there is also a short chapter on this work, not documented elsewhere.

The second part concerns two new as-yet unpublished studies which I have conducted over the last two years. The first, currently being prepared for publication by the INDRA collaboration, concerns a new method for the quantitative determination of impact parameter distributions for any experimental selection of data in the Fermi energy range. The second, more recent, and more exploratory work, presents an entirely new method for carefully selecting the most isotropic events produced by collisions, allowing at last for a correct study of the dependence of nuclear transparency with bombarding energy.

John Frankland
GANIL, 21st September 2020

¹The original text of the [law of 23rd November 1988](#), article 1, states: “L’habilitation à diriger des recherches sanctionne la reconnaissance du haut niveau scientifique du candidat, du caractère original de sa démarche dans un domaine de la science de son aptitude à maîtriser une stratégie de recherche dans un domaine scientifique ou technologique suffisamment large [et] de sa capacité à encadrer de jeunes chercheurs.”

Contents

I	Past & Present: “From the past until completion”	11
1	Introduction	15
2	Multifragmentation, EoS and Phase Transitions	19
2.1	Introduction	19
2.2	Multifragmentation and spinodal instabilities	21
2.2.1	Selection of “single source” or quasi-fused (QF) events	22
2.2.2	Spinodal decomposition & stochastic mean field calculations	24
2.3	Freeze-out properties and AMD calculations for $^{129}\text{Xe}+^{nat}\text{Sn}$ reactions	28
2.4	Multifragmentation and universal fluctuations	30
2.4.1	Identifying the nature of the phase transition	30
2.4.2	Form of the scaling function and pseudo-criticality	32
2.5	Multifragmentation and radial flow	34
2.5.1	Multifragmentation for different entrance channel asymmetries	35
2.5.2	Multifragmentation timescale and Z_{max} fluctuations	38
2.6	Summary	43
3	Reaction mechanisms at sub-Fermi energies	45
3.1	Introduction	45
3.2	Heavy residue production in $^{129}\text{Xe}+^{nat}\text{Sn}$ collisions below the Fermi energy	48
3.3	3-fragment exit channels at $\leq 20A$ MeV	48
3.4	Sequential fission chronology	50
3.5	Sequential fission chronometry	52
3.6	Comparisons with theoretical models	54
4	KaliVeda, or The Tao of Collaborative Software Development	59
4.1	Origins	59
4.2	Mission statement & current status	61
4.2.1	DAQ Slow Control software	63
4.3	Architecture	63
4.4	Technologies	65
4.4.1	Language	65
4.4.2	Build system	66
4.4.3	Version Control	66

II Present & Future: “What price to get out of going through all these things twice?”	69
5 Introduction	73
6 How central are the most central collisions ?	75
6.1 Introduction	75
6.2 Quantifying the centrality of collisions	77
6.2.1 Reconstructing impact parameter distributions for experimental data	79
6.2.2 Parametrizing the relationship between X and c_b	81
6.2.3 Procedure for reconstruction of impact parameter distributions	83
6.3 Reconstructing experimental impact parameter distributions	83
6.3.1 Results of fits to data	85
6.3.2 Bombarding energy and system dependence of deduced $k(c_b)$	87
6.3.3 New experimental constraints for dynamical reaction models?	89
6.3.4 Reconstructed impact parameter distributions	92
6.3.5 So just how central <i>are</i> the most central collisions?	93
6.4 Summary	95
7 How isotropic are the most isotropic events ?	97
7.1 Introduction	97
7.1.1 Global shape variables	98
7.2 New method for extracting the most isotropic events	102
7.2.1 Maximizing the isotropy of a single event sample	103
7.2.2 Minimizing the isotropy of an event sample?	104
7.2.3 Extracting all the most isotropic events	104
7.2.4 Most isotropic events for $^{129}\text{Xe} + ^{nat}\text{Sn}$ collisions from 25 to 50A MeV	108
7.3 So just how isotropic <i>are</i> the most isotropic events?	111
7.4 Energy dependence of nuclear transparency	113
7.5 Summary	116
III Appendixes	119
A A not at all definitive guide to some oft-mentioned models	121
A.1 Microscopic models of nuclear reactions	121
A.1.1 The time-dependent Hartree-Fock (TDHF) equation	122
A.1.2 Semi-classical approach: The nuclear Boltzmann equation	123
A.1.3 Beyond the nuclear Boltzmann equation	126
A.1.4 Effective forces	129
A.2 Statistical descriptions of multifragmentation	133
A.2.1 The Statistical Multifragmentation Model (SMM)	134
A.2.2 Microcanonical Multifragmentation Models (MMMC and MMM)	135

B Reconstruction of impact parameter distributions	137
B.1 Validation of the method	137
B.2 Minimum bias impact parameter distribution	139
B.2.1 Analytic expression for total cross-section	140
B.2.2 Analytic expression for centrality	141
B.3 Fit results for all systems	141
B.4 “Scaling” of variables correlated with impact parameter	141
C Simulation of momentum distributions	147
Bibliography	148

Acknowledgements

I have many people to thank for the fact that I am where I am now, that is to say writing the Acknowledgements in my Habilitation à Diriger des Recherches.

First of all, I would like to thank the director of GANIL, Navin Alahari, for allowing me to prepare and present this Habilitation in the best conditions possible. And, after Daniel Guerreau, Dominique Goutte, Sydney Galès, and Florent Staley, for being the first director of GANIL capable of making me actually knuckle down and finally do my damn HDR. Thanks also to Gilles de France, director of the Physics Division, and to Jean-Eric Ducret, head of the Research group. Special mention & thanks to Sabrina Lecerf for handling the technical part of the defence by Zoom.

Thank you to Francesca Gulminelli for accepting to “sponsor” my candidacy. As one of the main instigators of the paradigm shift in the understanding and the study of phase transition signals in experimental data on heavy-ion collisions over the last 25 years, it was essential for me to have her validation of the presentation of the state of the art that I have tried to make here, and to guide me in the parts where my understanding is still lacking.

I can never thank enough the three reporters, Yvonne Leifels, Sherry Yennello and Denis Lacroix, for accepting to read and evaluate the quality of the manuscript and the work it contains, and being kind enough to actually write on paper that they thought it not entirely ridiculous. I am still reeling from the shock. Thank you all.

An enormous thank you to Abdou Chbihi, who from the day I first set foot in GANIL has always had my back, and has always been there for me when I needed him. And, of course, many many thanks to Bernard Borderie for taking me on as his Ph.D student way back in 1995, and for inviting me to write the review article [1] with him which formed a solid base for attacking the HDR.

Thank you to the many colleagues from the INDRA and FAZIA collaborations, past and present, with whom it has been an honour and a joy to work over these 25 years, with special mentions for Rémi Bougault, Nicolas Le Neindre, Eric Bonnet and Diego Gruyer. Neither will I ever forget the many valuable lessons in scientific rigour (and British history) of Marie-France Rivet², she is sorely missed.

John Frankland
GANIL, 7th December 2020

²d. 2015

Part I

Past & Present: “From the past until completion”

*Those who came before me
Lived through their vocations
From the past until completion
They'll turn away no more*
[2]

Chapter 1

Introduction

My research activities are concerned with the dynamics and thermodynamics of nuclear matter. Nuclear matter is a theoretical idealization of the same quantum fluid which can be found microscopically at the heart of all atomic nuclei or macroscopically in the collapsing core of massive stars called supernovae, in the structure (or even in the collisions) of neutron stars [3, 4, 5]. On Earth the study of nuclear matter in extreme conditions of density, temperature or neutron-proton ratio is possible only through collisions between heavy ions (atomic nuclei) at bombarding energies from the Coulomb barrier (a few MeV per nucleon) up to a few 100s of MeV per nucleon. In the course of these reactions the nuclear “liquid drops” which are the projectile and target collide, deform, heat and disintegrate in many different ways depending on their mass and charge, the bombarding energy and the impact parameter of each collision. The experimental challenge of these studies lies in the exploitation of complex multi-detector systems capable of reconstructing each collision from the multi-parametric data on the dozens of nuclei which can be produced in each event.

After my Ph.D at IPN Orsay¹ supervised by Bernard Borderie and a short post-doctoral sojourn at IPN Lyon², I was recruited by the CNRS in 1999 and posted to GANIL³ in October of that year as a “Chargé de recherches”. Ever since my Ph.D most of my research activity has taken place within the INDRA collaboration which unites the main laboratories responsible for building and running the detector⁴. My principal areas of research are the dynamics of heavy-ion collisions in the nucleonic regime and thermodynamic properties of nuclear matter. These two lines of research are complementary: the dynamics of the collisions allows to explore thermodynamic aspects such as the equation of state or phase transitions. Most of my work has concentrated on the study of nuclear multifragmentation and the characterization of this process as a manifestation of a phase transition of nuclear matter in a finite system. All of this work features in a review article of the state of the art of the subject which I recently co-authored with Bernard Borderie [1]. In parallel I have also led studies on reaction mechanisms at lower energies, below

¹From 2020 onwards known as Laboratoire de Physique des 2 Infinis Irène Joliot Curie, or IJCLab for short.

²Now known as Institut de Physique des 2 Infinis de Lyon, or IP2I Lyon for short

³Grand Accélérateur National d'Ions Lourds, now known as GANIL.

⁴‘à la grande époque’, GANIL, IPN Orsay, LPC Caen, IPN Lyon, CEA DAPNI-SPhN, SUBATECH Nantes. Later on joined by (at one time or another): INFN/University of Napoli, NIPNE Bucharest, Université de Laval au Québec, INFN Catania, Ecole des Applications Militaires de l’Energie Atomique, Cherbourg and Conservatoire National des Arts et Métiers, Paris.

the multifragmentation threshold, for example by trying to establish upper limits to the fusion between heavy nuclei and studying their decay by sequential fission [6, 7, 8].

To better understand heavy-ion reactions in this energy range, I have carried out many comparisons of data with different dynamical models of nuclear collisions, or with statistical models concerning the more thermodynamic aspects, in collaboration with many theorists of the field in France and across the world. I have also participated in the organization of many workshops and international conferences, most notably IWM (International Workshop on Multifragmentation, to use the original - and less complicated - title) organized by the INDRA and CHIMERA collaborations conjointly in Catania or Caen, and of which I was part of the Scientific Committee in 2007*, 2009, 2011* and 2018 (*and local organizer at GANIL).

Throughout my career at GANIL I have supervised students from the University of Caen (now part of Normandy University), ENSICAEN (the Engineering School - considered to be a “cut above” the University in the French educational system) or elsewhere, either during internships as part of the first or second year of their Master’s degree, or by co-supervising Ph.D and post-doctoral students. The last Ph.D I co-supervised, Diego Gruyer, was recruited by the CNRS in 2018 and is now working at LPC Caen. My current Ph.D student, Julien Lemarié, is working on the analysis of the first INDRA-FAZIA experiment, in which he participated during his 2nd year Master’s internship in 2019.

I have dedicated most of the last twenty years to obtaining and analysing the best data possible on heavy-ion collisions (HIC) in the GANIL bombarding energy range (from ~ 5 to 95 MeV/u) with the charged particle multidetector INDRA [9, 10]. This work concerns not only the physics analysis which I will present in the following, but also the maintenance and development of the software used to pilot and monitor the detector as well as for data acquisition, which I took charge of on taking up my position at GANIL. Due to this commitment, besides the experiments directly connected to my research programme, I have also taken an important part in many experiments using or all or a part of INDRA, for example, to study giant resonances [11] or the limits of existence of super-heavy elements [12]. I have also participated in many other experiments either at GANIL using different instruments (ORION, VAMOS, SPEG), or outside GANIL, for example at GSI Darmstadt (INDRA, ALADIN) or at LNS Catania (CHIMERA, FAZIA).

In the early 2000s I also managed to convince the whole INDRA collaboration to undergo a paradigm shift concerning the software environment for data analysis, which up till then had been based on the Fortran computer language. Thus began the development of a new analysis environment based on the ROOT framework [13, 14] written in C++: KaliVeda [15]. Since 2005, I, along with several collaborators, have ensured the evolution of this environment in order to integrate new data with new challenges such as the coupling of INDRA & VAMOS in 2007, experiments with FAZIA since 2014 (see below), and most recently of all the data from the INDRA-FAZIA array. The expertise I gained in this adventure was put to another use, in collaboration with Daniel Cussol (LPC Caen), creating and supervising a ROOT/C++ training course for French-speaking nuclear physicists. Between 2003 and 2014, we trained (converted) a whole generation (or even several) of nuclear physicists (and more) at GANIL, at LPC, at LPNHE (Paris), at the CEA centres of Saclay, Bruyères-Le-Châtel, or Cadarache, at INSTN (Saclay), at IRMM Geel (Belgium), ...

Since 2011 I have been involved in the development of a new multidetector, FAZIA [16, 17], in the framework of a European collaboration, in order to improve experimental data on heavy-ion collisions thanks to a simultaneous identification of the Z and A of all reaction products up to

$Z \sim 25$ over a wide angular range. Between 2014 and 2018 there were many experiments at LNS Catania, first for commissioning the first prototype FAZIA blocks and the associated control systems for piloting and monitoring the detectors, and online analysis (which we developed in collaboration with Eric Bonnet and Diego Gruyer), and then for the first physics experiments using FAZIA [18]. In 2019 the first experiment coupling INDRA and FAZIA took place at GANIL, opening a new era in the study of hot, dilute, nuclear matter with a strong neutron-proton asymmetry. Currently we are involved in a project to replace the existing 30-year old VXI/CAMAC electronics and acquisition system of INDRA with a new, far more compact and lightweight, digital electronics system. Although the old warhorse has served us well and far beyond its expected lifespan, the last available spare modules (liberated by the detectors removed for the INDRA-FAZIA coupling) have all been used up and it is time to move on if INDRA is to survive another 10 (or more) years.

In the following I present a detailed summary of my research activities, concerning the studies I was most personally involved in, on multifragmentation, the nuclear matter equation of state and associated phase transitions, and reaction mechanisms at lower energies.

Chapter 2

Multifragmentation, Equation of State (EoS) and Phase Transitions of Nuclear Matter

2.1 Introduction

Nuclear matter is an idealized macroscopic system composed of neutrons and protons interacting solely via short range nuclear forces with a spatially uniform density ρ . The nucleon-nucleon interaction is comprised of two components according to their radial inter-distance: a very short-range repulsive part which takes into account the incompressibility of the medium and a longer range attractive part. Apart from the five orders of magnitude difference in energy and distance scales, the nuclear interaction is very similar to van der Waals' forces acting in everyday fluids, and indeed calculations using realistic effective nuclear interactions [21, 22] predict an analogy of the liquid-gas phase transition between normal- and low-density nuclear matter ("normal" density is the saturation density, ρ_0 , which is currently estimated as 0.155 ± 0.005 nucleons fm^{-3} [23]). As many recent works on the composition of low-density nuclear (stellar) matter have shown [24, 25, 26], the "gas" phase is predicted to be composed not only of nucleons but also of a wide range of nuclear clusters (including but far from limited to ${}^4\text{He}$). In some sense, strictly speaking, one should speak of a liquid-vapour phase transition for nuclear matter; in any case, the predicted phase transition is expected to be first order, *i.e.* proceeding through phase coexistence.

A schematic illustration of the phase diagram of dense matter is shown in Figure 2.1.1: the rather small portion of this diagram concerning nuclei, nuclear matter and the liquid-gas phase transition is limited to temperatures up to $T \sim 25$ MeV, and densities ρ not exceeding $\sim 2\rho_0$ and mostly exploring sub-saturation densities, where the expected phase coexistence region is situated. The coexistence zone terminates at a critical point, indicated by a black star in the figure, which is predicted by different models to be situated somewhere around $\rho \sim 0.4\rho_0$, $T \sim 16$ MeV.

The inset of Figure 2.1.1 show a typical prediction of an equation of state (EoS) for nuclear matter, which in this case is represented by isotherms in the pressure-density plane. All such predicted EoS for nuclear matter with a coexistence region also predict a region of mechanical instability in the phase diagram inside the coexistence region where $\partial p / \partial \rho < 0$ (shown by the

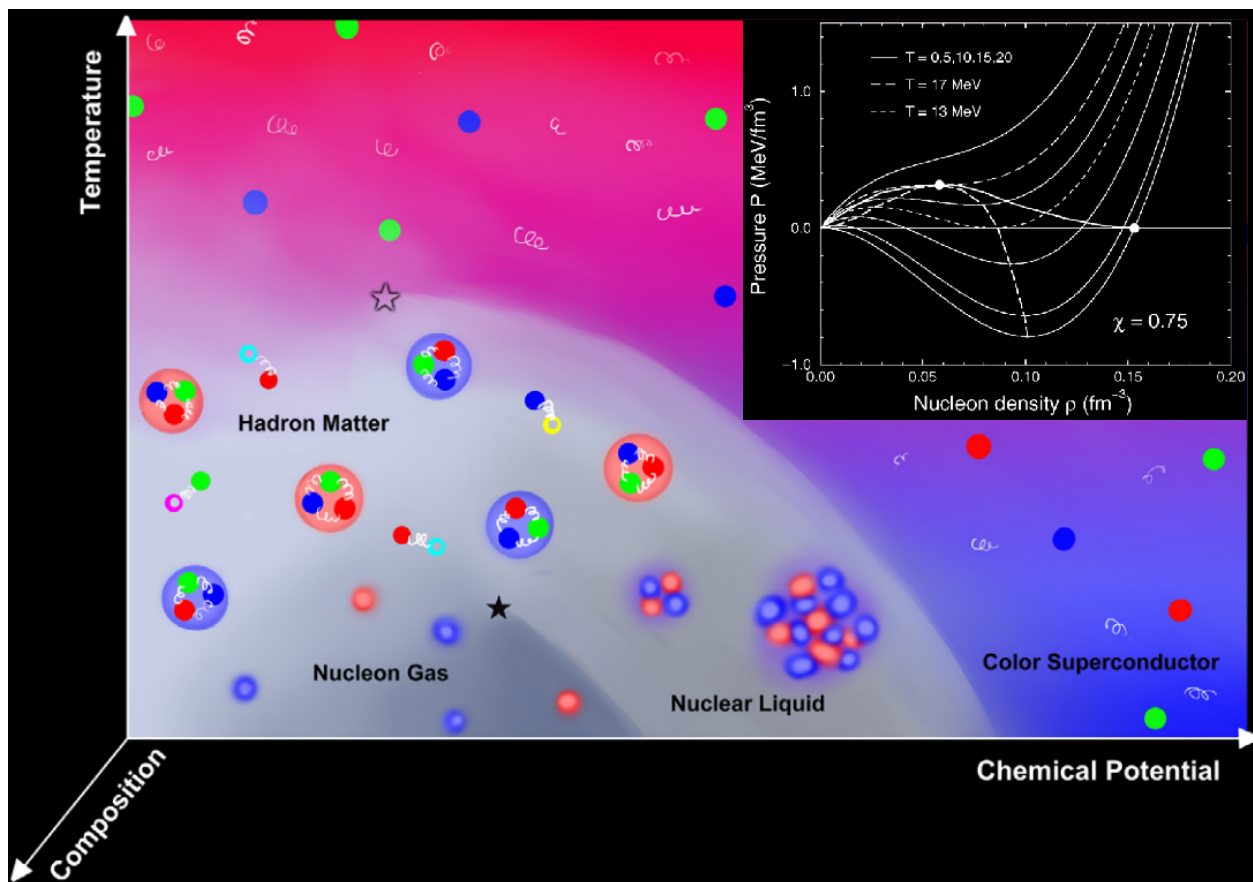


Figure 2.1.1 – (main picture): Schematic illustration of the phase diagram of dense matter [19]. (inset): Typical equation of state for symmetric nuclear matter (isotherms in pressure-density plane) [20]. The spinodal boundary (dashed) and the coexistence curve (solid) are indicated.

dashed lines in the inset of Figure 2.1.1). This is called the spinodal region, and the instability is known as spinodal instability. True first-order phase transitions are slow processes which require the establishment of an equilibrium across a phase boundary; Bertsch and Siemens [22] were the first to propose that the phase transition may manifest itself in collisions between finite nuclei through the exponentially rapid growth of density fluctuations due to spinodal instability, leading to the production of multiple fragments [20]: multifragmentation.

The experimental study of such reactions which occur in heavy-ion collisions (HIC) at 20 – 150A MeV requires powerful multi-detector arrays with high granularity and 4π angular coverage capable of impact parameter estimation and event sorting. Whether this sorting is based on the multiplicity or (transverse) energy of reaction products, the charge, mass or velocity of the largest product of each event, the event ‘shape’ (in momentum space), *etc.*, whatever observable(s) is(are) used need(s) to be measured by the array with as little bias as possible for the widest possible range of impact parameters. The DAQ dead-time must be kept low and the triggering system also has to bias as little as possible the sample of collisions recorded during the experiment.

Among the first generation of devices with these capabilities were the MSU 4π [27] and

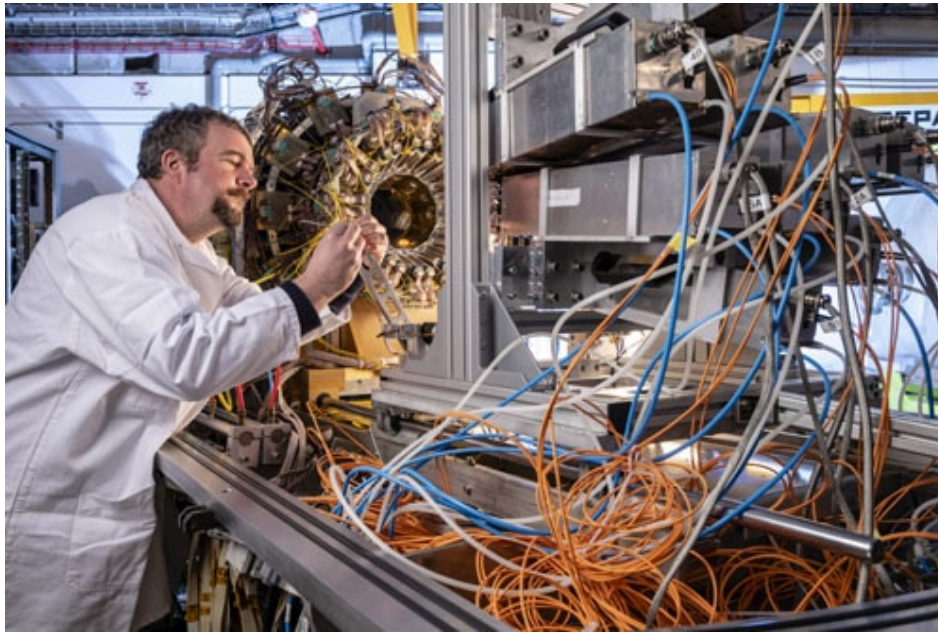


Figure 2.1.2 – An obviously faked photograph of the coupled INDRA and FAZIA arrays in the INDRA scattering chamber at the D5 cave in GANIL. I *never* wear a white coat and am not even *allowed* to touch the hardware. © P. Stroppa/CEA.

Miniball [28] arrays, and the combined Mur/Tonneau/DELF/XYZT arrays (commonly known as NAUTILUS) [29, 30] at GANIL, and indeed most of the pioneering works on impact parameter filtering in this energy range were made using these devices in the early 1990s [31, 32, 33].

INDRA [9, 10] is one of a second generation of 4π multidetector arrays, in continued use for the study of HIC at GANIL in Caen (and briefly at GSI, Darmstadt) since 1993. Its 336 multi-layer detection modules covering 90% of the solid angle around the target, low detection and identification thresholds, and minimum-bias trigger logic based on the number of fired modules make it ideally suited for studies of multifragmentation in the Fermi energy range and beyond. What follows is a presentation of my small contributions to the advances made in the understanding of nuclear multifragmentation and its link to the nuclear liquid-gas phase transition by the INDRA collaboration over the last 25 years. For a much wider review of the subject, including of course many important results from different groups and collaborations throughout the world, see the recent review article by Borderie and Frankland [1].

2.2 Multifragmentation and spinodal instabilities

My Ph.D. thesis [34] concerned a detailed study of multifragmentation reactions for the very heavy system $^{155}\text{Gd} + ^{238}\text{U}$ at $36A$ MeV, one of the reactions measured during the first INDRA campaign in 1993. The goal was to link multifragmentation to the nuclear liquid-gas phase transition by demonstrating that the spinodal instability mechanism proposed in [22] was indeed a plausible origin for the break up of the system into many different fragments, using the recently-developed Stochastic Mean Field approaches pioneered by, among others, Jørgen Randrup, Phil-

ippe Chomaz and Maria Colonna [20].

2.2.1 Selection of “single source” or quasi-fused (QF) events

First of all this required to isolate a sample of events as compatible as possible with the multifragmentation of a single source formed in central collisions from the majority of the projectile and target nucleons. The reliability of the event selection for heavy-ion collisions is a *sine qua non* for the quality of the subsequent analyses, especially regarding thermodynamic aspects. In order to find the most appropriate method, several different approaches were considered based on estimating either the collision centrality or the isotropy of the fragment momentum distributions event by event [35].

Selections based on the “centrality” of the collisions are not well adapted in this context, as, due to the large fluctuations occurring in collisions at Fermi energies, many different outcomes may coexist in the same range of impact parameter, and the “single source” events are expected to form a subset over a large range of impact parameters among the “most central” collisions. It is only very recently that it has become possible to quantify such effects and reconstruct the impact parameter distributions from experimental data without reference to a model of collisions: see Part II, Chapter 6. This recent work demonstrates even more clearly than before the impossibility of a meaningful event-by-event selection based on the impact parameter for central collisions.

Another expected characteristic of the “single-source” events is a high degree of isotropy of the fragments’ momentum distributions in the centre of mass frame. Unfortunately, the low multiplicity of intermediate mass fragments produced in the reactions, which for reasons of mass and charge conservation is typically less than 15, makes the event by event determination of the isotropy extremely unreliable [36, 37] (see Part II, 7.1.1). The response of global variables used to measure this isotropy is skewed by the low multiplicity, mean values for highly isotropic events resemble those of far less isotropic events, and fluctuations from one event to the next are very large [35].

On the other hand, the symmetric tensor

$$S_{\alpha\beta} = \sum_{i=1}^{M_f} \omega_i p_{\alpha}(i) p_{\beta}(i) \quad (2.2.1)$$

built from the c.m. momentum components of the M_f fragments in each event can be used to represent the event in momentum or kinetic energy space (depending on the chosen weight ω_i) as an ellipsoid defined by the three eigenvectors and eigenvalues of the tensor [38, 39]. This ellipsoid (or any other shape variable) is only representative of the real event shape if all or at least most of the (charged) reaction products of each event are detected, reconstructed and identified: this is why a prerequisite for such analyses is the selection of “complete” or “well-detected” events by cuts on the total reconstructed charge

$$Z_{tot} = \sum_{i=1}^{N_C} Z_i \quad (2.2.2)$$

and/or the total reconstructed momentum, which, as fragment masses are not identified by IN-

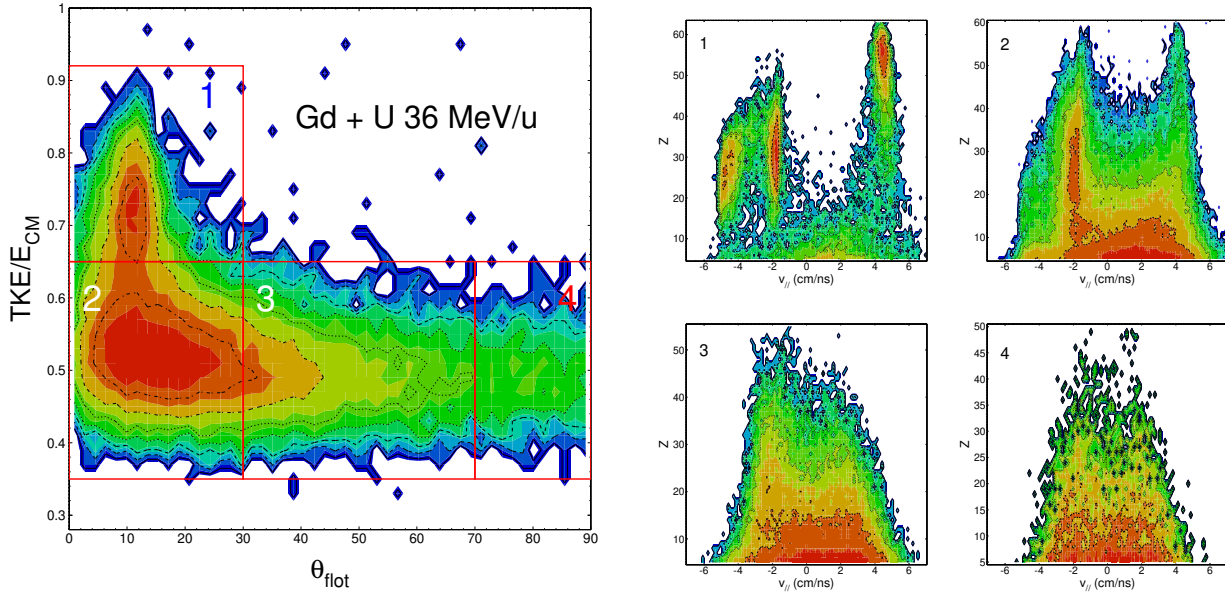


Figure 2.2.1 – (left) Pseudo-Wilczynski diagram for complete events (see text) measured for $^{155}\text{Gd}+^{238}\text{U}$ collisions at 36 MeV/u, total kinetic energy of reaction products in centre of mass frame versus the flow angle θ_f . (right) Atomic number-longitudinal velocity correlations for events in the four zones defined on the left.

DRA, is often approximated by the total pseudo-momentum,

$$ZV_{tot} = \sum_{i=1}^{N_C} Z_i v_{i,\parallel}$$

where the sums run over the total number of reconstructed charged products, N_C , and Z_i and $v_{i,\parallel}$ are respectively the atomic number and the longitudinal velocity (parallel to the beam direction) of the i^{th} nucleus of the event.

Although the “shape” variables derived from the eigenvalues suffer from the same Jacobian effects due to low multiplicity as any other, there is another information to be derived from this tensor which is independent of such effects. The eigenvector with the largest eigenvalue gives the direction of the largest flow of momentum or kinetic energy in the event, indicated by the polar angle θ_f it makes with the beam direction. Small flow angles then represent collisions with little change of the nucleon momentum distributions compared to the entrance channel, while larger and larger θ_f represent increasing violent and dissipative reactions. If fragments are produced by a single source in the centre of mass frame this angle should be isotropically distributed, even if the number of fragments is small: in this case θ_f is mostly determined by random fluctuations. Hence single source events, if present in the data, should be best isolated by a cut on θ_f corresponding to the value above which the distribution becomes approximately isotropic.

Selection of very heavy, compact, multifragmenting systems using the flow angle was first achieved by the Nautilus collaboration, but with a slightly different justification: Lecolley *et al.*

[40] related the θ_f angle to the orbiting time of the dinuclear system undergoing a deep-inelastic collision à la Wilczynski [41], with the largest angles supposed to correspond to infinite times, i.e. fusion. Although the validity of such reaction mechanisms to describe collisions at Fermi energies and above is far from certain, both interpretations lead to the same selection method. Figure 2.2.1(left) shows a pseudo-Wilczynski diagram (kinetic energy versus orbiting angle) constructed for well-measured (charge completeness criterion) $^{155}\text{Gd}+^{238}\text{U}$ collisions at $36A$ MeV, where the total centre of mass kinetic energy of all detected reaction products is plotted as a function of the flow angle calculated from the fragment ($Z \geq 5$) momentum tensor. It can be seen that most of the dissipation (decrease of total kinetic energy) takes place for forward-peaked events, $\theta_f \approx 10^\circ$, in zones 1 and 2 of this diagram, which the corresponding $Z-V_{\parallel}$ diagrams in Figure 2.2.1(right) show are the result of predominantly binary collisions with recognisable projectile- and target-like fragments and decay products. The remaining evolution towards the most compact events in the last zone (here for $\theta_f > 70^\circ$) takes place with hardly any further change in the degree of dissipation.

The flow angle selection for compact multifragmenting systems was first applied by the IN-DRA collaboration in [42] for collisions of $^{129}\text{Xe}+^{nat}\text{Sn}$ at $50A$ MeV. Then it was used in my Ph.D thesis as well as the accompanying and subsequent papers [43, 35, 44, 45] in order to select homogeneous samples of quasi-isotropic events for $^{155}\text{Gd}+^{238}\text{U}$ collisions at $36A$ MeV and $^{129}\text{Xe}+^{nat}\text{Sn}$ collisions at $32A$ MeV. Such events, originally termed “single source” events are nowadays more commonly referred to as events with quasi-fused or QF sources [46]. It is to event samples selected in this way (especially for $^{129}\text{Xe}+^{nat}\text{Sn}$ collisions) that the analyses of the collaboration demonstrating the occurrence of several of the expected signals of a first-order phase transition in a finite system were performed: spinodal decomposition [44, 45, 47] (see below), negative heat capacity [48, 49, 50], and back-bending constrained caloric curves [51]. The selection method was later validated *a posteriori*, at least for the $^{129}\text{Xe}+^{nat}\text{Sn}$ reactions, by Stochastic Mean Field (SMF) transport model calculations, published in Bonnet *et al.* [52]. I will try to shed some new light on the question of selecting homogeneous event samples corresponding to highly compact multifragmenting systems, and the significance of the large- θ_f events, in Part II, Chapter 7.

2.2.2 Spinodal decomposition & stochastic mean field calculations

The first evidence for a bulk effect, *i.e.* linking multifragmentation to bulk nuclear matter properties came from the comparison of the QF events for the two reactions $^{155}\text{Gd}+^{238}\text{U}$ at $36A$ MeV and $^{129}\text{Xe}+^{nat}\text{Sn}$ at $32A$ MeV, both of which lead to very similar available energies in the centre of mass frame, $E_{CM} = 8 \sim 8.5A$ MeV [43]. Although the $^{155}\text{Gd}+^{238}\text{U}$ system contains $\sim 50\%$ more protons than $^{129}\text{Xe}+^{nat}\text{Sn}$, the fragment atomic number distributions $P(Z)$ (shown in Figure 2.2.2) for the two systems are nearly identical (note that here “fragments” are defined as products with $Z \geq 5$). The difference in size of the two systems can be found in the mean multiplicity of fragments produced in each case, which increases exactly in the same ratio as the total charge of projectile and target: $\langle M_f^{Gd+U} \rangle / \langle M_f^{Xe+Sn} \rangle = 6.3/4.3 \approx 1.5$. Therefore we have here two nuclear systems prepared in similar conditions (similar excitation energy, similar temperature) which break up in the same way independently of their size; only the number of fragments produced depends on the amount of (nuclear) matter to be partitioned.

This behaviour is predicted by the hypothesis of multifragmentation due to spinodal instabil-

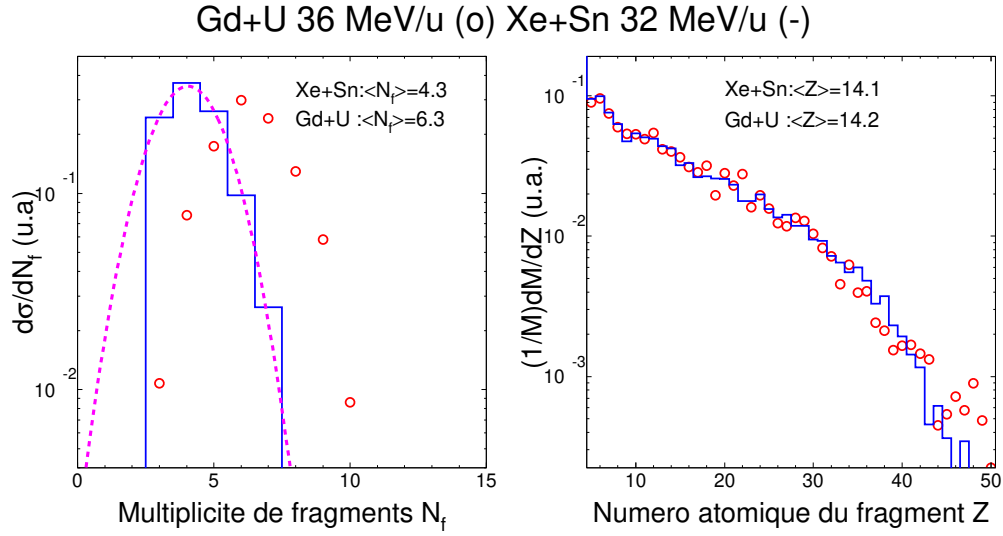


Figure 2.2.2 – Comparison of fragment ($Z \geq 5$) multiplicities (left) and atomic number distributions (right) for QF events from $^{155}\text{Gd}+^{238}\text{U}$ collisions at 36A MeV (red open symbols) and $^{129}\text{Xe}+^{nat}\text{Sn}$ collisions at 32A MeV (blue histograms).

ities. The dispersion relation for density fluctuations in unstable nuclear matter show that in case of spinodal instability there is always a “mode” of instability which develops faster than all others, and this mode is associated with a given wavelength [53, 54]. As the fragments form from the density fluctuations, they therefore have similar sizes/atomic numbers determined by this favoured wavelength, which at the typical temperatures reached in Fermi energy reactions ($T \sim 4 - 5$ MeV) corresponds to atomic numbers $Z \sim 10$. This prediction was the origin of attempts to demonstrate the presence of favoured partitions in multifragmentation initiated (unsuccessfully) by Moretto [55], and finally achieved thanks to the very high statistics of the 5th INDRA campaign data [47].

The next step was to perform a full dynamical simulation of the reactions using the (at the time) recently-developed stochastic mean field approaches [56]. Such approaches, based on the nuclear Boltzmann-Langevin equation [57], restore the fluctuations around the mean one-body evolution which are averaged out in approaches based on the nuclear Boltzmann equation [58] and so in case of the onset of instabilities in the reaction dynamics such an approach allows to explore the ensemble of possible exit channels *e.g.* in which the system undergoes multifragmentation (see Appendix A, A.1.3).

We used the BOB (Brownian One-Body dynamics model [56, 59]; see Appendix A, A.1.3.1) approximation to the full stochastic mean field dynamics for the simulation. In this model fluctuations are introduced *via* a stochastic force whose strength is tuned to correctly describe the growth rate of the most unstable modes in nuclear matter at a given temperature and density inside the spinodal region [54, 53]. As it was not possible to adjust the force during the dynamical evolution according to local equilibrium conditions, an initial calculation of the “source” conditions was performed for an impact parameter $b = 0$ using a standard BNV transport model (Boltzmann-Nordheim-Vlasov [58]; see Appendix A, A.1.2) employing a Skyrme interaction with

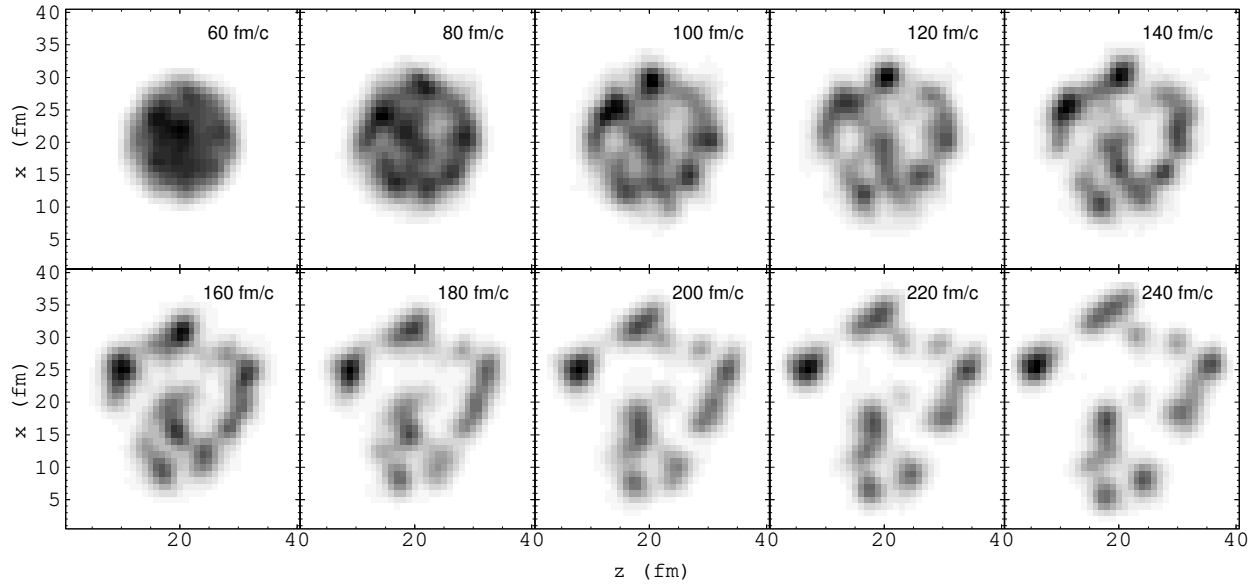


Figure 2.2.3 – BOB calculation of the spinodal decomposition of compact systems formed in head-on collisions of $^{155}\text{Gd}+^{238}\text{U}$. Grey-scale represents nucleon density in the xz -plane.

an incompressibility parameter $K_\infty = 200$ MeV (see [Appendix A, A.1.4](#)). The predictions of these calculations for both reactions is that, after a gentle compression phase ($\rho_{max} \approx 1.2\rho_0$), an isotropically expanding system is formed which enters the region of spinodal instability after $80 \sim 100$ fm/c at an average density $\rho \approx 0.4\rho_0$ and a temperature $T \approx 4$ MeV [44].

The total proton and neutron numbers, average density, temperature and expansion velocity of the “sources” calculated by BNV were then used as initial conditions for the BOB calculations with the appropriately-tuned stochastic force strength. Letting each expanding system evolve under the action of the mean field plus fluctuations, fragments form from the amplification of the unstable modes in the spinodal region, as shown in [Figure 2.2.3](#). The resulting fragments are well-separated after ≈ 240 fm/c and have an average excitation of $\sim 3.2A$ MeV. They were therefore used as input to an “after-burner” code (SIMON, [60]) capable of calculating their subsequent evaporative decay and Coulomb trajectories up to the detectors.

The results of the calculations [44] give an excellent reproduction of the experimental QF event characteristics such as the multiplicities and atomic number distributions of the fragments for the two systems, and therefore reproduce the initial experimental observation of the scaling of these observables with the system size (charge), confirming that such a bulk effect is linked to the origin of the observed multifragmentation in the spinodal instability of low density nuclear matter. This agreement extends to more detailed characteristics, such as the total charge bound in fragments, Z_{bound} , or the event-by-event distributions of the Z -ranked fragments, shown in [Figure 2.2.4](#) for the $^{129}\text{Xe}+^{nat}\text{Sn}$ data. The “shape” of the events in momentum space, *i.e.* their degree of isotropy was also well accounted for by the simulations. Later analyses of fragment-fragment velocity correlations [45] showed an excellent agreement concerning the topology of the system at freeze-out.

One aspect of the data which was not well reproduced, however, are the mean kinetic energies of the fragments for the $^{129}\text{Xe}+^{nat}\text{Sn}$ system, which were underestimated by $\approx 20\%$.

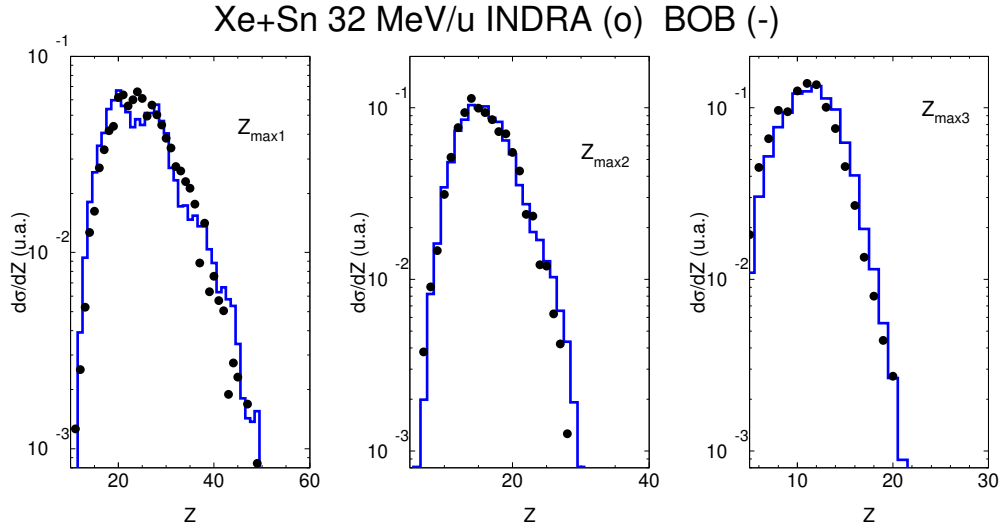


Figure 2.2.4 – Results of BOB calculations (after secondary decay) for QF reactions in $^{129}\text{Xe}+^{nat}\text{Sn}$ collisions at 32A MeV: distributions of the 3 first Z-ordered fragments of each event. Black full symbols are data, blue histograms calculations.

The $^{155}\text{Gd}+^{238}\text{U}$ system was not affected by this problem, presumably due to the much larger Coulomb repulsion in this case. This underestimation is a well-known drawback of attempts to include fluctuations of the correct amplitude in semi-classical mean-field approaches. In later calculations using the SMF model (see [Appendix A, A.1.3.1](#)) to calculate the full reaction dynamics beginning from $t = 0$ and at different impact parameters, the lack of radial flow for $^{129}\text{Xe}+^{nat}\text{Sn}$ at 32A MeV was such that this system did not even multi-fragment, as an abortive spinodal decomposition re-collapses to a compound nuclear state [61, 52]. Only more recently, with the inclusion of fluctuations in the full phase space, has the BLOB (Boltzmann-Langevin One-Body) model [62] reproduced the onset of multifragmentation through spinodal decomposition for $^{129}\text{Xe}+^{nat}\text{Sn}$ below 32A MeV.

This work was the first strong evidence that multifragmentation in central collisions is due to the onset of spinodal instability in finite systems composed of warm, dilute nuclear matter, as predicted by finite-temperature mean-field approaches employing effective nuclear interactions which lead to an Equation of State with a first-order liquid-gas phase transition at sub-saturation densities [21, 63, 64]. It provides a strong basis for the scenario of a compression-expansion cycle in central collisions which we will come back to later.

Let us mention in passing that calculations for the same two systems were made recently using the QMD model ([65]; see [Appendix A, A.1.3.2](#)) and compared to both the data and the BNV-BOB calculations [66]. The calculations, again performed for $b = 0$ collisions only, give a reasonable agreement with the fragment multiplicity and charge distributions, including the distributions of the first three Z-ranked fragments, although the Z_{bound} distribution for $^{155}\text{Gd}+^{238}\text{U}$ is not well reproduced. Unfortunately the authors of [66] gave no information on the kinematic properties of the simulated fragments. The interesting point about these calculations is that the fragments were reconstructed only 60-90 fm/c after the beginning of the reactions, when (accord-

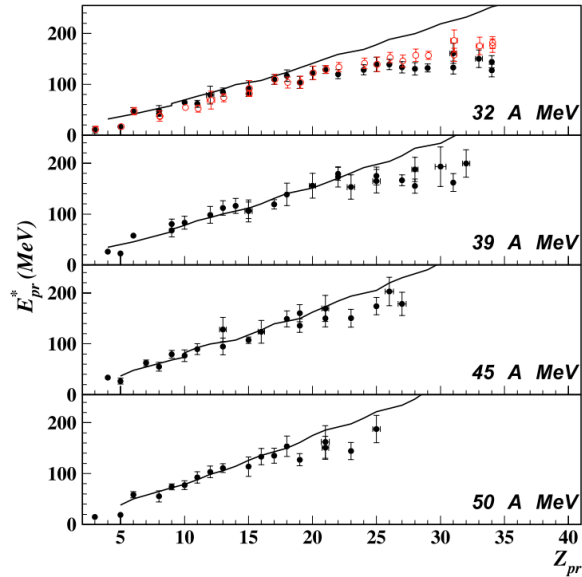


Figure 2.3.1 – Mean excitation energies of primary fragments (symbols) compared with SMM calculations (lines) for QF multifragmentation events of $^{129}\text{Xe}+^{nat}\text{Sn}$ from 32 to 50 A MeV [67].

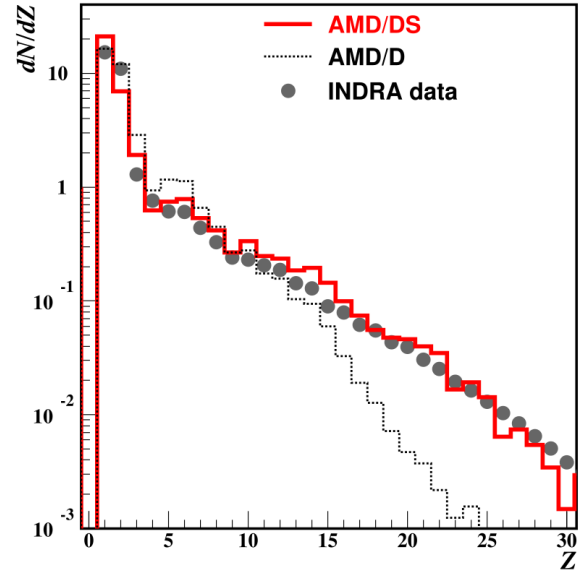


Figure 2.3.2 – AMD calculations for central $^{129}\text{Xe}+^{nat}\text{Sn}$ collisions at 50 A MeV with (DS) or without (D) the improvement introduced in [68].

ing to BNV) the system is compressed and/or expanding towards the spinodal density. However, the reconstructed fragments are found to be in their ground states, which is probably an artefact of the fragment reconstruction algorithm, and do not therefore undergo any evaporative decay, on the contrary to the experimental results of [67], presented in the next section.

2.3 Freeze-out properties and AMD calculations for $^{129}\text{Xe}+^{nat}\text{Sn}$ reactions

This study was part of the Ph.D. thesis of Sylvie Hudan [69], whose first aim was to extend the systematic study of $^{129}\text{Xe}+^{nat}\text{Sn}$ reactions begun during the 1st INDRA campaign at GANIL up to 150 A MeV using new data from the recently completed 4th campaign performed at the GSI laboratory. In addition, a detailed study of the multifragmentation reactions from 32 to 50 A MeV was used to quantify the statistical decay of the primary fragments, allowing to reconstruct for the first time experimentally the charge and excitation energy of the fragments at freeze-out [67]. It showed that the mean excitation energies of the primary fragments increases only slowly with the bombarding or available energy of the reactions, reaching an apparent maximum around 3 A MeV.

This is an important result as different models can give very different predictions for the excitation energies of primary fragments, while being equally good at describing the same data such

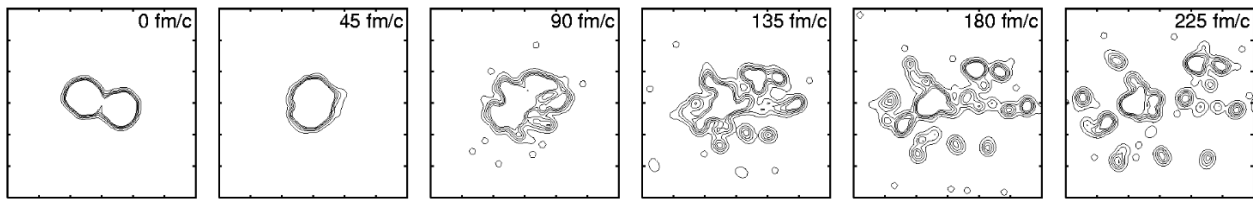


Figure 2.3.3 – Time evolution of the density in the centre-of-mass system projected onto the reaction plane calculated with AMD/DS for a typical collision of $^{129}\text{Xe}+^{nat}\text{Sn}$ at $50A$ MeV with impact parameter $b = 3.4$ fm. The beam direction is parallel to the horizontal axis, and the size of the shown area is $60\text{ fm} \times 60\text{ fm}$. From [68].

as charge distributions, mean energies, and angular distributions. In both Quantum Molecular Dynamics (QMD: [Appendix A, A.1.3.2](#)) or Microcanonical Metropolis Monte Carlo (MMMC: [Section §A.2](#)) calculations, the primary fragments are rather cold, *i.e.* they are almost unaffected by subsequent secondary decays and arrive unchanged in the detectors. In the former case, the lack of excitation energy in the nascent fragments is determined by the collision dynamics, whereas in the latter case, it is an assumption of the model when calculating the statistical weights of the partitions. On the other hand, Antisymmetrized Molecular Dynamics (AMD: [Appendix A, A.1.3.2](#)), as well as the stochastic mean field simulations presented in the previous section 2.2, both predict moderately “hot” primary fragments in reactions around the Fermi energy, with excitation energies $2 \sim 3A$ MeV.

Experimental results for primary fragment excitation energies are compared to calculations made with the Statistical Multifragmentation Model (SMM: [Section §A.2, A.2.1](#)) in [Figure 2.3.1](#). The SMM parameters (source charge, mass, excitation energy, freeze-out volume and radial flow) were fixed in order to well reproduce the experimental multiplicities, charge distributions and kinetic energies of fragments at each of the four bombarding energies from 32 to $50A$ MeV, with a fixed freeze-out volume equal to three times the volume of the source nucleus at normal nuclear density.

Over all, a satisfactory agreement is observed concerning the excitation energies of individual fragments (at least for $Z_{pr} \leq 20$). On the other hand, the average excitation energy of fragments in SMM calculations, although of the same order as the experimental values, is over-estimated and continues to increase with the incident energy. The saturation of primary fragment excitation energies was later confirmed using a different approach in the works of Piantelli et al [70, 71], where a vanishing level-density at high excitation energies of primary fragments was implemented following [72] by the introduction of a limiting temperature for the fragments; as a result, the temperatures associated to thermal motion of the fragments at freeze-out are no longer assumed to be the same as their intrinsic temperature (as in SMM), in agreement with the microcanonical treatment of [73].

The Ph.D. work of Sylvie Hudan also included the first comparisons of INDRA data with calculations performed with the AMD transport model. As far as $^{129}\text{Xe}+^{nat}\text{Sn}$ collisions at $50A$ MeV are concerned, it was the first time that AMD was used for such a heavy system, and at relatively low bombarding energies. The reactions were simulated for central impact parameters ($b < 4$ fm) and, after statistical decay using an afterburner and simulation of detection effects, compared to data for the 10% most central collisions selected with the total transverse energy of light charged

particles (see Part II, Chapter 6). Using the geometric prescription of [74] these collisions were estimated to correspond to impact parameters $b < 0.3b_{\max}$; for 50A MeV collisions a value of $b_{\max} = 9.8$ fm was deduced from the measured reaction cross-section [75]. The time evolution of a typical collision is shown in Figure 2.3.3.

A very satisfactory agreement with the data concerning fragment multiplicities, Z distributions and kinetic energies was achieved [76] at both energies, and especially at the lower energy of 50A MeV this was due to a significant improvement of the model made specifically in order to reproduce these data. The improvement concerns the treatment of the mean-field propagation of the wave packets used to represent each nucleon [68]. In previous versions of AMD (referred to as 'AMD/D' in Figure 2.3.2), wave packet diffusion during the propagation was implemented as a stochastic branching process, which could not consistently reproduce the one-body dynamics as predicted by mean field models.

The new version (referred to as 'AMD/DS'), incorporating wave packet shrinking as well as diffusion in order to have a coherent mean-field evolution, modified the dynamics so as to lower the expansion velocity of the fragmenting systems formed in central collisions, which is why the yields of the heavier fragments are much better reproduced by AMD/DS than by AMD/D (see Figure 2.3.2). The resulting AMD is a transport model incorporating many-body correlations (essential to describe cluster/fragment formation) while respecting the correct mean-field dynamics, as shown by later comparisons with Stochastic Mean Field calculations [77]. The need for a correct treatment of the mean-field and one-body dynamics in order to reproduce the data at 50A MeV also underlines the fact that the nuclear mean field still plays an important role at these energies.

2.4 Multifragmentation and universal fluctuations

2.4.1 Identifying the nature of the phase transition

A new approach to the study of critical phenomena in finite systems was developed in the early 2000s by Marek Płoszajczak¹ and Robert Botet²: the theory of universal order parameter fluctuations [78]. Initially conceived in the framework of continuous phase transitions³, the theory describes the fluctuations of the order parameter in a finite system as

$$\sigma_m^2 \sim \langle m \rangle^{2\Delta} \quad (2.4.1)$$

where the parameter Δ can take values in the range $1/2 \leq \Delta \leq 1$, the two extremes being associated with sub- or supercritical behaviour, respectively. This relationship provides a valuable tool for multifragmentation data analysis when looking for evidence of an underlying phase transition: in order to identify critical behaviour and the associated order parameter, it is sufficient to find an observable whose fluctuations change amplitude depending on an appropriate control parameter.

¹GANIL

²Laboratoire de Physique des Solides d'Orsay

³Continuous (or second-order) phase transitions occur without phase coexistence; as a function of the control parameter x , the order parameter m characterising the phase transition changes value from $m = 0$ to $m \neq 0$ at the so-called critical value of x .

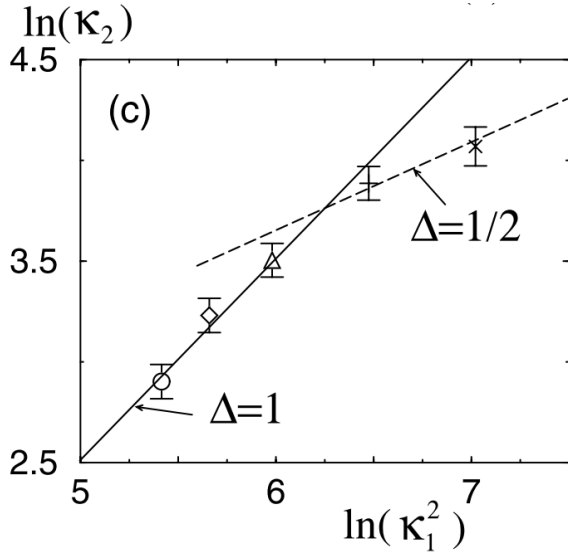


Figure 2.4.1 – Log variance $\ln(\kappa_2 = \sigma^2)$ of Z_{\max} distributions vs. log squared mean values $\ln(\kappa_1^2 = \langle Z_{\max} \rangle^2)$ for QF events from $^{129}\text{Xe} + ^{\text{nat}}\text{Sn}$ collisions from 25A MeV (right) to 50A MeV (left). From [79].

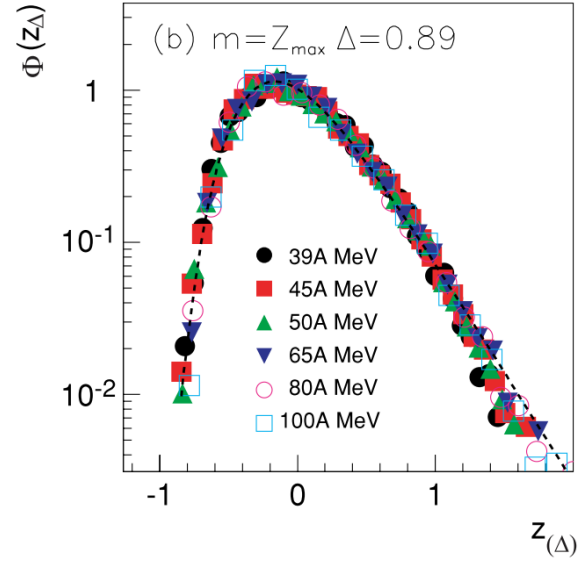


Figure 2.4.2 – Scaled Z_{\max} distributions for $^{129}\text{Xe} + ^{\text{nat}}\text{Sn}$ collisions from 39A MeV to 100A MeV reduced to a single Gumbel distribution, Equation (2.4.4) [82].

Such behaviour was first demonstrated experimentally for the QF multifragmentation events from $^{129}\text{Xe} + ^{\text{nat}}\text{Sn}$ reactions studied with INDRA, where, with $m = Z_{\max}$ (the largest atomic number Z measured in each event), Δ was shown to switch from $1/2$ to 1 between the bombarding energies of 32A MeV and 39A MeV (see Figure 2.4.1), whereas the fluctuations of the total multiplicity scale with $\Delta = 1/2$ at all energies [79]. This means that Z_{\max} , or the size (charge) of the largest fragment of each event, is closely related to the order parameter of a phase transition, whereas the number of fragments is not.

This result is far from trivial, as all generic models of critical clusterization phenomena can be classed into two groups, each with a characteristic order parameter: for *fragmentation* models (breaking a large cluster into smaller pieces) it is the number (multiplicity) of clusters, whereas for *aggregation* models (small clusters group together into larger ones) it is the size of the largest cluster.

Therefore just the simple observation that the reduced fluctuations $\sigma^2 / \langle Z_{\max} \rangle$ change scaling behaviour with increasing energy answers two of the oldest questions concerning multifragmentation. The first, asked ever since Finn et al. observed a power law mass distribution for fragments [80], is: *is multifragmentation linked to a phase transition?* The definitive answer from the universal fluctuations analysis is yes, because we can identify an order parameter associated with multifragmentation which exhibits “critical” behaviour, Z_{\max} . The second comes from the title of a paper from 1984 by Jörg Aichelin and Joerg Huefner [81]: *condensation of vapour or shattering of glass?* The identification of Z_{\max} as the order parameter of the transition clearly shows that we are dealing with a phenomenon much closer to the former than to the latter.

2.4.2 Form of the scaling function and pseudo-criticality

In reality, the scaling of an observable's fluctuations as in Equation (2.4.1) is not a sufficient condition for it to be considered an order parameter: the observable's probability distributions $P(m)$ must also collapse to a unique scaling function when expressed in terms of the scaling variable $z_{(\Delta)} = (m - \langle m \rangle) / \langle m \rangle^\Delta$,

$$\Phi(z_{(\Delta)}) = \langle m \rangle^\Delta P(m) \quad (2.4.2)$$

as was indeed shown in [79] for Z_{\max} . However the theory tells us next to nothing about the functional form of $\Phi(z_{(\Delta)})$, except that close to a critical point the tail of the distribution for large $z_{(\Delta)}$ should fall off faster than $\exp -z_{(\Delta)}^2$, which is never observed in data.

In [82] we extended the analysis to the full set of data for symmetric collisions studied up to that point with INDRA (from Ar+KCl to Au+Au). For nearly all data, at low energy when $\Delta \sim 1/2$ the scaling function is approximately Gaussian (but see 2.5.2 below). On the other hand, for all systems which exhibit the $\Delta \sim 1$ scaling, the scaling function has a very particular form known from extremal statistics: to a good approximation it can be described by the Gumbel distribution [83]

$$\phi_k(s_k) = \frac{k^k}{(k-1)! b_M} e^{-k(s_k + e^{-s_k})} \quad (2.4.3)$$

with $s_k = (Z_k - a_M) / b_M$, which is one of the limiting forms for the probability distribution of the k -largest value Z_k among a set of (uncorrelated) random variables. For $k = 1$ we have $Z_1 \equiv Z_{\max}$ and the asymmetric distribution with an exponential tail seen in Figure 2.4.2 is given by

$$P(Z_{\max}) \sim \exp \left(-(Z_{\max} - e^{-Z_{\max}}) \right) \quad (2.4.4)$$

The Gumbel distribution is the equivalent, for extremal statistics, of the Gaussian distribution for the central limit theorem: the Gaussian is the asymptotic distribution of the sum of a set of (uncorrelated) random variables, whereas Gumbel is the asymptotic distribution of the extremum (maximum or minimum) of the set. Note that in both cases, the random variables are assumed to follow the same underlying probability law.

It was noted in [82] that the $P(Z_{\max})$ data tend to resemble more and more the Gumbel distribution the higher the bombarding energy, but also the higher the considered system mass (or charge). For the heaviest system studied in [82], the agreement can in fact be extended beyond Z_{\max} using Equation (2.4.3). Fig. 2.4.3 presents the distributions for the first three Z -ranked fragments, with $Z_1 > Z_2 > Z_3$, produced in each central collision⁴ of $^{197}\text{Au} + ^{197}\text{Au}$ at bombarding energies 40, 60, 80 and 100 A MeV. It can be seen that each of these distributions is very well-fitted by Equation (2.4.3) using the appropriate value of $k=1, 2$ or 3.

This was first time that the presence and importance of the Gumbel distribution, and therefore of extremal statistics, had been recognized in multifragmentation data. Asymptotically, the large- Z_{\max} tail of the Gumbel distribution is exponential, therefore in the universal fluctuations

⁴Here the selection was made by retaining events belonging to the upper centile of the distribution of $Z_{\text{tot}} \times E_{\text{t12}}$.

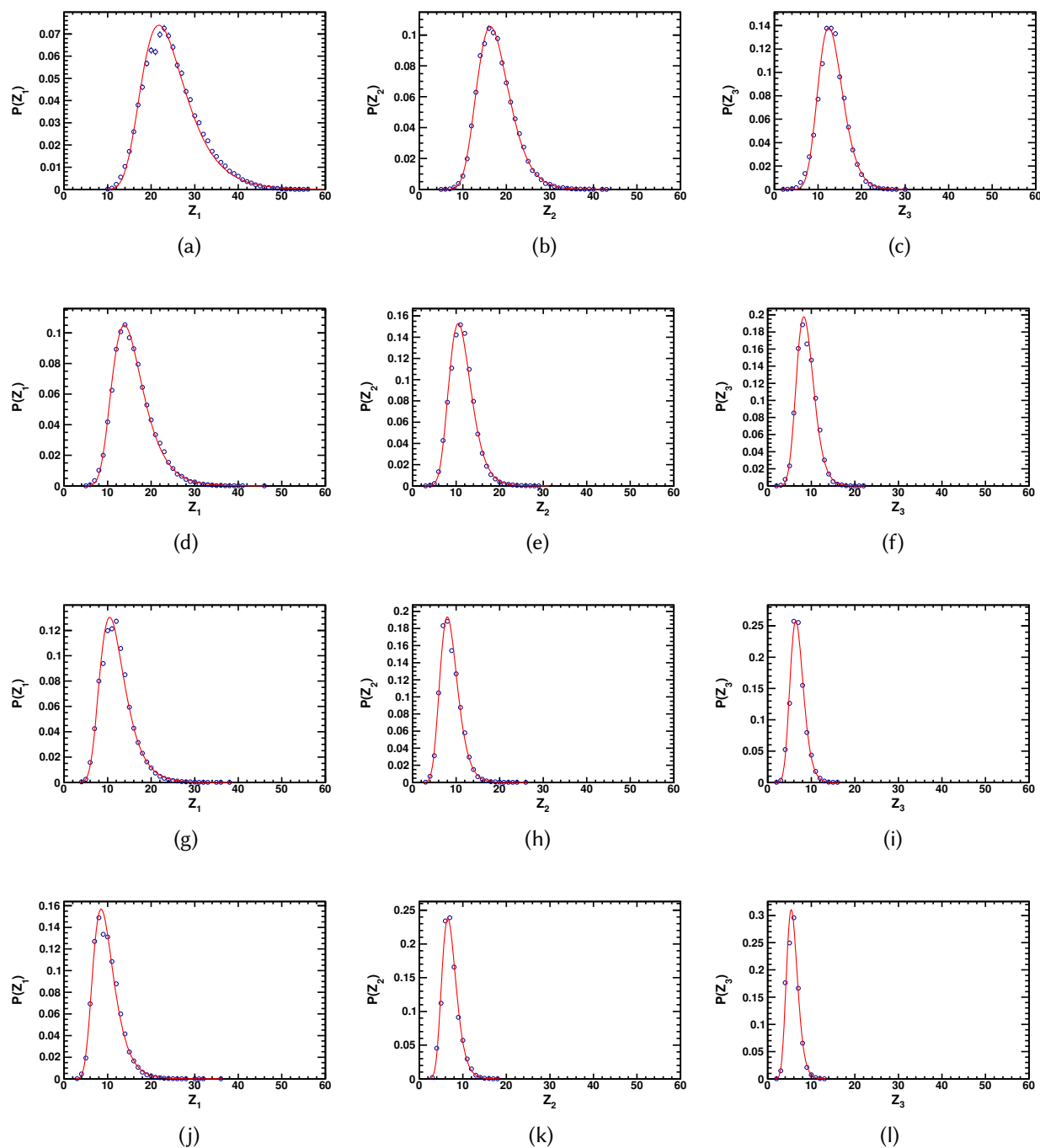


Figure 2.4.3 – Fits to the probability distributions of the atomic numbers of the three largest fragments, $Z_1 > Z_2 > Z_3$, produced in each event in central collisions of $^{197}\text{Au} + ^{197}\text{Au}$ at different bombarding energies: (a)-(c): 40A MeV; (d)-(f): 60A MeV; (g)-(i): 80A MeV; (j)-(l): 100A MeV.

framework the observation of this form of $P(Z_{\max})$ in the $\Delta = 1$ scaling regime means that although fluctuations become very large, systems never approach a critical point. This is consistent with [84], where it was shown that a critical behaviour in fragment observables can be consistent with phase coexistence and the occurrence of a low freeze-out density due to finite size effects.

Indeed, for finite (small) systems it is sufficient for fluctuations (or, equivalently, the correlation length) to be of the same order as the size of the system to mimic critical fluctuations on all length scales which would be induced by a divergence of the correlation length in an “infinite” system, *i.e.* in the thermodynamic limit. There is no contradiction between the scenario of nuclear fragmentation inside the coexistence or the spinodal region associated with a first order phase transition and the observation of various scaling laws and other pseudo-critical behaviour [49]. For more on these aspects, see Sec. 6.2 of [1].

An example of such pseudo-criticality can be derived from the Gumbel fits with Equation (2.4.3) shown in Figure 2.4.3. As mentioned above, the underlying statistical law governing the “random variables” Z is assumed to be the same, in which case the parameters b_k of Equation (2.4.3) should be the same for all k (*i.e.* for fits to Z_1 , Z_2 and Z_3) at a given energy. This is approximately satisfied by the fits shown here, and the mean value of $\bar{b} = \sum_{k=1}^3 b_k/3$ exhibits a bombarding energy E_b dependence which is highly reminiscent of the behaviour of critical exponents near a critical point [85]:

$$\bar{b} \sim |E_b - 24.4|^{-\nu}$$

with $\nu = 0.5$. Needless to say, there are currently no plans to search for evidence of this “critical” point for multifragmentation by performing $^{197}\text{Au}+^{197}\text{Au}$ collisions at $24.4A$ MeV.

2.5 Multifragmentation and radial flow

One of the most important contributions of the INDRA collaboration since 1993 has been to demonstrate, through many different works (some of which are presented here; for the rest, see [1]), that the origin of multifragmentation lies in the clusterization of excited nuclear matter at sub-saturation densities, as described in the [Introduction](#) of this chapter. In central heavy-ion collisions, such densities are reached through a compression-expansion cycle: during the approach and stopping phase of the collision, matter is compressed and heated; a combination of Coulomb repulsion, thermal pressure and the incompressibility of nuclear matter then provokes a “rebound” and the system begins to expand towards low densities, where fragments form through spinodal instability. This is the typical scenario long predicted by semi-classical mean field models such as [86, 87, 88].

Traces of this expansion can be found in the kinetic energies of the fragments, which exceed the values expected solely from thermal and Coulomb contributions [89, 90, 91, 92] which can be calculated using statistical multifragmentation models (see Section §A.2). For example, the Microcanonical Multifragmentation Model (MMM: see A.2.2) was successfully used to reproduce the data for the QF events of $^{129}\text{Xe}+^{nat}\text{Sn}$ 32A MeV and $^{155}\text{Gd}+^{238}\text{U}$ 36A MeV in [93], not only the fragment partition properties but also mean kinetic energies and fragment-fragment velocity correlations. The best agreement was achieved for freeze-out volumes $V \approx 8.5V_0$ and a non-Hubbleian radial flow of $\approx 1.8A$ MeV for both systems. Nevertheless, without an independent experimental measurement of the freeze-out volume this method can only give a model-

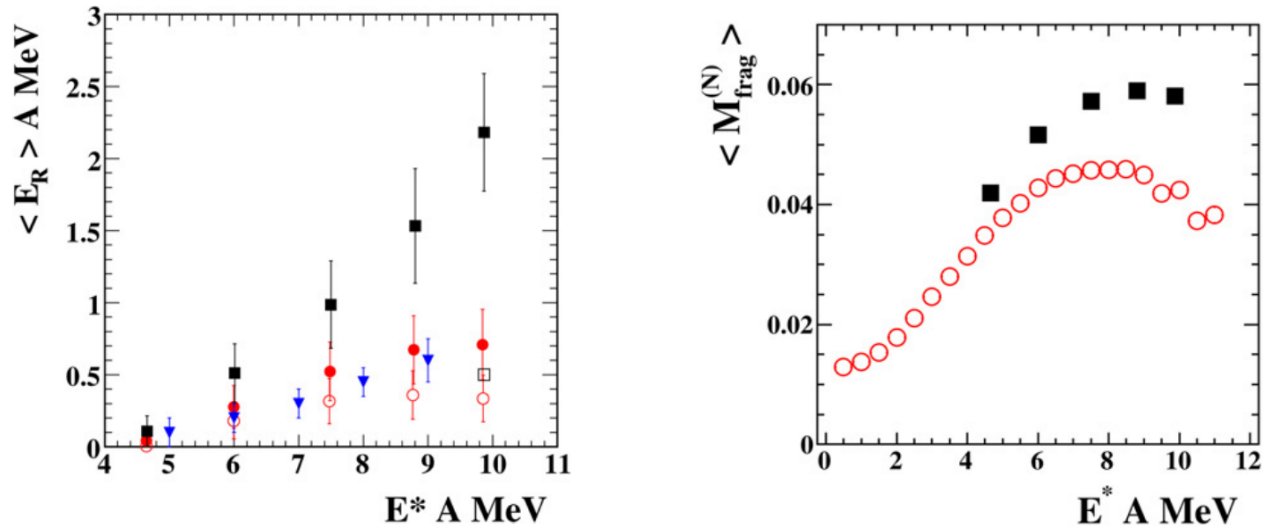


Figure 2.5.1 – (left) Radial collective energy E_R as a function of excitation energy per nucleon E^* for $^{129}\text{Xe} + \text{nat}\text{Sn}$ QF sources (black squares), QP sources from 80 (red open circles) and 100 MeV (red full circles) $^{197}\text{Au} + ^{197}\text{Au}$ reactions, and for $\pi^- + ^{197}\text{Au}$ reactions (blue triangles). (right) Mean fragment multiplicities normalised to source size (charge), $M_{frag}^{(N)}$, as a function of excitation energy per nucleon E^* . Symbols as for left panel. From [46].

dependent estimate of the expansion energy: the larger the assumed volume, the lower the inter-fragment repulsion due to Coulomb, and the larger our estimate of the radial flow energy.

During the Ph.D thesis of Diego Gruyer (2011-2014), new evidence of the important role played by collective radial expansion in the multifragmentation of excited nuclear systems was brought to light in two original works presented in this section.

2.5.1 Multifragmentation for different entrance channel asymmetries

Estimates of radial expansion energy from experimental data on multifragmentation have mostly been obtained from comparisons of kinetic properties of fragments with statistical model calculations or any other method of reconstructing the system at freeze-out, which can provide an estimate of the part of the fragment kinetic energies which can be attributed to thermal motion and Coulomb repulsion; any extra radial motion of the fragments can then be attributed to expansion energy (for the best example of an application of this method, see [71]).

Nevertheless any such reconstruction necessarily involves a large amount of hypotheses and resulting ambiguities, therefore a new method of estimating the expansion energy was developed by Eric Bonnet during his Ph.D (2003-2006) which is far less model-dependent. Based on the Coulomb-corrected mean relative velocities between fragments in each event, it was used to measure and compare the radial flow for multifragmenting sources with the same excitation energies produced in different reactions [46]. Figure 2.5.1(left) compares the expansion energy for $^{129}\text{Xe} + \text{nat}\text{Sn}$ QF sources produced in central collisions with that deduced from fragments produced by the break-up of quasi-projectile (QP) sources from peripheral $^{197}\text{Au} + ^{197}\text{Au}$ collisions

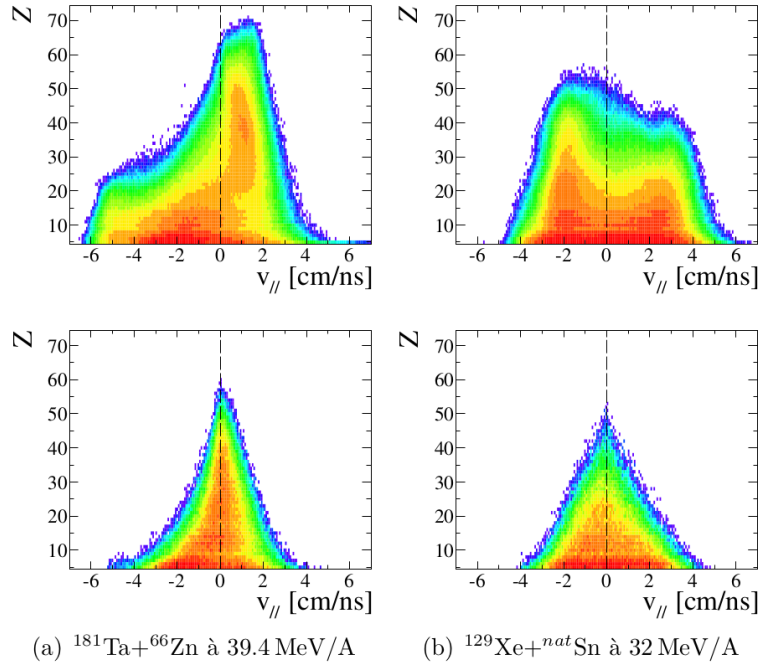


Figure 2.5.2 – Atomic number Z and longitudinal velocity $v_{||}$ correlations for fragments in (top row) well-detected events (see text) and (bottom row) QF events selected with $\theta_f > 70^\circ$. From [96].

at $80A$ MeV and $100A$ MeV⁵. The large differences in E_R which are observed beginning from $E^* = 6A$ MeV demonstrate the importance of the compression-expansion cycle in the QF reactions, absent in the case of semi-peripheral collisions producing an excited QP fragment. For comparison, radial flow energies for hadron-induced multifragmentation reactions at similar excitation energies, measured by the ISIS collaboration [95], are also shown in the figure: in such a reaction ($\pi^- + ^{197}\text{Au}$) there can be no doubt that only thermal pressure and Coulomb repulsion contribute to the expansion. This shows that radial collective energy is essentially produced by thermal pressure in semi-peripheral heavy-ion collisions while for QF sources produced in central collisions the contribution from the compression-expansion cycle becomes more and more important as the incident energy increases.

For similar-sized systems produced by the two reaction mechanisms at the same E^* , quantities such as the total charge bound in fragments ($Z \geq 5$) normalized to the total charge of the source, the mean charge of the largest fragment $\langle Z_{max} \rangle$, or the normalized multiplicity of light charged particles are the same. However, thermal excitation energy alone does not determine the way in which nuclear systems undergo multifragmentation. Figure 2.5.1(right) shows that the mean normalised fragment multiplicity, $M_{frag}^{(N)}$, is greater for QF multifragmentation than for QP sources, and in [97] it was shown that at a given total excitation energy per nucleon the amount of radial collective energy, E_R , fixes $M_{frag}^{(N)}$, which in turn fixes the properties of the fragment

⁵In fact, the values of E_R for the $32 - 50A$ MeV $^{129}\text{Xe}+^{nat}\text{Sn}$ data are from the Ph.D of Nicolas Le Neindre [94], deduced from comparisons with SMM; these values were used to “calibrate” the relative velocity measurement, allowing to deduce values of E_R for the $25A$ MeV data as well as for the $^{197}\text{Au}+^{197}\text{Au}$ QP data.

partitions, which are in general more symmetric in the presence of larger collective expansion.

We decided to put this new understanding of the link between radial flow and fragment partitions to the test with a new experiment. To make the simplest comparison possible between multifragmentation reactions induced with different amounts of radial flow, we decided to reproduce the $^{129}\text{Xe}+^{nat}\text{Sn}$ QF sources using a different entrance channel: $^{181}\text{Ta}+^{66}\text{Zn}$. By using an asymmetric entrance channel, we can trigger multifragmentation in systems of the same size/charge, at the same excitation energy per nucleon, using the same reaction mechanism of central collisions, but with a smaller compression-expansion cycle as the reduced overlap volume for the asymmetric system limits the amount of stopping and hence the maximum densities achieved.

The bombarding energies used in the experiment, 31.8 and 39.4 A MeV, were fixed to give the same available centre of mass energies as for the existing $^{129}\text{Xe}+^{nat}\text{Sn}$ data at 25 and 32 A MeV, *i.e.* $E_{cm} \sim 6A$ MeV and $E_{cm} \sim 8A$ MeV respectively. A higher maximum energy would have been possible with a lighter projectile *i.e.* using direct kinematics; however in that case the reduced velocity of the centre of mass frame makes complete detection and identification of the reaction products less likely, as was already seen for the $^{58}\text{Ni}+^{197}\text{Au}$ system (which is indeed approximately an asymmetric version of $^{129}\text{Xe}+^{nat}\text{Sn}$) measured during the 2nd INDRA campaign [98]. The experiment, numbered E613, presented to the GANIL PAC in 2010, was accepted and scheduled for October 2011, which coincided perfectly with the beginning of Diego Gruyer's Ph.D thesis.

Figure 2.5.2 shows atomic number-longitudinal velocity correlations for the two reactions with the highest available energy in the centre of mass ($E_{cm} \sim 8A$ MeV). In the top row, these correlations concern only the most well-detected ("complete") events (see Sec. 2.2.1). The bottom row presents the same correlations for QF events selected with a flow angle cut $\theta_f > 70^\circ$. The effectiveness of the cut in isolating compact events is clear from the comparison between these figures, especially for the asymmetric $^{181}\text{Ta}+^{66}\text{Zn}$ system which shows a strong contribution from heavy quasi-projectile nuclei without the θ_f cut. Another result can also be seen in the correlations for the QF events: the fragments for the asymmetric entrance channel have slightly larger Z than for $^{129}\text{Xe}+^{nat}\text{Sn}$.

As shown in Figure 2.5.3(left), this is not solely due to the largest fragment of each event: even when Z_{\max} is excluded, the distribution of all the remaining fragments still extends further in Z for the QF sources produced by the asymmetric $^{181}\text{Ta}+^{66}\text{Zn}$ reaction. The mean total charge bound in fragments is the same within 3% for each pair of reactions, therefore unsurprisingly the reason for the heavier fragments in the asymmetric reaction is the fragment multiplicity which is 20% larger on average for the symmetric $^{129}\text{Xe}+^{nat}\text{Sn}$ reaction at both energies.

The expected effects on the fragment partitions are therefore observed, but are they due to a difference of radial expansion energy? A first answer to this question can be obtained by looking at mean fragment kinetic energies in the centre of mass frame as a function of their atomic number (Fig. 2.5.3(right)). Sorting the mean energies according to Z means that at least to a first order approximation we can consider that the Coulomb contribution to $\langle E \rangle$ for each of the two reactions is the same (especially as the overall total charge is the same in both cases). As can be clearly seen, the mean kinetic energies of all fragments (again, excluding the largest fragment of each event) are significantly higher for the $^{129}\text{Xe}+^{nat}\text{Sn}$ data than for $^{181}\text{Ta}+^{66}\text{Zn}$, although fragments in the $^{129}\text{Xe}+^{nat}\text{Sn}$ case are on average smaller in Z , as expected if collective flow is more important for the symmetric reaction.

This is confirmed by the Coulomb-corrected mean relative velocity between fragments in

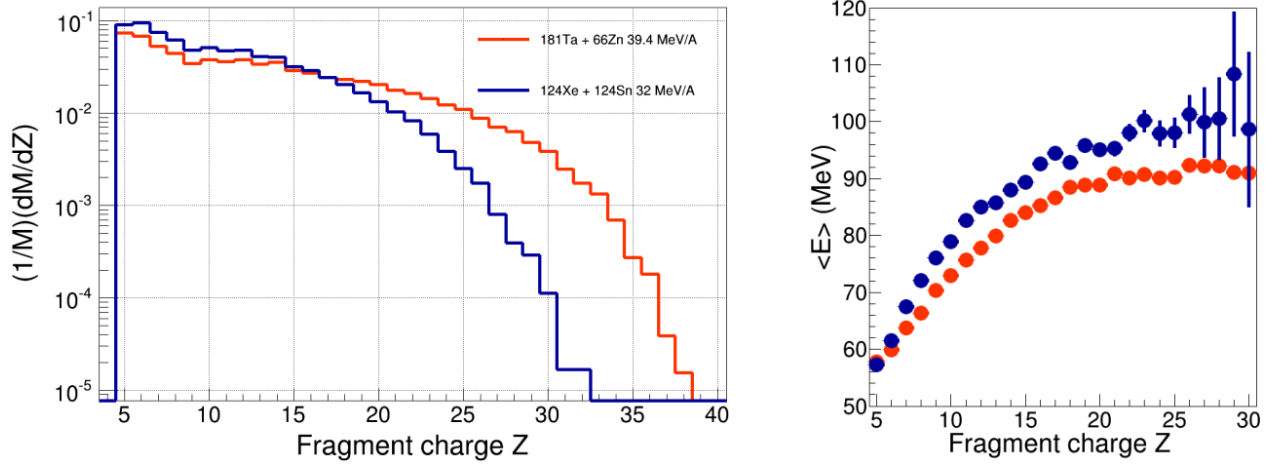


Figure 2.5.3 – Comparison of QF multifragmentation events with $E_{cm} \sim 8A$ MeV for symmetric or asymmetric entrance channel. (left) distributions of fragment ($Z \geq 5$) atomic number; (right) mean centre of mass kinetic energy of fragments as a function of Z . In both cases, the largest Z fragment of each event is excluded. From [99].

each event, which is 23% higher for the $^{129}\text{Xe} + ^{nat}\text{Sn}$ data at $E_{cm} \sim 8A$ MeV (bombarding energy $32A$ MeV). Using the calibration curve given in Fig. 8 of [46] we can estimate that there is a difference of $1A$ MeV in the radial expansion energy E_R produced in $^{129}\text{Xe} + ^{nat}\text{Sn}$ central collisions at $32A$ MeV compared to $^{181}\text{Ta} + ^{66}\text{Zn}$ reactions at $39.4A$ MeV.

These results are therefore the strongest confirmation to date that for a given excitation energy per nucleon and source size it is the amount of radial flow which determines the fragment multiplicity and partition properties, as first proposed in [46]. It should be recalled that in all statistical models of multifragmentation [100, 101] collective flow is not included in the calculation of the statistical weights. For a further, final, surprising confirmation of the difference in radial flow between the two reactions, however, we will have to wait until the end of the next section.

2.5.2 Multifragmentation timescale and Z_{max} fluctuations

In 2004, even before publication of our article [82] extending the universal fluctuations analysis to cover most of the INDRA dataset, Abdou Chbihi suggested that, rather than separating the data into two distinct classes of order parameter distributions, Gaussian at low energies and Gumbellian at high energies, we should fit the Z_{max} distribution for each bombarding energy with a weighted sum of the two distributions,

$$P(Z_{max}) = \eta P_{\text{Gauss}}(Z_{max}) + (1 - \eta) P_{\text{Gumbel}}(Z_{max}) \quad (2.5.1)$$

with $0 \leq \eta \leq 1$.

As Figure 2.5.4 shows, the shapes of the experimental $P(Z_{max})$ distributions are very well fitted by this admixture of the two asymptotic distributions, and far better than by one or the other distribution alone (according to the comparison of χ^2 values for fits, see [102]). However,

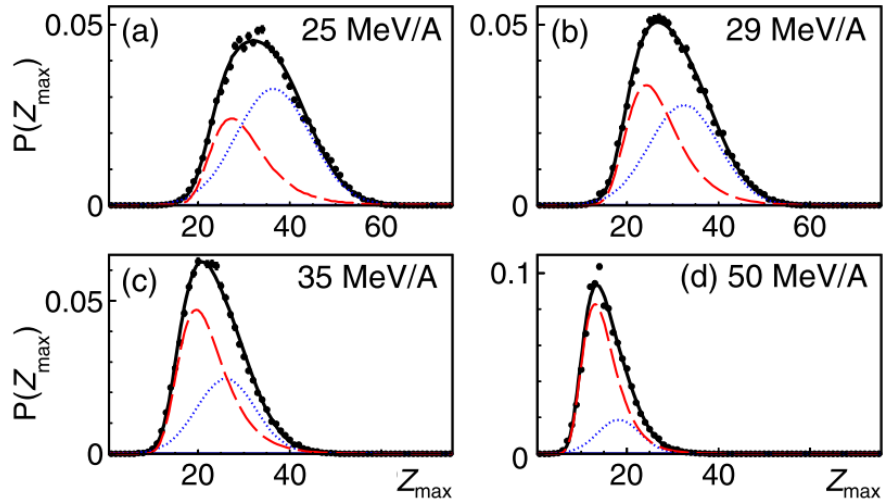


Figure 2.5.4 – Experimental Z_{\max} distributions for central $^{129}\text{Xe}+^{nat}\text{Sn}$ collisions (black points) at the bombarding energies shown in the figure, fitted with the weighted sum of Equation (2.5.1) (black curve) and showing the Gaussian (blue) and Gumbellian (red) component of each fit. From [102].

until 2011 we had no way to interpret the meaning of this result, until Robert Botet made some new calculations with an irreversible aggregation model applied to finite (small) systems.

The irreversible sol-gel transition can be modelled using the coupled non-linear differential equations in cluster concentrations c_s (the Smoluchowski equations [103])

$$\frac{dc_s}{dt} = \frac{1}{2} \sum_{i+j=s} K_{i,j} c_i c_j - \sum_j K_{s,j} c_s c_j \quad (2.5.2)$$

where s is cluster size and the concentrations are given by

$$c_s = \lim_{N \rightarrow \infty} \frac{n_s}{N}$$

with n_s the number of clusters of size s in a system of size $N = \sum_s n_s s$. Coefficients $K_{i,j}$ (aggregation kernels) represent the probability of aggregation per unit time between clusters of mass i and j . The sol-gel transition in this model, as in percolation [104], corresponds to the appearance of an “infinite” cluster which contains a finite fraction of the total mass of the system. The transition occurs when the order parameter, which is the gel fraction

$$m_G = \lim_{N \rightarrow \infty} \frac{1}{N} \langle s_{\max} \rangle \quad (2.5.3)$$

where s_{\max} is the size of the largest cluster, becomes non-zero. The size of the largest cluster can therefore be treated as an order parameter of the model, as for percolation. In the specific case with $K_{i,j} = ij$ the gel fraction $m_G = 0$ for times $t < t_c$, where the critical time $t_c = 1$, and $m_G \rightarrow 1$ for $t > t_c$ ⁶.

⁶It is interesting to note that the cluster size distribution is a power law, $P(s) \sim s^{-\tau}$ (with $\tau = 5/2$) for all times

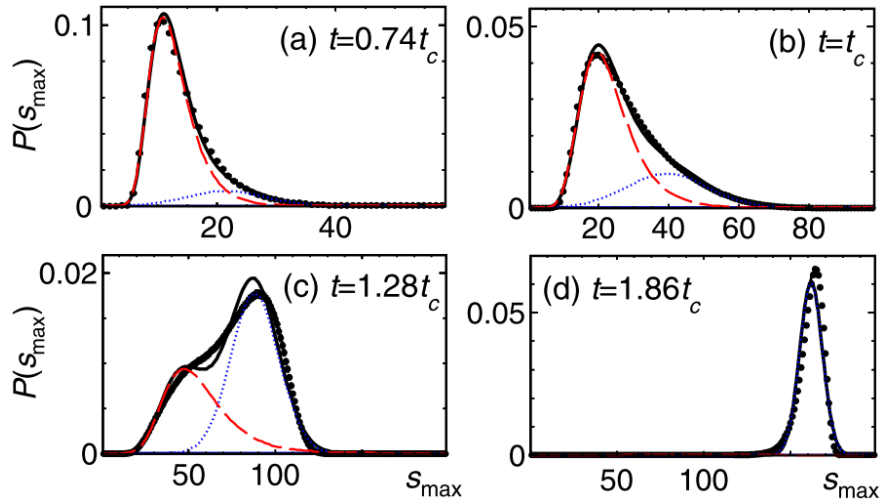


Figure 2.5.5 – Distributions of the largest cluster size s_{max} calculated using the Smoluchowski equations Equation (2.5.2) for a system size $N = 216$ at different times (black points) fitted with the weighted sum of Equation (2.5.1) (black curve) and showing the Gaussian (blue) and Gumbellian (red) component of each fit. From [102].

Botet and Ploszajczak had already shown in 2000 that the distribution $P(s_{max})$ of the largest cluster could have two distinct forms, Gaussian for $t \gg t_c$ in the gel phase, where the distributions scale with $\Delta = 1/2$, whereas for $t = t_c$ and the $\Delta = 1$ scaling, Figure 5 of [78] presents a characteristically asymmetric distribution with a long large- s_{max} tail: although not identified as such at the time (that did not occur until our paper [82] of 2005), it appears very close to a Gumbel distribution. These calculations were made for quasi-infinite systems with $N = 2^{10} - 2^{14}$: what Robert did now was to repeat the model calculations with $N = 216$, comparable to nuclear system “sizes”.

What the new calculations showed (see Figure 2.5.5) was a continuous evolution of $P(s_{max})$ from the Gumbel form at early times before t_c , with a Gaussian component appearing at large s_{max} for $t \sim t_c$ and becoming dominant for $t \gg t_c$. What this also means is that the order parameter s_{max} changes nature over time: from extremal (largest among a random set of clusters) to additive (largest because of successive addition *i.e.* aggregation of random clusters).

Of course, the physical picture of clusters being built-up over time by agglomeration described by the Smoluchowski equations recalls microscopic approaches in which fragments result from the spinodal decomposition of hot, expanding nuclear matter. In order to make the link between the Smoluchowski result (Fig. 2.5.5) and that for data (Fig. 2.5.4) requires to make a link between bombarding energy and the timescale of fragment formation, for which a determining factor is the amount of collective radial expansion: then the similarity between Fig. 2.5.5 and 2.5.4 can be understood in terms of fragment size distributions being determined on shorter and shorter time scales due to increasing radial flow with increasing bombarding energy (see Figure 2.5.1(left),

$t > t_c$, not only at the critical threshold. The whole distribution of finite-size clusters evolves self-similarly, and the appearance of a power-law behaviour is not a sign of a critical behaviour but a specific characteristic of the gelation phase [78].

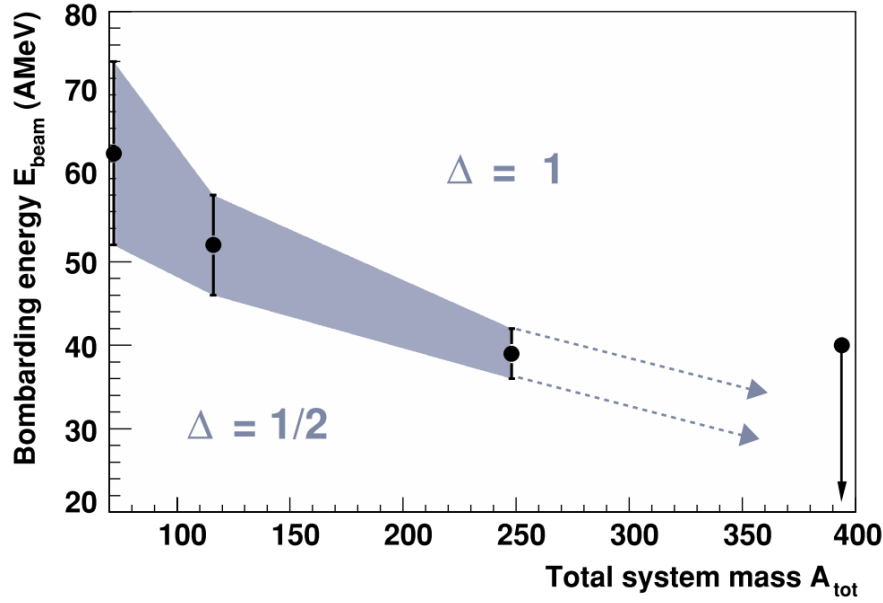


Figure 2.5.6 – Δ -scaling map showing the total system mass-dependence of the bombarding energy at which the change of Δ -scaling regime takes place for $^{36}\text{Ar}+\text{KCl}$, $^{58}\text{Ni}+^{58}\text{Ni}$, $^{129}\text{Xe}+^{\text{nat}}\text{Sn}$ and $^{197}\text{Au}+^{197}\text{Au}$ collisions. From [82].

Sec. 2.5.1). A similar scenario was earlier proposed by the FOPI collaboration of nuclear droplets forming in hot expanding nuclear matter, where radial expansion provides a local cooling mechanism allowing the survival of clusters heavier than α particles [105]: however, in their case, the reactions studied were at $400A$ MeV so the surviving fragments remained quite small ($Z < 10$) compared to the data presented here.

Furthermore, this interpretation of the results allowed us to finally understand the Δ -scaling “phase map” for the four systems $^{36}\text{Ar}+\text{KCl}$, $^{58}\text{Ni}+^{58}\text{Ni}$, $^{58}\text{Ni}+^{58}\text{Ni}$ and $^{197}\text{Au}+^{197}\text{Au}$, shown in Figure 2.5.6, that was the main result of [82]. This figure captures the essential results of the universal fluctuations analysis applied to central collisions for these 4 systems, concerning the bombarding energy at which the scaling of the Z_{max} fluctuations changes from $\Delta = 1/2$ to $\Delta = 1$, and the distributions $P(Z_{\text{max}})$ change from (dominantly) Gaussian to (dominantly) Gumbellian form. In fact, the actual change of regime is only observed for $^{58}\text{Ni}+^{58}\text{Ni}$ and $^{129}\text{Xe}+^{\text{nat}}\text{Sn}$ reactions, whereas the lightest system, $^{36}\text{Ar}+\text{KCl}$, exhibits only $\Delta = 1/2$ scaling with Gaussian $P(Z_{\text{max}})$ distributions and the heaviest, $^{197}\text{Au}+^{197}\text{Au}$, only $\Delta = 1$ scaling and Gumbellian $P(Z_{\text{max}})$ distributions (see Figure 2.4.3).

Radial expansion in central heavy-ion collisions occurs after significant compression of the incoming nuclear fluid, and as such depends not only on static nuclear matter properties such as incompressibility, but also on transport properties such as the degree of stopping achieved in the collision, shown to increase with system mass above the Fermi energy for the same data in [106], and linked to the energy dependence of the in-medium nucleon-nucleon cross-section or mean free path in [107]. Thus for light systems, such as $^{36}\text{Ar}+\text{KCl}$ or $^{58}\text{Ni}+^{58}\text{Ni}$, the bombarding energy required to achieve sufficient initial compression for there to be significant radial expansion is higher than for heavier systems like $^{129}\text{Xe}+^{\text{nat}}\text{Sn}$ or $^{197}\text{Au}+^{197}\text{Au}$.

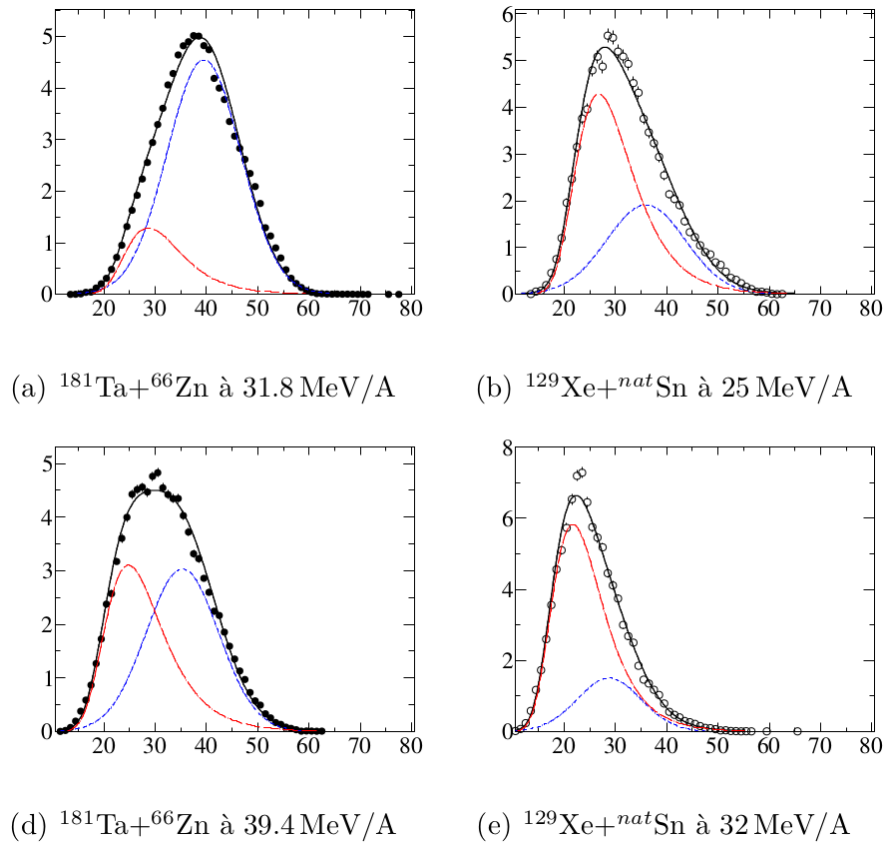


Figure 2.5.7 – Z_{max} distributions for the symmetric and asymmetric QF reactions of 2.5.1 (black points) fitted with the weighted sum of Equation (2.5.1) (black curve) and showing the Gaussian (blue) and Gumbellian (red) component of each fit. From [96].

In this way we can understand why the Δ -scaling and $P(Z_{\max})$ transition occurs at higher bombarding energies for $^{58}\text{Ni}+^{58}\text{Ni}$ than for $^{129}\text{Xe}+^{nat}\text{Sn}$. For the very light $^{36}\text{Ar}+\text{KCl}$ system we must assume that the threshold is higher than the maximum measured bombarding energy of $74A$ MeV, whereas for $^{197}\text{Au}+^{197}\text{Au}$ perhaps both the greater degree of stopping and far larger Coulomb repulsion contribute to increase radial flow and reduce the fragment formation timescale even at the lowest measured bombarding energy of $40A$ MeV. Since publication of [102] analysis of data for the virtually identical $^{208}\text{Pb}+^{197}\text{Au}$ system measured during the 5th INDRA campaign has partially confirmed this conclusion: the $P(Z_{\max})$ distribution for central collisions is also Gumbellian at the even lower bombarding energy of $29A$ MeV.

Finally let us now come back to the question of the difference of radial flow for the QF sources produced by the two reactions $^{129}\text{Xe}+^{nat}\text{Sn}$ and $^{181}\text{Ta}+^{66}\text{Zn}$. As we showed in 2.5.1, these two reactions with the same total mass and charge at the same centre of mass energy lead to significantly different fragment partitions, with some evidence that the collective flow for the asymmetric reaction $^{181}\text{Ta}+^{66}\text{Zn}$ is smaller than that for $^{129}\text{Xe}+^{nat}\text{Sn}$. Now, as shown above, we have a new tool to compare the importance of flow for different reactions: the decomposition of the $P(Z_{\max})$ distributions into Gaussian and Gumbellian components. Figure 2.5.7 presents the different components deduced from fits to the four $P(Z_{\max})$ distributions using Equation (2.5.1). Figures 2.5.7(a),(b) compare the results at $E_{cm} \sim 6A$ MeV while Figures 2.5.7(d),(e) compare the results at $E_{cm} \sim 8A$ MeV. The overall fits to each distribution are of excellent quality, especially in Figure 2.5.7(d) where the distribution has a very particular form. It is clear from these figures that in both cases the asymmetric $^{181}\text{Ta}+^{66}\text{Zn}$ reaction has a much more predominant Gaussian component in its $P(Z_{\max})$ distribution than the equivalent symmetric reaction, which confirms once more that the radial collective flow is smaller for $^{181}\text{Ta}+^{66}\text{Zn}$ than for $^{129}\text{Xe}+^{nat}\text{Sn}$.

2.6 Summary

To summarize this long chapter which concerns the major part of my research activities, the work that I have participated in and/or led since my Ph.D has contributed to the following important cornerstones of current understanding of multifragmentation in central heavy-ion collisions around the Fermi energy and the nuclear liquid-gas phase transition [1]:

Spinodal decomposition In the $^{129}\text{Xe}+^{nat}\text{Sn}$ $32A$ MeV and $^{155}\text{Gd}+^{238}\text{U}$ $36A$ MeV reactions two systems with similar excitation energy per nucleon and similar importance of radial flow (see Section §2.5) were shown to lead to very similar multifragmentation patterns, with the same Z partitions and a mean multiplicity of fragments which increases with the total charge of the system [43]. This was a first evidence for multifragmentation as a bulk process, linked to the properties of the low density excited nuclear matter formed in both reactions.

Confrontation of these results with calculations using a stochastic transport model in which spinodal decomposition occurs in the course of both reactions brought further evidence that such a mechanism is responsible for nuclear multifragmentation [44, 45]. Later studies with very high statistics data revealed the fossil signal of the spinodal decomposition in the fragment partitions, which is a “smoking gun” for this mechanism [47].

Freeze-out properties of fragments The experimental reconstruction of the primary fragments at freeze-out for multifragmentation events in $^{129}\text{Xe}+^{nat}\text{Sn}$ from $32A$ MeV to $50A$ MeV showed that with increasing bombarding/available energy of the reactions the mean excitation energies per nucleon of the primary fragments do not increase continuously, but rather “saturate” at a maximum value of $\approx 3A$ MeV [67]. This is partly due to the onset and increase of collective flow [46], but can also be ascribed to a vanishing level-density of nuclei at high excitation energies [71]. In this case the temperatures associated with thermal kinetic motion of the fragments can be much higher than those associated with their intrinsic excitation energy [51]: then the back-bending of the “true” caloric curve associated with the liquid-gas phase transition in a finite system [108, 109] is revealed in the kinetic temperatures at freeze-out.

Order parameter for multifragmentation The application of the universal fluctuations theory [78] to multifragmentation data first for the $^{129}\text{Xe}+^{nat}\text{Sn}$ reactions [79] and then for a wide range of colliding systems and bombarding energies [82] showed in the simplest and most model-independent way possible that the largest- Z fragment of each event, Z_{max} , behaves like the order parameter of a critical phenomenon, *i.e.* a phase transition. All generic models of cluster/fragment production by a process of aggregation have the largest cluster as their order parameter, therefore the phase transition associated with multifragmentation is necessarily of this type.

Although the observed change of scaling behaviour of the order parameter fluctuations is predicted near the critical point of a continuous phase transition, this and other pseudo-critical behaviours [49] are fully consistent with the fact that Z_{max} was also shown to exhibit the expected bimodal behaviour associated with the order parameter of a first order phase transition in a finite system [110, 111].

Flow and multifragmentation Evidence that multifragmenting systems with the same excitation energy per nucleon formed by different reaction mechanisms leading to very different amounts of collective expansion have different partition properties was presented in [46]: at a given total excitation energy per nucleon the amount of radial collective energy decides the mean normalised fragment multiplicity which in turn fixes the properties of the fragment partitions [97]. Our new data have shown that multifragmenting systems with the same excitation energy per nucleon formed by the same reaction mechanism but using symmetric (asymmetric) collisions to maximise (minimise) the radial flow also have different partition properties [96, 99], confirming the conclusions of [46, 97].

In addition it was shown in [102] that the relative importance of collective flow determines the probability distribution (and hence the fluctuations) of the Z_{max} order parameter, as in a generic model of the irreversible aggregation process. The observed continuous evolution of $P(Z_{\text{max}})$ from that of an additive to an extremal order parameter with bombarding energy is further evidence that multifragmentation in central collisions occurs at low densities during the expansion of an initially hot and compressed finite blob of nuclear matter.

Chapter 3

Reaction mechanisms at sub-Fermi energies

3.1 Introduction

It is a truth universally acknowledged that heavy nuclei are very difficult to fuse together [113], which makes synthesis of potential superheavy elements a very laborious process with small cross-sections that decrease by factors of 10 for every increase of Z (see Figure 3.1.1(left)). Writing the evaporation residue production cross-section as [112]

$$\sigma_{ER} = \pi\lambda^2 \sum_{\ell=0}^{\infty} (2\ell + 1) T_{\ell} P_{CN}(\ell) P_{surv}$$

with T_{ℓ} the ℓ -dependent transmission coefficient for the interaction potential, and λ the wavelength of the colliding system in the centre of mass frame,

$$\lambda = \frac{\hbar}{\sqrt{2\mu E_{CM}}}$$

we can identify the two main limiting factors which are the probability to form a compound nucleus for a given partial wave, $P_{CN}(\ell)$, and the probability that the compound will leave an evaporation residue, P_{surv} . The latter is drastically reduced because of the propensity of moderately excited heavy compound nuclei to decay by fission, rather than particle and γ emission. We will be more concerned with the probability to form a compound nucleus, P_{CN} .

There are two factors which affect P_{CN} , as illustrated in the figure. In order to form a compound nucleus, the two nuclei of the entrance channel must first of all “stick” together, *i.e.* there has to be a pocket in the internuclear potential where they can be trapped. An example of an internuclear potential, $V(R)$, for $^{129}\text{Xe} + ^{nat}\text{Sn}$ is shown in Figure 3.1.1(right). This potential is given by

$$V(R) = V_{BSS}(R) + V_{prox}(R) + \frac{\ell(\ell + 1)\hbar^2}{2\mu R}$$

where V_{BSS} is the Bondorf-Sobel-Sperber modified Coulomb potential [114], V_{prox} is the nuclear proximity potential of [115], and the last term is simply the centrifugal repulsion due to the

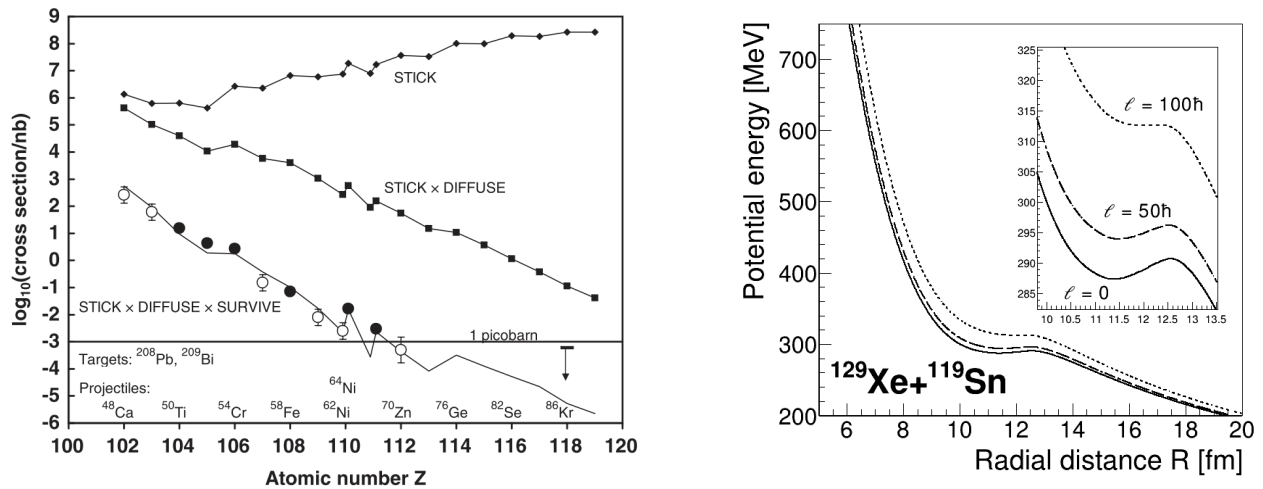
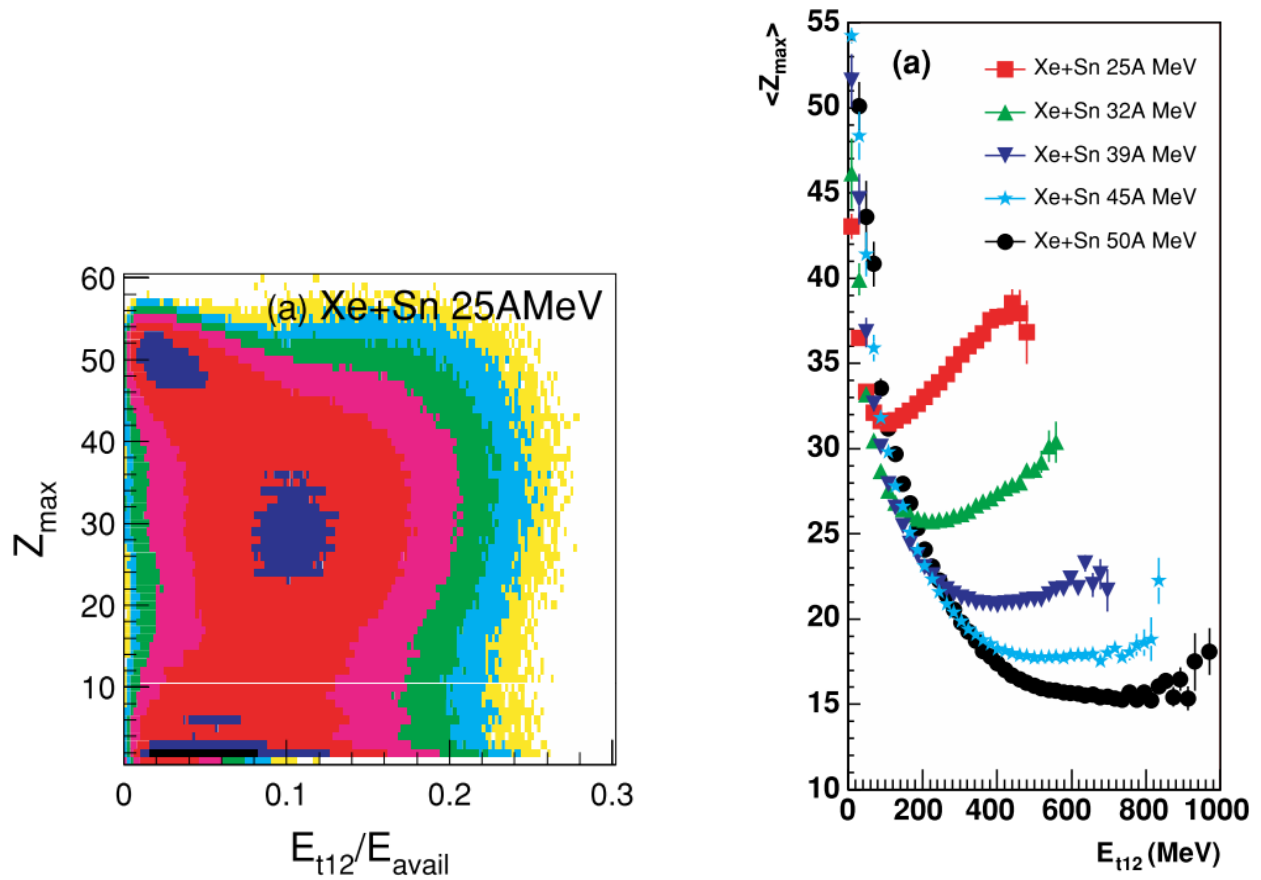


Figure 3.1.1 – (left) Cross-sections for $1n$ evaporation channels leading to SHE residues compared to model calculations for capture (“STICK”), compound nucleus formation (“STICK x DIFFUSE”) and residue survival (“STICK x DIFFUSE x SURVIVE”). From [112]; (right) Calculated total potential energy of $^{129}\text{Xe}+^{nat}\text{Sn}$ entrance channel as a function of internuclear radial distance. The inset is a zoom to show the disappearance of the pocket with increasing angular momentum.

angular momentum. It can be seen that in the case of $^{129}\text{Xe}+^{nat}\text{Sn}$ there is only a very shallow pocket in the potential, due to the largely repulsive Coulomb potential which is maximised for this quasi-symmetric system (for an asymmetric entrance channel with approximately the same total mass and charge such as $^{181}\text{Ta}+^{66}\text{Zn}$ or $^{58}\text{Ni}+^{197}\text{Au}$, the repulsion is reduced, making the pocket slightly deeper). Figure 3.1.1(right) also shows that with increasing angular momentum, the pocket rapidly disappears, somewhere between $\ell = 50\hbar$ and $\ell = 100\hbar$.

Even if the two nuclei do stick together, they still have to evolve towards a compact compound nuclear configuration. This process is described theoretically as a diffusion process in the potential energy landscape of the shape of the system [116, 117], which is why the combined probability for capture and formation of a compound nucleus is labelled “STICK x DIFFUSE” in Figure 3.1.1(left). As shown in the figure, it is the evolution towards the compound nucleus which is the most penalising factor limiting the probability P_{CN} . For very heavy and superheavy nuclei the fission barrier of the compound, if one exists, is small and disappears for moderate angular momenta [118, 119]; even if the barrier is sufficiently large, very heavy nuclei have compact fission saddle shapes, and it is quite probable that the dinuclear system of captured projectile and target is more deformed than the CN saddle point. In both cases, the system rapidly disintegrates into two fragments without ever forming a fully-equilibrated compound nucleus: this is called quasi-fission [120, 121, 122].

From the preceding discussion, it should be clear that we do not expect fusion reactions to occur with any sizeable cross-section for sub-Fermi energy collisions of $^{129}\text{Xe}+^{nat}\text{Sn}$, both from the point of view of the unfavourably symmetric ($Z_p * Z_t$) entrance channel and the fact that the compound nucleus would be a (neutron-deficient) superheavy isotope of $^{248}_{104}\text{Rf}$, with an $\ell = 0$ fission barrier of at most $4 \sim 6$ MeV [118, 119]. Ngô et al [122] gave a handy rule of thumb in order to know if fusion can or cannot occur for collisions between two nuclei, using the effective



(a) For $^{129}\text{Xe}+^{nat}\text{Sn}$ at 25A MeV colour contours indicate measured cross-sections as a function of Z_{\max} and E_{t12} relative to available centre of mass energy.

(b) For $^{129}\text{Xe}+^{nat}\text{Sn}$ from 25 to 50A MeV mean Z_{\max} as a function of E_{t12} , for complete events (at least 80% of total charge detected).

Figure 3.2.1 – Evidence for a fusion-like process in central collisions of $^{129}\text{Xe}+^{nat}\text{Sn}$ at sub-Fermi energies, both figures from [82]. The total transverse energy of light charged particles, E_{t12} , is here used as an impact parameter sorter.

fissility

$$\left(\frac{Z^2}{A}\right)_{\text{eff}} = \frac{4Z_p Z_t}{A_p^{1/3} A_t^{1/3} (A_p^{1/3} + A_t^{1/3})} \quad (3.1.1)$$

In their approach, based only on static potential energy arguments, if $(Z^2/A)_{\text{eff}} \geq 48$, fusion is not possible (dynamical effects can reduce the possibilities for fusion event further). For $^{129}\text{Xe}+^{nat}\text{Sn}$ we find $(Z^2/A)_{\text{eff}} \approx 44$, therefore we are really at the limits.

3.2 Heavy residue production in $^{129}\text{Xe}+^{nat}\text{Sn}$ collisions below the Fermi energy

However, evidence that “something else happens” in central collisions of $^{129}\text{Xe}+^{nat}\text{Sn}$ below Fermi energies is not hard to find. Figure 3.2.1a presents contours of double differential cross-section for the atomic number of the largest- Z fragment of each event, Z_{max} , as a function of the total transverse energy of light charged particles, E_{t12} , normalised to the available centre of mass energy, E_{avail} , for the 25A MeV reactions. E_{t12} is here used, as in the rest of [82], in order to sort events according to impact parameter (see Part II, Chapter 6). This map of the reactions is dominated by peripheral (low E_{t12}) collisions with ($Z_{max} \approx 50$) or without ($Z_{max} \approx 2$) a detected projectile-like fragment, and mid-peripheral collisions where the excited PLF appears to have undergone fission ($Z_{max} \approx 30$), probably after significant angular momentum transfer.

Nevertheless, in the upper right-hand corner of this map there appears a definite contribution from events with a heavy residue, with atomic numbers Z up to that of the projectile, which seem to occur for central collisions (large E_{t12})¹. Indeed, for the heaviest observed residues ($Z_{max} \geq 48$) a clear separation of their measured energy spectra at forward angles ($\theta_{lab} < 15^\circ$) into two components is observed, corresponding to high energy projectile-like fragments and low-energy fusion-like residues with very small centre of mass velocities, while Galilean-invariant velocity diagrams for coincident light charged particles (LCP) also show well-defined Coulomb rings centred on the c.m. velocity [76].

Figure 3.2.1b shows the evolution of this “heavy residue” production with bombarding energy and centrality. The mean charge of the largest- Z fragment of each event, $\langle Z_{max} \rangle$, is here presented as a function of E_{t12} (collision centrality), but now only considering complete events where at least 80% of the total charge of the projectile and target nuclei were measured. This is to ensure that the largest *detected* fragment is most probably the largest *produced* fragment of each event. For the 25A MeV reactions, there is a very clear increase of $\langle Z_{max} \rangle$ going towards what we assume to be more central collisions. The same effect, but weaker, can also be observed at 32A MeV; for bombarding energies $\geq 39A$ MeV, *i.e.* from the Fermi energy upwards, $\langle Z_{max} \rangle$ decreases monotonously with increasing violence of the collisions.

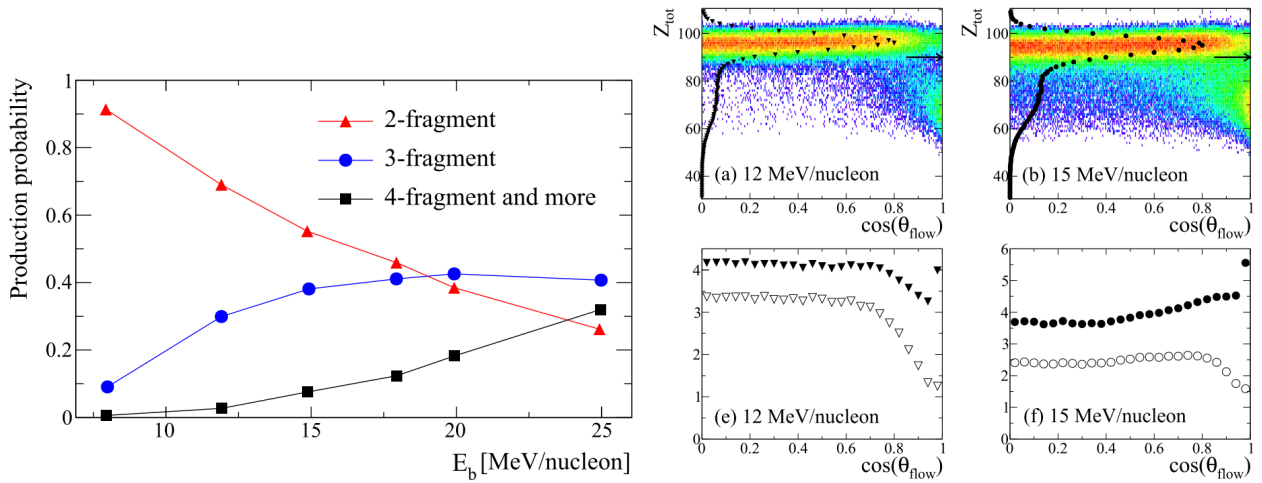
As 25A MeV was the lowest bombarding energy measured for this system in the first INDRA campaign in 1993, and as the heavy residue production clearly increases with decreasing beam energy, A. Chbihi and I proposed an experiment as part of the fifth INDRA campaign in 2001, to study $^{129}\text{Xe}+^{nat}\text{Sn}$ collisions below 25A MeV.

3.3 3-fragment exit channels at $\leq 20A$ MeV

Figure 3.3.1a shows the probability of different exit channels classified according to the number of heavy ($Z > 10$) fragments observed², as a function of bombarding energy, E_b , for the 5 new re-

¹A very similar map is obtained for the lighter $^{58}\text{Ni}+^{58}\text{Ni}$ system at 32A MeV (see [82], Figure 2), for which fusion-like reactions are not forbidden by systematics, and indeed for which the corresponding cross-sections were measured and reported by Lattes *et al.* [123].

²To avoid ambiguities, only well-measured events with detection of at least 80% of the projectile and target charge are considered.



(a) Evolution of different exit channel production probabilities as a function of the beam energy for $^{129}\text{Xe}+^{nat}\text{Sn}$ collisions from 8 to 25 A MeV.

(b) (top) Total detected charge Z_{tot} versus $\cos\theta_{flow}$ for 3-fragment events. (bottom) $\cos\theta_{flow}$ distributions for all 3-fragment events (full symbols) or with isotropic selection $Z_{tot} \geq 90$ (open symbols).

Figure 3.3.1 – Beam-energy dependence and selection of isotropic 3-fragment exit channels for low energy $^{129}\text{Xe}+^{nat}\text{Sn}$ collisions. From [7].

actions measured in 2001. The 1-fragment “heavy residue” events (with probabilities $< 5\%$ at all energies [6]) are not included here; these were exclusively studied in [124]. As often happens, the original motivation for the experiments was not in the end the most interesting subject thrown up by this new data. Rather, we will concentrate in the following on the 3-fragment events, which, as shown in Figure 3.3.1a, become increasingly likely exit channels above 8 A MeV bombarding energy, and are even more probable than binary reactions for $E_b \geq 20$ A MeV. The question of the origin of such events, and their eventual link to the threshold/onset of the multifragmentation process observed in central $^{129}\text{Xe}+^{nat}\text{Sn}$ collisions for ≥ 32 A MeV (see Chapter 2), became one of the subjects of the Ph.D thesis of Diego Gruyer [96].

In Figure 3.3.1b are the measured cross-sections as a function of total detected charge, Z_{tot} , and the cosine of the flow angle, θ_{flow} , calculated from the c.m. momentum tensor (Equation (2.2.1)) for the 3 heavy fragments ($Z > 10$) of each event, for two bombarding energies. What is clear from these correlations is that there are two distinct contributions to these reactions: one strongly forward-peaked and less well-measured ($Z_{tot} < 80$) mechanism, highly suggestive of deep inelastic collisions followed by fission of projectile-like and/or target-like fragments³, and another which is very nearly kinematically complete ($Z_{tot} \geq 90$) with a near-isotropic θ_{flow} distribution, indicating that the 3 fragments were produced by a highly relaxed, possibly composite, system.

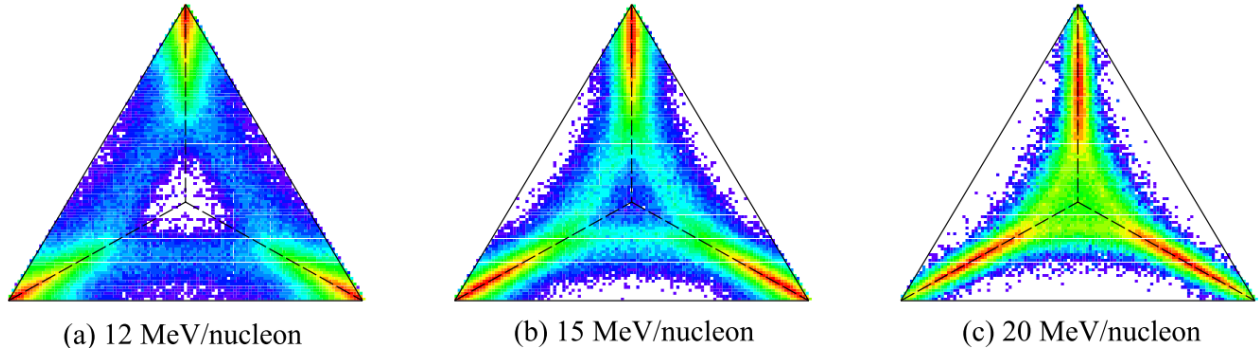


Figure 3.4.1 – Bizard-Dalitz plots of P_i (see text) for isotropic 3-fragment events in reactions of $^{129}\text{Xe} + ^{\text{nat}}\text{Sn}$ at 12, 15 and 20A MeV. From [7].

3.4 Sequential fission chronology

By considering the relative velocity of each pair among the 3 fragments in these events, and comparing with systematics for symmetric or asymmetric fission [126, 127], it can be shown that they result from a sequence of splittings, using a method developed by Bizard *et al.* [128]: for each event, we calculate the quantities

$$P_i = \Delta v_{i,(jk)}^2 + \Delta v_{j,k}^2 \quad (3.4.1)$$

$$\Delta v_{\alpha,\beta} = v_{\alpha,\beta}^{\text{exp}} - v_{\alpha,\beta}^{\text{sys}} \quad (3.4.2)$$

with $i = 1, 2, 3$ representing each of the 3 possible sequences of splitting of the initial composite made of the sum of all 3 fragments, (ijk) :

$$(ijk) \rightarrow i + (jk) \quad (3.4.3)$$

$$(jk) \rightarrow j + k \quad (3.4.4)$$

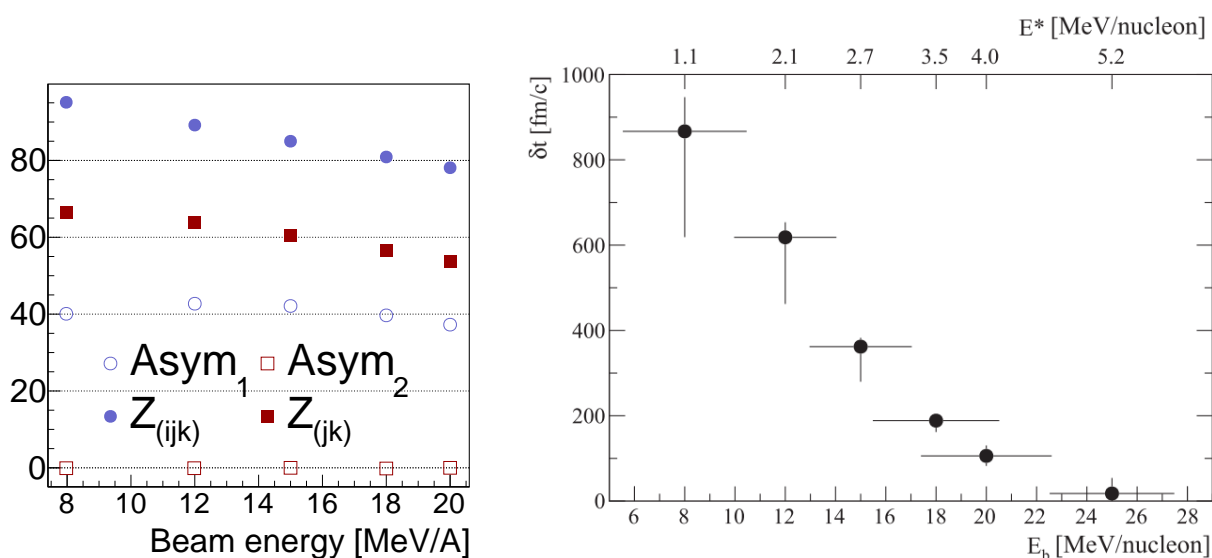
In Equation (3.4.2), $v_{\alpha,\beta}^{\text{exp(sys)}}$ is the experimental (systematic) relative velocity between the fragments with indices α and β .

Plotting the 3 values $\{P_i\}$ in a pseudo-Dalitz plot where the distances of each point (event) from the sides of the triangle are given by

$$a_i = \frac{P_i}{\sum_{i=1}^3 P_i}$$

allows to easily visualize the evolution of the sequentiality of the splittings (Figure 3.4.1). Events with a clear sequential splitting then cluster on branches parallel to the sides of the triangle ($P_i \ll P_j, P_k$) or in the corners ($P_i, P_j \ll P_k$), while for quasi-simultaneous break-up (“democratic decay”) they lie close to the centre ($P_i \approx P_j \approx P_k$). The sequential decay is then clear to see for 12A MeV, while the sequential nature gradually disappears with increasing bombarding energy.

³Such ternary events were previously studied for $^{129}\text{Xe} + ^{\text{nat}}\text{Sn}$ reactions at 12.5A MeV by Glässel *et al.* [125].



(a) $Z_{(ijk)}$, $Z_{(jk)}$: mean atomic number of the initial composite and intermediate systems; $Asym_1$, $Asym_2$: mean charge asymmetry (expressed as a percentage) of the first and second splitting, respectively.

(b) Evolution of the mean inter-splitting time δt as a function of either beam energy E_b (lower scale) or estimated excitation energy of the initial composite systems E^* (upper scale). Horizontal error bars refer to E^* .

Figure 3.4.2 – Deduced properties of the sequential fission leading to 3-fragment exit channels observed in $^{129}\text{Xe} + ^{nat}\text{Sn}$ collisions from 8 to 20 A MeV.

The sequence of splittings was then identified event by event by finding the pair of fragments $\{j, k\}$ with the smallest value of $\Delta v_{j,k}^2$ *i.e.* with the most fission-like relative velocity. The remaining fragment, i , is then trivially deduced to result from the first splitting, and the three fragments can be sorted according to their order of production, with reconstruction of the intermediate (jk) system.

Figure 3.4.2a presents the results of this reconstruction. $Z_{(ijk)}$ is the mean atomic number of the initial composite system *i.e.* the sum of the 3 fragments' charges in each event⁴. It decreases from ≈ 95 to ≈ 78 with increasing bombarding energy, which shows that very heavy composite systems can be formed in these reactions, from platinum to americium. As the total detected charge for all events is constrained by the selection $Z_{tot} > 90$, this decrease reflects the increasing multiplicity of emitted light charged particles with bombarding energy (see Figure 3 of [7]). $Asym_1$ is the charge asymmetry of the first splitting, defined as

$$Asym_1 = \frac{Z_{(jk)} - Z_i}{Z_{(ijk)}} \quad (3.4.5)$$

i.e. the difference between the charges of the two fragments resulting from the first splitting (the light fragment Z_i detected in the final event, and the intermediate composite nucleus $Z_{(jk)}$ reconstructed from the charges of the two fragments Z_j and Z_k resulting from the second splitting), normalised to the charge of the initial composite system. In the figure $Asym_1$ is given as a percentage: the first splitting is on average highly asymmetric, the value $\approx 40\%$ corresponding to a ratio of 1:2.3 between the charges of the fission fragments. It is interesting to note that this asymmetry is practically constant for all bombarding energies. One may then speculate whether 3-fragment events are observed only when the initial fission is asymmetric enough to produce an intermediate system which is sufficiently heavy to fission again; the probability for a second scission will be further increased if in addition this intermediate system has high angular momentum (spin).

$Z_{(jk)}$ and $Asym_2$ in Figure 3.4.2a are, respectively, the mean charge of the intermediate heavy fragment produced by the first splitting, and the charge asymmetry of the second splitting, defined as in Equation (3.4.5). The intermediate fragment's mean atomic number decreases slightly less than that of the composite system, from ≈ 66 (dysprosium) to ≈ 54 (xenon) with increasing bombarding energy, while the mean asymmetry of the second splitting $Asym_2$ is very different: it is virtually zero for all bombarding energies, meaning that the second splitting is on average a symmetric fission.

3.5 Sequential fission chronometry

The timescale of the process was subsequently deduced using a new Coulomb chronometry method based on proximity effects between the different fragments in the exit channel. These effects can introduce a modulation of the relative velocity between the fragments coming from the second fission step depending on the orientation of this fission axis with respect to that of the

⁴Note that $Z_{(ijk)}$ is a lower limit for the size of the initial composite system, neglecting the light charged particles which are detected in coincidence.

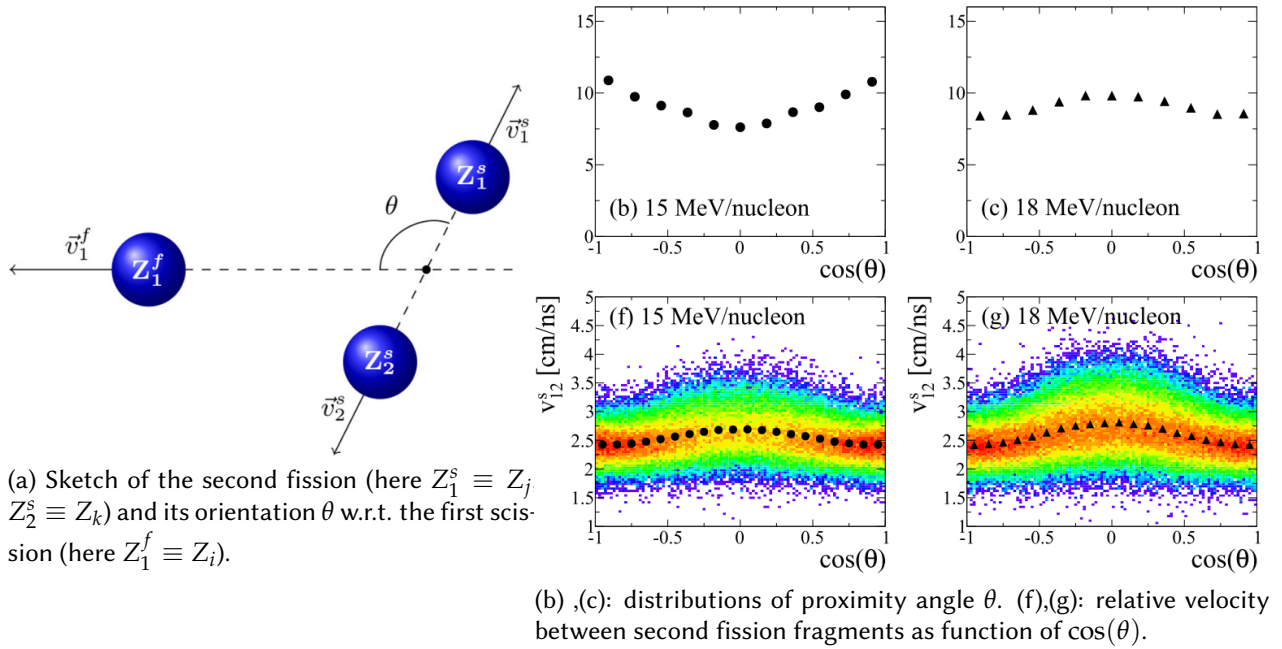


Figure 3.5.1 – Proximity effects between fragments from sequential fissions used to deduce the timescale of the 3-body break-up. From [7].

first splitting (see Figure 3.5.1a). Indeed, for short inter-splitting time the second splitting occurs close to the first emitted fragment, Z_i . The Coulomb field of Z_i will then favour, in the second break up (Equation (3.4.4)), kinematic configurations where the fragments Z_j and Z_k are emitted perpendicular to the first scission axis.

The proximity effects can be seen in Figure 3.5.1b,c which shows distributions of the cosine of the proximity angle $\cos \theta$ for two bombarding energies. For data at 15A MeV the distribution has a U-shape symmetric with respect to 90° which is characteristic of statistical fission of an equilibrated hot nucleus. For 18A MeV and above, on the other hand, the distribution becomes more and more peaked at 90° , showing the increasing importance of the proximity effects. Indeed, such large final-state interactions requires the second splitting to take place at a distance from the first emitted fragment of the same order of magnitude as the distance between the centres of the fissioning fragments at scission.

Also shown in Figure 3.5.1f,g is the effect of increasing proximity between first and second splitting on relative velocity of the fission fragments of the second scission. A clear modulation of v_{12}^s with θ is evident, the relative velocity is highest when the second fission occurs perpendicular to the first scission axis, due to the Coulomb repulsion. It is this modulation which can be used in order to deduce the inter-splitting time between the first and second fissions. To do so, Coulomb trajectory calculations were performed simulating sequential breakups using the mean charges of the different fragments extracted from the data, and with initial conditions tuned to reproduce the systematics of asymmetric fission [127].

The results are shown in Figure 3.4.2b, where the deduced inter-splitting time δt is plotted as a function of bombarding energy. For the lowest energy, a mean fission time of $\delta t \approx 900$ fm/c (3×10^{-21} sec., or 3 zeptoseconds [129, 130]) is found. This is already a short time compared to

typical lifetimes for fission of excited nuclei formed in fusion-fission reactions, typically $t_{FF} \geq 10^{-20}$ seconds [131]. With increasing beam energy, the inter-splitting time decreases gradually until at $20A$ MeV it reaches the limit of $\delta t = 100$ fm/c (0.33 zs) below which the simulation shows that the two nuclei resulting from the first splitting do not have sufficient time to move beyond the range of their mutual nuclear interaction before the second splitting occurs. This is therefore the sensitivity limit of the method, and it means that to all intents and purposes from $20A$ MeV upwards 3-fragment emission is quasi-simultaneous. In this sense, the beam energy $20A$ MeV can be considered as the threshold of multi-fragment emission⁵.

3.6 Comparisons with theoretical models

Although the preceding analysis clearly established the mechanism responsible for the observed 3-fragment events as sequential splittings of an assumed very heavy composite system, there remains much doubt over the formation of such a system given the high value of the pseudo-fissility parameter Equation (3.1.1) for the $^{129}\text{Xe} + ^{\text{nat}}\text{Sn}$ reactions. In such a case fusion is certain to be hindered to such an extent that quasi-fission must surely dominate even the most central collisions of this system [121, 122, 116, 112]. Another possibility would be fully-relaxed deeply-inelastic reactions. For either quasi-fission or deeply-inelastic reactions the “first splitting” in the scenario above would not be the first step in the decay of an excited composite system, but rather the last step of the entrance channel dynamics.

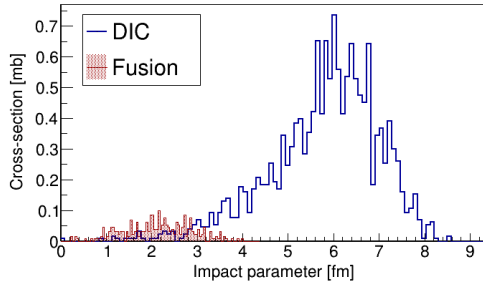
In order to try to clarify the origin of the sequential fission, calculations were performed with the Deep Inelastic Transfers model (DIT) of Tassan-Got and Stéphan [132] for the reactions at $12A$ MeV [8]. As this model of binary dissipative collisions does not handle non-binary exit channels, for a small cross-section of 92 mb among the most central simulated reactions we used one of two *ansatz*: either complete fusion⁶, or a pseudo-quasi-fission event. In all cases, the primary excited fragments resulting from the entrance channel calculation were then used as inputs to the statistical decay code GEMINI++ [133, 134] and detection of all final charged reaction products in INDRA was then simulated using KaliVeda ([15] and see Chapter 4).

The model calculations vastly underestimate the measured cross-section for 3-fragment events, which was found for data to be ≈ 40 mb, whereas DIT+GEMINI leads to only 8 mb for this exit channel⁷. Moreover, in the DIT model, 90% of the observed 3-fragment events result from PLF or TLF fission following a mid-peripheral deep-inelastic collision (Figure 3.6.1a), for which the angular momentum (spin) transferred to the primary fragments reaches a maximum (Figure 3.6.1b). These are exactly the type of ternary events which were observed and studied by Glässel et al. in [135, 136, 125]. Such an origin for the experimentally observed 3-fragment events in our data can be excluded thanks to the measured coincident light charged particle multiplicities (Figure 3.6.1c): mid-peripheral collisions produce far smaller LCP multiplicities, reflecting the much lower excitation energies of the primary fragments in this case ($\langle E^* \rangle \approx 0.9A$ MeV). Statistical decay of the

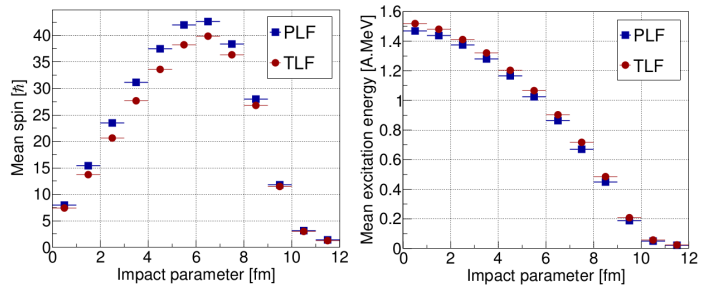
⁵Not to be confused with the onset of true multifragmentation *i.e.* clustering of low density nuclear matter due to spinodal instability, for which the onset in central $^{129}\text{Xe} + ^{\text{nat}}\text{Sn}$ collisions occurs at $\approx 32A$ MeV (see Section §2.2 and [62]).

⁶Pre-equilibrium emission is not included in the model either.

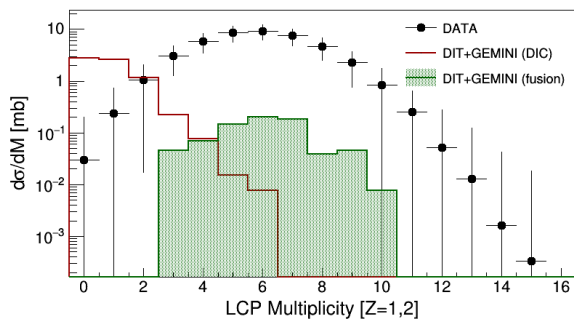
⁷It should be noted that the total measured reaction cross-section for all events was well reproduced by this simulation.



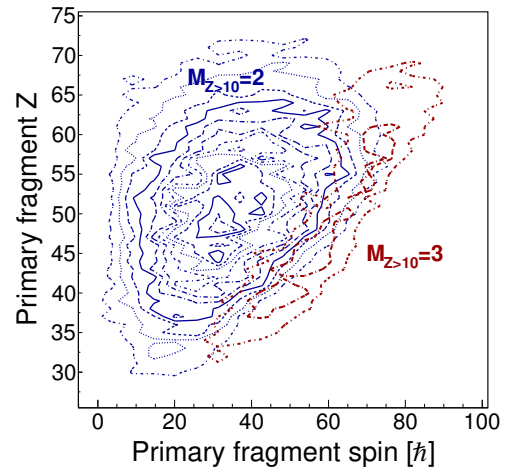
(a) Impact parameter distributions for simulated 3-fragment events from either deep inelastic (DIC) or fusion reactions.



(b) Mean spin and excitation energy of PLF and TLF fragments calculated with DIT.

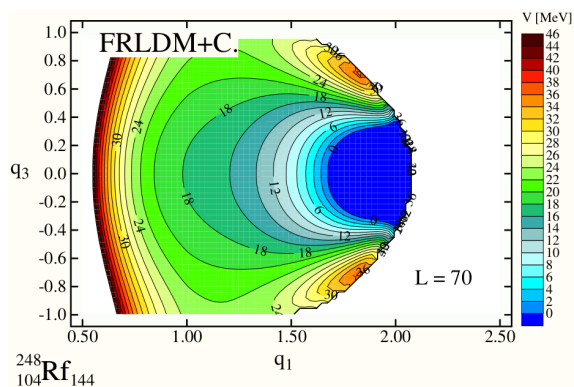


(c) Light charged particle (LCP) multiplicities for 3-fragment events from data, binary deep inelastic collisions (DIC) calculated with DIT or statistical decay following complete fusion calculated with GEMINI++.

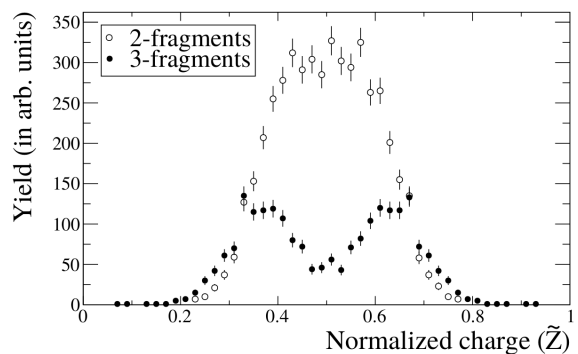


(d) Z-spin correlations for primary quasi-fission fragments leading to either $M_{Z>10} = 2$ - or $M_{Z>10} = 3$ -fragment events.

Figure 3.6.1 – DIT+GEMINI++ calculations for $^{129}\text{Xe} + ^{nat}\text{Sn}$ collisions at 12A MeV. From [8].



(a) PES for ^{248}Rf calculated with the Finite Range Liquid Drop Model (FRLDM) [138], for spin $\ell = 70\hbar$.



(b) Normalized primary fragment charge distributions for 2- or 3-fragment events calculated for a ^{248}Rf compound nucleus with $E^* = 223$ MeV.

Figure 3.6.2 – Sequential fission calculations with the 4D Langevin fission model.

compound nucleus formed by complete fusion, with excitation energies up to $1.9A$ MeV (for $\ell = 0$), on the other hand produces on average 6.9 LCP in coincidence with the 3 fragments. Although the width of the experimental distribution for M_{LCP} is not reproduced, it can be remarked that the most probable/mean value are very closely matched by the simulations.

The M_{LCP} distribution for simulated quasi-fission events (not shown in Figure 3.6.1c) is very similar to the one for fusion. The simulation of these events (see [8] for details) included a hypothesis on the amount of entrance channel angular momentum transferred into the fragment spins, using the sticking limit [137]. With this hypothesis, the simulated quasi-fission reactions only produce 0.4 mb of 3-fragment events, *i.e.* 50% of the cross-section obtained with the complete fusion hypothesis. It is possible to increase the cross-section to 4 mb with the assumption that all entrance channel angular momentum is converted into fragment spin. Although this assumption is physically unrealistic, an interesting result in this case is that the primary fragments for the 3-fragment exit channel are those with the largest spin for a given Z (Figure 3.6.1d), while their Z distribution becomes asymmetric, as observed for the “first splitting” in the experimental data.

The question of the possibility to observe sequential fission due to part of primary fission fragments possessing sufficient residual excitation energy and angular momentum is the subject of an ongoing collaboration with Katarzyna Mazurek⁸, using the 4D Langevin fission model of [139, 140]. In this model the evolution of an excited nucleus towards fission is obtained by solving the coupled Langevin classical equations of motion in a four-dimensional deformation space, where the combined action of the driving potential, friction, and diffusion forces determines the trajectory of the nucleus on a three-dimensional potential energy surface (PES) here calculated using the Finite Range Liquid Drop (FRLDM) model [138]. An example PES, for the ^{248}Rf compound nucleus with spin $\ell = 70\hbar$ is shown in Figure 3.6.2a. During its path to fission the system can de-excite by evaporating light particles (with $A \leq 3$) and γ -rays using a Monte Carlo approach.

In our calculations [141] the reactions $^{129}\text{Xe} + ^{nat}\text{Sn}$ at 8, 12, and 15A MeV were simulated

⁸IFJ PAN, Krakow, Poland.

by following the evolution of ^{248}Rf compound nuclei with excitation energies $E^* = 223, 471$ and 656 MeV, respectively, and angular momenta sampled from a triangular distribution up to $\ell_{max} = 130\hbar$. In this original application of the model, either fragment resulting from fission is itself used as the starting point for a new Langevin calculation, thus allowing for sequential fission in a self-consistent way. A preliminary result is shown in Figure 3.6.2b. As can be seen, we recover the behaviour observed experimentally: by considering 3-fragment events, we select the most asymmetric primary fission, independently of the global charge distribution. However, in this model the lowering of the fission barrier is mainly due to the residual angular momentum. In such a case, the heavy fragments could undergo secondary fission if the angular momentum is high enough to lower the fission barrier. Since residual angular momentum increases with the charge/mass of the primary fission fragments, only the most asymmetric primary fission leads to 3-fragment events, thus confirming the interpretation we proposed above. The fragments coming from the symmetric division of the compound nucleus have mass around $A = 120$ and angular momenta around $10 - 20\hbar$ which provide high fission barriers. These nuclei de-excite by particle evaporation and their secondary fission probability is very low.

Chapter 4

KaliVeda, or The Tao of Collaborative Software Development

“All men dream: but not equally. Those who dream by night in the dusty recesses of their minds wake in the day to find that it was vanity: but the dreamers of the day are dangerous men, for they may act their dream with open eyes, to make it possible.” [142]

4.1 Origins

From the very beginning of the INDRA project, given the large number of detectors to calibrate (628 originally, 640 by the 4th campaign) and identification matrices to treat (864 originally, 876 by the 4th campaign), it was decided that all the data should be centralised at the IN2P3 Computing Centre (Centre de Calcul) near Lyon, and that the responsibility for reduction of all the data of each campaign would be shared among the different teams of the collaboration, with the resulting software for reading and analysing the data being equally centralised at CC-IN2P3. This was handled by two FORTRAN¹ programmes, `ka.li.f` (for calibration, identification, and preparation of data for analysis) and `veda.f` (for analysis of the reduced data), which were responsible for uniting all the different subroutines written by different members of the collaboration into a coherent whole. Or rather, there were two programmes for the 1st campaign data, two for the 2nd campaign (`ka.li2.f`, `veda2.f`), two for the 3rd, *etc. etc.* In addition, many of the “utility” subroutines which could and should have been written once and for all, compiled into a standard library and reused, were copy-pasted from one version to another, or between different laboratories’ versions of the data reduction software, often with “minor” tweaks that could be user-specific.

Although the initial design was modular and quite well conceived for the time and the limits of the programming language, the cumulated effects of time, increasing amounts of data to treat, pressure to obtain results, and the generally low awareness of software engineering “best

¹FORTRAN77 to be precise, not the modular variety introduced in Fortran 90.

practices” of the average physicist had led to a situation after the 4th campaign in 1998/9 which would soon become unmanageable:

- although the data reduction software for each campaign shared a common architecture, and many of the component parts (particle identification routines, calibration functions, etc.) were basically the same from campaign to campaign, each campaign had an entirely independent code base, in which many thousands of lines of code were replicated: code re-use was virtually non-existent;
- similarly, the data analysis software for each campaign, although performing essentially the same functions, was rewritten each time, either from scratch or starting from a copy of the entire code base of the previous campaign;
- on the plus side, in order to analyse the final data, physicists needed only code a few subroutines which would then be compiled and linked with the main analysis program; however, due to subtle but important differences between the software for each campaign, physicists would also have to remember to add or remove small pieces of code at certain key places in the subroutines depending on the campaign being analysed: failure to do so could result in her analysis being (undetected) false;
- in addition, due to the lack of a shared code base, each member of the collaboration would be left to implement her own version of whatever analysis tools were required, often even re-implementing the same tools from one analysis to another (no code re-use). This was, at best, a waste of time; at worst, astonishing new results could turn out to be the result of avoidable programming errors.

Many of the above-listed problems can be traced back to the fact that all software development for INDRA was (and, indeed, still is) carried out by the physicists of the collaboration. At the time, not only in the INDRA collaboration, but in the (French) nuclear physics community as a whole, there were precious few physicists with any computer science culture, apart from a thorough mastery of Fortran². Generations of Ph.D. students who had been introduced to programming using C++ at university would have to abandon modern software development practices and adopt F77 in order to prepare their thesis: not the best way to make their CV attractive to potential employers. In 2001, the 5th INDRA campaign took place at GANIL and I volunteered to take over the software for data reduction and analysis for this campaign³. Being the one who had to manage the unmanageable, I decided it was time to change everything.

During the 4th campaign of data-taking, which took place at GSI Darmstadt, I had had a glimpse of the future, as the Ph.D. students (and some senior physicists) had started using the ROOT framework [13, 14] in order to perform some data reduction tasks, using custom-built graphical user interfaces (GUI) which made the whole job look terribly easy. There was no comparison with the existing FORTRAN- and KUMAC⁴-based solutions based on PAW (Physics Ana-

²Only in its classic procedural incarnation Fortran77 or, for the more mature practitioners, Fortran66

³as well as taking over responsibility for the data acquisition software environment, which was also based on FORTRAN from the user-analysis programmes of the VAX-based GANIL acquisition system to the graphical user interfaces (GUI) developed by the collaboration for the slow control of the detectors.

⁴KUMAC was a custom scripting language developed in tandem with PAW in order to provide user-defined macros.

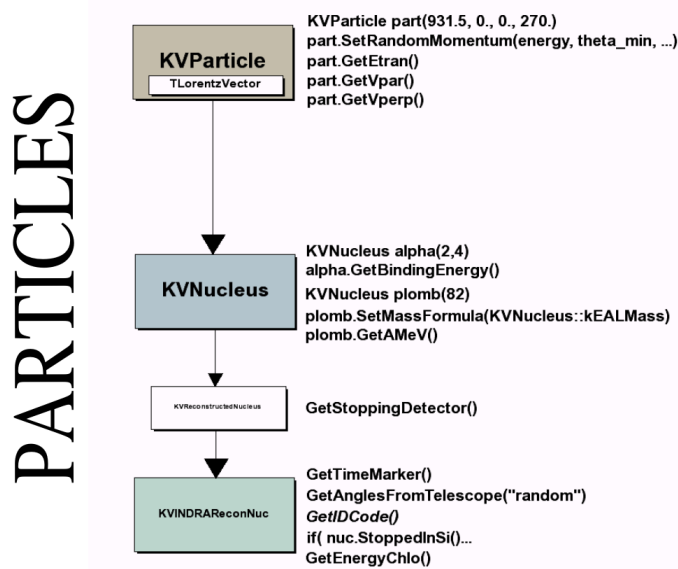


Figure 4.1.1 – Slide from the first presentation of the KaliVeda toolkit to the INDRA collaboration in July 2003. Note that nearly all of the code examples in the slide are still valid today.

lysis Workstation, the direct ancestor of ROOT and coordinated by the same René Brun of CERN), which had already seemed a little old-fashioned when I began my Ph.D. in 1995, but by 2000 was simply antiquated. Of course, one major obstacle to changing framework was that ROOT was written in C++, which hardly anybody in the collaboration knew at the time having been exclusively reared on FORTRAN since university. However it was clear to me from the example of ROOT itself how the possibilities offered by the C++ language could be leveraged in order to handle in a structured way the evolutive nature of the software for data reduction and analysis. Therefore a proposal for the future environment was written and submitted to the collaboration, it was accepted and the first presentation of the new software took place in July 2003 (see Figure 4.1.1).

4.2 Mission statement & current status

The proposal⁵ set out the problems we had identified in the context of the beginnings of the modernisation of the CC-IN2P3 computing environment (to prepare for the LHC) and also that of GANIL, where DEC VMS workstations were beginning to be phased out in favour of, first, DEC Unix and, later, Linux-based solutions. The initial aim of KaliVeda was to propose solutions to these problems, by:

- ensuring durability of the data from different previous (and all future) campaigns at CC-IN2P3 by storing them in a platform-independent and future-proof file format;

⁵“Réflexions et propositions sur la gestion de l’évolution de l’environnement logiciel associé au multidétecteur INDRA et son successeur éventuel”, J.D. Frankland, A. Chbihi, A. Mignon and D. Cussol, November 2002.

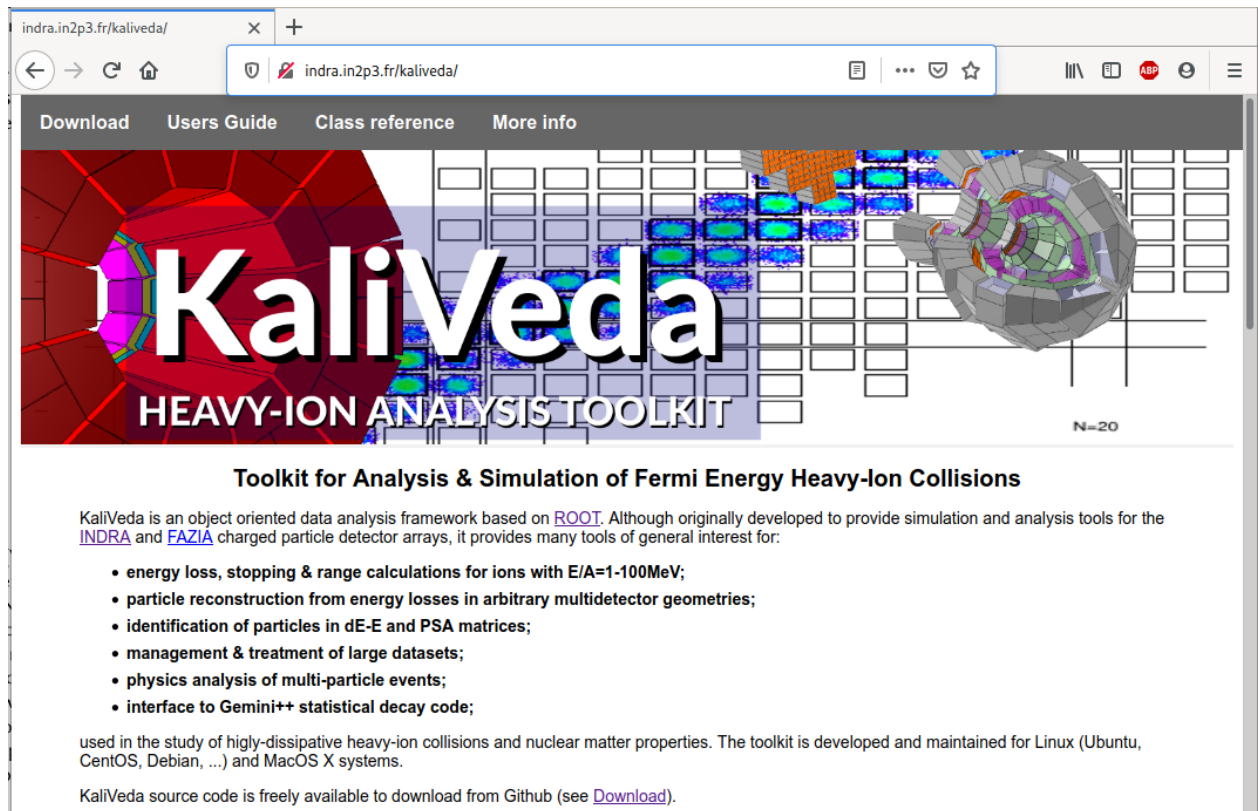


Figure 4.2.1 – Screenshot of the KaliVeda [website](http://indra.in2p3.fr/kaliveda/) taken on 11th August 2020.

- ensuring a single “official” version of the data for each campaign, centralising and making fully traceable all steps of the data reduction process;
- providing a single environment for data reduction and analysis;
- making large-scale analyses of data from different campaigns feasible by harmonising the software environment used for all data;
- centralising all additional information required for data analysis, such as target thickness, ionisation chamber gas pressure, dead time and other scaler information run by run, *etc.*;
- providing a standardised and fully documented set of libraries containing a toolkit of tried and tested versions of all support software needed for data analysis;
- providing an accurate software “filter” for each dataset almost as a by-product of the data reduction process, without need for further software development.

Of all these aims, it is only the last which has still not been fully realized, although partial solutions exist and the goal has not been abandoned. The toolkit has a dedicated [website](http://indra.in2p3.fr/kaliveda/) (see Fig. 4.2.1) which provides links to download the toolkit and instructions on how to build and install it, an on-line and frequently updated Users Guide, and links to the documentation of all classes in the toolkit.

Initially conceived solely in the framework of the INDRA collaboration and INDRA data, the toolkit has been extended successfully to manage data from the INDRA-VAMOS campaign of 2007, data taken with FAZIA [16, 17] starting from 2014 (KaliVeda was adopted as software environment by the FAZIA collaboration from the outset), and most recently the data from the first campaign coupling INDRA and 12 FAZIA blocks at GANIL in 2019.

4.2.1 DAQ Slow Control software

Although not listed above, another of the initial aims of KaliVeda was to replace the existing graphical user interfaces developed by the collaboration (mostly Daniel Cussol) for the setting and control of the DAQ electronics, high voltage supplies, and on-line data controls. Not because they didn't work (they did, very well), but because they were so strongly dependent on the DEC VMS system that trying to extend their life beyond that of VMS was far too difficult to envisage. Thus solutions based on the ROOT GUI back-end and KaliVeda were promised. However it took a lot longer than planned, and the first replacement GUI (for setting the parameters of the electronics) wasn't ready until 2011, with the high voltage and VXI signal inspection interfaces following in 2014, until which we had to artificially prolong the life of the last remaining DEC VMS workstations at GANIL in order to continue using INDRA.

As noted above, the FAZIA collaboration adopted KaliVeda as standard, and so it was natural that the task of creating the software to handle the parameter setting for this new detector would fall to GANIL. With Eric Bonnet we began development on the new interfaces in 2011, and they were ready long before the first experiments with prototype FAZIA blocks in 2014. During his Ph.D (2011-2014) and continuing during his post-doc in Florence (2015-2017), Diego Gruyer also made many major contributions to the on-line software for FAZIA, going far beyond what we initially imagined, including a real-time oscilloscope capable of visualising the signals produced by the FAZIA detectors.

4.3 Architecture

At the core of KaliVeda is a set of C++ class libraries which are extensions to the ROOT framework. The essential functionalities of ROOT which are leveraged at the heart of KaliVeda are:

- inheritance of classes from `TObject` allowing data storage in platform-independent ROOT files;
- interactive use of the toolkit classes on the ROOT command line;
- building graphical user interfaces using the ROOT widgets and GUI base classes;
- toolkit extension using “plug-in” derived classes defined in a plain text configuration file while existing code is unchanged;
- `TTree` class for data storage and `TSelector` class for data analysis;
- `xrootd` for reading & analysing data provided by a remote server;

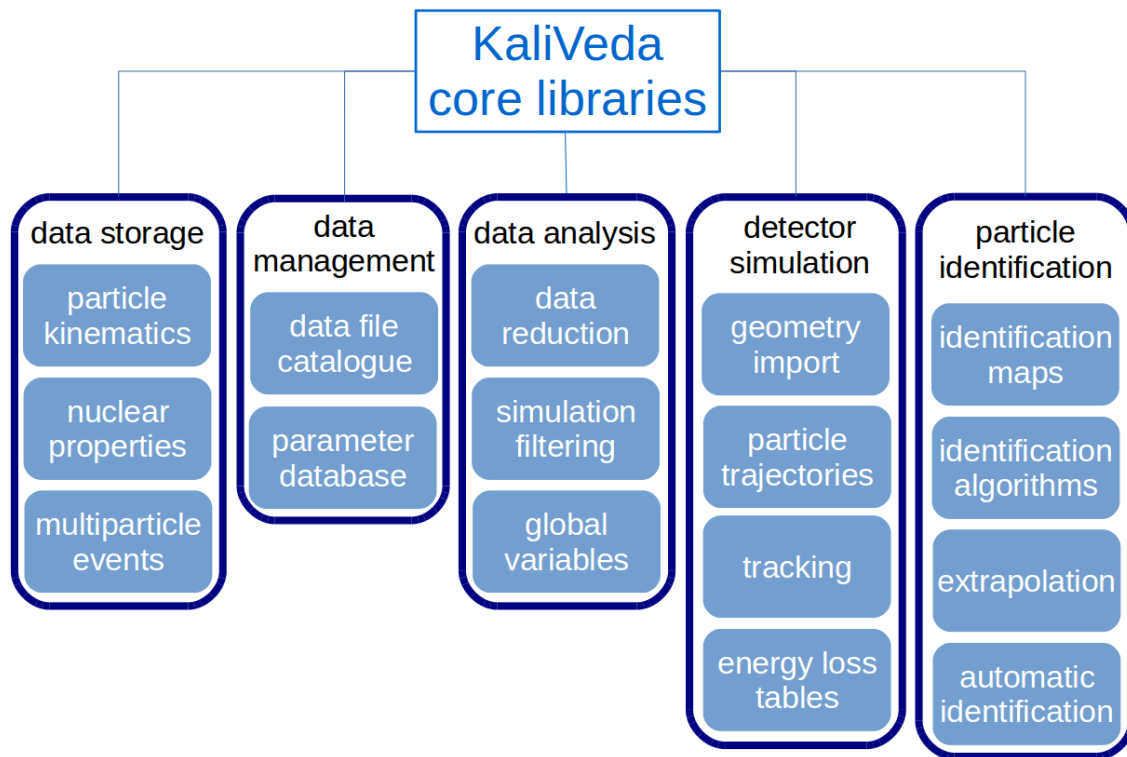


Figure 4.3.1 – Overview of the main components of the core libraries of the KaliVeda toolkit

- PROOFLite (Parallel ROOT Facility) for efficient data analysis on multi-core machines;
- ROOT geometry package for description of array geometries, deduction of particle trajectories, and tracking.

KaliVeda is built on 10 main pillars⁶ which are:

Geometry Description of detector array geometries, including deduction of geometrical relationships between detectors of the array, possible trajectories of particles through the detectors and the resulting possibilities for identification by $\Delta E - E$ (or other) methods;

Stopping Calculation of energy losses and ranges of charged particles in matter, both for calibration purposes and array response to simulated data (“filtering”);

Nuclei Description of atomic nuclei, including databases of binding energies, charge radii, lifetimes, level schemes and excited states;

Kinematics Handling of relativistic kinematics for multi-particle events, providing simple handling of transformations between different reference frames;

Data Management Manage large catalogues of data from different experiments, providing transparent access to data whether it is stored locally or remotely (interfaces to IRODS data

⁶This is actually 3 more than T.E. Lawrence, who only had 7 [142].

management system used at CC-IN2P3, and access through XROOTD remote file server). Moreover, each dataset has an associated database containing full details of the experimental conditions of each run (beam energy, gas pressures, DAQ trigger, *etc.*);

Reconstruction Reconstruction of multi-particle events beginning from raw data *i.e.* DAQ recorded signals in detectors, using the knowledge of the geometry of the array;

Calibration Object-oriented approach to detector calibration based on successive transformations of the raw detector signals;

Identification A large range of tools for implementing $\Delta E - E$ (or other) identification of nuclei from data, including many graphical user interfaces for drawing, adjusting and testing identification grids;

Analysis Sophisticated environment for analysis of data, thanks to which the user's only direct concern is the implementation of the required analysis, for which many tools are provided such as semi-automatic calculation of commonly-used or user-defined global variables (multiplicities, total charge/momentum/energy, flow tensor, *etc.*). The same user analysis code and graphical user interface can be used to launch either large-scale batch analysis at CC-IN2P3 or for parallel processing on the user's multi-core PC;

Simulation Tools for both generating simulated events (including an interface to the statistical decay code Gemini++ [133, 134]) and for importing the results of calculations using different models (HIPSE, ELIE, MMM, SMF, INC++, ...), and a graphical user interface dedicated to "filtering" the simulated events with different experimental set-ups and analysing the results.

4.4 Technologies

4.4.1 Language

Obviously, the bedrock of KaliVeda is the C++ programming language along with the ROOT framework. As was the case with ROOT before version 6 (first released in May 2014) KaliVeda is mostly written using C++03, heavily reliant on run-time polymorphism (inheritance), with little use of templates or the Standard Library [containers and algorithms](#). As ROOT6 has matured and compiler support for C++11/C++14 has become more widespread, KaliVeda has begun to exploit more and more possibilities of the new standard, following the evolution of ROOT, but in all cases backwards compatibility is ensured (a C++03 alternative is provided for those poor souls still stuck with a very old compiler). Thus, it is now possible to loop over all nuclei in an event and print their atomic number by simply writing

```
for(auto nuc : event)
{
    std::cout << nuc.GetZ() << std::endl;
}
```

or select nuclei to be included in the calculation of global variables using [lambda expressions](#):

```
glob_var.SetSelection("Z<3",
    [](const KVNucleus* nuc){ return nuc->GetZ()<3; });
```

4.4.2 Build system

Over the years, the environment has grown to currently include over 600 classes which are compiled into 30-40 shared object libraries. Correct compilation without errors on as many different systems (different Linux distributions of differing ages, such as Ubuntu, Debian, CentOS, but also MacOS) with different compilers and as many versions of ROOT as possible was one of the initial mission statements of KaliVeda. This has to be ensured by the build system, which must also check the availability and suitability of various 3rd-party packages that can alter which classes can/should be compiled.

Until version 1.10 in March 2015, this was handled (more-or-less well) by a home-made build system based on [GNU Makefiles](#). However, rather like the original FORTRAN environment for IN-DRA, the project had outgrown this approach and maintenance or further expansion had become unfeasible. In parallel to the “official” version, attempts were made to transition to the successor of make, [automake](#), partly out of a desire to provide pre-compiled packages for Ubuntu Linux⁷. Then ROOT changed build system as part of the evolution towards ROOT6, choosing the [cmake build system](#), which has now become a standard for open source software projects. Compared to make and automake, writing and maintaining a flexible build system with many complicated dependencies with cmake is remarkably easy. In addition, it makes it easy for users to write and compile their own code using KaliVeda. The following is an example CMakeLists.txt file (taken from the [KaliVeda User’s Guide](#)) for generating an executable from some code MyCode.cpp using KaliVeda and ROOT frameworks:

```
cmake_minimum_required(VERSION 2.8.11)

project(MyProject)

#----- locate KaliVeda installation
find_package(KaliVeda REQUIRED)
include(${KALIVEDA_USE_FILE})
#----- locate ROOT installation
find_package(ROOT REQUIRED)
include(SetupROOTBuild)

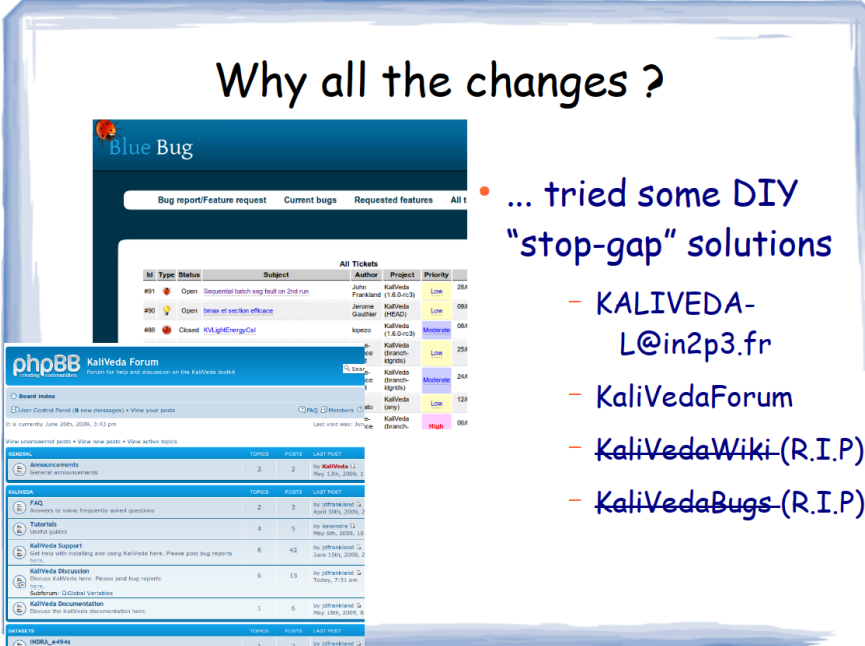
add_executable(MyExec MyCode.cpp)
target_link_libraries(MyExec ${KALIVEDA_LIBRARIES})
```

4.4.3 Version Control

An essential part of any software project is a decent version control system (VCS), but it is surprising how many physicists (and not only...) are still either unaware of the existence of VCS or

⁷Currently this is impossible since the ROOT packages were removed from the Debian archive for non-conformity a few years ago. However, it now seems that they might be [coming back](#).

Why all the changes ?



- ... tried some DIY "stop-gap" solutions
 - KALIVEDA-L@in2p3.fr
 - KaliVedaForum
 - KaliVedaWiki (R.I.P)
 - KaliVedaBugs (R.I.P)

Figure 4.4.1 – Slide from presentation of the migration to Launchpad/bzr in June 2009, illustrating some of the stop-gap solutions which tried (and failed) to fill the absence of a CC-IN2P3-hosted TRAC server.

are reticent to use one. My first contact was again a side-effect of the 4th INDRA campaign at GSI, following which in 1999 or 2000 Walther Mueller visited GANIL in order to share some of the experience he had gained in software development for INDRA using ROOT during the campaign. He mentioned that all the source code was stored in a “CVS server” which allowed to keep track of all the changes to the code and even to get back to a previously working version if someone hacked the wrong way. It all seemed a bit too much, and I think I can remember saying after the meeting “We won’t need that”. Luckily before getting far with the KaliVeda project, I had time to think and the first versions of the code were stored in a centralised CVS repository on a server at CC-IN2P3⁸.

By 2008 however, KaliVeda was getting harder and harder to manage with CVS, which provides limited support for example for renaming or moving directories around in the project, unless you find clever tricks to hack the system (and I did). In addition, in order to maximize efficiency and exchange with the “users” it was becoming more and more clear that some kind of website with bug-tracker, discussion forum, code history and development planning tools would be of great use. Such tools had recently become available in an integrated package called Trac which was based on a new, modern version control system, SVN, which had been developed as a successor to and major improvement on CVS, and which had recently been adopted by the ROOT development team instead of CVS. Along with François Mauger and Daniel Cussol of LPC Caen, we therefore asked CC-IN2P3 if they would consider hosting a Trac server for software development in IN2P3 laboratories. This was refused (I think on the grounds of security), and so I started

⁸Released in 1990, there has been no further development of CVS since 2008.

looking around and playing with various solutions (see Figure 4.4.1).

For a long time I had been using Ubuntu Linux on my laptops, and it turned out that the company behind Ubuntu, Canonical Ltd., hosted a website for software projects with exactly the features I was looking for: [Launchpad](#) (in fact, the principal role of the Launchpad site is to host all of the projects which are included in Ubuntu). In May 2009, all code-hosting, bug-reporting, *etc.* for KaliVeda was migrated to Launchpad, which also meant migrating to a new VCS, b`z`r (pronounced “bazaar”), which was a breath of fresh air compared to CVS, making it far easier for different people to contribute to the code. Indeed it was from this point on that different contributors⁹ really began to take part in developing and maintaining the software.

Since early 2015 we have again changed VCS, and are currently using the standard tool for open source software projects, `git`. This has again been a major improvement compared to `bzr` (I admit, not all of my fellow contributors agree), and the code is now hosted on the ubiquitous [github](#). Once again, we have thus realigned ourselves with the development path taken by ROOT, now also hosted on github. In the meantime, somewhere between 2015 and 2018, the CC-IN2P3 finally began hosting the necessary tools for modern software development, most notably in the form of a [gitlab](#) platform, entirely equivalent to github and also to what we had requested in 2007. Some time in the near future, KaliVeda’s code repositories will migrate to this platform.

⁹see the list [here](#)

Part II

Present & Future: “What price to get out of going through all these things twice?”

*It all seems so well timed
An' here I sit so patiently
Waiting to find out what price
You have to pay to get out of
Going through all these things twice
[143]*

Chapter 5

Introduction

After having presented a detailed summary of my past scientific and software development activities over the last twenty-five years in Part I, I will now present some more recent works and look towards the future. The first new work has been a focus of my activity for the last two years and is currently under discussion within the INDRA collaboration for publication. It concerns the quantification of the rather nebulous concept of “centrality” in heavy-ion collisions, through the reconstruction of impact parameter distributions for experimental event samples. As a by-product, this work confirms (and quantifies) the long-held suspicion that the “most central” collisions we can select using experimental observables are in fact not as central as one might hope.

The second new work, begun just before the Covid-19 lock-down this spring, will bring us full circle back to not only one of the main preoccupations of my Ph.D but also the subject of the Masters’¹ internship which immediately preceded it: how best to isolate homogeneous event samples corresponding to compact multifragmenting systems? This began from a long-standing regret that we (the INDRA collaboration, or indeed anybody else) have never found a better method for the selection of the single-source (QF) events, on which so much of our understanding of the links between multifragmentation and the liquid-gas phase transition of nuclear matter is based (see Borderie and Frankland [1]), than an arbitrary cut restricting to large flow angles θ_f , where the distribution becomes supposedly isotropic.

I will show here that it is possible to extract, in a non-arbitrary way, an homogeneous subset of events from a given set of data which are more isotropic than the others, and that the properties of these events are those of the QF events: indeed the large- θ_f events make up the majority of these “most isotropic” events, which therefore justifies *a posteriori* this selection method. Having isolated the most isotropic events, I will then show how to extract from them an unambiguous measurement of the degree of anisotropy of the underlying momentum distributions, which could be used, knowing the associated impact parameter distributions, in conjunction with transport model calculations in order to deduce the energy dependence of nuclear transparency in this energy range.

¹DEA for those old enough to remember, for Diplôme d’Etudes Approfondies.

Chapter 6

How central are the most central collisions in Fermi energy heavy-ion collisions ?

6.1 Introduction

For the last thirty years, there has only ever been one way to estimate the centrality of a sample of experimental events: the geometrical prescription of Cavata *et al.* [74]. This simple method for determining the impact parameter was first proposed for relativistic nucleus-nucleus collisions, for which the total reaction cross-section is well approximated by the geometrical cross-section $\sigma = \pi(R_p + R_t)^2$ calculated from the equivalent hard-sphere radii of the projectile and target nuclei, respectively. At these energies the essential features of the reaction dynamics are fixed by the size of the participant zone which is determined by the geometrical overlap of two spheres separated by impact parameter b [144].

Although the geometrical prescription which consists of transforming the measured cross-section for collisions assumed to be the most central into an upper limit of impact parameter was not new (see for example [145]), Cavata *et al.* extended this *sharp cut-off approximation* (SCA) over the whole range of centrality and it is always [74] which is cited when one or the other is used.

The well-known method is illustrated in Figure 6.1.1, taken from their paper. Given an observable X which is expected to increase with the number of participant nucleons, and therefore have a monotonic dependence on b , it is assumed that the largest measured value of X (*i.e.* the last occupied bin in the histogram in the left panel of Figure 6.1.1) occurs for collisions with $b = 0$. Then the total measured cross-section for $X \geq \mathbb{X}$, where \mathbb{X} is any smaller value of the observable, can be transformed into a value of impact parameter $b > 0$ using the SCA. In this way a one-to-one correspondence between observable X and impact parameter b can be constructed and used to provide an impact parameter scale for the experimental data.

To directly quote Cavata *et al.*, “[t]his procedure is rigorous if there is no dispersion in the correlation between [the observable] and impact parameter. In practice, there will always be a finite dispersion, but the method should remain valid as long as the correlation is large enough in comparison to the dispersion [...]”. In the Fermi energy domain, of course, fluctuations (“dis-

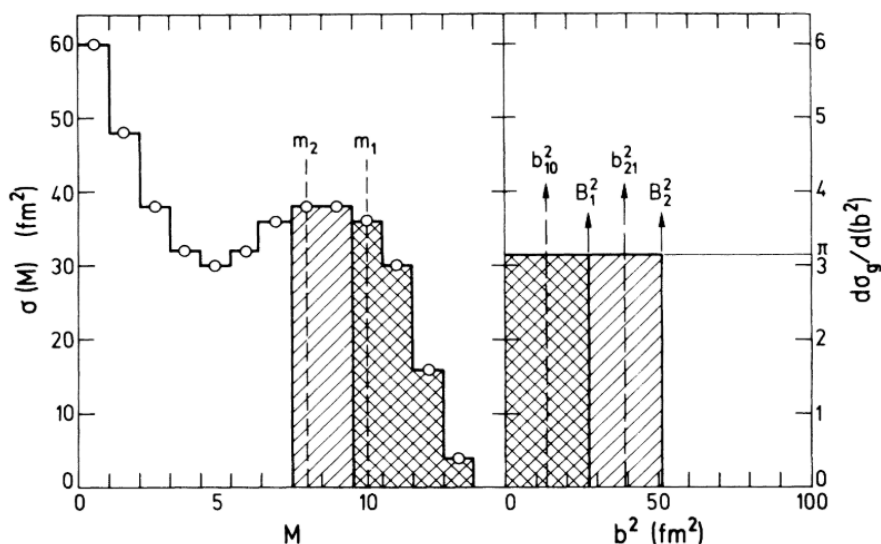


Figure 6.1.1 – Principle of the Cavata prescription [74]: (left) measured cross section versus multiplicity; (right) geometrical cross-section versus b^2 , the square of the impact parameter. The hatched areas correspond to equal integrated cross-sections on both diagrams, with three multiplicity limits $m_0 = \infty$, m_1 and m_2 .

persion”) dominate the dynamics of reactions, especially for more central collisions where, as we saw in Part I, Chapter 2, instabilities may lead to bifurcations and multifragmentation. The essential features of the reaction dynamics are not necessarily uniquely fixed by the geometrical overlap between projectile and target (participant-spectator scenario), as the nuclear mean field may still play an important role at these energies. Therefore in our case the dispersion in the correlation between the observable and the impact parameter is unlikely to be negligible.

This was of course realised right from the start when the Cavata prescription was used in the Fermi energy range [31, 32]. Figure 6.1.2 shows, for simulated events, the effect of fluctuations in the relationship between observable and impact parameter¹ [31]. The thick curve in the figure represents the impact-parameter-integrated, inclusive distribution of an observable ν which decreases on average monotonically with b , such as the total multiplicity. The upper impact parameter limits (in fm) corresponding to various values of ν deduced from the inclusive distribution using the method of [74] are represented by the figures presented along this curve.

As this is a model calculation, it is also possible to decompose the inclusive distribution into the contributions from different impact parameter ranges. This is what is represented by the individual distributions shown under the main curve and labelled with an upper impact parameter (in fm) x : each of these are the ν distributions for $(x - 1) < b \leq x$ fm. Although for the more peripheral collisions ($b > 4$ fm) there is a reasonable correspondence between the real impact parameter range and that deduced from the Cavata prescription (although of course Cavata cannot describe the width or the shape of each distribution), for the more central collisions ($b \leq 4$

¹I used this figure in my Ph.D thesis, as the question of the impact of the fluctuations on the estimation of the impact parameter has long been a preoccupation. As at the time it was not possible to simply “snapshot” any figure in the PDF of any article (as I have done in this manuscript), I wrote to ask Jean Péter for a copy of the figure which I could use. He sent me the original version of the figure on tracing paper which I still have and treasure.

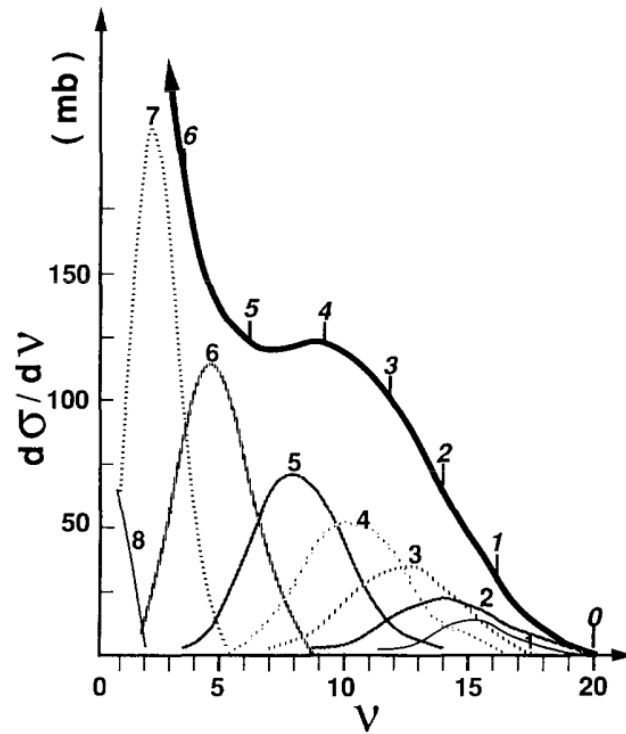


Figure 6.1.2 – Simulated effect of fluctuations in the relationship between impact parameter b and global variable ν on the selectivity of the latter. See text for explanations. From [31].

fm) the distributions for different impact parameter bins overlap more and more due to a combination of decreasing cross section and increasing relative fluctuation of the observable ν . Therefore whereas the Cavata prescription implies that higher cuts in ν select more and more exclusively central collisions, in reality above a certain limit (here somewhere between $\nu = 10$ and $\nu = 15$) the actual mix of impact parameters which are retained by higher and higher cuts evolves far less than the decreasing statistics retained for analysis.

This was the *status quo* for nearly thirty years, until, once again, a new approach arrived from higher energies, although this time it came from the ultra-relativistic regime of collisions at the LHC. Two papers published in 2018, [146] and especially [147], proposed to explicitly take into account the fluctuations in the relationship between any observable X and b (even at such energies where fluctuations could have been thought to be negligible) in order to deduce the evolution of the mean value of the observable with centrality by fitting the inclusive measured distributions $P(X)$. In the following I will show how the same method can be applied to collisions in the Fermi energy range and as a result give quantitative answers to the question “how central are the most central collisions in intermediate energy heavy-ion collisions?”

6.2 Quantifying the centrality of collisions

The impact parameter of a nucleus-nucleus collision is classically defined by the distance between the straight-line trajectories of the centres of the two nuclei before their interaction. The cent-

rality, c (also called b -centrality or c_b in [146]), is defined as the cumulative distribution function of the impact parameter distribution of collisions,

$$c_b \equiv \int_0^b P(b') db' = \Pr(b' \leq b) \quad (6.2.1)$$

which varies between 0 (most central collisions) and 1 (most peripheral collisions). By definition we have

$$\frac{dc_b}{db} = P(b) \quad (6.2.2)$$

The impact parameter probability distribution for collisions leading to inelastic reactions can be written as

$$P(b) = \frac{2\pi}{\sigma_R} b \cdot P_R(b) \quad (6.2.3)$$

where the first part is the purely geometrical semi-classical approximation of interaction between hard spheres corresponding to the short-range nuclear interaction, and σ_R is the total reaction cross-section. $P_R(b)$ is the probability for an inelastic reaction to occur at a given b , taking into account all effects due to the physics of the collisions, such as surface diffusivity and nuclear transparency; when considering experimental data P_R includes also acceptance and other detection effects, and should be considered the probability for an inelastic reaction to occur *and be detected* at a given impact parameter.

The *sharp cut-off approximation* (SCA) assumes a simple form for $P_R(b)$,

$$P_R(b) = \begin{cases} 1 & b \leq b_{\max} \\ 0 & b > b_{\max} \end{cases} \quad (6.2.4)$$

In this case, the impact parameter distribution Equation (6.2.3) is triangular up to a maximum impact parameter b_{\max} given by

$$\sigma_R = \pi b_{\max}^2 \quad (6.2.5)$$

and the relationship between impact parameter and centrality is given by

$$c_b^{SCA} = \frac{\pi b^2}{\sigma_R} = \left(\frac{b}{b_{\max}} \right)^2 = \hat{b}^2 \quad (6.2.6)$$

where in the last equality we have defined the reduced impact parameter, \hat{b} .

Experimental centrality can be quantified as in [74] using an observable X expected to have a monotonic relationship with b , typically because it measures the violence or the degree of energy dissipation of the collisions: examples are the total number of reaction products per event, or the total kinetic energy in directions transverse to the beam axis [32, 35]. The experimental (or *apparent*) centrality $c_{\mathbb{X}}$ of an event sample \mathbb{S} selected with a cut $X \geq \mathbb{X}$ is then defined as the cumulative distribution

$$c_{\mathbb{X}} \equiv \int_{X \geq \mathbb{X}} P(X) dX = \Pr(X \geq \mathbb{X}) \quad (6.2.7)$$

where $P(X)$ is the probability distribution of X for all recorded collisions, and we have assumed that, as in most cases, X increases as $b \rightarrow 0$. It should be noted that $c_{\mathbb{X}}$ is quite simply the fraction of all measured events retained by the cut.

Experimental selections of “central” collisions are usually defined using the quantile function associated with Equation (6.2.7) in order to find a cut which gives a value of $c_{\mathbb{X}}$ deemed small enough for the required selectivity (typically $c_{\mathbb{X}} = 1 - 10\%$), while retaining a statistically significant number of events for the analysis. Up to now, in order to estimate the impact parameter range associated with such a selection of data, the prescription of Cavata et al [74] has been used. This consists in equating the apparent centrality $c_{\mathbb{X}}$ of Equation (6.2.7) with the sample’s *true* centrality calculated in the sharp cut-off approximation, Equation (6.2.6); equating with $c_{\mathbb{X}}$ defined by the cut $X \geq \mathbb{X}$, the upper limit of reduced impact parameters $\hat{b}_{\mathbb{X}}$ corresponding to the cut is deduced to be

$$\hat{b} \leq \hat{b}_{\mathbb{X}}, \hat{b}_{\mathbb{X}} = \sqrt{c_{\mathbb{X}}} \quad (6.2.8)$$

which is the main result of [74] and has been used in every analysis aiming to study impact parameter dependence of heavy ion collisions at intermediate energies ever since.

6.2.1 Reconstructing impact parameter distributions for experimental data

The method of [74] can give no information on the actual impact parameter distribution $P(b|\mathbb{S})$ associated with an event sample \mathbb{S} : the triangular distribution of the sharp cut-off approximation (SCA) is simply assumed, and the fluctuations in the relationship between X and b are ignored. The new method proposed in [146, 147] on the other hand makes no *a priori* assumption about the form of $P(b|\mathbb{S})$ but rather allows to reconstruct this impact parameter distribution from the data, as will now be demonstrated.

For any observable X whose functional dependence on the impact parameter can be written in terms of a conditional probability distribution $P(X|b)$, the inclusive distribution of X resulting from all collisions with an impact parameter distribution $P(b)$ is given by

$$P(X) = \int_0^{\infty} P(b) P(X|b) db \quad (6.2.9)$$

Let us assume for the moment that we know $P(X|b)$. The impact parameter distribution corresponding to a finite range of X values can be calculated from

$$P(b|X_1 < X \leq X_2) = \frac{\int_{X_1}^{X_2} P(b|X)P(X)dX}{\int_{X_1}^{X_2} P(X)dX} = \frac{1}{c_{X_1} - c_{X_2}} \int_{X_1}^{X_2} P(b|X)P(X)dX$$

where we have used Equation (6.2.7) for the integral in the denominator. Using Bayes’ theorem,

$$P(b|X)P(X) = P(X|b)P(b) \quad (6.2.10)$$

we can rewrite this as

$$P(b|X_1 < X < X_2) = \frac{P(b)}{c_{X_1} - c_{X_2}} \int_{X_1}^{X_2} P(X|b) dX \quad (6.2.11)$$

or, for a sample $\mathbb{S} : X \geq \mathbb{X}$,

$$P(b|\mathbb{S} : X \geq \mathbb{X}) = \frac{P(b)}{c_{\mathbb{X}}} \int_{X \geq \mathbb{X}} P(X|b) dX \quad (6.2.12)$$

More generally, we may wish to obtain impact parameter distributions for any sample of events, not necessarily using a cut on the observable X : such selections may be effected using several cuts on different observables, or using an observable whose relationship with b is not so evident or monotonic. In this case we can generalise Equation (6.2.12) for any sample \mathbb{S} to give

$$P(b|\mathbb{S}) = P(b) \frac{\int P(X|b) \frac{P(X|\mathbb{S})}{P(X)} dX}{\int P(X|\mathbb{S}) dX} \quad (6.2.13)$$

where $P(X|\mathbb{S})$ is the sample distribution of X (i.e. a histogram of X filled from the events in the sample), and the integrals are over the full domain of X . This is an extension of the method proposed in [146, 147].

From Equations (6.2.11)–(6.2.13) we can therefore calculate impact parameter distributions for experimental data samples if we can deduce the conditional probability distribution $P(X|b)$ by fitting the experimentally measured $P(X)$ distribution using Equation (6.2.9). In order to do this, however, we need to deal with the unknown distribution of impact parameters for all events, $P(b)$.

6.2.1.1 Removing the uncertainty on the overall impact parameter distribution

In Equations (6.2.9)–(6.2.13) $P(b)$ is the impact parameter distribution of all collisions recorded by the experiment (those responsible for $P(X)$) and is in principle unknown: although in an ideal case it would simply be the sharp cut-off approximation of Equation (6.2.4), it will be affected by any experimental bias due to detection (in)efficiency and triggering conditions, etc., which could be simulated but would then be model-dependent.

However, by a change of variable using the b -centrality c_b of Equation (6.2.1) the uncertainty on the distribution of recorded impact parameters disappears, as by definition the cumulative distribution function for any distribution $P(b)$ is uniformly distributed between 0 and 1 and $P(c_b) = 1$. We then find for the distribution of X

$$P(X) = \int_0^1 P(c_b) P(X|c_b) dc_b = \int_0^1 P(X|c_b) dc_b \quad (6.2.14)$$

and just by knowing $P(X|c_b)$ we can calculate the experimental distribution of X . Similar simplifications follow for Equations (6.2.10)–(6.2.13), which become

$$P(c_b|X)P(X) = P(X|c_b) \quad (6.2.15)$$

$$P(c_b|X_1 < X < X_2) = \frac{1}{c_{X_1} - c_{X_2}} \int_{X_1}^{X_2} P(X|c_b) dX \quad (6.2.16)$$

$$P(c_b|\mathbb{S} : X \geq \mathbb{X}) = \frac{1}{c_{\mathbb{X}}} \int_{X \geq \mathbb{X}} P(X|c_b) dX \quad (6.2.17)$$

and

$$P(c_b|\mathbf{S}) = \frac{\int P(X|c_b) \frac{P(X|\mathbf{S})}{P(X)} dX}{\int P(X|\mathbf{S}) dX} \quad (6.2.18)$$

Therefore if we can deduce the form of $P(X|c_b)$ by fitting the experimental $P(X)$ distributions using Equation (6.2.14) and a suitable parametrization of $P(X|c_b)$ (see 6.2.2 below), we can calculate centrality distributions $P(c_b|\mathbf{S})$ for experimental event samples using Equation (6.2.18). Then the impact parameter distribution for \mathbf{S} is given by a change of variables as

$$P(b|\mathbf{S}) = P(b)P(c_b(b)|\mathbf{S}) \quad (6.2.19)$$

where we have used Equation (6.2.2).

6.2.2 Parametrizing the relationship between X and c_b

The *ansatz* for $P(X|c_b)$ employed in [147] consists in separating the problem into two parts: (i) the centrality dependence of the mean value of the observable, $\bar{X}(c_b)$, and (ii) the fluctuations of X around this mean. Concerning part (ii), the advantages of using a gamma distribution

$$P(X|c_b) = \frac{1}{\Gamma(k)\theta^k} X^{k-1} e^{-X/\theta} \quad (6.2.20)$$

for the observable rather than a Gaussian or other symmetric distribution were demonstrated in [147]. The mean and standard deviation of this distribution are given by

$$\bar{X}(c_b) = k(c_b)\theta \quad (6.2.21)$$

$$\sigma_X = \sqrt{k(c_b)\theta} \quad (6.2.22)$$

where the parameter $\theta = \sigma_X^2 / \bar{X}$ determines the relative importance of fluctuations of the observable, and is assumed to be independent of centrality.

Concerning the parametrization of $k(c_b)$, the authors of [147] proposed a very general polynomial form for a monotonically decreasing function of centrality. However, we have found that when the order of the polynomial is sufficient to correctly describe the evolution of \bar{X} by fitting $P(X)$ (typically order 3 or 4), the monotonicity of their function is no longer guaranteed without imposing several non-trivial constraints on the parameters of the fit. Therefore we have sought a simpler functional form which guarantees monotonicity while being sufficiently general to describe the typical shapes of $\bar{X}(b)$ curves as predicted by various transport model simulations in this energy range (see for example [148, 75, 149, 150, 52]).

We have found that the following monotonically decreasing function of centrality

$$k(c_b) = k_{\max} [1 - c_b^\alpha]^\gamma + k_{\min} \quad (6.2.23)$$

can perform this role quite satisfactorily, with only 4 free parameters². In addition, the values of α and γ can be directly linked to the shape of $k(c_b)$, making interpretation of fit results more

²if a monotonically increasing function of centrality is required, replace c_b by $1 - c_b$ in Equation (6.2.23)

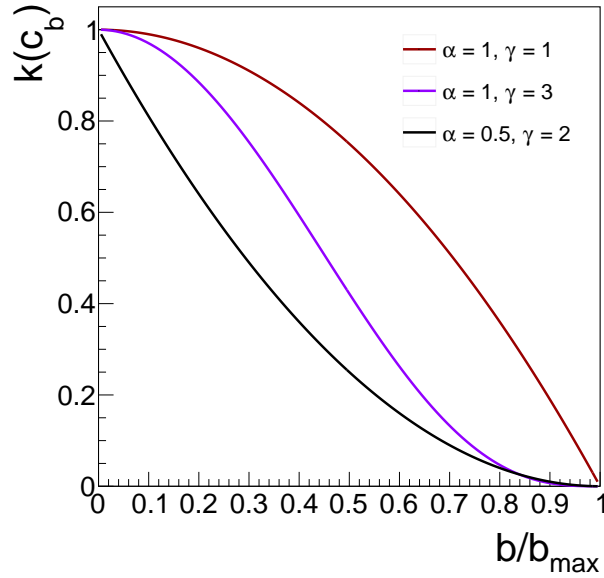


Figure 6.2.1 – Examples of $k(c_b)$ curves obtained with the parametrization of Equation (6.2.23), as a function of reduced impact parameter $\hat{b} = b/b_{\max}$. In all cases $k_{\max} = 1$ and $k_{\min} = 0$. The geometric relation $c_b = (b/b_{\max})^2$ has been used.

immediate. Examples of $k(c_b)$ for different values of α, γ are presented in Figure 6.2.1. The value of α determines whether or not the observable's evolution with b presents a plateau for the most central collisions, i.e. when $\alpha \geq 1$ there exists a range of small impact parameters for which the derivative $dk/db \approx 0$ which implies a lower limit to the observable's sensitivity to variations of b ; the larger the value of α , the larger the range. The γ -parameter determines the concavity of the curve: values of $\gamma > 1$ lead to S-shaped curves with an asymptotically zero derivative at $c_b = 1$.

The shapes of these curves can be related (but are not limited) to the participant-spectator scenario [144]: Equation (6.2.23) with $\alpha \approx 0.5$ and $\gamma \approx 2$ gives a perfect fit to the geometrical overlap volume between two equal-radii spheres whose centres are separated by a distance b . The overlap volume between unequal spheres (which reaches its maximum and presents a plateau for $b < |R_{\text{proj}} - R_{\text{targ}}|$) can be approximated by $\alpha > 1$ and γ values in the range 2-10.

k_{\max} and k_{\min} determine the maximum mean value of the observable achieved in head-on collisions:

$$X_{\max} = \bar{X}(b = 0) = \theta(k_{\max} + k_{\min}) \quad (6.2.24)$$

The 'offset' parameter k_{\min} is important because we cannot make the approximation that $X_{\min} = \theta k_{\min}$ is zero for the most peripheral recorded collisions. This is especially clear when considering $X = N_C$, the total multiplicity of charged products. All INDRA data analysed in the following were obtained with an online acquisition trigger corresponding to a minimum number of fired telescopes of between 3 and 5 depending on the system studied. For the lightest systems considered in our study, the maximum charged particle multiplicity can be as small as 20; in this case the role of k_{\min} is far from negligible.

6.2.3 Procedure for reconstruction of impact parameter distributions

For each dataset, we fit the inclusive probability distributions $P(X)$ of each observable considered using a numerical implementation of Equations (6.2.14), (6.2.20) and (6.2.23), using the latest version of the ROOT software toolkit [13, 14] in order to benefit from its built-in multithreading capabilities which considerably speed up calculations. The 5 parameters α , γ , θ , k_{min} and k_{max} were allowed to vary freely within reasonable limits and were adjusted using the MINUIT fitting algorithm. The range of X considered for each fit was varied in order to optimize the reduced χ^2 for each distribution: in all cases the largest values (most central collisions) were included, and in general only the smallest X (most peripheral collisions) needed to be excluded in order to achieve convergence of the fitting procedure. Fits to each distribution typically required a few seconds of processing time on a laptop with an Intel Core i7 processor.

For the validation of the method, see [Appendix B](#), Section §B.1.

6.3 Reconstruction of impact parameter distributions for experimental data

In the following we will present the results of applying the methods presented above to data for a wide range of different colliding systems measured with INDRA, which are summarized in [Table 6.1](#). The data concern the two observables which are most commonly used with INDRA for centrality estimation and/or selection, namely the total multiplicity of charged reaction products, N_C , and the total transverse energy of light charged particles (LCP, isotopes of $Z = 1, 2$ nuclei), E_{t12} . N_C is the most commonly-used impact parameter filter by many different groups in the intermediate energy range, while E_{t12} has been especially used by the INDRA collaboration as it exploits the very high, angle-independent efficiency of the array for detection of LCP.

In [Table 6.1](#), as well as the mass asymmetry, projectile energy and number of recorded events, are given also the trigger multiplicity (corresponding to the minimum number of fired modules which may include γ -ray, electron, pion or neutron detection in the CsI scintillators) for each reaction. In the offline analysis the same condition was applied to the reconstructed events (corresponding to a minimum number of correctly identified charged products, thus excluding γ -rays *etc.*).

From simulations with many different reaction models and different software “filters” to simulate the acceptance of the INDRA array we expect that minimum bias data (*i.e.* with no selection other than trigger multiplicity) has an unbiased geometrical distribution for all but the most peripheral collisions (see for example [Figure 2\(a\)](#) of [157]) and can be well described by [Equation \(6.2.3\)](#) with an inelastic reaction probability distribution of the form

$$P_R(b) = \frac{1}{1 + \exp\left(\frac{b-b_0}{\Delta b}\right)} \quad (6.3.1)$$

with typical Δb values of 0.3-0.4 fm, where $b_0 \approx \sqrt{\sigma_R/\pi}$. Although the use of such an assumed distribution changes nothing for the deduced impact parameter distributions for central

System	Mass asymmetry	E_{proj} [MeV/A]	Trigger multiplicity	Events
$^{36}\text{Ar} + \text{KCl}$ [151]	0.00	31.54	3	3216332
		39.97	3	3496188
		51.66	3	2391311
		74.00	3	3337570
$^{36}\text{Ar} + ^{58}\text{Ni}$ [152, 153]	0.23	31.54	3	8259867
		39.97	3	7234383
		51.66	3	8599855
		63.03	3	5020363
		74.00	4	7648474
		83.63	4	4657028
$^{58}\text{Ni} + ^{58}\text{Ni}$ [154, 155]	0.00	95.22	4	9799670
		31.98	4	4538513
		52.00	4	4738429
		63.63	4	4473639
		73.96	4	5198692
$^{58}\text{Ni} + ^{197}\text{Au}$ [98]	0.55	82.00	4	5578566
		90.00	4	9144521
		31.98	4	7448285
		52.00	4	7941858
		63.63	4	4720169
$^{129}\text{Xe} + ^{119}\text{Sn}$ [42, 75]	0.04	73.96	4	6685519
		82.00	4	7398023
		90.00	4	11664617
		24.98	4	5288164
		32.00	4	3916797
$^{129}\text{Xe} + ^{124}\text{Sn}^*$ [82]	0.02	38.98	4	5261377
		45.00	4	6067739
		50.13	4	5792220
		65.00	3	881642
$^{197}\text{Au} + ^{197}\text{Au}^*$ [156]	0.00	80.00	3	424357
		100.00	3	1328486
		40.00	3	2783629
		60.00	3	7589902
		80.00	3	3545170
		100.00	3	10691556
		150.00	5	928692

Table 6.1 – Characteristics of collisions studied in this work: mass asymmetry $|A_p - A_t| / (A_p + A_t)$, beam energy, DAQ trigger multiplicity and total number of recorded events. References are given to the original papers where details of the data-taking can be found. Systems marked with an asterisk were measured at GSI, all others at GANIL.

collisions, it allows to better reproduce impact parameter distributions $P(b|S)$ for the most peripheral collisions. For more details on the properties and use of this distribution, see [Appendix B](#), Section §B.2.

When comparing data it is important to remember that not only will the upper limit for recorded impact parameters depend on the trigger conditions, but also on the colliding nuclei and beam energy. As events are only recorded/analysed for collisions producing at least a minimum number of charged products, the full reaction cross-section is not recorded. Very peripheral reactions, leading for example only to evaporation of neutrons, are excluded (unless projectile- or target-like fragments are detected, which is unlikely for such peripheral reactions where the projectile is hardly deviated from the beam direction and the recoil of the target is insufficient to overcome detection thresholds). For each colliding system and an on-line trigger $M \geq m_T$, b_0 will to a great extent be determined by the most peripheral reactions which produce at least m_T charged products, which at the threshold are most likely to be m_T light charged particles (LCP, $Z = 1, 2$) for reasons of detection efficiency.

Even for the same projectile-target combination, it is evident that the upper limit for impact parameters will depend on the beam energy, as shown in [75] for $^{129}\text{Xe}+^{nat}\text{Sn}$ collisions with a multiplicity trigger $M \geq 4$: in this case where the cross-section was measured during the experiment, the deduced sharp cut-off b_{max} was found to increase by 15% in the limited energy range 25 – 50A MeV. On the other hand, if no cross-section measurement is available we cannot talk of absolute but only reduced impact parameters, $\hat{b} = b/b_{\text{max}}$. Without an estimation of the experimental b_{max} for each reaction, it is far from guaranteed that collisions with similar \hat{b} have equivalent geometry even for the same projectile and target at different energies, let alone when comparing different systems or even data from different experiments. This is often overlooked.

Finally, let us note that for most of the studied reactions a small fraction of the beam time was dedicated to an absolute minimum bias trigger of $M \geq 1$, for normalization purposes. Although these data should contain the largest possible unbiased range of impact parameters, closer to the full reaction cross-section (once elastic scattering events are suppressed by off-line analysis), they obviously have very low statistics for central collisions and so were not used in the analysis. It has been shown that the higher multiplicity triggers do not bias the event distribution for higher multiplicities compared to the $M \geq 1$ data [158].

6.3.1 Results of fits to data

Examples of fits to the inclusive distributions of the observables N_C and E_{t12} are presented in Figure 6.3.1, for the $M \geq 4$ $^{129}\text{Xe}+^{nat}\text{Sn}$ data. Using the published measured cross-sections for this data [75]³, the $P(X)$ distributions are presented here as differential cross-sections. To better appreciate the quality of the fits, for both low and high statistics regions of the distributions, each is presented with both linear (left panels) and logarithmic (right panels) y -axes. Apart from the lowest N_C or E_{t12} the shapes of the experimental distributions are extremely well-reproduced by each fit, including the exponential tails for the highest multiplicities/energies. Reduced χ^2

³Actually, the published equivalent sharp cut-off b_{max} values from [75] which were deduced from the measured cross-sections, $\sigma_R = \pi b_{\text{max}}^2$, were used. Moreover an impact parameter distribution like Equation (6.3.1) was assumed with $\Delta b = 0.3$ fm, and b_0 calculated by numerical inversion of Equation (B.2.3). To relate centrality and impact parameter Equation (B.2.4) was used.

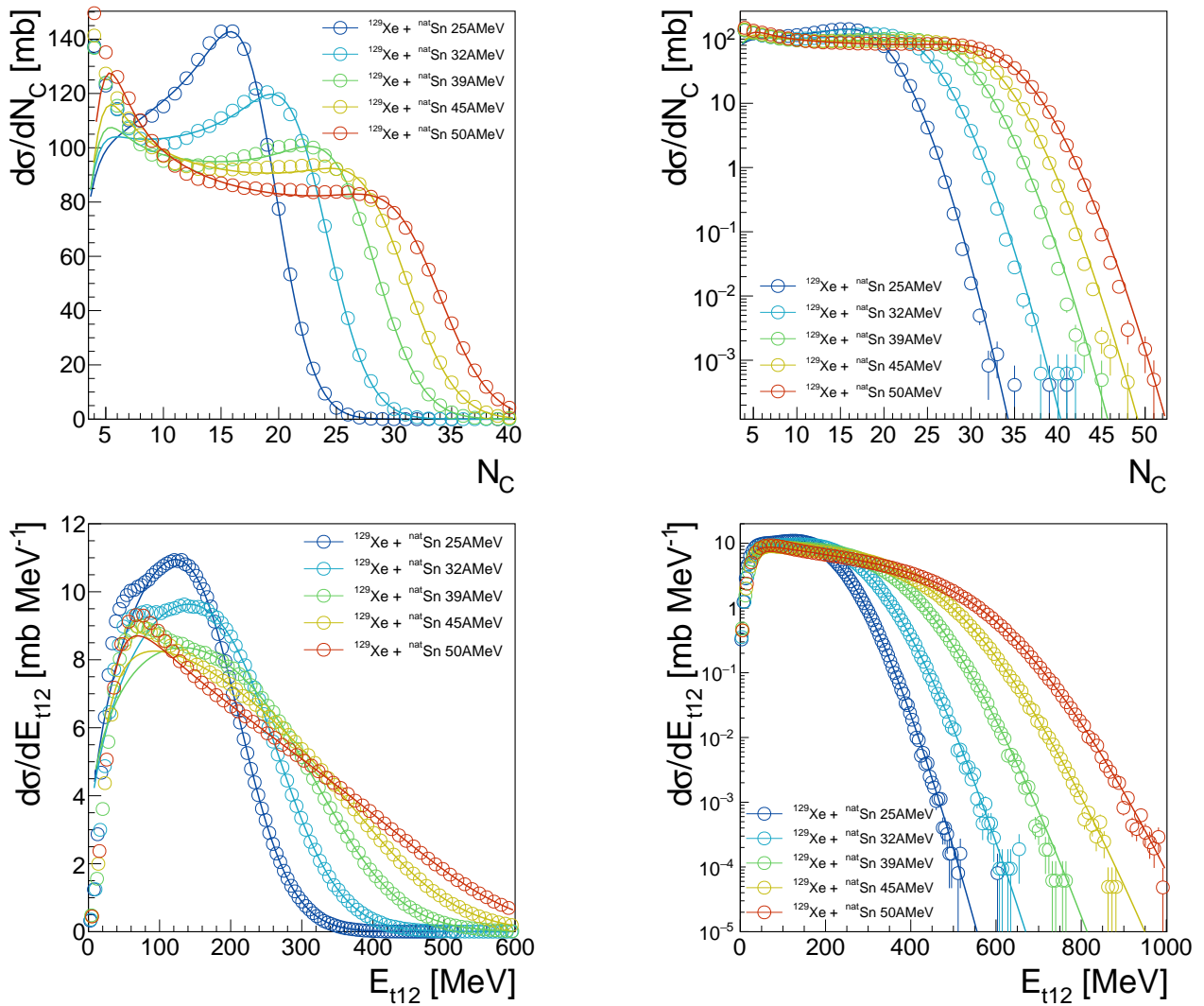


Figure 6.3.1 – Results of fits to the inclusive distributions of N_C (upper row) and E_{t12} (lower row) for the $^{129}\text{Xe} + \text{natSn}$ data. Each distribution is presented with both linear (left panel) and logarithmic (right panel) y -axis. Statistical uncertainties on the data are shown when not smaller than the symbols.

values for each fit are reported in Tables B.1 and B.2. For E_{t12} this goodness-of-fit parameter is generally excellent ($\chi^2 \sim 1$), whereas for N_C the values are far from satisfactory, despite the visual impression of adequate fits. This may in part be due to the necessarily finite binning used with this integer variable compared to a continuous variable like E_{t12} ; the upper left panel of Figure 6.3.1 also shows that the fit generally fails to reproduce the distribution for small N_C (close to the DAQ trigger), decreasing sharply for small N_C instead of increasing as in the experimental data, and it is this discrepancy which dominates the χ^2 values. Nevertheless, the X_{\min} values for N_C follow remarkably well the minimum multiplicity imposed by the trigger, including the increase from $M \geq 3$ to $M \geq 4$ for the $^{36}\text{Ar}+^{58}\text{Ni}$ data at 74A MeV (see Table B.1). Fits of similar quality for both observables were obtained for all data in this study.

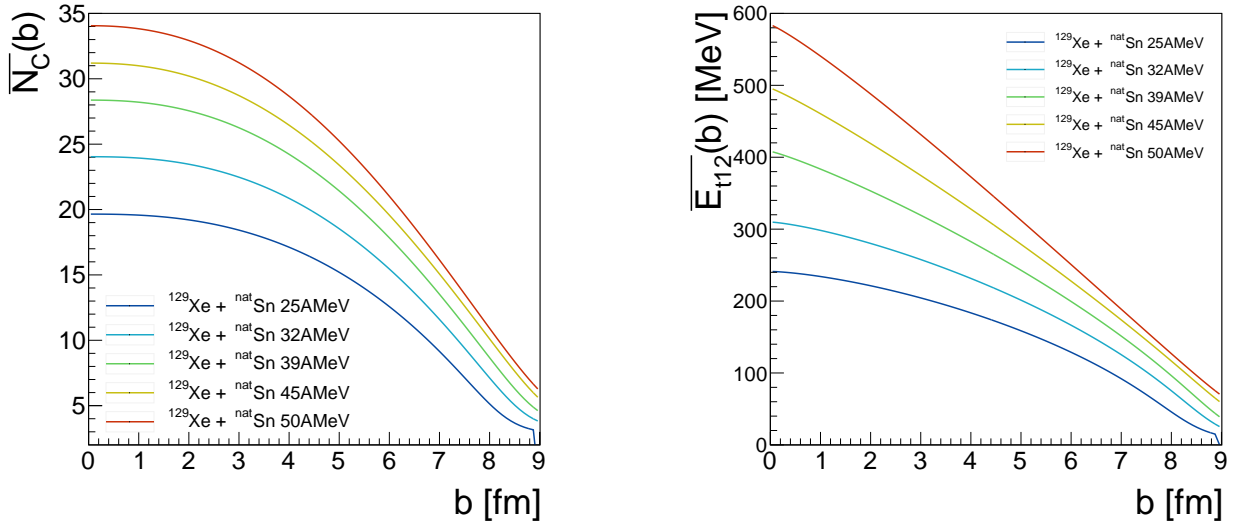
The shapes of the $P(X)$ distributions for both N_C and E_{t12} show a marked evolution with bombarding energy, which is especially clear in the left panels of Figure 6.3.1, with the linear scale of $d\sigma/dX^4$. At the lowest energies there is a pronounced shoulder at the upper end of the distributions which disappears for higher energies, as if to signal a change of weight between central and the more peripheral collisions. Obviously no such change can occur in the relative (geometrical) weighting of different impact parameters; rather the change of shape is due to the evolution of the way in which the mean value of each observable depends on impact parameter, as shown in Figure 6.3.2 which presents how $\overline{N_C}(b)$ and $\overline{E_{t12}}(b)$ change with bombarding energy. Apart from the regular increase of the maximum values reached at $b = 0$ (which will be studied in more detail in 6.3.3 below), the figure shows the gradual disappearance of the flattening of the curve for central collisions seen at 25A MeV (in terms of the shape parameters, α decreases: see Table B.1).

It is this saturation of $\overline{N_C}(b)$ for the most central collisions which leads to the accumulation of events with $N_C \sim X_{\max}$ observed in $P(N_C)$ (and at the same time reduces its effectiveness for selecting very central collisions). The evolution for $\overline{E_{t12}}(b)$ is similar, evolving from a slight plateau at 25A MeV to a near-linear impact parameter dependence for 50A MeV collisions. As a result, $P(E_{t12})$ distributions at low energies have a less marked shoulder than for N_C and any sign of a shoulder disappears for bombarding energies above 32A MeV. Similar evolutions with bombarding energy and similar differences between N_C and E_{t12} are observed for all data.

6.3.2 Bombarding energy and system dependence of deduced $k(c_b)$

We will now concentrate solely on the shapes of the relationship between the mean value of the observables and the impact parameter, and how they depend on not only bombarding energy but also the mass asymmetry of the entrance channel. To this aim Figure 6.3.3 shows the normalized shape functions $k(c_b)$ of E_{t12} for three different systems as a function of reduced impact parameter (cross-section measurements are not available for all data). In these figures all data has been normalized to have a mean value of 0 for $\hat{b} = 1$ and reach the maximum value 1 for $\hat{b} = 0$. The system and energy dependence of the mean values of the observables for $b = 0$, seen to increase regularly with bombarding energy in Figure 6.3.2, will be studied in 6.3.3.

⁴Consequently, the distributions cannot be said to “scale” with the incident or available energy, as has previously often been claimed in various publications of the collaboration as proof of the close relationship between E_{t12} and the impact parameter. See Appendix B, Section §B.4.



(a) mean total charged particle multiplicity, N_C , versus impact parameter

(b) mean total transverse energy of LCP, E_{t12} , versus impact parameter

Figure 6.3.2 – Impact parameter dependence of observables deduced from fits to $^{129}\text{Xe}+^{nat}\text{Sn}$ data.

Figure 6.3.3a presents the $k(c_b)$ function for $^{129}\text{Xe}+^{nat}\text{Sn}$ and $^{129}\text{Xe}+^{124}\text{Sn}$ data. For the $^{129}\text{Xe}+^{nat}\text{Sn}$ data these curves are the same as in Figure 6.3.2b apart from the normalization. Here it is clearer that the (negative) slope of $k(c_b)$ at small b continuously increases with bombarding energy, and the correlation is nearly linear for 50A MeV, as remarked above. Also shown in the figure is the expected form of $k(c_b)$ if it were proportional to the geometrical overlap between two spheres of equal radii. Such a b -dependence for an observable could be interpreted as evidence for a reaction dynamics dominated by the collision geometry, as in the participant-spectator scenario. If so, then the $k(c_b)$ curve deduced from fits to the data shows the evolution towards this regime with bombarding energy, although clearly at 50A MeV it has not yet been reached. The 3 curves for the near-identical $^{129}\text{Xe}+^{124}\text{Sn}$ collisions measured at GSI show the continuation of the trend at higher energies, at least up to 80A MeV.

The other panels of Figure 6.3.3 concern the two asymmetric colliding systems, $^{36}\text{Ar}+^{58}\text{Ni}$ and $^{58}\text{Ni}+^{197}\text{Au}$. In a purely geometrical picture of such reactions we would expect a plateau for central collisions, below the impact parameter for which the smaller of the two nuclei is entirely contained within the larger, $b < |R_p - R_t|$: below this value the overlap volume remains that of the smallest nucleus. This hardly appears to be the case for $^{36}\text{Ar}+^{58}\text{Ni}$ collisions at 32A MeV (Figure 6.3.3b) (it does on the other hand appear more clearly in the $k(c_b)$ for N_C), whereas a more pronounced plateau is evident for the far more asymmetric $^{58}\text{Ni}+^{197}\text{Au}$ system at the same energy (Figure 6.3.3c).

The correct interpretation of the deduced $k(c_b)$ functions requires comparison with different models of the reactions, for whom the generation of correlations such as those presented in Figure 6.3.2 and Figure 6.3.3 is quite direct; for example, to investigate how Pauli blocking or the onset and increase of nuclear transparency, previously studied for many of the same data

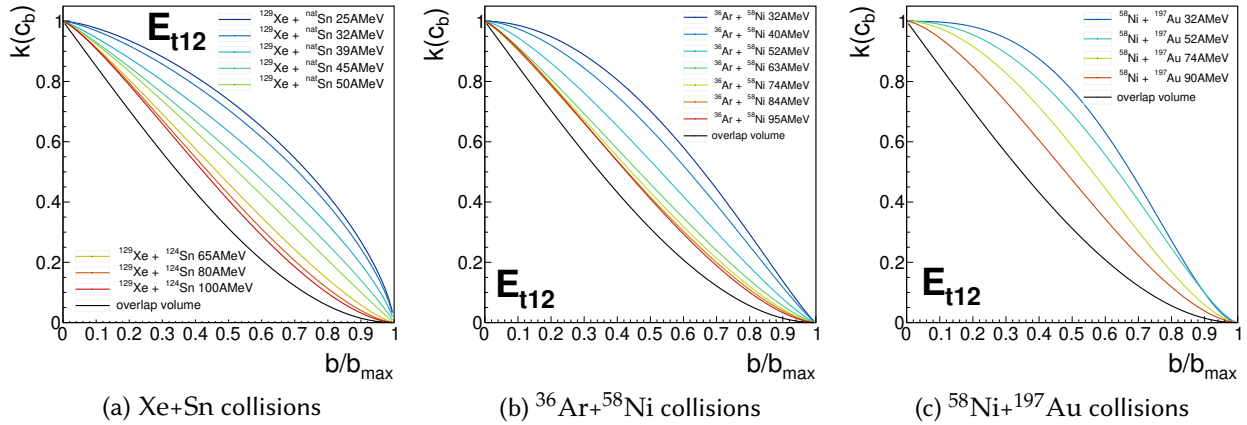


Figure 6.3.3 – Normalized shape functions $k(c_b)$ (with $k_{\min} = 0$, $k_{\max} = 1$) for E_{t12} fits versus reduced impact parameter for different colliding systems. The black curves show the overlap volume for *symmetric* collisions (see text).

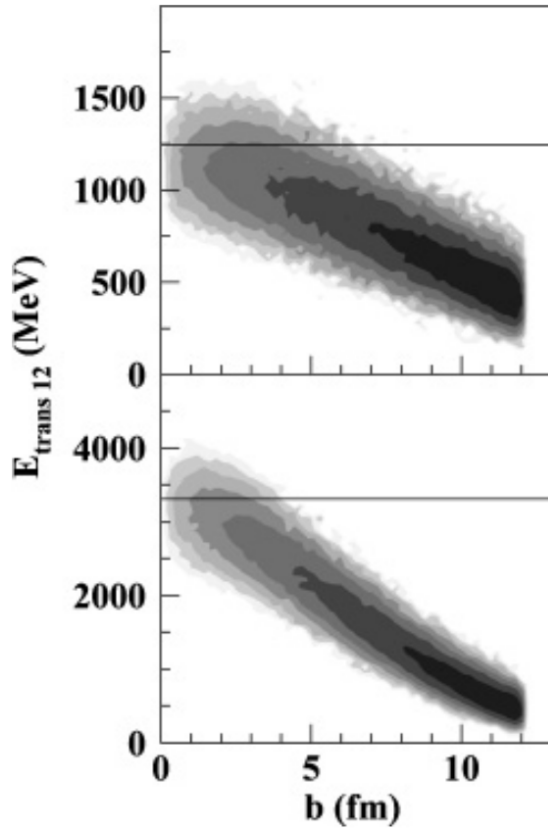
as presented here [107], would affect the simple geometrical picture of the participant-spectator scenario. No further attempt to interpret them will be made here; rather we hope that these previously unavailable experimental correlations will provide new constraints for a wide range of dynamical models of heavy-ion collisions at Fermi energies.

6.3.3 New experimental constraints for dynamical reaction models?

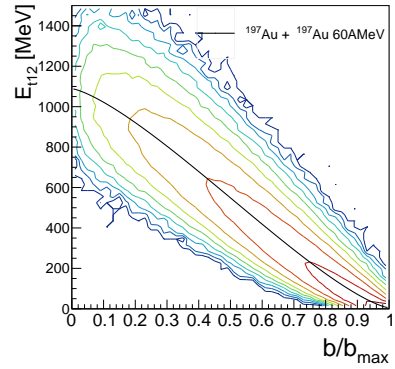
It should not be forgotten that the correlations of Figures 6.3.2 and 6.3.3 concern only the b -dependence of the *mean* values of the observable, whereas a major improvement of the present approach is to take into account the *fluctuations* in the $P(X|b)$ distribution relating the observable with the impact parameter. Examples of what can be achieved with this new method are shown in Figure 6.3.4. Using the fit parameters for E_{t12} for two bombarding energies of $^{197}\text{Au}+^{197}\text{Au}$ collisions, it is possible to generate the full joint probability distribution $P(E_{t12}, b)$ including impact parameter weighting and the fluctuations around the mean value $\overline{E_{t12}}(b)$ (also shown in the Figures 6.3.4b and 6.3.4c). These distributions can be directly compared with the same correlations calculated using the QMD model ([65]; see Appendix A, A.1.3.2) which are shown in Figure 6.3.4a.

Several similarities between the present experimental correlations with the QMD calculations may be remarked, including the slight change of convexity of the correlation (which may again be interpreted as evidence for an evolution towards the participant-spectator regime, as was in part the subject of the study presented in [149]), and the reduced importance of the fluctuations compared to the evolution of the mean value of E_{t12} with increasing bombarding energy. Nevertheless, our point here is once again not to put forward one particular interpretation of the data, in agreement (or otherwise) with one particular model, but to underline the fact that such correlations were previously only possible with model calculations, whereas now they are also experimentally accessible.

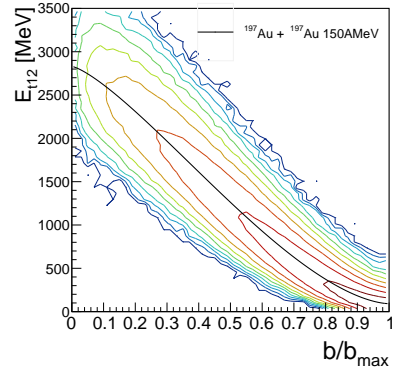
6.3.5a presents another previously inaccessible experimental information: the mean values of



(a) QMD calculations of Zbiri *et al.* [149] for 60A MeV (top) and 150A MeV (bottom).

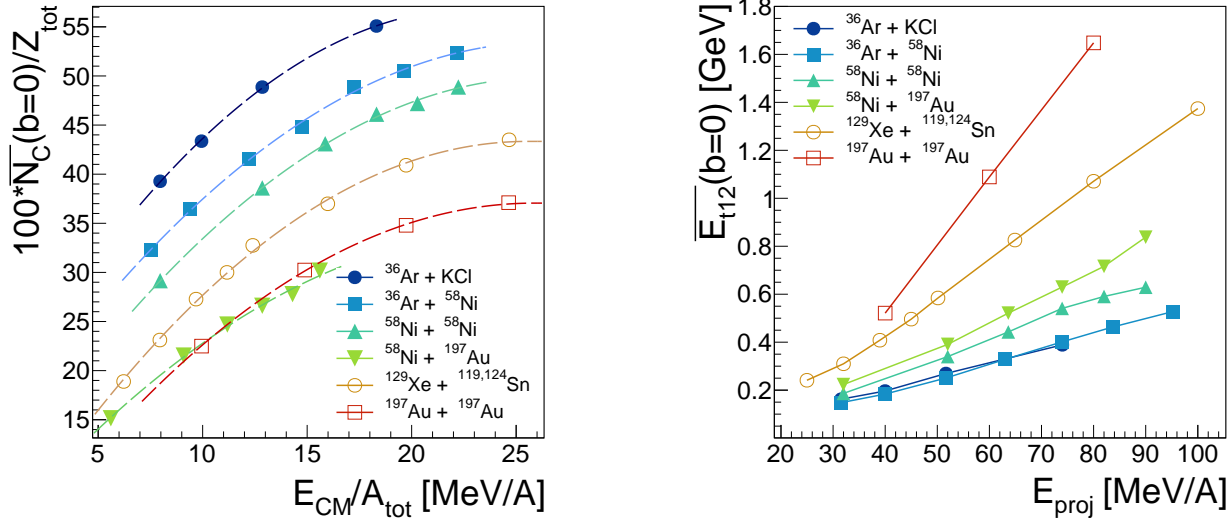


(b) Data for 60A MeV.



(c) Data for 150A MeV.

Figure 6.3.4 – Comparison between joint probability distributions $P(E_{t12}, b)$ calculated with the QMD model or deduced from data for $^{197}\text{Au} + ^{197}\text{Au}$ collisions. Colour contours represent a logarithmic scale of double differential cross-section. Black curves show the mean value $\overline{E_{t12}}(b)$ as a function of impact parameter given by Equations (6.2.21), (6.2.23).



(a) Mean values of total charged product multiplicity for $b = 0$ collisions deduced from fits, $\overline{N_C}(b = 0)$, normalized to total system charge Z_{tot} , as a function of available centre of mass energy per nucleon $E_{\text{CM}}/A_{\text{tot}}$ for all systems. Dashed curves are to guide the eye.

(b) Mean values of total transverse energy of light charged particles for $b = 0$ collisions deduced from fits, $\overline{E_{t12}}(b = 0)$, as a function of bombarding energy per nucleon E_{proj} for all systems.

Figure 6.3.5 – Mean values of N_C and E_{t12} observables for head-on ($b = 0$) collisions.

observables for head-on ($b = 0$) collisions. These would be the easiest constraints for dynamical models to test, as it is sufficient to run the calculation for a single impact parameter. Figure 6.3.5a presents the maximum mean multiplicity $\overline{N_C}(b = 0)$ for each system, normalized to the total system charge, $Z_{\text{tot}} = Z_{\text{proj}} + Z_{\text{targ}}$. These all increase with the available energy, $\epsilon = E_{\text{CM}}/A_{\text{tot}}$, in a non-linear fashion suggesting the appearance of a maximum for each curve (the dashed lines represent a fit using an *ad hoc* parabolic function). An exception to this regular behaviour is the $^{58}\text{Ni} + ^{197}\text{Au}$ system, which seems to follow more closely $^{197}\text{Au} + ^{197}\text{Au}$ than the expected similar-mass/charge $^{129}\text{Xe} + ^{\text{nat}}\text{Sn}$ system.

Figure 6.3.5b shows the maximum mean E_{t12} values achieved for head-on collisions deduced from the fits to $P(E_{t12})$ for all systems. A linear increase is observed for almost all data, the slope increases roughly with the total size of the colliding system, and there is no sign of the values reaching a maximum in the explored energy range, on the contrary to the behaviour seen for total multiplicity in Figure 6.3.5a. In fact, a near-universal behaviour is observed when $\overline{E_{t12}}(b = 0)$ is normalized to the total charge, Z_{tot} , of each colliding system and plotted as a function of the available centre of mass energy per nucleon, $E_{\text{CM}}/A_{\text{tot}}$. Such a scaling suggests that whatever the mechanism responsible for the transverse energies of LCP there is no sign of its weakening in this energy range. It would be very interesting to know if dynamical models of reactions at these energies reproduce this trend.

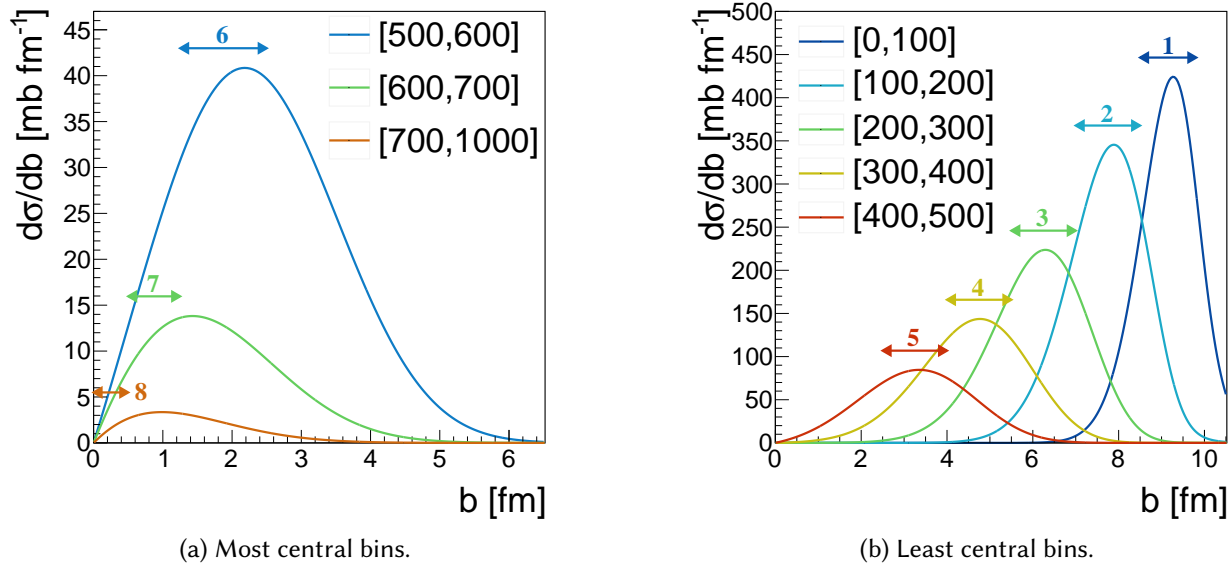


Figure 6.3.6 – (curves) Reconstructed impact parameter distributions for $^{129}\text{Xe}+^{nat}\text{Sn}$ collisions at 50A MeV selected using the 8 centrality bins defined by E_{t12} cuts in [75] (indicated by intervals in the figure legend). (arrows) For each bin (indicated by the number), the range of impact parameters expected to be selected according to [74].

6.3.4 Reconstructed impact parameter distributions

Let us now turn to the impact parameter distributions which can be reconstructed for different data selections using Equations (6.2.17)-(6.2.19) and the previously discussed parameters deduced from fitting the inclusive distributions of different observables. We will study a common case, where the same observable is used both to define centrality cuts and to evaluate the effective centrality of the different selections⁵.

In [75] $^{129}\text{Xe}+^{nat}\text{Sn}$ collisions from 25 – 50A MeV were studied as a function of impact parameter using 8 centrality bins defined in terms of the total transverse energy of LCP, E_{t12} . In Figure 6.3.6 are shown the differential cross-section distributions for these centrality bins, calculated from Equation (6.2.11) using the fitted parameters. The numbered arrows in the figure represent the expected impact parameter range for each bin, deduced from the approach of Cavata *et al.* [74]. It can be seen that for the least central bins (up to bin 5), near-Gaussian distributions of b are obtained, with centroids very close to the centre of the expected ranges.

Nevertheless, even for the most peripheral bins 1 and 2, the actual widths of the deduced b distributions largely exceed the naïve sharp cut-off expectation and considerable mixing of impact parameters between different bins is evident. For the “most central” selections, bins 6 to 8, there is total overlap between the selected impact parameter ranges, although the $\langle b \rangle$ for each bin continues to decrease as E_{t12} cuts increase. For bin 8, the mean impact parameter is $\langle b \rangle = 1.4$ fm compared to the expected upper limit for the bin of $b \leq 0.5$ fm. It is also important

⁵There is of course nothing to stop us from using one observable to select the data, and a different one to evaluate the effective centrality of the selected data, as was done in [32].

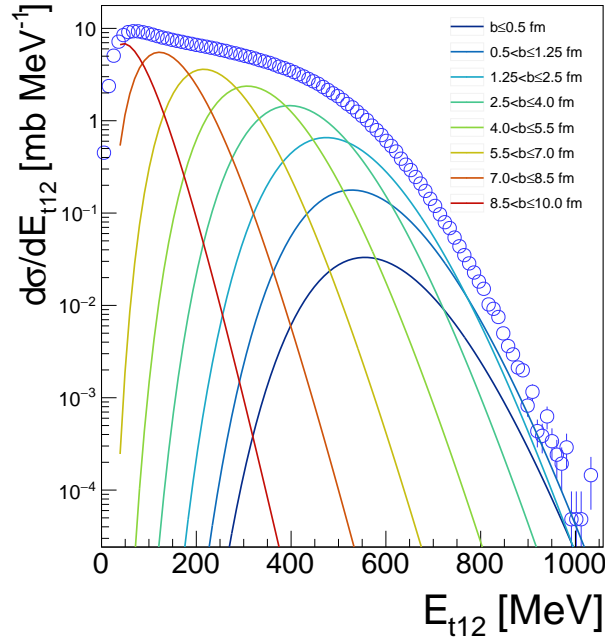


Figure 6.3.7 – Distributions of E_{t12} for $^{129}\text{Xe}+^{nat}\text{Sn}$ collisions at $50A$ MeV for data (symbols) and impact parameter bins indicated in the legend.

to realize that the sharp cut-off approximation of [74] supposes that the events in this bin should occupy the full (triangular) differential cross-section below 0.5 fm; instead they are widely spread out and represent only a small fraction of the differential cross-section for all impact parameters $b \lesssim 5$ fm.

We can also turn the question around and ask what would be the distribution of our observable for any given centrality bin, but now determined by the “true” impact parameter, by using Equation (6.2.9) with different limits for b . Figure 6.3.7 shows such distributions for the same data and using the same intervals of b as in Figure 6.3.6. This is the equivalent of Figure 6.1.2, from Péter *et al.* [31], with the difference being that this is experimental data, not a model calculation. It can clearly be seen that the 3 most central impact parameter bins, for $b \leq 2.5$ fm, are mainly responsible for populating the high- E_{t12} tail of the distribution, and that they cover very similar ranges of the observable. It is then obvious that any attempt to isolate events with impact parameters below this limit using such an observable would be futile.

6.3.5 So just how central are the most central collisions?

Figure 6.3.8 presents the mean values of reduced impact parameters $\hat{b} = b/b_{max}$ (measured cross-sections are not available for all systems) for two different centrality cuts defined using E_{t12} , either $c_{E_{t12}} \leq 10\%$ or $c_{E_{t12}} \leq 1\%$, for all studied colliding systems. In both cases $\langle \hat{b} \rangle$ values for most systems seem to follow similar trends as a function of the available centre of mass energy per nucleon, E_{CM}/A_{tot} . Similar results are found using the total charged product multiplicity, N_C .

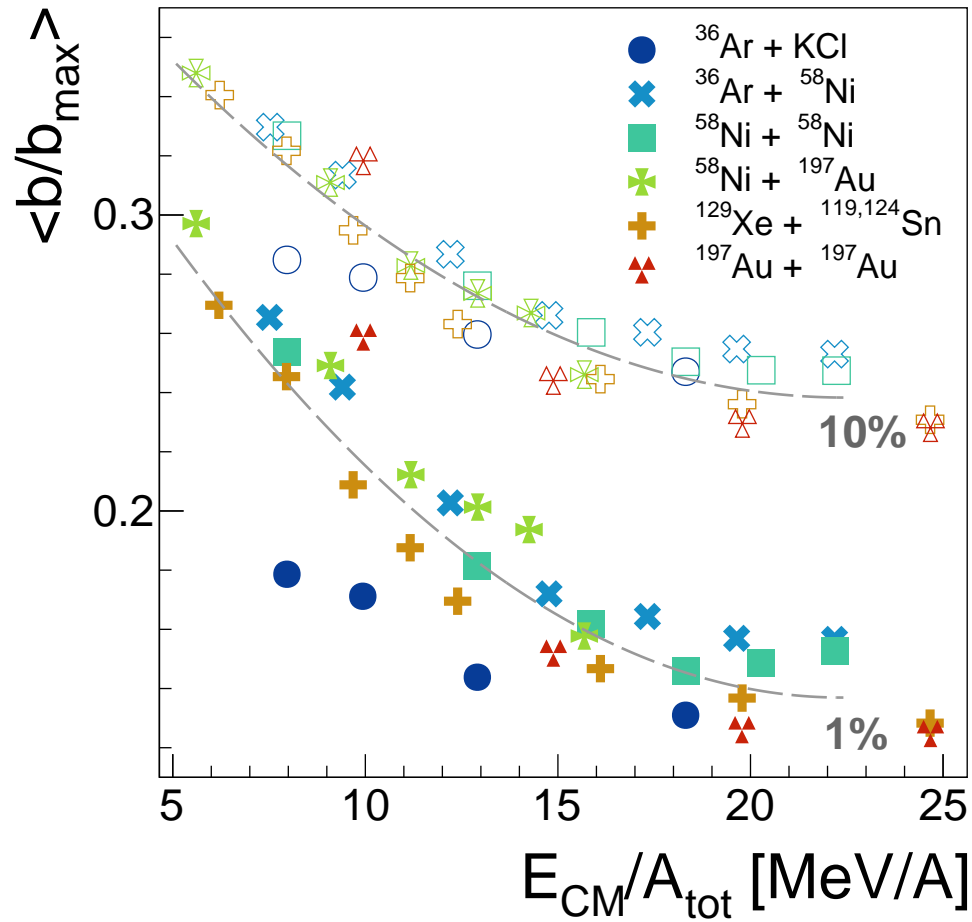


Figure 6.3.8 – Mean reduced impact parameter $\langle b/b_{\max} \rangle$ for central collisions selected with a 10% (open symbols) or 1% (full symbols) centrality cut using E_{t12} , as a function of available centre of mass energy per nucleon, $E_{\text{CM}}/A_{\text{tot}}$. Dashed curves are to guide the eye.

The effective centrality of the event samples increases (i.e. $\langle \hat{b} \rangle$ decreases) with increasing energy, as is to be expected from the overall evolution of the $k(c_b)$ relations (Figures 6.3.2 and 6.3.3) which become steeper at small b with increasing bombarding energy, while at the same time the maximum values reached in central collisions, $\overline{E_{t12}}(b=0)$, also increase with energy for each system (Figure 6.3.5b), decreasing the relative importance of fluctuations as shown in Figure 6.3.4: all these effects contribute to increase the selectivity of the observable for the most central collisions.

For the 1% centrality cut the effective $\langle \hat{b} \rangle$ decreases by a factor of 2 from ~ 0.3 at the lowest energies to ~ 0.14 at the minimum, which is a large effect. It is commonly assumed that centrality cuts like these select similar collision geometries for a wide range of colliding systems and energies, which is clearly shown to be false in Figure 6.3.8. In all future analyses it will be possible, even mandatory, to take this effect into account by providing a quantitative estimate of the effective impact parameter distribution for each data sample.

Now we come to a crucial question: just how central *are* the most central collisions? Or, to put it another way, is there a limit to the effective centrality ($\langle \hat{b} \rangle$) of events we can select with stricter and stricter centrality cuts?

Clearly we can see in Figure 6.3.8 that reducing the cut from 10% to 1% reduces $\langle \hat{b} \rangle$ for all systems and energies: to have a quantitative idea of the improvement, the “minima” observed for the highest energies is $\langle \hat{b} \rangle = 0.24$ for the 10% centrality cut while for the 1% cut it is $\langle \hat{b} \rangle = 0.14$. How low can we go? For a cut $c_{E_{t12}} \leq 10^{-3}$ there is a further reduction to $\langle \hat{b} \rangle = 0.1$, but stricter cuts of 10^{-4} or 10^{-5} lead to negligibly smaller values of $\langle \hat{b} \rangle = 0.09$ and $\langle \hat{b} \rangle = 0.08$, respectively (it should be remembered that the widths of these distributions are of the same order of magnitude as the mean value, see Figure 6.3.6).

What increasingly restrictive centrality cuts *are* very efficient at, of course, is diminishing the statistics of the selected event sample. For most of the data studied, a few million events were recorded for each system and bombarding energy (see Table 6.1), therefore a $c_{E_{t12}} \leq 10^{-3}$ cut is probably the absolute lower limit in order to retain a statistically significant number of events, while a 1% cut retains a comfortable statistics with a $\langle \hat{b} \rangle$ which is sufficiently small to be considered “central”.

6.4 Summary

Ever since the Cavata prescription [74] was proposed it has been known that it probably underestimates the true centrality of collisions selected with cuts defined using the experimental centrality calculated for observables assumed to be strongly correlated with the impact parameter. Even for less central collisions, where the deduced mean centrality has been shown to be generally well estimated by this method, the approach of [74] can tell us nothing about the impact parameter distributions retained by selections.

The new approach proposed in [146, 147] and adapted here to Fermi energy heavy-ion collisions greatly improves the previous situation by allowing for the first time to reconstruct in a model-independent way the impact parameter distributions for any selection of experimental data. This has allowed to confirm and quantify the suspicions concerning the true centrality of the “most central collisions”, which should be taken into account for example when comparing

experimental data with theoretical calculations. More generally, given the current uncertainties in the codes implementing various different transport model approaches [159, 160], it is more important than ever to be able to provide, in a quantitative way, experimental data as a function of impact parameter in order to further constrain the modelisation of heavy-ion collisions in this energy range.

Chapter 7

How isotropic are the most isotropic events in Fermi energy heavy-ion collisions ?

7.1 Introduction

As collisions become more and more central in the Fermi energy regime and above, where the dynamics are governed both by the nuclear mean field and the residual interaction in the form of elastic nucleon-nucleon collisions, one expects the momentum distributions of the outgoing nucleons and any clusters they may form to become more and more isotropic. Whether or not isotropy is achieved in the most central collisions of a given system at a given energy, even for the theoretical $b = 0$ case, will of course depend on such things as the nuclear incompressibility, momentum dependence of the mean field, in-medium nucleon-nucleon collision cross-sections, *etc.*, therefore it is very interesting to track the evolution of the maximum isotropy achieved as a function of collision system mass, asymmetry and bombarding energy.

A study was performed for INDRA data in [106] which related the apparently decreasing isotropy observed in central collisions to the weakening of the in-medium NN cross-section [107]. The event samples used for this study were selected using a multiplicity cut defined so that the mean isotropy ratio (see 7.1.1 below) becomes approximately constant above the cut. Therefore, strictly speaking, they were not selected because they are “the most isotropic events”. From the previous Chapter 6 we now know that such events, selected with a high-multiplicity cut, do not correspond to “the most central collisions” either: rather they are a subset of central collisions covering a wide range of impact parameters. Therefore now I would like to try to directly answer the question: how isotropic are the most isotropic events in Fermi energy heavy-ion collisions?

The first obstacle to this endeavour is of course the finite-number effects on event shape determination caused by the low multiplicities ($N_C \ll 100$) encountered in reactions at these energies. Figure 7.1.1 shows two examples for simulated isotropic events with a total number of charged reaction products $N_C = 50$ or $N_C = 5$. Of course, when we say isotropic, what we mean is that the momentum of each reaction product was drawn at random according to an isotropic distribution. The resulting events do not look particularly isotropic, especially for the

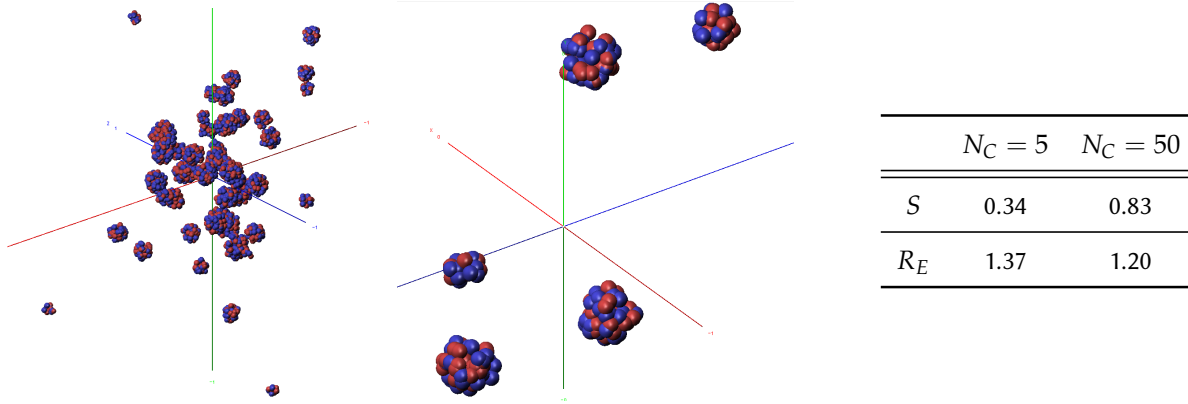


Figure 7.1.1 – Simulated isotropic events in velocity space with $N_C = 50$ (left) or $N_C = 5$ (right) reaction products. The values of the isotropy variables sphericity, S , and energy-based isotropy ratio, R_E , for each event are given in the table.

case $N_C = 5$; but, even with 50 nuclei, determining the degree of isotropy by eye (not to mention comparing one event with another) is no mean feat¹. Luckily we dispose of several global variables with which we can quantify the apparent isotropy of events.

7.1.1 Global shape variables

The simplest way to gauge the isotropy of product momentum distributions is through the ratio of some global kinetic property perpendicular and parallel to a given fixed axis. For example, using the total kinetic energy in the centre of mass frame perpendicular and parallel to the beam axis, we can define an **isotropy ratio**,

$$R_E = \frac{\sum_i E_{i,\perp}}{2 \sum_i E_{i,\parallel}} = \frac{\sum_i E_i \sin^2 \theta_i}{2 \sum_i E_i \cos^2 \theta_i} \quad (7.1.1)$$

where E_i, θ_i are the centre of mass kinetic energy and polar angle (w.r.t. the beam axis) of the i^{th} product. Within a factor of 2, this is the same as the “stopping variable” E_{rat} used by the FOPI collaboration [91] which was calculated using only products emitted in the forward hemisphere of the centre of mass frame: a variant of R_E , which we will call R_E^{fw} , using only forward-emitted c.m. products was in fact the isotropy ratio used in Lehaut *et al.* [106]. The characteristic asymptotic values of R_E are 0 for “rod-shaped” events and 1 for a spherical distribution. Note however that there is no upper bound to the value of R_E as both shape and orientation of the event determine its value: a rod-shaped event orientated perpendicular to the beam axis will have $R_E \rightarrow \infty$.

A more sophisticated tool is the flow tensor of Gyulassy *et al.* [38]

$$T_{\alpha\beta} = \sum_{i=1} \omega_i p_\alpha(i) p_\beta(i) \quad (7.1.2)$$

¹And yet that is exactly what was done in early works on multifragmentation using (nuclear) photographic emulsions: for example Barz *et al.* [89] even managed to deduce and measure a radial flow of the fragments in this way!

which was already presented in equation (2.2.1) (section 2.2.1, Chapter 2), built from the Cartesian components ($\alpha, \beta = x, y, z$) of particle momenta in the centre of mass frame. For nuclear collisions where composite particles may be produced, the weight factor ω_i must take into account differences in particle masses: with $\omega_i = (m_i(\gamma_i + 1))^{-1}$, Equation (7.1.2) becomes the (relativistic) kinetic energy flow tensor. Diagonalization of $T_{\alpha\beta}$ allows to characterize the momentum distributions in terms of an ellipsoid in momentum space. The ellipsoid has a shape (described by the 3 eigenvalues $\lambda_1 \geq \lambda_2 \geq \lambda_3$)² and a direction (described by 3 eigenvectors). Several different combinations of the eigenvalues can be used to simplify the shape description; among these, the **sphericity**,

$$S = \frac{3}{2}(1 - \lambda'_1) \quad (7.1.3)$$

defined using the normalised eigenvalue $\lambda'_1 = \lambda_1 / \sum_{\alpha} \lambda_{\alpha}$, which takes values from $S = 0$ (limit of extremely prolate event shapes) to $S = 1$ (a perfect sphere). It should be noted that the sphericity is independent of the event orientation relative to any fixed set of axes (which, relative to the beam axis, is given by the flow angle θ_f).

To overcome the inherent ambiguity of the isotropy ratio, R_E , we can calculate it with respect to the major axis of the kinetic energy flow tensor of Equation (7.1.2). After diagonalization of the latter, its only non-zero components in the basis described by its eigenvectors are

$$T_{\alpha\alpha} = \sum_i \omega_i p_{\alpha}^2(i) = \lambda_{\alpha}$$

so that the total kinetic energy parallel to the major axis is given by λ_1 while the sum of kinetic energies in the two perpendicular directions is given by $\lambda_2 + \lambda_3$. We then find for the isotropy ratio calculated in the ellipsoid frame

$$R_E^{ell} = \frac{\lambda_2 + \lambda_3}{2\lambda_1} = \frac{S}{(3 - 2S)} \quad (7.1.4)$$

This will be used in Section §7.3.

7.1.1.1 Response for isotropic events

Figure 7.1.1 gives the values of the sphericity and isotropy ratio for the two finite-multiplicity events shown. For the $N_C = 50$ case the values of all 3 variables are quite close to their asymptotic values: this multiplicity is typical of central collisions at bombarding energies $\sim 50A$ MeV when all charged reaction products are included. On the other hand, we may try to determine the isotropy of the source of the fragments (*e.g.* $Z \geq 5$), and only consider the latter. Then a typical multiplicity corresponds more to the $N_C = 5$ event in the figure, for which the shape variables have very unrepresentative values.

Figure 7.1.2 shows how each variable responds to simulated isotropic events³ over a wide range of multiplicities, from $N_C = 3$ to $N_C = 50$. For each value of N_C 10^3 events were generated

²Strictly speaking, with the given weight ω_i the flow tensor is characterized by an ellipsoid in kinetic energy flow space; the shape of the event in momentum space is represented by the square roots of the eigenvalues, $\sqrt{\lambda_1} \geq \sqrt{\lambda_2} \geq \sqrt{\lambda_3}$.

³See Appendix C for details of the simulation method.

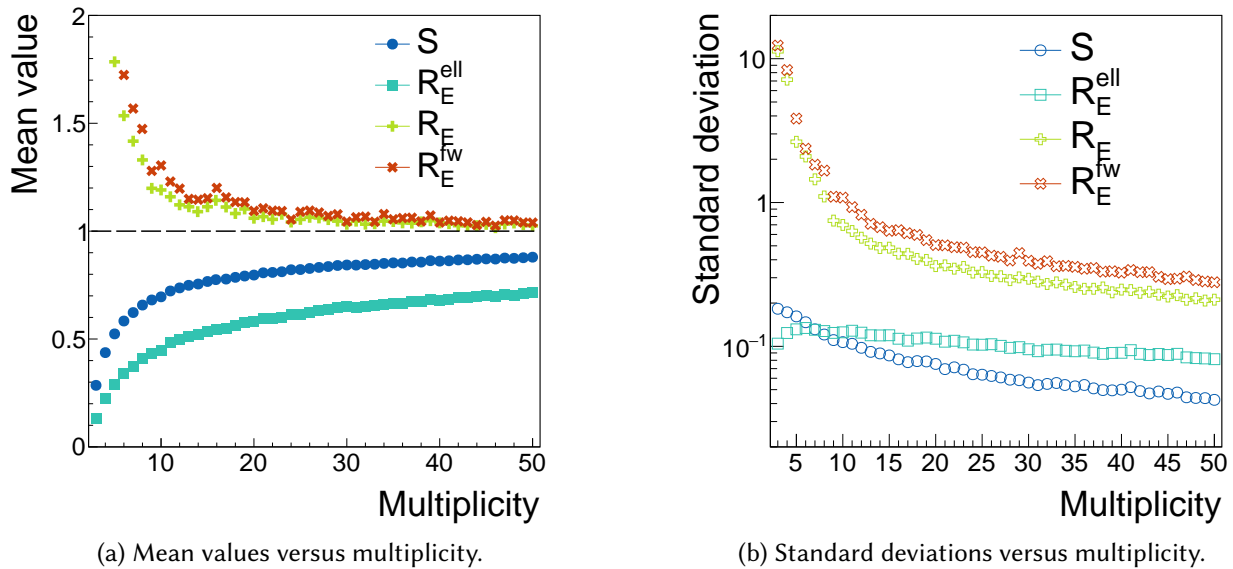
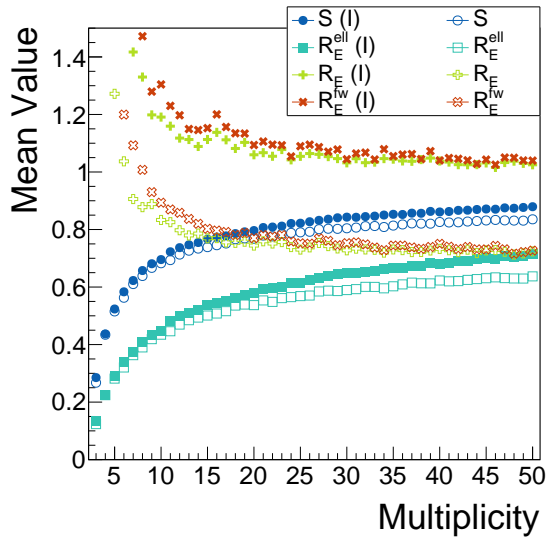


Figure 7.1.2 – Multiplicity-dependent response of shape variables defined in the text to simulated isotropic emission events. Note that for R_E^{fw} the actual number of nuclei used to calculate the values is on average one half of the multiplicity reported on the axis.

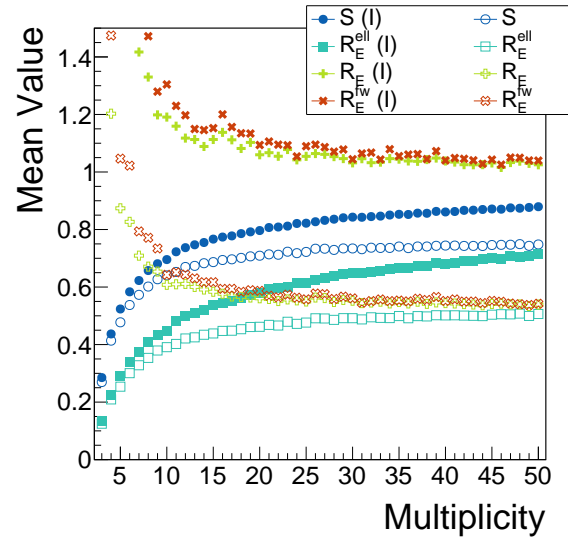
in order to have a statistically significant measure of both the mean value and the standard deviation of the distribution for each variable. It should be noted that although here a random partition was generated for each multiplicity, the same evolution is found if partitions of identical nuclei are used (*i.e.* N_C protons or N_C ^{12}C nuclei): the result is independent of the partition.

Figure 7.1.2a shows the multiplicity-dependence of the mean apparent isotropy deduced for each variable, and some comparisons can be made. Both isotropy ratios perform equally well and are close to their asymptotic value for multiplicities greater than 20. It should be noted however that they approach the asymptote from the “wrong” side: instead of mimicking less isotropic events with $R_E < 1$, for all finite multiplicities the ratios are > 1 if the distribution is truly isotropic. The two variables derived from the flow tensor approach their asymptotic value much more slowly, on the other hand, with the isotropy ratio R_E^{ell} being worst affected. For multiplicities $N_C < 10$ the multiplicity dependence of all 4 variables is very strong.

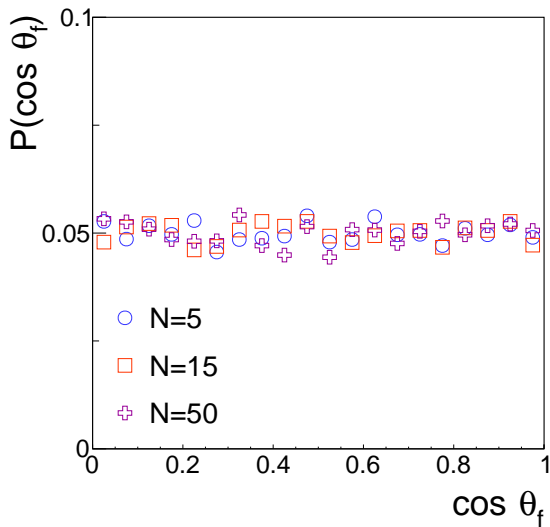
Fluctuations of the variables are of course very important, as shown in Figure 7.1.2b: for low multiplicities the widths of distributions are so large that separating events with different degrees of isotropy using the value of one or other of these variables is hopeless. Although fluctuations of all variables decrease with increasing multiplicity, it can be noted that fluctuations of S are an order of magnitude smaller than for the isotropy ratios, of which R_E^{fw} has a slightly worse performance than R_E as on average only 50% of the nuclei in each event contribute to its calculation.



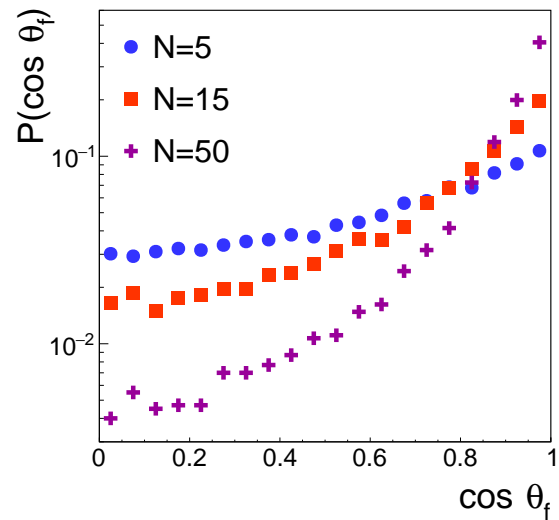
(a) Elongation 1.2:1.



(b) Elongation 1.4:1.



(c) $\cos \theta_f$ distributions for isotropic events with different multiplicities.



(d) $\cos \theta_f$ distributions for anisotropic events with elongation 1.2:1.

Figure 7.1.3 – (top row) Tests of power of shape variables to discriminate between isotropic and anisotropic simulated events corresponding to an ellipsoidal momentum distribution with the indicated ratio between major and minor axes (see Appendix C). Variables calculated for isotropic events are labelled (I). (bottom row) $\cos \theta_f$ distributions for isotropic and anisotropic events for different multiplicities.

7.1.1.2 Discrimination of less isotropic events.

Having examined the ability of the shape variables to recognize isotropic events of different multiplicities, let us now examine their power to discriminate between such events and non-isotropic events. To do so, we generate random events with an ellipsoidal momentum distribution whose elongation is characterised by the ratio between its major and minor axes (see [Appendix C](#)). The resulting events are anisotropic with a favoured emission along the beam direction.

The resulting mean values of the different shape variables are shown in [Figures 7.1.3a](#) and [7.1.3b](#) for momentum distributions with elongation ratios 1.2:1 and 1.4:1, respectively, as a function of the multiplicity. The tensor-based variables S and R_E^{ell} decrease steadily with increasing elongation of the momentum distributions, while the isotropy ratios decrease much more rapidly, especially when going from isotropic to slightly elongated events. Note however that for the smallest multiplicities values $\langle R_E \rangle > 1$ can still be observed. For the larger elongation, the multiplicity dependence of all variables becomes weaker for multiplicities $N > 15$: the mean values are almost constant. For $N < 10$ however the multiplicity dependence is always as strong.

Finally, the multiplicity dependence of flow angle θ_f distributions is shown in [Figures 7.1.3c](#) and [7.1.3d](#). For this variable there are two regimes: for an isotropic emission the distribution of θ_f is isotropic for any multiplicity ([Figures 7.1.3c](#)). For anisotropic events on the other hand $P(\cos \theta_f)$ becomes peaked at forward angles, and this peaking increases with the multiplicity: in the limit of an infinite multiplicity it would be a delta function at the “true” flow angle (*i.e.* in this case 0°).

7.2 New method for extracting the most isotropic events

One way to overcome the finite multiplicity distortions of estimated isotropy is to take a homogeneous sample of events and extend the sum of [Equation \(7.1.2\)](#) to run over all particles of interest in all events, giving an effective tensor

$$\mathcal{S}_{\alpha\beta} = \sum_{e=1}^{\mathcal{E}} \sum_{i=1}^{N_e} \omega_i p_\alpha(i) p_\beta(i) = \sum_{e=1}^{\mathcal{E}} T_{\alpha\beta}^e \quad (7.2.1)$$

with an effective multiplicity $N^* = \sum_{e=1}^{\mathcal{E}} N_e$ where \mathcal{E} is the total number of events in the sample and N_e is the multiplicity of event e . Clearly in this case N^* can be made very large even if the mean multiplicity $\langle N \rangle$ is small as long as the event sample size \mathcal{E} is large enough, and the diagonalization of $\mathcal{S}_{\alpha\beta}$ will give an undistorted estimate of the isotropy of the events in the sample, *for an homogeneous sample*. The problem is to build the homogeneous sample, and that is what we will now try to do.

The new method which we present here is vaguely inspired by the Metropolis algorithm for sampling multivariate probability distributions (it is not really a Metropolis algorithm⁴). The aim of the algorithm is best described by the following problem:

⁴In a true Metropolis algorithm, a part of the trial exchanges leading to a smaller sphericity $S' < S$ would also be accepted, for example with a probability $P(S', S) = S'/S$. Tests using this method have shown that it does not converge to the maximum sphericity of the sample, and therefore we only accept trial exchanges of events if $S' > S$. There is no contradiction however: in a true Metropolis algorithm, where the values of S and S' would correspond to statistical weights for different equilibrium states, such ‘bad’ trials must be accepted in order to ensure detailed

Problem. Beginning from a dataset \mathbb{D} , find the event sample \mathbb{S} containing a fixed number \mathcal{E} of events which maximizes the effective isotropy given by Equation (7.2.1).

We propose the following algorithm in order to solve this problem. Each event e in \mathbb{D} can be characterised by the six values of $T_{\alpha\beta}^e$ which correspond to its contribution to the tensor of Equation (7.2.1). Beginning from a sample \mathbb{S} , we can attempt to maximise the isotropy of this sample by picking a random event e from \mathbb{D} and a random event e' from the sample and calculating the trial tensor

$$\mathcal{S}'_{\alpha\beta} = \mathcal{S}_{\alpha\beta} - T_{\alpha\beta}^{e'} + T_{\alpha\beta}^e \quad (7.2.2)$$

which corresponds to replacing event e' of the sample by event e of the dataset. If the sample sphericity \mathfrak{S}' obtained by diagonalization of Equation (7.2.2) is greater than the current sphericity of the sample, the two events are exchanged. This procedure can be iterated until the sample sphericity \mathfrak{S} converges to a constant value, when no further exchanges are accepted.

Note that in the wording of the problem (and the coding of the algorithm), it is stated that the isotropy is to be maximised for a sample of fixed size, *i.e.* with a fixed number \mathcal{E} of events. Ideally, we would like our algorithm to pick the events constituting the most isotropic sample \mathbb{S} possible from among all events of the dataset \mathbb{D} , without fixing *a priori* the size of the sample, \mathcal{E} . However, one can trivially increase the apparent isotropy of the sample just by increasing its effective multiplicity N^* , *i.e.* by increasing the number of events in the sample. We have also found that below a certain sample size the algorithm may seek to reduce the sample size in order to increase its sphericity. Therefore it seems that if \mathcal{E} is not fixed, the problem is not well defined.

In the following we will apply this algorithm to complete events ($Z_{tot} \geq 0.8(Z_P + Z_T)$) measured for $^{129}\text{Xe}+^{nat}\text{Sn}$ collisions. As we will calculate the tensor using fragment ($Z \geq 5$) momenta, requiring to have measured at least $\approx 80\%$ of the total charge of each event is a good way to be certain not to have missed too much information on the fragments' momentum distributions.

7.2.1 Maximizing the isotropy of a single event sample

As a first test, we apply the algorithm to the data for $^{129}\text{Xe}+^{nat}\text{Sn}$ collisions at 50A MeV. Beginning with a random sample of size $\mathcal{E} = 2000$ events and an initial sample sphericity $\mathfrak{S} = 0.392$, the algorithm tries to increase the overall sphericity of the sample by picking random events from the reservoir constituted by all events not in the sample \mathbb{S} . Figure 7.2.1 shows how the algorithm converges. In Figure 7.2.1(a) the sample sphericity increases steadily with the number of trial swaps from the initial value to its final value of $\mathfrak{S} = 0.999941$. At the same time, the rate of exchange of events with the reservoir decreases steadily until, after 37000 trials, no more exchanges are successful for 3000 attempts, which is our condition to stop the process (Figure 7.2.1(b)).

After isotropy maximization with our algorithm, the degree to which the sample corresponds to a set of isotropic events can be judged from Figure 7.2.1(c), where we compare the fragment flow angle θ_f distributions for all complete events and those which are in the maximized sample, calculated event by event. All $\cos \theta_f$ values for the sample are very nearly equiprobable and cover the full range of flow angles from 0° to 90° . This is a very isotropic sample of events indeed.

balance and hence the correct sampling. Here we are only concerned with maximizing (or minimizing) the sphericity of the sample \mathbb{S} .

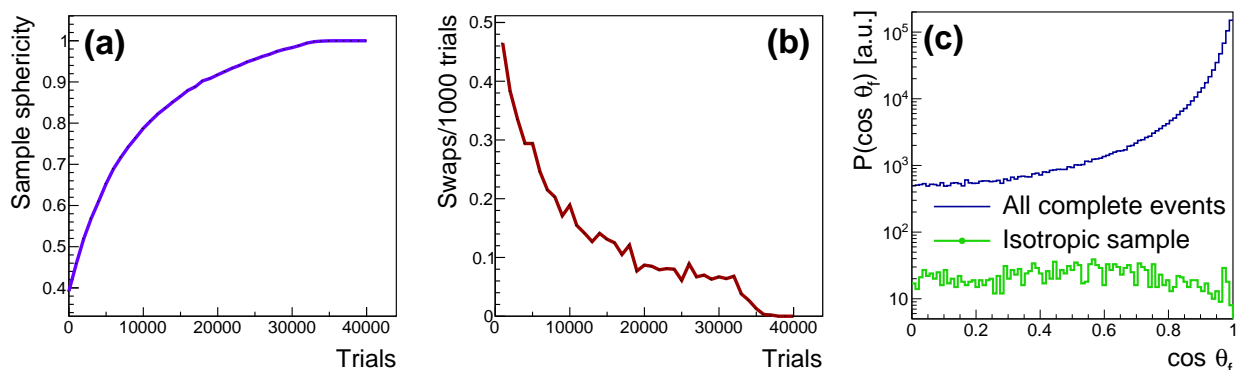


Figure 7.2.1 – Convergence of the isotropy maximization algorithm for a sample of $\mathcal{E} = 2000$ events of $^{129}\text{Xe} + ^{nat}\text{Sn}$ collisions at 50A MeV (complete events). (a) sample sphericity \mathfrak{S} calculated with the tensor of 7.2.1 as a function of the number of trials. (b) Number of swapped events per 1000 trials as a function of the number of trials. (c) Distribution of $\cos \theta_f$ for the sample after maximization compared to that of all complete events.

7.2.2 Minimizing the isotropy of an event sample?

Before going further in our quest to extract a homogeneous set of the most isotropic events from the data, and as further proof of the soundness of the method, let us demonstrate that the same method can also be used to find the *least* isotropic events in a given set, just by inverting the trial success criterion. However, it generally takes a lot more trials to converge, which may in itself be significant.

The results are shown in Figure 7.2.2. The correlations between atomic number Z and centre of mass longitudinal velocity V_{\parallel}^{cm} for fragments show a clear binary character, with sometimes quasi-projectile fragments with $Z \approx 54$ seen in the forward direction close to the projectile velocity (in the centre of mass frame) of $V_{\parallel}^{cm} = 4.7$ cm/ns, sometimes what appear to be fission fragments of more excited quasi-projectile nuclei, in coincidence with a fragment originating from the target, with $V_{\parallel}^{cm} < 0$. Figure 7.2.2(b) presents the distribution of the flow angle θ_f for these events. As expected, it is very narrow and limited to the most forward angles, with a mean value of $\theta_f \approx 5^\circ$, not far from the CM grazing angle of the reaction (5.5°).

7.2.3 Extracting all the most isotropic events

Of course there is no reason to think that the 2000-event sample \mathbb{S} extracted above corresponds to all of the most isotropic events in our dataset. The sample size of $\mathcal{E} = 2000$ events is completely arbitrary, as arbitrary as making a cut in the distribution of a shape variable for a set of finite-multiplicity events, or a cut in the flow angle distribution, $\theta_f > 60^\circ$. It is precisely this kind of arbitrariness that we want to remove from the event selection here.

The only way to know if our sample does indeed contain all of the most isotropic events is to take another sample from the reservoir and apply our algorithm to that one (which we will call \mathbb{S}_2 , the first sample becoming therefore \mathbb{S}_1), and so on and so on. If there exists within our dataset a homogeneous set of events whose degree of isotropy is superior to all others, we would

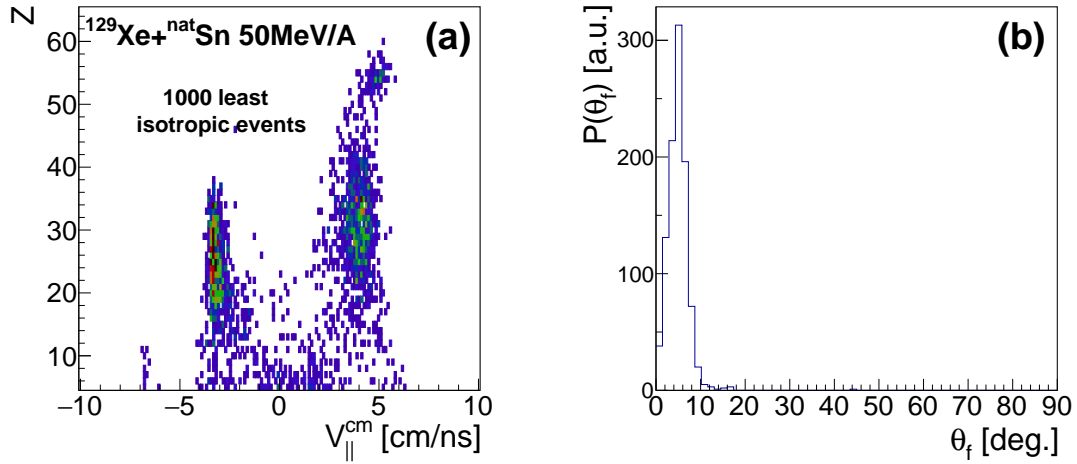


Figure 7.2.2 – Results of applying the algorithm in order to minimize the isotropy of a sample of 1000 events of $^{129}\text{Xe} + ^{\text{nat}}\text{Sn}$ collisions at 50 A MeV (complete events). (a) Correlation between atomic number Z and centre of mass longitudinal velocity $V_{\parallel}^{\text{cm}}$ for fragments ($Z \geq 5$). (b) Distribution of the flow angle θ_f for fragments.

expect to be able to extract N samples S_1, \dots, S_N with the same sample isotropy, while for all samples $S_{i>N}$ the sample isotropy will decrease with increasing sample number i .

In fact, this is exactly what happens. Figure 7.2.3(a) shows the sample sphericity \mathfrak{S} for each of 50 consecutive samples of $\mathcal{E} = 2000$ events whose isotropy was maximised using the algorithm and then removed from the dataset (and stored for safe keeping). \mathfrak{S} is approximately constant (and very nearly equal to 1) for the first 26 samples and then begins to rapidly decrease. To check if the isotropy calculated event-by-event for each event in the samples follows this trend, and to see if it concerns not only the fragments but all charged products, Figure 7.2.3(b) presents the mean isotropy ratio for forward-emitted $Z \geq 1$ products, R_E^{fw} , as a function of sample number. This shape variable, which is calculated completely independently from the sphericity used for the isotropy maximization algorithm (see 7.1.1), also displays the same characteristics: a constant mean value $\langle R_E^{fw} \rangle \approx 0.7$ for the first 26 samples, and then a trend of decreasing isotropy for the other samples. It can be noted also in this figure that the fluctuations (standard deviation) of R_E^{fw} are also constant for samples 1 to 26, which further confirms the impression that these samples constitute an homogeneous set of events.

Figures 7.2.3(c) and (d) compare the correlations between fragment atomic numbers and their longitudinal velocity in the centre of mass frame for the full set of complete events (c) and for the 26 most isotropic samples of events (d). The complete events show a clear forward-backward pattern in their correlations which is typical of binary dissipative collisions in this energy range (compare with Figure 7.2.2). For the most isotropic events on the other hand all such correlations between the fragments' velocities and Z are absent except for momentum conservation effects which mean that heavier fragments tend to have lower velocities (narrowing of the correlations with increasing Z). These events are therefore compact in velocity space and are compatible with the multifragment decay of a single heavy system which is on average at rest in the centre of

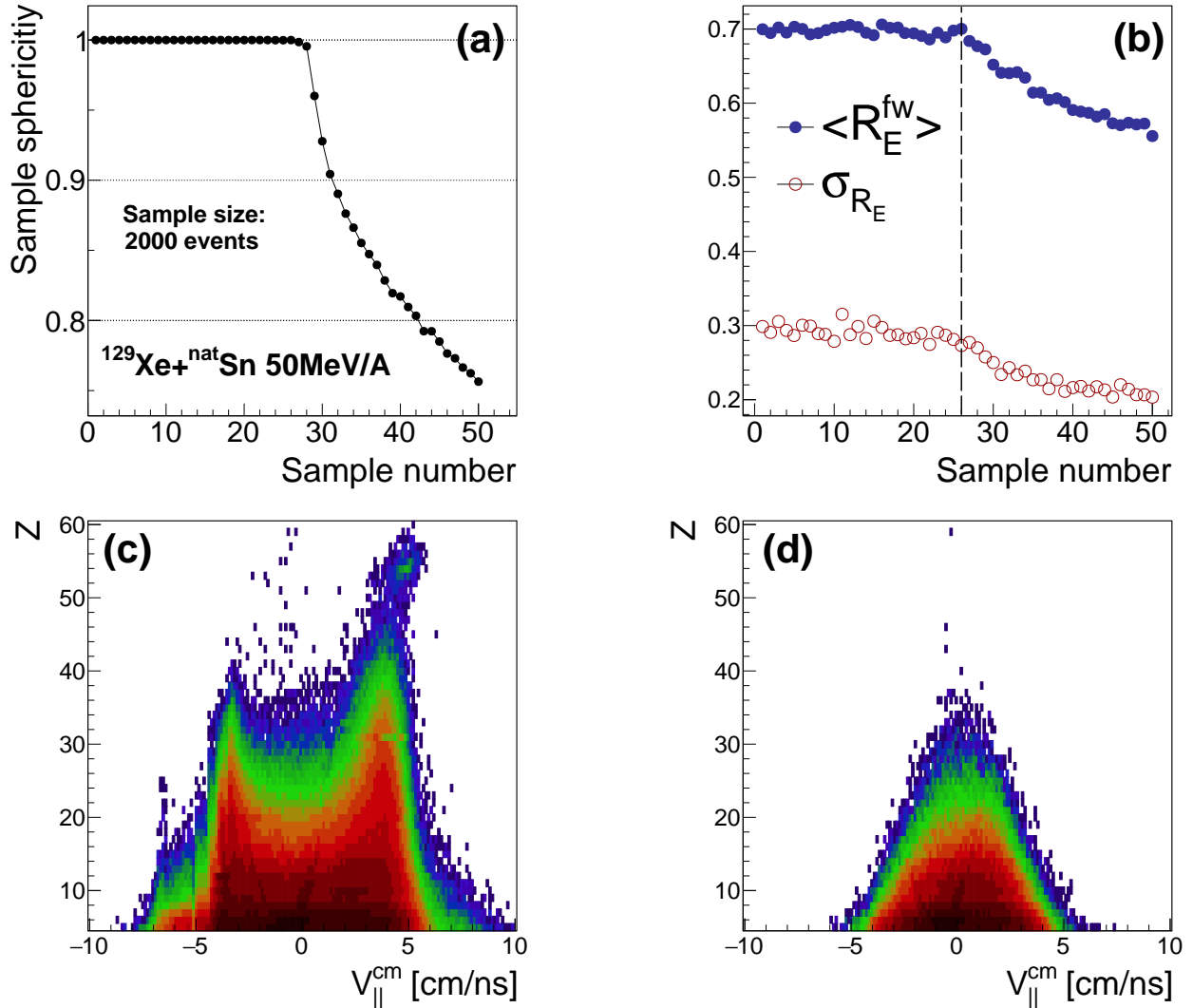


Figure 7.2.3 – (a) Sample sphericity \mathfrak{S} versus sample number for 50 samples of size $\mathcal{E} = 2000$ events extracted from complete events of $^{129}\text{Xe} + ^{\text{nat}}\text{Sn}$ collisions at 50 MeV/A. (b) Mean value $\langle R_E^{fw} \rangle$ and standard deviation σ_{R_E} of the isotropy ratio calculated in the forward CM hemisphere as function of sample number. The dashed line indicates the last sample with a constant sample sphericity \mathfrak{S} in (a). (c) Correlations between fragment Z and longitudinal c.m. velocity $V_{||}^{cm}$ for all complete events. Logarithmic colour contours represent measured double differential cross-sections. (d) As in (c), but for the 26 most isotropic samples.

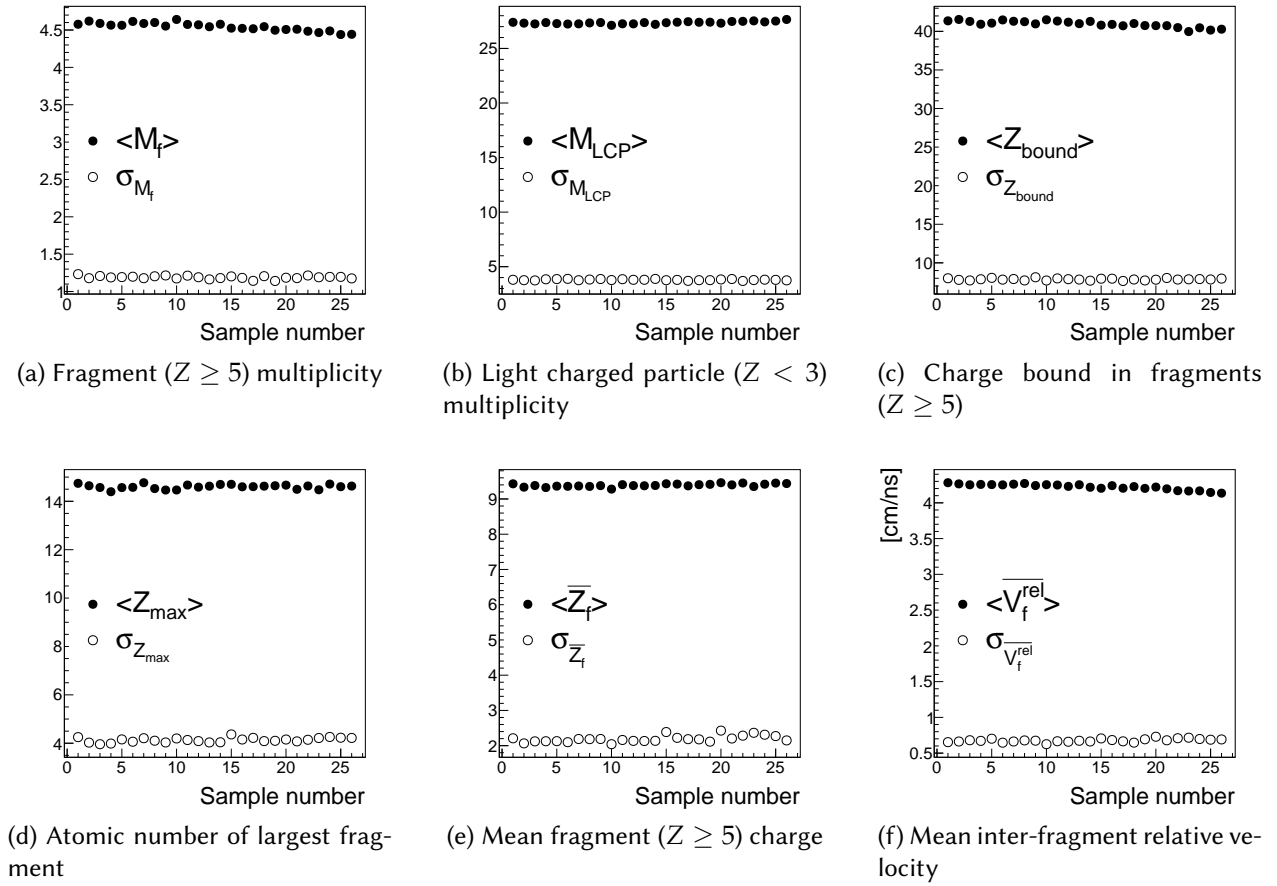


Figure 7.2.4 – Homogeneity of the 26 event samples corresponding to the most isotropic events of $^{129}\text{Xe} + ^{nat}\text{Sn}$ collisions at 50A MeV. Full symbols: mean values. Open symbols: standard deviations.

mass frame.

In order to converge for the 50 samples shown in Figure 7.2.3 (10^5 events), and for the other beam energies shown below, the sorting programme was run for 6 ~ 12 hours on a 20-core Dell workstation. All cores were utilised thanks to the implicit multi-threading capabilities of the latest versions of the ROOT software framework [13, 14]. The implementation of the algorithm was only possible thanks to the direct access to any event in a ROOT database file provided by the `TTree` storage class. Although it has taken 25 years for me to correctly answer the problem set for my Masters' internship, in my defence I would like to plead that it took most of those 25 years for the necessary computer hardware and software to become available.

Figure 7.2.4(a)-(f) gives a general survey of the homogeneity of the 26 samples corresponding to the most isotropic events. Both the mean value and standard deviation of each of the following quantities calculated event by event are presented as a function of sample number:

- the fragment ($Z \geq 5$) multiplicity, M_f ;
- the multiplicity of Light Charged Particles ($Z < 3$), M_{LCP} ;

Beam energy	25A MeV		32A MeV	39A MeV		45A MeV	50A MeV
Sample size \mathcal{E}	5000	2000	2000	2000	500	2000	2000
Number of samples	40	99	24	23	98	23	26
Cross-section [mb]	82.5	81.7	29.7	22.6	24.1	20.9	25.8
$2 \times [\theta_f > 60] \text{ [mb]}$	97.0		38.2	28.3		24.5	28.5

Table 7.1 – Most isotropic events for $^{129}\text{Xe}+^{nat}\text{Sn}$ collisions from 25 to 50A MeV. Sample size, number of samples in the set of most isotropic events, deduced cross-section. Last row is twice the cross-section for the $\theta_f > 60^\circ$ selection of [35].

- the total charge contained in the fragments, Z_{bound} ;
- atomic number of the largest fragment by charge, Z_{max} ;
- mean charge of the fragments, \overline{Z}_f ;
- and the mean relative velocity between each pair of fragments, \overline{V}_f^{rel} .

All of these observables have constant or approximately constant mean values for all 26 samples in the event set. Not only their mean values are constant, but also the fluctuations represented by the standard deviation for each variable's distribution (open symbols). The values are no longer constant for the samples after 26, as for the sample sphericity and forward isotropy ratio (Figure 7.2.3). We can therefore consider that these events constitute an homogeneous set corresponding to the most isotropic events produced by $^{129}\text{Xe}+^{nat}\text{Sn}$ collisions at 50A MeV.

7.2.4 Most isotropic events for $^{129}\text{Xe}+^{nat}\text{Sn}$ collisions from 25 to 50A MeV

The same method has been applied to complete events ($Z_{tot} \geq 80$) for $^{129}\text{Xe}+^{nat}\text{Sn}$ data from 25 to 50A MeV. Results for the different sets of most isotropic events are presented in Table 7.1. Note that the method was applied twice to the data at 25A MeV and 39A MeV with different sample sizes, \mathcal{E} . It can be seen that the results are hardly sensitive to this numerical parameter, which demonstrates the robustness of the method.

The cross-section corresponding to these most isotropic events for each energy has been calculated using measured cross-sections for all $M \geq 4$ trigger data in [75]. The cross-sections are unsurprisingly low, around 25 mb; nevertheless, this corresponds to $7 \sim 10\%$ of the cross-section for complete events. An exception is the 25A MeV data, for which the cross-section is $3 \sim 4$ times higher than for the other bombarding energies. This may of course be linked to the previously observed prevalence of fusion-like processes at this energy and below (see Part I, Chapter 3).

It is of course interesting to compare the cross-sections for the event sets we have isolated here with the cross-sections for data selected using the “old” single-source/QF selection, $\theta_f > 60^\circ$, of [35] and Part I, section 2.2.1. These are given in the last row of the table, doubled in order to estimate the total cross-section for all events assuming an isotropic θ_f distribution. It can be seen

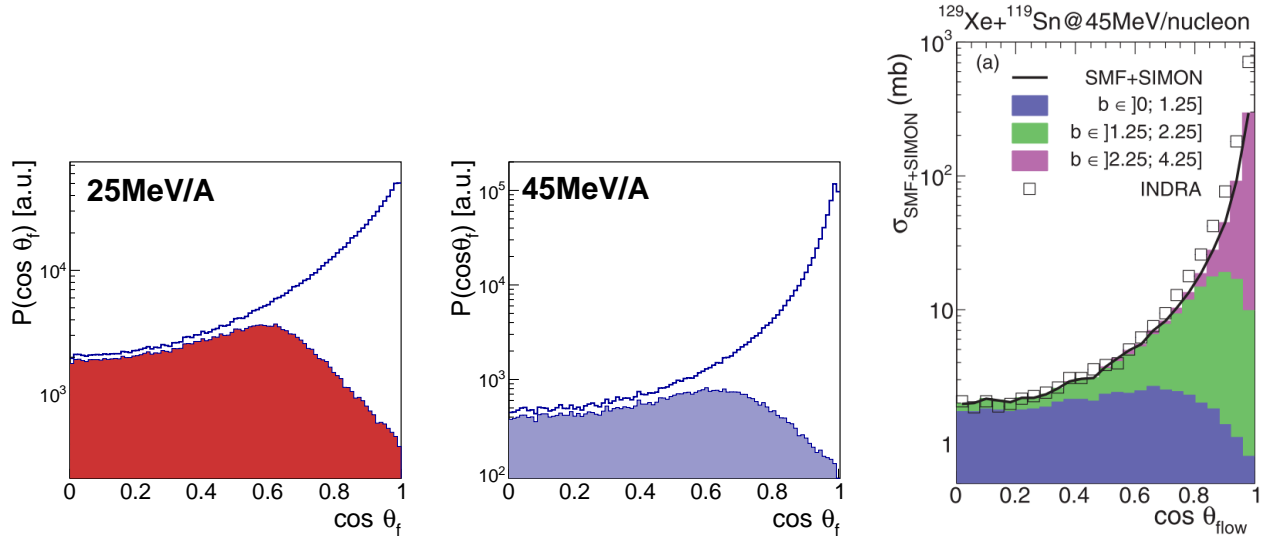


Figure 7.2.5 – (left, middle): Flow angle distributions for complete events (open histograms) and for the most isotropic events (shaded histogram) for two bombarding energies. (right) (shaded histograms) Flow angle distributions for multifragmentation events in different impact parameter ranges from SMF calculations.

that the new isotropic event sets follow the same evolution of cross-section as for QF events, but are always slightly lower in size.

The reason for this can be seen in Figure 7.2.5 which shows the distributions of $\cos \theta_f$ for all complete events and the most isotropic events, for 25A MeV and 45A MeV bombarding energies. The first thing to notice is that for $\theta_f > 60^\circ$ ($\cos \theta_f < 0.5$), the distributions for the most isotropic events follow almost identically the distributions for complete events, which in this range of θ_f correspond to the QF events selected with the flow angle selection. They are however slightly lower: therefore the most isotropic events we have isolated include nearly but not quite all of the previously-defined QF events.

On the other hand, the θ_f distributions for our selections are far from isotropic (non-equiprobable $\cos \theta_f$ distribution): at all bombarding energies they display a strong suppression of events with flow angles $\theta_f \lesssim 50^\circ$. This is not entirely unexpected, as we know that events with the most forward flow angles are dominated by reactions that are not fully relaxed in momentum space and which keep a strong memory both of the beam direction and the entrance channel nuclei. Nevertheless we might have expected the most isotropic events to have a perfectly isotropic θ_f distribution “underneath” the dominantly forward-peaked distribution for less isotropic events.

However, it is very instructive to compare these distributions with that shown in Figure 7.2.5-(right), which comes from our paper [52] investigating collective radial expansion and stopping in central heavy ion collisions around the Fermi energy. In this paper, the Stochastic Mean Field transport model (SMF, see Appendix A, section A.1.3.1) was used to simulate central $^{129}\text{Xe} + ^{nat}\text{Sn}$ collisions at impact parameters $b \leq 4$ fm. For bombarding energies 39A MeV and above, the most central collisions ($b \lesssim 1.5$ fm) lead to the formation of compact sources which undergo multifragmentation through spinodal decomposition. The θ_f distribution for these events is the blue shaded histogram in Figure 7.2.5(right). It is clear that the flow angle distributions for our

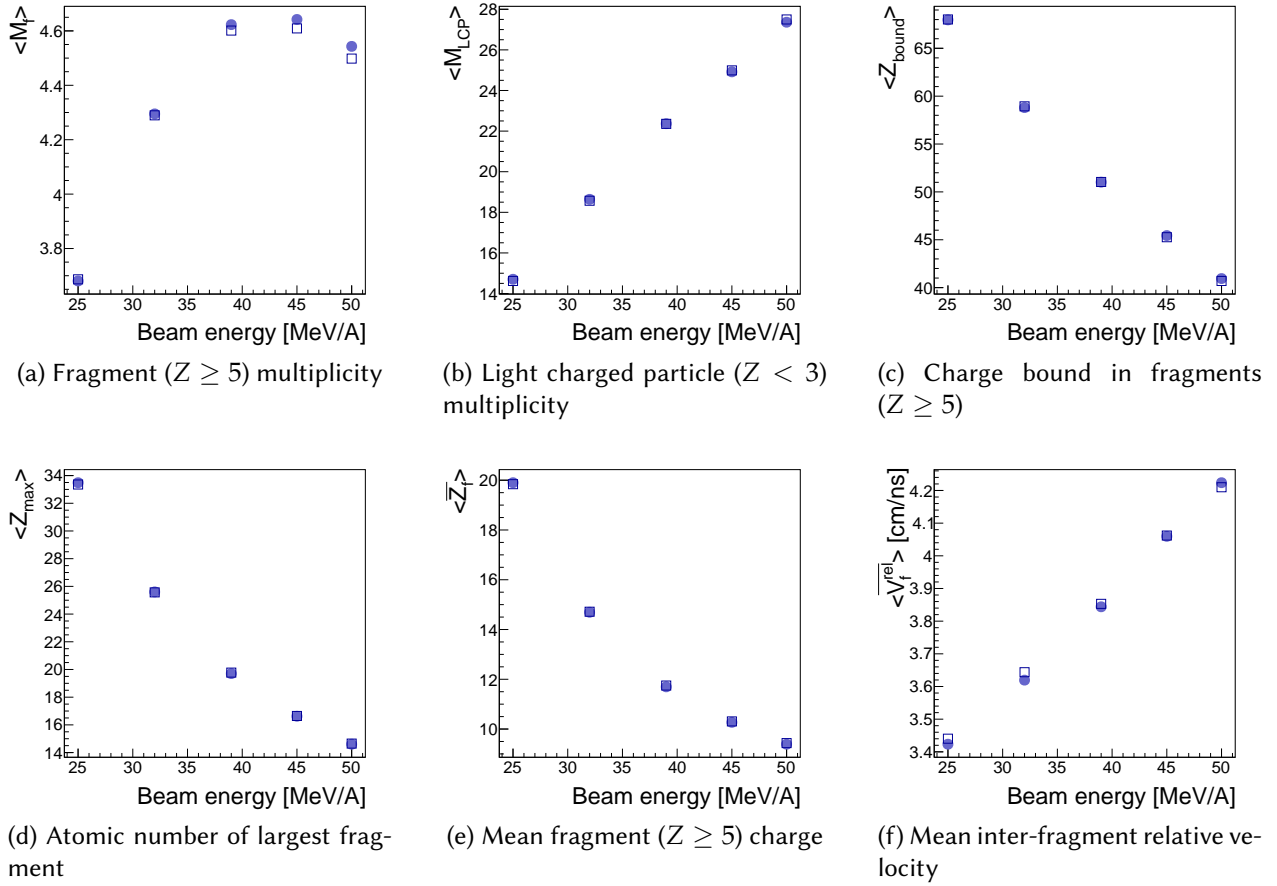
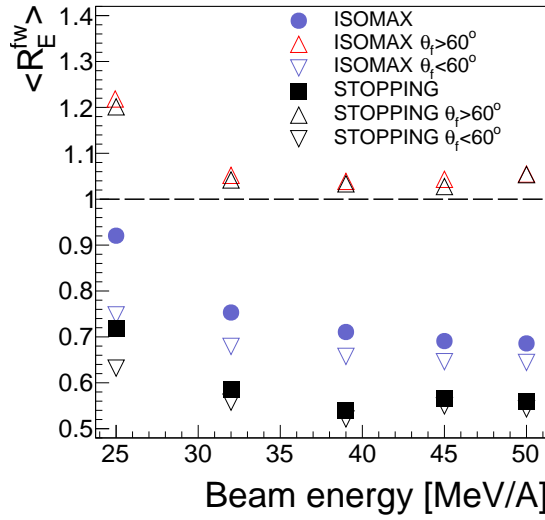


Figure 7.2.6 – (closed symbols) Fragment properties of the most isotropic events as a function of beam energy for $^{129}\text{Xe} + ^{nat}\text{Sn}$ collisions from 25 to 50 A MeV. (open squares) results for QF ($\theta_f > 60^\circ$) events.

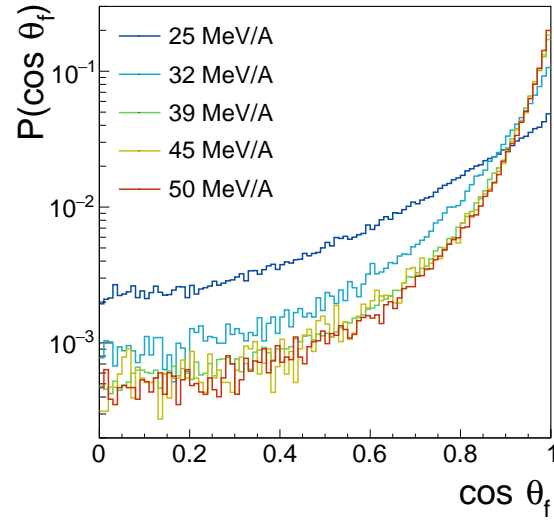
selection of the most isotropic events are entirely compatible with these calculations.

Figure 7.2.6 presents the same observables as in figure 7.2.4, but now with the mean value of each observable for the most isotropic dataset at each bombarding energy. The “rise and fall” of mean fragment multiplicity $\langle M_f \rangle$ with a maximum for $\approx 45A$ MeV, the near-linear increase of mean light charged particle multiplicities $\langle M_{LCP} \rangle$, the decrease of the mean charge bound in fragments $\langle Z_{bound} \rangle$, of the mean charge of the largest fragment $\langle Z_{max} \rangle$, of the mean fragment charge $\langle \overline{Z_f} \rangle$, and the increase of the mean inter-fragment relative velocity $\langle \overline{V_f^{rel}} \rangle$ are the same as for the QF events selected with the flow angle cut and studied in [46]: the only difference is that here they are presented simply as a function of the bombarding energy, whereas in [46] they were shown as a function of the reconstructed excitation energy per nucleon of the multifragmenting systems.

Therefore we can conclude that the previously-studied QF or “single-source” multifragmentation events are a (representative) subset of the most isotropic events at each bombarding energy, which validates *a posteriori* the θ_f -cut selection method. The main difference here is that events



(a) Comparison of mean isotropy ratios $\langle R_E^{fw} \rangle$ for all events (full symbols) and for different θ_f ranges (open symbols).



(b) Flow angle probability distributions for the STOPPING events.

Figure 7.3.1 – Comparison of the selected most isotropic events (ISOMAX) and the events used in the nuclear stopping analysis of Lehaut *et al.* [106] (STOPPING). Here flow angles θ_f are from the tensor Equation (7.1.2) calculated with all $Z \geq 1$.

are selected without using any arbitrary or *a priori* assumption.

7.3 So just how isotropic are the most isotropic events?

Let us begin by comparing the apparent isotropy of our “most isotropic events” (from now on referred to as ISOMAX events) with that of the events retained in [106] which were used to deduce the bombarding energy and system dependence of nuclear stopping. Let us first recall how the STOPPING events were selected: the isotropy ratio R_E^{fw} was calculated event by event using all charged products ($Z \geq 1$) in the forward centre-of-mass hemisphere (*i.e.* with centre-of-mass velocity $v_i^{cm} > 0$), for events satisfying a charge completeness criterion applied to these same products

$$Z_{tot}^{fw} = \sum_{v_i^{cm} > 0} Z_i > 0.8Z_p \quad (7.3.1)$$

with $Z_p = 54$ the atomic number of the projectile. STOPPING events were then selected with a total multiplicity cut N_C^{min} defined in such a way that for $N_C > N_C^{min}$ the value of $\langle R_E^{fw} \rangle$ becomes approximately constant as a function of N_C (in reality, above N_C^{min} the value of $\langle R_E^{fw} \rangle$ shows a small linear increase).

Let us compare the mean isotropy ratio $\langle R_E^{fw} \rangle$ for each bombarding energy of $^{129}\text{Xe} + ^{nat}\text{Sn}$ collisions. For the ISOMAX events the ratio is calculated exactly equivalently using all charged

products ($Z \geq 1$) in the forward centre-of-mass hemisphere, but without the Z_{tot}^{fw} completeness criterion (we recall that the completeness criterion for ISOMAX events is applied to the total charge of all products in the full velocity space).

At first glance, the mean apparent isotropy of the ISOMAX events is significantly higher for all bombarding energies, while the same trend of decreasing isotropy with increasing beam energy as for STOPPING events can be observed (full symbols in Figure 7.3.1a). However the isotropy ratio calculated with respect to the beam axis has an inherent ambiguity: any change in the “orientation” of non-isotropic events, *i.e.* the flow angle θ_f , will modify the value of R_E^{fw} so that it no longer measures just the apparent isotropy of the events but also their orientation. Therefore we cannot compare the apparent isotropy of two sets of events with different θ_f distributions using R_E^{fw} ⁵.

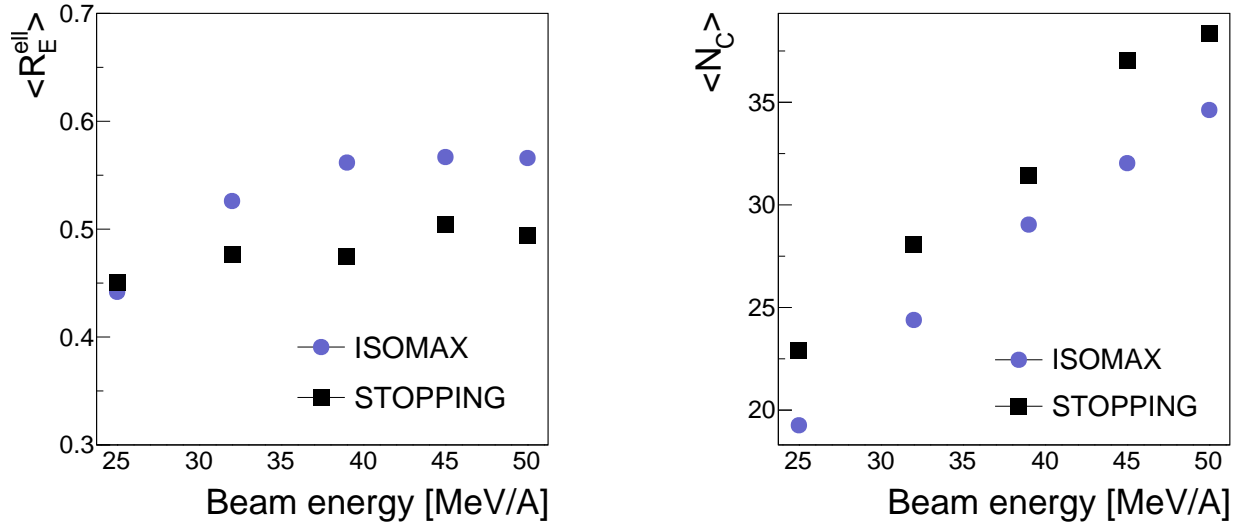
As Figure 7.3.1b shows, the flow angle distributions for the STOPPING events are strongly peaked at small θ_f , much more so than for ISOMAX events⁶ (see figure 7.2.5). The apparent increase of $\langle R_E^{fw} \rangle$ for each bombarding energy seen for ISOMAX events in Figure 7.3.1a is then simply due to the different weighting of the θ_f distributions in each case, as shown in the figure, where the mean values for each set of events have been calculated for small ($\theta_f < 60^\circ$) and large ($\theta_f > 60^\circ$) flow angles (open symbols). Very different apparent isotropies are found in each case, and it can be seen that for $\theta_f > 60^\circ$ almost identical $\langle R_E^{fw} \rangle > 1$ values are found (note the particularly high value for 25A MeV), but this is simply due to the auto-correlation between the two variables, not an indication of greater isotropy. It can be noted on the other hand that for “small” flow angles where auto-correlation is not so strong, the ISOMAX events still display a higher apparent isotropy than the STOPPING events.

To remove this ambiguity we will now consider the isotropy ratio calculated in the ellipsoid frame, R_E^{ell} , of Equation (7.1.4). As Figure 7.3.2a shows, the evolution of the apparent isotropy measured with this variable is very different to that seen in Figure 7.3.1a: for both STOPPING and ISOMAX events the apparent isotropy increases with incident energy, in the latter case reaching a plateau at around 39A MeV. Let us note also that the mean apparent isotropy for data at 25A MeV is very nearly the same for both data selections. There is however one more possible source of ambiguity which we have not dealt with and which affects all shape variables: the number of nuclei used in the calculation of R_E^{ell} in each case, which here is nothing but the total charged product multiplicity N_C . However, Figure 7.3.2b shows that at each bombarding energy $\langle N_C \rangle$ is in fact a few units larger for stopping events; as they were selected with a cut in the upper tail of the N_C distribution, this is not all that surprising. Whatever the reason, the increased apparent isotropy for stopping events in Figure 7.3.2a cannot be trivially explained by an increase in the mean multiplicity.

In order to compare the actual degree of anisotropy of the momentum distributions for ISOMAX

⁵This is of course equally true for R_E , the isotropy ratio using the full centre of mass velocity space. Almost identical results are obtained as in Figure 7.3.1 using R_E .

⁶As we are dealing with all $Z \geq 1$ products in the calculation of R_E^{fw} , the flow angles in Figure 7.3.1b are calculated for the tensor Equation (7.1.2) using all $Z \geq 1$, not just for fragments with $Z \geq 5$ as in Figure 7.2.5 and in the super-tensor of Equation (7.2.1), used to select the ISOMAX events. The $\cos \theta_f$ distributions for all $Z \geq 1$ products for ISOMAX events are also peaked at small angles (except for 25A MeV) but much less so than for stopping events: by a factor of ~ 2 for 50A MeV, ~ 3 for 32A MeV.



(a) Mean values of isotropy ratio calculated in the $Z \geq 1$ ellipsoid frame R_E^{ell} Equation (7.1.4).

(b) Mean total charged product ($Z \geq 1$) multiplicity.

Figure 7.3.2 – Comparison of the selected most isotropic events (ISOMAX) and the events used in the nuclear stopping analysis of Lehaut *et al.* [106] (STOPPING).

and STOPPING events, we present in Figure 7.3.3 the evolutions of the mean value $\langle R_E^{ell} \rangle$ with total multiplicity for each bombarding energy. Comparing mean isotropy ratios multiplicity by multiplicity is the only way to avoid any ambiguity due to differences in the distributions of N_C . As the STOPPING events were selected with a cut in multiplicity (clearly evident in these figures), they effectively have very different N_C distributions. What is also evident in these figures is that at all bombarding energies and for all multiplicities the STOPPING events have a lower apparent isotropy than the ISOMAX events (even at $25A$ MeV where the mean value for STOPPING events shown in Figure 7.3.2a is slightly higher; this is a clear demonstration of the danger of studying apparent isotropies without taking into account the underlying multiplicity distributions).

7.4 Energy dependence of nuclear transparency

Another difference in Figure 7.3.3 concerns the shape of the $\langle R_E^{ell} \rangle$ - N_C correlations which increase more steeply for STOPPING than for ISOMAX events (except at $25A$ MeV). Such correlations are of the same type as we saw in 7.1.1.2 when studying the multiplicity dependence of the different shape variables for momentum distributions with different degrees of anisotropy. In fact, for the ISOMAX events the correlations observed in Figure 7.3.3 can be exactly reproduced by simulations for a momentum distribution with a fixed elongation of $\approx 1.25 : 1$, for bombarding energies above the Fermi energy, $E_b \geq 39A$ MeV. At the two lower energies, the slopes of the correlations resemble more those of the stopping data, and cannot be reproduced by a fixed anisotropy. Without fully understanding the significance of this observation for the moment, we can at least estimate upper and lower limits for the degree of elongation of the momentum distributions in

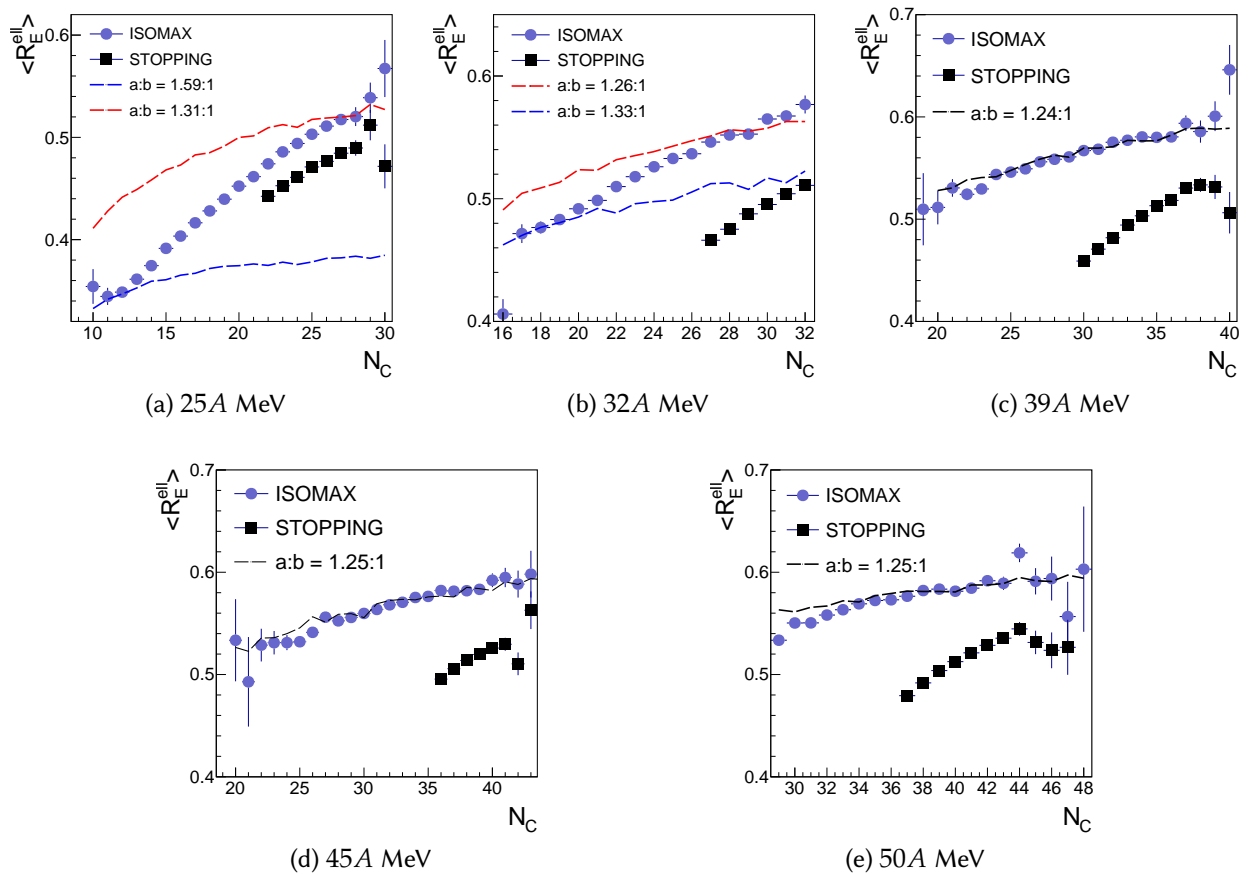
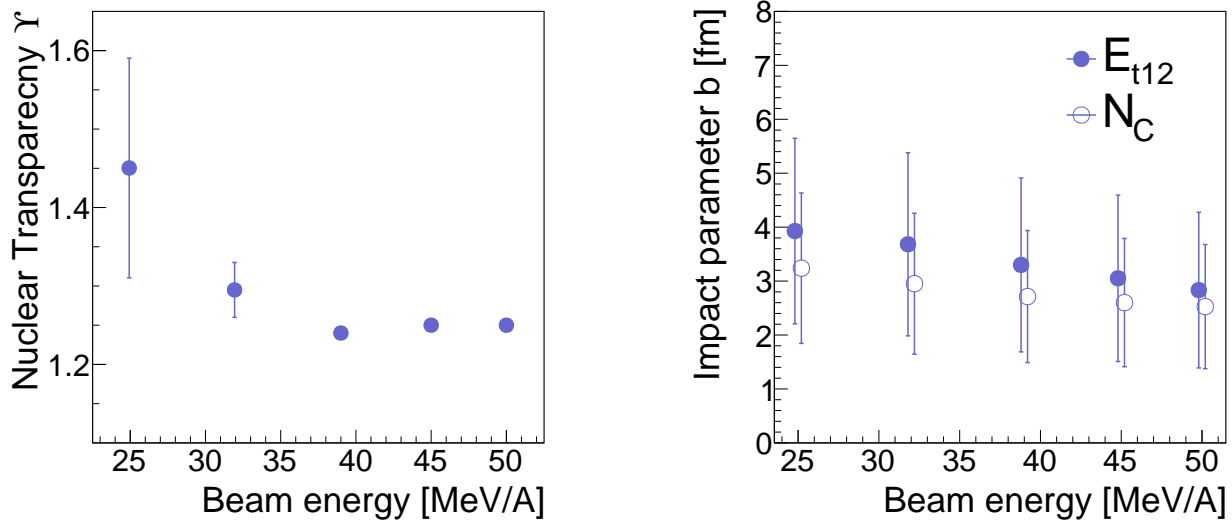


Figure 7.3.3 – Mean isotropy ratios calculated in the ellipsoid frame, $\langle R_E^{ell} \rangle$, as a function of total multiplicity N_C for ISOMAX and STOPPING events for each bombarding energy. Dashed lines are simulated results for momentum distributions with the elongations indicated in the legends.



(a) Apparent nuclear transparency Υ as a function of bombarding energy.

(b) Mean values and standard deviations (vertical bars) of impact parameter distributions.

Figure 7.4.1 – Apparent nuclear transparency and impact parameter distributions for the most isotropic events in $^{129}\text{Xe} + ^{\text{nat}}\text{Sn}$ collisions from 25 to 50 A MeV.

this case, which are shown by the red and blue curves in this case.

The values of the momentum distribution elongation parameter Υ deduced in this way for each bombarding energy are shown in Figure 7.4.1a. As in fact this parameter is representative of the amount of nuclear transparency in the collisions, we shall call it the nuclear transparency parameter. Obviously $\Upsilon = 1$ corresponds to a fully isotropic momentum distribution, while increasing values of the elongation correspond to increasing transparency. The nuclear transparency is seen to decrease with bombarding energies up to the Fermi energy, where it becomes approximately constant.

However this transparency parameter is only a measure of the *apparent* transparency of nuclear matter in these reactions: as we spent Chapter 6 demonstrating and quantifying, any sample of selected events corresponds to collisions with a distribution of different impact parameters. The observed transparency (or stopping) then depends on a convolution of nuclear matter properties and collision geometry. The only way to disentangle the two is by comparison with the results of microscopic transport model calculations, which must be performed in such a way that the impact parameter distributions used are representative of the experimental data.

Therefore the values of Υ given in Figure 7.4.1a are of little significance unless accompanied by the information given in Figure 7.4.1b, which concerns the estimated impact parameter distributions for the ISOMAX events. We present the distributions using both E_{t12} and N_C for this purpose, as they do not give exactly the same results. In both cases the full distributions for all energies are very wide, up to $7 \sim 8 \text{ fm}^7$: as can be seen in the figure where the standard deviations are represented by vertical bars, the distributions are slightly narrower when deduced from the total

⁷Let us note in passing that in [161] where the data of [106] was compared with IQMD, the calculated impact parameter distributions for events selected with an N_C cut also reach up to 8 fm (see Figure 2d of [161]).

multiplicity. The mean impact parameters decrease slightly with bombarding energy, from $3 \sim 4$ fm at $25A$ MeV to ≈ 2.5 fm at $50A$ MeV.

These data should now be used with transport model calculations in order to give a definitive answer to the question of the dependency of nuclear transparency on bombarding energy.

7.5 Summary

In this chapter it has been shown, for well-measured $^{129}\text{Xe}+^{nat}\text{Sn}$ collisions, that it is possible to extract from the data homogeneous event samples which correspond to the events with the highest degree of isotropy (or the most “compact” events) amongst all those measured. The novel selection method is performed in such a way that, unlike all previous approaches, it involves no arbitrary cuts or *a priori* definitions of how isotropic the most isotropic events should be. It is important to note that it is possible for this method to give the result that there are no “special” events, *i.e.* that starting from the first sample of arbitrary size \mathcal{E} events the sample isotropy decreases continuously. This was not observed for $^{129}\text{Xe}+^{nat}\text{Sn}$ data, but may be observed if the method is applied to other data.

The ISOMAX events were then compared with the single-source or quasi-fused (QF) source events selected with an arbitrary cut in the θ_f flow angle distribution, which have been studied many times over the years by the INDRA collaboration and are largely seen as a paradigm for multifragmentation in central collisions. It turns out that the QF events are in fact a representative subset of the ISOMAX sample, with near-identical fragment partition properties, and showing the same signs of collective radial expansion through their mean inter-fragment relative velocities. This is the strongest *a posteriori* experimental validation to date of the selection of compact multifragmenting sources using a θ_f cut.

The question of the actual degree of isotropy of these most isotropic samples was then carefully considered. At all bombarding energies considered here, the ISOMAX events present a finite anisotropy: “full stopping” is not achieved. However, perfect isotropy, like $b = 0$ collisions and thermodynamic equilibrium, is a theoretical idealization and not to be expected when dealing with real experimental data. Using the methods introduced in Chapter 6 we estimate that the ISOMAX events result from collisions with mean impact parameters in the range $\langle b \rangle \approx 2.5 - 4$ fm therefore a finite anisotropy is to be expected from the collision geometry. Comparing the multiplicity dependence of the measured apparent isotropy with simulated events having ellipsoidal momentum distributions, we have quantified the anisotropy for each bombarding energy, which, for $E_b \geq 39A$ MeV, corresponds to a ratio between the major and minor axes of the ellipsoid in momentum space of 1.25:1, which is a small deformation compared to spherical isotropy.

Taking this elongation ratio Y to be a measure of the apparent nuclear transparency, we find that when considering carefully-selected samples of the most isotropic events, the nuclear transparency decreases with bombarding energy and reaches a minimum at the Fermi energy. This is exactly what we expect to happen if, as the Fermi energy is approached, the phase space for elastic nucleon-nucleon collisions opens up, increasing the stopping power of nuclear matter beyond that of the weakening mean-field one-body dissipation.

Of course, this is the exact opposite of the conclusions of [106] where the nuclear *stopping*, supposed to be measured by $\langle R_E^{fw} \rangle$, was shown to decrease and reach a minimum at the Fermi

energy. As we have shown above, the interpretation of this variable in terms of anisotropy of event momentum distributions is far from direct, and requires to take into account the ambiguities introduced by differences in event orientation (θ_f distributions) and multiplicity distributions. When such effects *are* taken into account the nuclear stopping (isotropy ratio) calculated from the STOPPING data is in fact shown to be, at worst, constant, or at best, slightly increasing in this energy range (Figure 7.3.2a).

Part III

Appendixes

Appendix A

A not at all definitive guide to some oft-mentioned models

In order not to clutter the manuscript with expositions of the many and varied models used in this work, I have tried to collect them together here. As a result, the manuscript is now cluttered with references to this chapter. You just can't win.

A.1 Microscopic models of nuclear reactions

There are basically two families of transport approaches which are used in the study of heavy-ion collisions [159]. One is the Boltzmann-Vlasov type, which is formulated for the evolution of the one-body phase-space density under the influence of a mean field. The other is the molecular-dynamics type, which is formulated in terms of nucleon coordinates and momenta under the action of a many-body Hamiltonian. Both are supplemented with a two-body collision term. The following presentation concerns non-relativistic transport models for nuclear reactions and relies heavily on the following publications: [162, 163, 164, 65, 58, 20, 165, 166]. For relativistic nuclear transport models, see [167].

The evolution of an interacting N -particle system described by the wave function

$$|\Psi(\mathbf{r}_1, \dots, \mathbf{r}_N; t)\rangle$$

is given in the non-relativistic limit by the Schrödinger equation

$$\hat{H}|\Psi\rangle = i\hbar \frac{\partial |\Psi\rangle}{\partial t} \quad (\text{A.1.1})$$

where \hat{H} is the microscopic Hamiltonian of the system, or equivalently by the time variation of the N -particle density matrix in configuration space,

$$\Phi_N(\mathbf{r}_1, \dots, \mathbf{r}_N, \mathbf{r}'_1, \dots, \mathbf{r}'_N; t) = |\Psi\rangle\langle\Psi| \quad (\text{A.1.2})$$

which is given by the von Neumann equation

$$i\hbar \frac{\partial \Phi_N}{\partial t} = [\hat{H}, \Phi_N] \quad (\text{A.1.3})$$

The utility of such equations for describing nuclear reactions is rather limited, as, even assuming that we had a perfect knowledge of \hat{H} , this equation can be solved exactly for simple cases only. Generally, one has to rely on some approximations.

A.1.1 The time-dependent Hartree-Fock (TDHF) equation

To reduce the complexity of the N -body dynamics we can work at the level of the 1-body density operator

$$\hat{\rho} = N \text{Tr}_{2,3,\dots,N} \Phi_N \quad (\text{A.1.4})$$

Practically all transport models try to solve the time evolution of this operator (or its semi-classical Wigner transform - see Sec. A.1.2 below). This is sufficient for most cases, as knowing the 1-body density operator $\hat{\rho}(t)$ at a time t allows to calculate the expectation value of any 1-body observable $O = \sum_{i=1}^N o_i$, as $\langle \Psi(t) | O | \Psi(t) \rangle = \text{Tr}[o\hat{\rho}(t)]$, and most observables are 1-body in nature. However the equation for the time evolution of the 1-body density is still not necessarily tractable; for example, assuming only two-nucleon interactions $\sum_{i<j} v_{ij}$, this equation will depend on the 2-body density operator:

$$i\hbar \frac{d}{dt} \hat{\rho} = \left[\frac{-\hbar^2}{2m} \nabla^2, \hat{\rho} \right] + \text{Tr}_2 \left[v_{12}, \hat{\rho}^{(2)} \right] \quad (\text{A.1.5})$$

and the 2-body density operator $\hat{\rho}^{(2)} = N(N-1) \text{Tr}_{3,\dots,N} \Phi_N$ in turn depends on the 3-body density, and so on and so on: this is the quantum BBGKY¹ hierarchy, known as the Martin-Schwinger hierarchy (or BBGG according to Bonasera et al. [58], for Bogoliubov, Born, Green and Gurov).

The Hartree-Fock *ansatz* then allows to find a closed solution to Equation (A.1.5), by assuming that the N -fermion state $|\Psi\rangle$ is given by a Slater determinant of single particle wave functions, which is equivalent to assuming that the N fermions behave as independent particles moving in a mean field generated by averaging over their mutual interactions. In such a state, all the information is contained in the 1-body density matrix and the 2-body density operator becomes

$$\hat{\rho}_{12}^{(2)} = \hat{A}_{12} \hat{\rho}_1 \hat{\rho}_2 \quad (\text{A.1.6})$$

Then the Time Dependent Hartree-Fock (TDHF) equation for the evolution of the 1-body density operator is

$$i\hbar \frac{d}{dt} \hat{\rho} = \left[\frac{-\hbar^2}{2m} \nabla^2 + U_1[\hat{\rho}], \hat{\rho} \right] \quad (\text{A.1.7})$$

with the one-body mean-field potential which is defined depending on $\hat{\rho}$ as

$$U_1[\hat{\rho}] = \text{Tr}_2 \hat{A}_{12} v_{12} \hat{\rho}_2$$

¹for Bogoliubov, Born, Green, Kirkwood and Yvon - the BBGKY hierarchy relates each of the reduced density functions $\rho_s(r_1, \dots, r_s; p_1, \dots, p_s; t)$ in $6N$ -dimensional phase space to the next, ρ_{s+1} , in the classical description of the statistical physics of an N -particle system.

This equation provides a self-consistent mean-field evolution where the interaction between the particles is replaced by a 1-body mean-field potential generated by all the particles. It is, then, assumed that each particle evolves independently in this potential.

The TDHF approach provides an excellent treatment of one-body dissipation mechanisms which are crucial to properly describe low-energy (well below Fermi energy) heavy-ion collisions [165], in the presence of phenomena such as coupling of macroscopic collective motions with microscopic excitations (distortion of the single-particle wave functions by the collision partner of a heavy-ion collision, particularly when, in dissipative reactions — *i.e.* deep-inelastic collisions — nucleons are transferred from one partner to the other leading to transfer of the kinetic energy of the relative motion of the two nuclei into intrinsic excitations; or, in fusion reactions, multiple reflections of single-particle wave functions on the mean field “wall” which dissipate collective translational energy into particle excitations and collective vibrations of the compound system) and emission of nucleons into the continuum, which is a natural cooling mechanism of excited nuclei.

On the other hand, with bombarding energies increasing towards the Fermi energy and beyond, the inclusion of beyond-mean-field correlations, specifically in-medium two-body correlations *i.e.* nucleon-nucleon collisions, which are hindered or completely suppressed at lower energies by the Pauli principle, become increasingly important for the correct description of the dynamics. These could in principle be taken into account by going to the next order of the BBG hierarchy, *i.e.* using the equation for the time evolution of the 2-body density operator and neglecting 3-body correlations. However, such an approach demands far more computational effort than the standard TDHF approach, and even now only a few applications have been attempted (see [165] and references therein).

Historically, inclusion of residual interactions and other beyond-mean-field effects in transport models for nuclear reactions in the Fermi energy range has proceeded via the use of semi-classical approximations to the TDHF equation (but see also [168, 169]). Let us note in passing some very recent work by the Nantes group, who, after their earlier work on a quantal Boltzmann-like approach (DYWAN: Dynamical Wavelets in Nuclei [170]) are currently working to include fluctuations in an extended TDHF (ETDHF) approach [171].

A.1.2 Semi-classical approach: The nuclear Boltzmann equation

The N -particle Wigner function, $f_N(\mathbf{r}_1 \dots \mathbf{r}_N; \mathbf{p}_1 \dots \mathbf{p}_N; t)$, is an auxiliary function analogous to but distinct from the classical distribution function and quantum density matrix which may be defined as a Fourier transform of the N -particle density matrix [58],

$$f_N = \int d^3y_1 \dots d^3y_N \prod_{j=1}^N \exp\left(ip_j \cdot y_j / \hbar\right) \times \Phi_N(\mathbf{r}_1 + \mathbf{y}_1/2, \dots, \mathbf{r}_N + \mathbf{y}_N/2; \mathbf{r}_1 - \mathbf{y}_1/2, \dots, \mathbf{r}_N - \mathbf{y}_N/2; t) \quad (\text{A.1.8})$$

Applying this transform to the TDHF equation, Equation (A.1.7), and truncating the resulting expansion in terms of powers of \hbar , we recover the Vlasov equation [162]

$$\left[\frac{\partial}{\partial t} + \frac{\mathbf{p} \cdot \vec{\nabla}_r}{m} - U(\mathbf{r}) \overleftarrow{\nabla}_r \cdot \overrightarrow{\nabla}_p \right] f = \frac{\partial f}{\partial t} + \{f, H\} = 0 \quad (\text{A.1.9})$$

for the time evolution of a fluid of particles moving in a (momentum-independent) mean field potential $U(\mathbf{r})$ generated by their own mutual interactions, with the effective Hamiltonian here given by $H = \mathbf{p}^2/2m + U(\mathbf{r})^2$. Here $f = f(\mathbf{r}, \mathbf{p}; t)$ is the 1-body Wigner distribution, which is the closest analogue to classical phase-space density that can be obtained from quantum mechanical wave functions (however, in certain cases f can be negative, unlike the classical case) [163]. The Vlasov equation, Equation (A.1.9) is nothing but the Boltzmann equation minus the collision term on the right hand side:

$$\frac{\partial f}{\partial t} + \{f, H\} = \frac{\partial f}{\partial t} + [\nabla_p H \cdot \nabla_r - \nabla_r H \cdot \nabla_p] f = I[f] \quad (\text{A.1.10})$$

The collision term $I[f]$ can be related back to the “residual” interactions between nucleons, *i.e.* all the beyond-mean-field correlations beyond the truncation of the BBGKY hierarchy at the level of the 2-body Wigner densities, rather than at the 1-body level, as for TDHF (Equation (A.1.7)) or the semi-classical Vlasov equation, Equation (A.1.9). As such, note that $I[f]$ is not necessarily limited to 2-body collisions (see [58]).

However, rather than deriving $I[f]$ from the same interaction which gives the mean field part, usually the Uehling-Uhlenbeck modified version of the Boltzmann 2-body collision term is used [172]:

$$\begin{aligned} I[f] &= \frac{1}{2m} \iiint d\mathbf{p}_2 d\mathbf{p}_{1'} d\mathbf{p}_{2'} \delta^4(\mathbf{p}_1 + \mathbf{p}_2 - \mathbf{p}_{1'} - \mathbf{p}_{2'}) \\ &\quad \times w(\mathbf{p}_1, \mathbf{p}_2, \mathbf{p}_{1'}, \mathbf{p}_{2'}) [f_{1'} f_{2'} (1 - f_1)(1 - f_2) - f_1 f_2 (1 - f_{1'})(1 - f_{2'})] \\ &= \iint d\mathbf{p}_2 d\Omega |\mathbf{v}_2 - \mathbf{v}_1| \frac{d\sigma}{d\Omega} [f_{1'} f_{2'} (1 - f_1)(1 - f_2) - f_1 f_2 (1 - f_{1'})(1 - f_{2'})] \end{aligned} \quad (\text{A.1.11})$$

with w a suitable transition matrix for the scattering process $1 + 2 \rightarrow 1' + 2'$, which in the last line is given by the product of the relative velocity of the incoming pair and the (possibly energy-, angle-, isospin- and density-dependent) differential cross-section for elastic nucleon-nucleon collisions. The modification of $I[f]$ compared to classical Boltzmann takes account of the fermionic nature of nucleons via the inclusion of the Pauli blocking factors, $(1 - f)$, which suppress scattering to states which are already occupied.

The nuclear Boltzmann equation, Equation (A.1.10), along with the collision integral, Equation (A.1.11), is the basis for the semi-classical transport models Landau-Vlasov [162], BUU [163] and BNV [58], among others (see [159] for a full and recent list of transport codes, plus comparisons of their performance *i.e.* how well they actually simulate the equations given above). Such models provide quantitative simulations of heavy-ion collisions in the Fermi energy regime where both the nuclear mean field (calculated by an appropriate effective force: see A.1.4 below) and Pauli-blocked nucleon-nucleon collisions play an important role.

²The second form of the equation using the $\{\cdot, H\}$ Poisson brackets is more general, and is valid also for the case where H contains a momentum-dependent potential.

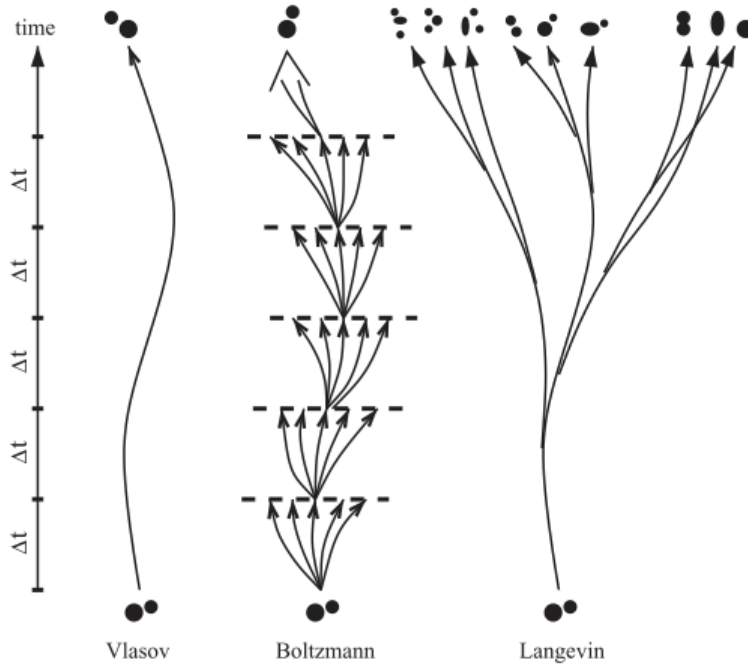


Figure A.1.1 – Illustration of differences between the evolution of the 1-body phase space density in various semi-classical treatments of microscopic nuclear dynamics. From [20]

A.1.2.1 The test particle method

The nuclear Boltzmann equation is a non-linear integro-differential equation which generally cannot be solved analytically or in a direct numerical way. Rather the common method is to simulate the solution by using the test-particle (TP) technique, which was introduced to nuclear physics in the beginning of the 1980s by Wong [173] for the solution of the TDHF equation. The one-body Wigner distribution $f(\mathbf{r}, \mathbf{p}; t)$ for A nucleons is then approximated by a sum of N_{TP} distributions per nucleon,

$$f(\mathbf{r}, \mathbf{p}; t) = \frac{1}{N_{TP}} \sum_{i=1}^{AN_{TP}} G(\mathbf{r} - \mathbf{r}_i(t)) \tilde{G}(\mathbf{p} - \mathbf{p}_i(t)) \quad (\text{A.1.12})$$

where G, \tilde{G} are shape functions in position and momentum space, respectively, which may be δ -functions, triangular functions or Gaussian distributions, depending on the implementation. Injecting Equation (A.1.12) into the Vlasov equation, Equation (A.1.9), we find the Hamiltonian equations of motion for the centroids of the shape functions,

$$\begin{aligned} \frac{d\mathbf{p}_i}{dt} &= -\nabla_{\mathbf{r}} H \\ \frac{d\mathbf{r}_i}{dt} &= \nabla_{\mathbf{p}} H \end{aligned} \quad (\text{A.1.13})$$

which therefore move like real “test” particles in the effective mean field.

The test particles are also used to simulate the Boltzmann collision integral Equation (A.1.11), according to the prescription of Bertsch and Das Gupta [163]. Stochastic two-body collisions take place between pairs of test particles when they approach closer than the geometrical distance of closest approach $d_{min} = \sqrt{\sigma^*/\pi}$. σ^* may be the vacuum or in-medium elastic NN collision cross-section; collisions may take place only between pairs of test particles belonging to one of the A ensembles of N_{TP} test particles (parallel ensembles method), or between all pairs among the AN_{TP} test particles (full ensemble method), in the latter case with the reduced cross-section σ^*/N_{TP} . See [160] for a recent and thorough comparison of implementations of the collision integral in different codes.

A.1.3 Beyond the nuclear Boltzmann equation

An essential shortcoming of the nuclear Boltzmann equation, is the fact that the propagation of the 1-body density is, in principle, entirely deterministic. This is because in the collision integral, Equation (A.1.11), the various possible outcomes of the residual collisions are averaged at each step (see Figure A.1.1), leading to a significantly different evolution compared to mean-field alone (Vlasov approach), but still a unique dynamical trajectory for a given set of initial conditions. In reality the number of collisions should fluctuate from one realisation of the evolution to another, due to the neglect of 3, 4, . . . , N -body correlations. This lack of stochasticity precludes the spontaneous appearance of fluctuations and thus renders the description inadequate when bifurcations and instabilities are encountered in the dynamics.

Several ways to avoid this shortcoming have been explored. The first consists in going beyond the mean value of the collision integral in order to calculate and include the associated fluctuations: these are the so-called Boltzmann-Langevin approaches. A second way tries to retain all N -body correlations while still maintaining a correct description of the mean field dynamics: this is the molecular dynamics approach.

A.1.3.1 Boltzmann-Langevin approaches

The Boltzmann-Langevin model allows the various stochastic collision outcomes to develop independently, thus leading to a continual trajectory branching and a corresponding ensemble of histories. This is done by now considering the collision term of Equation (A.1.10) to be a stochastic variable,

$$I[f] = \bar{I}[f] + \delta I(\mathbf{r}, \mathbf{p}; t) \quad (\text{A.1.14})$$

with a mean value $\bar{I}[f]$ given by the Uehling-Uehlenbek expression, Equation (A.1.11), while the fluctuating term, arising from correlations not accounted for by the mean value, is characterised by the correlation function [174]

$$\langle \delta I(\mathbf{r}, \mathbf{p}; t) \delta I(\mathbf{r}', \mathbf{p}'; t) \rangle = C(\mathbf{p}, \mathbf{p}') \delta(\mathbf{r} - \mathbf{r}') \delta(t - t') \quad (\text{A.1.15})$$

which is assumed local in space and time. Such stochasticity is typical of a reduced description of a dynamical system using a limited number of degrees of freedom; the fluctuations represent the coupling to the (many more) unknown degrees of freedom [57]. The correlation function is completely determined by the averaged properties of the single-particle density and is closely related

to the average collision term; no new parameters are required for describing fluctuation properties, in an equivalent way to the fluctuation-dissipation theorem in descriptions of Brownian motion.

Exact numerical solutions of the Boltzmann-Langevin equation (BLE), Equation (A.1.14), are very difficult to implement and so various approximate methods have been developed in order to allow realistic simulations of collisions:

- in the Brownian one-body (BOB) dynamics, developed in [56, 59], the fluctuating part of the collision integral δI is replaced by a stochastic force added to the standard Boltzmann–Nordheim–Vlasov (BNV) implementation of Equation (A.1.10), the strength of which can be tuned to correctly describe the growth of the most important unstable modes in an equilibrated system at a given density and temperature. It is not possible to use BOB in order to simulate the full collision dynamics from $t = 0$ and for any impact parameter. This is the approach used in my Ph.D work to simulate collisions of $^{155}\text{Gd} + ^{238}\text{U}$ 36A MeV and $^{129}\text{Xe} + ^{\text{nat}}\text{Sn}$ 32A MeV at $b = 0$ leading to multifragmentation by spinodal decomposition (see section 2.2.2);
- in the Stochastic Mean Field (SMF) approach, developed in [175, 176], the assumption of local thermal equilibrium allows to mimic the fluctuation δI with density fluctuations corresponding to the kinetic equilibrium values typical of a Fermi gas at (local) temperature T and chemical potential μ ,

$$\sigma_{p,\text{eq}}^2(r;t) = \frac{1}{V} \int \frac{dp}{h^3/4} \sigma_f^2(r,p;t) = \frac{T}{V} \frac{3\rho}{2\epsilon_F} \left(1 - \frac{\pi^2}{12} \left(\frac{T}{\epsilon_F} \right)^2 + \dots \right) \quad (\text{A.1.16})$$

SMF can simulate full collision dynamics for any impact parameter. This model was used to investigate compression-expansion dynamics and stopping for central collisions ($b \leq 4$ fm) of $^{129}\text{Xe} + ^{\text{nat}}\text{Sn}$ at different bombarding energies in [52];

- in the Boltzmann-Langevin One-Body model [62] two-body nucleon-nucleon collisions take place between “nucleon wave packets” defined as agglomerates of test particles based on proximity in phase space, following the prescription of Bauer *et al.* [86], but with an improved implementation of the Pauli blocking factors for wave packet collisions. In this way the Langevin fluctuations in the evolution of the one-body distribution function are implemented in full phase space with the correct amplitude at all times of the evolution;
- Recently, Lin and Danielewicz [177] reformulated the beyond-mean-field dynamics in heavy-ion collisions in terms of Brownian motions of nucleons in the viscous, out-of-equilibrium nuclear medium, as opposed to the typical two-body scatterings. The Brownian motions are, in effect, the momentum and energy exchange between a nucleon and the nuclear medium it is immersed in. They are governed by a set of Langevin equations consisting of a friction-like term and a stochastic term. This approach describes the dissipation and fluctuation dynamics consistently and simultaneously.

A.1.3.2 Molecular dynamics approaches

A different way to overcome the limitations of the essentially one-body transport models presented above, in essence trying to make the N -body quantum dynamics tractable while retaining as much as possible of the N -body correlations needed to describe clusterization, are the so-called molecular dynamics approaches. These are not derived from a semi-classical approximation to the truncated 1-body dynamics in the same way as the BUU-like models, but rather take as starting point a variational principle applied to an ansatz for the N -body description of the system which may be more or less quantal. Examples are the Constrained Molecular Dynamics (CoMD) model of Papa *et al.* [178], the Quantum Molecular Dynamics (QMD) model of Aichelin [65], the Anti-symmetrized Molecular Dynamics (AMD) model of Ono and Horiuchi [179], and the Fermionic Molecular Dynamics model of Schnack and Feldmeier [180].

“Quantum” Molecular Dynamics (QMD) The QMD model of Aichelin [65, 149] can be derived from a time-dependent Hartree (TDH) theory (antisymmetrization is neglected) with a trial wave function of the form

$$\Phi = \prod_{i=1}^{A_t+A_p} \phi_i \quad (\text{A.1.17})$$

which is a product of Gaussian single-particle wave functions [159]

$$\phi_i(\mathbf{r}; t) = \left(\frac{1}{2\pi\Delta x^2} \right)^{3/4} \exp \left\{ -\frac{[\mathbf{r} - \mathbf{R}_i(t)]^2}{(2\Delta x)^2} + i\mathbf{r} \cdot \mathbf{P}_i(t) \right\} \quad (\text{A.1.18})$$

with positions $\mathbf{R}_i(t)$ and momenta $\mathbf{P}_i(t)$ as variational parameters. Using a two-body interaction $V^{ij}(\mathbf{r}', \mathbf{r})$ including zero-range Skyrme, finite-range Yukawa and Coulomb components (see section A.1.4 below), the centroids of the Gaussian packets are found to follow equations of motion very similar to those of the test particles in BUU approaches (see section A.1.2.1 above):

$$\begin{aligned} \dot{\mathbf{R}}_i &= \frac{\mathbf{P}_i}{m} + \nabla_{\mathbf{P}_i} \sum_j \langle V_{ij} \rangle \\ \dot{\mathbf{P}}_i &= -\nabla_{\mathbf{R}_i} \sum_{j \neq i} \langle V_{ij} \rangle \end{aligned} \quad (\text{A.1.19})$$

with

$$\langle V_{ij} \rangle = \int d^3r d^3r' \phi_i^*(\mathbf{r}') \phi_j^*(\mathbf{r}) V^{ij}(\mathbf{r}', \mathbf{r}) \phi_i(\mathbf{r}') \phi_j(\mathbf{r})$$

Nucleon-nucleon collisions are implemented in much the same way as for BUU; however in QMD nucleons, not test particles, collide with the NN in-medium cross section, and so a collision will affect the evolution considerably more than a TP collision in BUU. The treatment of collisions in QMD approaches is intrinsically stochastic. In contrast to BUU, two-nucleon collisions induce event-by-event fluctuations, and so can lead to clusterisation and formation of fragments.

A recent improved and widely-used version of QMD including isospin-dependent forces and cross-sections is IQMD (Isospin-dependent QMD) of [181, 161, 182].

Antisymmetrized Molecular Dynamics (AMD) In AMD, the A -nucleon system is described by an anti-symmetrized Slater determinant of Gaussian wave packets,

$$|\Phi(\mathbf{Z})\rangle = \hat{A} \prod_{i=1}^A \phi_i(i) \quad (\text{A.1.20})$$

with the full antisymmetrization operator \hat{A} . Each single-particle state is a product of a Gaussian function and a spin-isospin state,

$$\langle \mathbf{r} | \phi_i \rangle = \exp \left[-v \left(r - \frac{\mathbf{Z}_i}{\sqrt{v}} \right)^2 \right] \otimes \chi_{\sigma_i} \quad (\text{A.1.21})$$

The spin and isospin of each nucleon are fixed, as is the Gaussian width parameter, v . The many-body state is thus parametrized by the (complex) Gaussian centroids $\mathbf{Z} = \{\mathbf{Z}_1, \mathbf{Z}_2, \dots, \mathbf{Z}_A\}$ whose time evolution may be determined by the time-dependent variational principle

$$\delta \int_{t_1}^{t_2} dt \frac{\langle \Phi(\mathbf{Z}) | \left(i\hbar \frac{d}{dt} - H \right) | \Phi(\mathbf{Z}) \rangle}{\langle \Phi(\mathbf{Z}) | \Phi(\mathbf{Z}) \rangle} = 0 \quad (\text{A.1.22})$$

An effective interaction is employed in the Hamiltonian H , such as the Gogny or Skyrme forces (see A.1.4). The resulting equations of motion then represent the motion of the wave packets in the mean field. Stochastic NN collisions are implemented using in-medium elastic cross-sections, and are only allowed for final states which are also Slater determinants, thus respecting the Pauli principle. NN collisions in AMD are therefore treated as a quantum branching process in which the system stochastically jumps from one Slater determinant to another (this can be seen as an approximation to the approach of [169]). Recently, the two-nucleon collision process in AMD has been generalized to allow the possibility that each colliding nucleon may form a cluster of mass number $A = 2, 3$ or 4 with some other wave packets [166].

At the present time, AMD is probably the best available microscopic model for heavy-ion (and especially multifragmentation) reactions in the Fermi energy domain, as it respects both the coherent mean field propagation (a thorough and positive comparison between reaction dynamics with AMD and SMF was presented in [183]) and the existence of strong many-body correlations, essential for the description of clusterization and fragmentation.

A.1.4 Effective forces

The most microscopic way to calculate empirical properties of nuclear matter is to start from a realistic two-body free nucleon-nucleon (NN) interaction with parameters fitted to NN scattering phase shifts in different partial wave channels and to properties of the deuteron [184]. By taking these bare interactions as input into a many-body formalism, such as the non-relativistic Bruckner-Hartree-Fock [185] or relativistic Dirac-Bruckner-Hartree-Fock approximations [186], an effective in-medium NN interaction can in principle be derived. Such an approach has been used with success to reproduce infinite nuclear matter properties. However, these interactions are

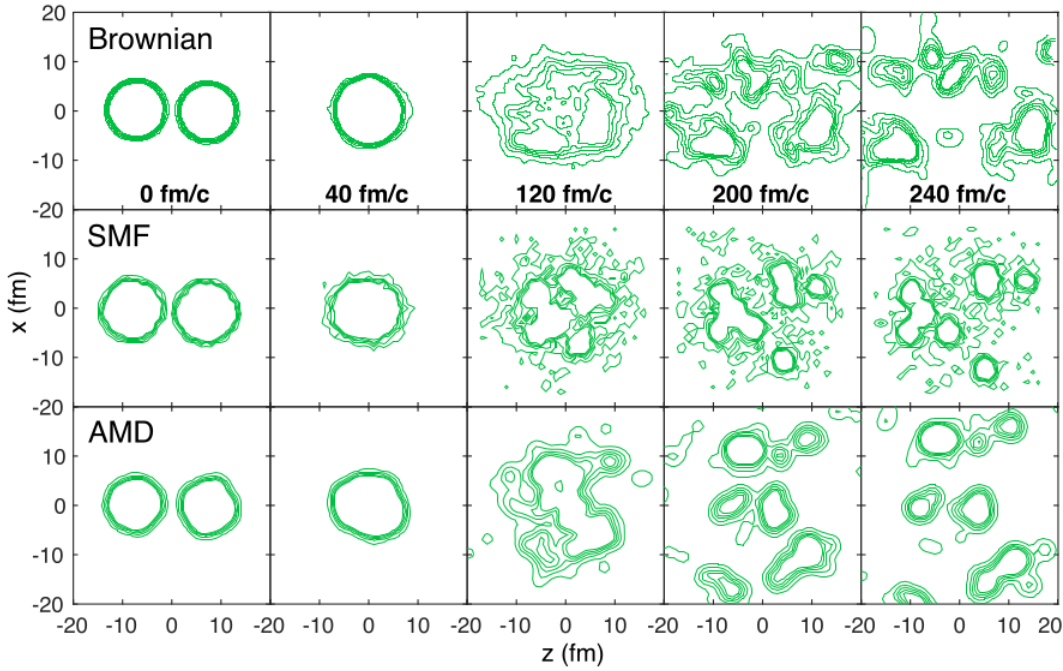


Figure A.1.2 – Comparison of three beyond-nuclear-Boltzmann-equation transport models: the Brownian one-body Langevin dynamics of [177], SMF and AMD. Density contours in the reaction plane for $^{112}\text{Sn}+^{112}\text{Sn}$ collisions at $50A$ MeV with $b = 0.5$ fm. From [177].

far too computationally intensive for calculations of reaction dynamics using the transport models presented above. Rather they employ effective density-dependent phenomenological interactions which are fitted to describe the ground-state properties of finite nuclei and nuclear matter, using either zero-range (Skyrme model) or short finite-range (Gogny model) density functionals.

Skyrme interactions The Skyrme interaction [187, 188, 63, 189], originally constructed for finite nuclei and nuclear matter at saturation density, is a low-momentum expansion of the effective two-body NN interaction in momentum space. In its simplest form, the isoscalar part of the effective two-body Skyrme interaction is a zero-range density-dependent interaction,

$$v_{ij} = -t_0\delta(\mathbf{r}_i - \mathbf{r}_j) + \frac{t_3}{6}\rho^\sigma(\mathbf{r}_{ij})\delta(\mathbf{r}_i - \mathbf{r}_j) \quad (\text{A.1.23})$$

with $\mathbf{r}_{ij} = (\mathbf{r}_i + \mathbf{r}_j)/2$ and where the parameters t_0 , t_3 and σ are fitted to nuclear properties at zero temperature (see [190] for a large compilation of much more recent versions of Skyrme interactions). The second, density-dependent, term, which Vautherin and Brink [188] showed to be equivalent to a three-body contact force, provides a short-range repulsion thus ensuring saturation at a certain density ρ_0 . The interaction of Equation (A.1.23) leads to a density-dependent mean field potential

$$U(\rho) = A\frac{\rho}{\rho_0} + B\left(\frac{\rho}{\rho_0}\right)^{\sigma+1} \quad (\text{A.1.24})$$

which may be supplemented by an isospin-dependent term,

$$U_{q=n,p} = C \frac{\rho_n - \rho_p}{\rho_0} \tau_q$$

where $\tau_n = 1$ and $\tau_p = -1$. For the description of finite nuclei, a term proportional to $\nabla^2 \rho$ is usual added to the potential which is adjusted to reproduce nuclear surface energies. Coulomb repulsion between protons is also included by solving the Poisson equation for the proton charge distribution,

$$\nabla^2 U_{Coul}(\mathbf{r}) = -\frac{1}{\epsilon_0} \rho_p(\mathbf{r})$$

The Skyrme force has been most often used with BUU, BNV and SMF models. In our calculations for $^{155}\text{Gd} + ^{238}\text{U}$ and $^{129}\text{Xe} + ^{nat}\text{Sn}$ reactions in [44] and [52] this potential with parameters $A = -356$ MeV, $B = 303$ MeV, $\rho_0 = 0.16 \text{ fm}^{-3}$ and $\sigma = 1/6$ was used, leading to saturation properties of cold symmetric nuclear matter $E/A = -16$ MeV/nucleon and incompressibility $K_\infty = 200$ MeV. In [52] the isospin-dependent part with $C = 36$ MeV was also implemented.

It should be noted that in [190], of 240 existing Skyrme parametrizations used in the literature, only 16 fulfilled a set of constraints derived from a wide range of macroscopic properties of symmetric or pure neutron nuclear matter and mixtures of the two. Including four further more microscopic constraints, only 5 Skyrme parameter sets agree with existing experimental and empirical data.

Gogny interactions The advantage of the structure of the Skyrme density functional is that it allows analytical expression of all variables characterizing infinite nuclear matter, but as it neglects the finite range of the nuclear interaction there is no momentum dependence in the mean field. On the other hand the effective interaction proposed by Gogny [191] explicitly considers the finite range of the nuclear force. Again neglecting the spin-orbit and isospin dependent terms for simplicity, this force has a form [192]

$$v_{ij} = \sum_{k=1}^2 (W_k + B_k P^\sigma - H_k P^\tau - M_k P^\sigma P^\tau) \exp[-(\mathbf{r}_i - \mathbf{r}_j)^2 / a_k^2] + t_3 \delta(\mathbf{r}_i - \mathbf{r}_j) (1 + P^\sigma) \rho \left(\frac{\mathbf{r}_i + \mathbf{r}_j}{2} \right)^{1/3} \quad (\text{A.1.25})$$

which is composed of two finite range two-body terms and a density-dependent zero range two-body term (almost the same as that of the Skyrme interaction, Equation (A.1.23)). The operators P^σ and P^τ are the spin and isospin exchange operators, respectively. The mean-field potential corresponding to this force (here given *with* the dependence on the isospin asymmetry, $\delta =$

t_3 [MeV]	k	W_k [MeV]	B_k [MeV]	H_k [MeV]	M_k [MeV]	a_k [fm]
1350	1	-402.4	-100	-496.2	-23.56	0.7
	2	-21.3	-11.77	37.27	-68.81	1.2

a_V [MeV]	p_F [MeV/c]	ρ_0 [fm $^{-3}$]	m^*/m	K_∞ [MeV]	a_S [MeV]
-16.3	266.4	0.166	0.67	228	20.2

Table A.1 – (top) Parameters of the Gogny D1-G1 force, and (bottom) Nuclear matter characteristics with the above Gogny force: bulk energy a_V , Fermi momentum p_F at saturation density ρ_0 , effective mass of nucleons m^*/m , bulk incompressibility modulus K_∞ and surface energy coefficient a_S [192].

$(\rho_n - \rho_p)/\rho$), as required for BUU-type calculations, is given by [193]

$$\begin{aligned}
U(\rho, \delta, p, \tau) = & A_u \frac{\rho_{\tau'}}{\rho_0} + A_l \frac{\rho_\tau}{\rho_0} + B \left(\frac{\rho}{\rho_0} \right)^\sigma (1 - x\delta^2) \\
& - x \frac{B}{\sigma + 1} \frac{\rho^{\sigma+1}}{\rho_0^\sigma} \frac{d\delta^2}{d\rho_\tau} \\
& + \frac{2C_{\tau,\tau}}{\rho_0} \int d^3\mathbf{p}' \frac{f_\tau(\mathbf{r}, \mathbf{p}')}{1 + (\mathbf{p} - \mathbf{p}')^2/\Lambda^2} \\
& + \frac{2C_{\tau,\tau'}}{\rho_0} \int d^3\mathbf{p}' \frac{f_{\tau'}(\mathbf{r}, \mathbf{p}')}{1 + (\mathbf{p} - \mathbf{p}')^2/\Lambda^2}
\end{aligned} \tag{A.1.26}$$

where Λ is a cut-off parameter (typically $\sim p_F$, the Fermi momentum at saturation density; see [193]), and x is a parameter introduced to cover the largely uncertain density dependence of the nuclear symmetry energy $E_{sym}(\rho)$ [194]. For the meaning and values of other parameters, see [193]. The Gogny mean field has a realistic momentum dependence below at least $E \lesssim 200$ MeV [192]. The Gogny interaction has been utilized most frequently in AMD calculations (see [179, 166]).

QMD interaction The interaction used in QMD [149] includes zero-range Skyrme, finite-range Yukawa and Coulomb components and can be written

$$V^{ij}(\mathbf{r}', \mathbf{r}) = \delta(\mathbf{r}' - \mathbf{r}) \left[t_1 + t_2 \left[\rho \left(\frac{\mathbf{r}' + \mathbf{r}}{2} \right) \right]^{\gamma-1} \right] + t_3 \frac{\exp(-|\mathbf{r}' - \mathbf{r}|/\mu)}{|\mathbf{r}' - \mathbf{r}|/\mu} + \frac{Z_i Z_j e^2}{|\mathbf{r}' - \mathbf{r}|}$$

It should be noted that Z_i, Z_j are the effective charges of baryons i and j (Z_{proj}/A_{proj} for projectile nucleons, Z_{targ}/A_{targ} for target nucleons).

A.2 Statistical descriptions of multifragmentation

The starting point for statistical models of multifragmentation is to suppose that a highly-excited nuclear system will arrive, at some point in its evolution, at a moment commonly known as the *freeze-out* after which the characteristics of the fragments produced by its decay will no longer significantly change, apart from the effects of secondary decay (evaporation of light particles due to residual excitation energy) and Coulombian acceleration due to mutual repulsion between charged fragments. The original statistical model, and ancestor of all others, is commonly recognised to be that of Randrup and Koonin [195].

It is a common fallacy, oft-repeated not only by the users of such models, but also by their creators and *a fortiori* by their detractors, that the basic hypothesis of these models is that a multifragmenting system is in statistical equilibrium at freeze-out. This is a common misapplication of the ergodic theorem to non-ergodic finite systems (see Chapter 3 of [1] for a detailed discussion of this and related points). What is actually supposed is that a given set (ensemble) of multifragmenting systems populate uniformly the phase space corresponding to the chosen description of the freeze-out, which is not the same thing.

Another misconception is that the use of statistical equilibrium concepts implies that in some way processes must be “sufficiently slow”. To quote D.H.E. Gross, who stands as one of the pioneers in the application of finite-system statistical mechanics to multifragmentation reactions, “a statistical process populates the accessible phase-space uniformly [*sic*], *i.e.* every quantum state of **the system** [my emphasis] that is not excluded by basic conservation laws [...] is populated independently of how easy or difficult this might be. That is, a statistical process must also be in general a slow process and thus will be an idealisation. In reality most reactions will not go slowly enough that remote parts of the phase space may not be reached [...]” [196].

The apparent difficulty arises from the mistake of thinking that the aim of the statistical model being constructed is to describe *a single system* using a Gibbs ensemble of an infinite number of replicates of **the system** having the same macroscopic properties, as one commonly does when dealing with systems in the thermodynamic limit. Obviously in this case, any single system *would* need “sufficient time” to explore the whole phase space mapped out by the ensemble of replicates – the ergodic theorem.

But Gross himself then gives the solution in the next lines: “The quantal transition probability $P_{ik} = (2\pi/\hbar)|T_{ik}|^2\rho_k$ is split into two factors: the square of the T matrix [reaction dynamics] times the final-state density ρ_k . Because of equipartition in a statistical process $|T_{ik}|^2$ is roughly constant and only ρ_k determines the cross-section”. In other words, if data from heavy-ion collisions are carefully sorted into homogeneous event samples corresponding to similar reactions so that for a given sample “ $|T_{ik}|^2$ is roughly constant”, the properties of the selected events are determined mainly by the statistical weights ρ_k regardless of whether the reaction represented by T_{ik} is “fast” or “slow”.

Specific statistical multifragmentation models differ in their description of the freeze-out configuration, the implementation of the initial conditions (constraints), and the numerical methods employed to make predictions based on the corresponding ensembles. See Botvina and Mishustin [197] for a good review. Here I will just present the most salient points of some of the models mentioned in the manuscript.

$p(A_0 = 58)$ [198]	$p(A_0 = 58, Z_0 = 28)$ [200]	$p(^{58}\text{Ni})$ [15]
715,220	221,170,802,387	27,476,011

Table A.2 – Partition counting for $A_0 = 58$. $p(A_0 = 58)$: number of partitions of the number 58; $p(A_0 = 58, Z_0 = 28)$: number of partitions into two-component clusters (A, Z) ; $p(^{58}\text{Ni})$: number of partitions of ^{58}Ni nucleus containing only physical nuclei calculated with a parallel processing algorithm.

A.2.1 The Statistical Multifragmentation Model (SMM)

In SMM [198, 199, 100] the break-up channels of an excited nuclear system (A_0, Z_0, E_0) are described by the partitions

$$f : \{N_{AZ}; 1 \leq A \leq A_0, 0 \leq Z \leq Z_0\}$$

For fixed (A_0, Z_0) the number of all possible partitions of this type can be calculated [200]: it rapidly becomes astronomical with increasing A_0 ($\sim 10^5$ for $A_0 = 20$, $\sim 10^{10}$ for $A_0 = 50$, with $N_0 = Z_0$), but is greatly decreased if only physical combinations of (N, Z) are kept in the partitions (see Table A.2).

The fragmented systems at freeze-out are represented as a set of (spherical) nuclei at normal density contained in a spherical volume large enough to contain all nuclei without overlapping: typical values are $V \approx 3 - 6V_0$ where V_0 is the volume occupied by A_0 nucleons at saturation density. Internal excitation of all but the lightest ($A > 4$) nuclei is taken into account using the Fermi gas relation (see below). Collective flow can be included in the calculations, but is not included in the calculation of the statistical weights, and is therefore decoupled from the partitions. To my knowledge, only a linear (Hubbleian) velocity profile

$$v_F(r) = \left(\frac{r}{R}\right) v_0$$

has been used with SMM, for which the total flow energy is given by a simple expression, $E_F = \frac{3}{10} u A_0 v_0^2$, where r is the radial distance of a fragment from the centre of mass, R is the root-mean-square radius of all fragments in the break-up configuration, and u is the mass of the nucleon.

The statistical weights for partitions are determined by their free energy

$$F_f(T, V) = F_f^{\text{tr}}(T, V_f) + \sum_{A,Z} F_{AZ}(T, V) N_{AZ} + E_0^{\text{C}}(V) \quad (\text{A.2.1})$$

where the first term corresponds to the translational motion of the fragments (within a free volume V_f smaller than the freeze-out volume V due to the finite size and strong interaction of fragments), the second term is the sum of the free energies of the nuclei in the partition, given as a sum of bulk, surface, Coulomb and symmetry energy terms,

$$F_{AZ}(T, V) = F_{AZ}^{\text{B}}(T) + F_{AZ}^{\text{S}}(T) + E_{AZ}^{\text{C}}(V) + E_{AZ}^{\text{sym}}$$

and the last term is the Coulomb repulsion energy of the partition. Initially calculated in a Wigner-Seitz approximation, since the introduction of the Markov chain Metropolis sampling version of SMM [201, 202] E_C^0 can be calculated exactly for each freeze-out configuration from fragment positions.

SMM can be used with “microcanonical” or “canonical” weights, although strictly speaking they do not fully respect either ensemble³. In the “microcanonical” case, a temperature T_f is calculated for each partition in order to respect the energy conservation condition averaged over all microscopic states (fragment momenta, excitation energies, positions) leading to a given partition

$$E_f(T_f, V) = E_f^{\text{tr}}(T_f, V) + \sum_{A,Z} E_{AZ}(T_f, V) N_{AZ} + E_C^0(V) = E_0$$

Then the “microcanonical” partition weight is given by

$$W_f^{\text{mic}} = \frac{1}{\xi} \exp S_f(A_0, Z_0, E_0, V) = \exp \left(-\frac{\partial F_f(T, V)}{\partial T_f} \right), \quad \xi = \sum_{\{f\}} \exp S_f(A_0, Z_0, E_0, V)$$

In the “canonical” case a single temperature T is determined so that the mean energy of all partitions respects the energy conservation condition

$$\langle E_f(T_f) \rangle = \sum_{\{f\}} W_f E(T, V) = E_0$$

and the partition weights are

$$W_f^{\text{can}} = \frac{1}{\zeta} \exp (-F_f(T, V)/T), \quad \zeta = \sum_{\{f\}} \exp (-F_f(T, V)/T)$$

In both cases, the same temperature is used to determine both the thermal translational motion, intrinsic thermal excitation and surface energies of the fragments, although the excitation energy sharing can be modified by adjusting the level density parameter ϵ_0 used in the bulk free energy,

$$F_{AZ}^B(T) = \left(-W_0 - \frac{T^2}{\epsilon_0} \right) A$$

where $W_0 \approx 16A$ MeV is the binding energy of bulk nuclear matter at saturation density.

A.2.2 Microcanonical Multifragmentation Models (MMMC and MMM)

The original microcanonical multifragmentation model is that of Gross [203, 204, 196], MMMC (Metropolis Multifragmentation Monte Carlo), which uses a Metropolis importance sampling technique to explore the phase space defined by microcanonical statistical weights for the freeze-out configurations. In MMMC internal excitation of primary fragments is limited to particle

³“Strictly speaking, the above described [microcanonical] approach corresponds to the canonical approximation when considering a given partition. However, henceforth it will be called microcanonical because for every partition we fix the total fragment energy averaged over microscopic states, but not over partitions.” [100]

stable levels only, which leads to relatively cold fragments, while it is assumed that any excess excitation energy of the primary fragments was previously evacuated through neutron evaporation, which are therefore present in the freeze-out description and contribute to the statistical weight. Given our current experimental knowledge and other model evidence for excitation and secondary decay of primary fragments [67, 71], this is not a very realistic assumption. Note however that kinematic properties, notably the observed anisotropy of momentum distributions, for central collisions for $^{129}\text{Xe} + ^{nat}\text{Sn}$ at 50A MeV were well-reproduced with a modified version, MMMC-NS, using a non-spherical freeze-out volume and/or non-Hubbleian flow profile [205, 206].

A more recent version of a Microcanonical Multifragmentation Model (MMM) is that of Raduta and Raduta [101, 93]. As in SMM, fragments are assumed to be spherical, non-overlapping, normal density nuclei in a spherical recipient of volume V . The basic assumption of the model is equiprobability between all configurations

$$C : \{A_i, Z_i, \epsilon_i, \mathbf{r}_i, \mathbf{p}_i; i = 1, \dots, N\}$$

(the mass number, the atomic number, the excitation energy, the position, and the momentum of each fragment i of the configuration C , composed of N fragments) which respect the conservation laws, including momentum and angular momentum conservation in [93]. The integration over fragment momenta in the centre of mass frame can then be analytically performed subject to the aforementioned constraints,

$$\begin{aligned} & \int \prod_{i=1}^N d\mathbf{p}_i \delta(H - E) \delta\left(\sum_i \mathbf{p}_i\right) \delta\left(\sum_i \mathbf{r}_i \times \mathbf{p}_i - \mathbf{L}\right) \\ &= \frac{2\pi}{\Gamma\left[\frac{3}{2}(N-2)\right]} \left(\frac{\prod_i m_i}{\sum_i m_i}\right)^{3/2} \frac{1}{\sqrt{\det \mathbf{I}}} \left[2\pi \left(K - \frac{1}{2} \mathbf{L}^T \mathbf{I}^{-1} \mathbf{L}\right)\right]^{(3/2)(N-2)-1} \end{aligned}$$

with H the total energy of the configuration, E the total energy of the system prior to break-up, \mathbf{L} the total angular momentum and \mathbf{I} the inertial tensor of the configuration, and K the total kinetic energy.

As in SMM, all but the lightest ($A \leq 4$) fragments can have intrinsic excitation energies $\epsilon_i > 0$, but the corresponding level density formula

$$\rho(\epsilon) = \frac{\sqrt{\pi}}{12a^{1/4}e^{5/4}} \exp(2\sqrt{a\epsilon}) \exp(-\epsilon/\tau)$$

includes a cut-off factor with parameter $\tau = 9$ MeV which is introduced to account for the dramatic decrease of the excited levels lifetime at high excitation energies according to the prescription of Randrup and Koonin [207].

Again as in SMM, radial flow can be included in the calculation, but it does not intervene in the calculation of the statistical weights, except in so much as collective flow energy reduces the available energy for all other degrees of freedom, to conserve energy. The following parametrization for the flow velocity of fragment i is used:

$$\mathbf{v}_i^F = v_0 \left(\frac{r_i}{R}\right)^\alpha, \quad v_0 = v_0 \left(\frac{r_i}{r_i}\right)$$

Non-linear velocity profiles can be treated, when the parameter $\alpha \neq 1$.

Appendix B

Reconstruction of impact parameter distributions

B.1 Validation of the method

To test the numerical implementation of the method, we have generated pseudo-events using the probability distribution of Equation (6.2.20) with a set of parameters taken from a typical fit to data for the total multiplicity of charged products, N_C (the parameters for the fit to $^{Ni}58+^{Ni}5852$ data were used, see Table B.1). We have deliberately limited the generated statistics in order to accentuate statistical fluctuations (only 10^4 events were generated, far less than the experimental datasets: see Table 6.1).

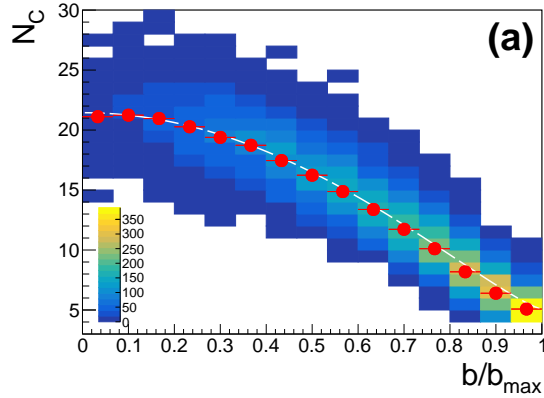
For each event a random value of c_b was uniformly generated in the range $[0, 1]$, this was then used in Equation (6.2.23) to calculate k and a random value of X drawn according to the gamma distribution Equation (6.2.20). For the multiplicity N_C we used the nearest integer value to this X , and as for data we rejected events with multiplicity less than the DAQ multiplicity trigger, $N_C \geq 4$ (see Part II, Section §6.3).

Figure B.1.1a shows the resulting joint probability distribution of N_C and b/b_{max} and the mean multiplicities calculated for the pseudo-events in each impact parameter bin. To calculate the impact parameter corresponding to each centrality c_b we have simply assumed a triangular distribution for $P(b)$: in this case $c_b = (b/b_{max})^2$.

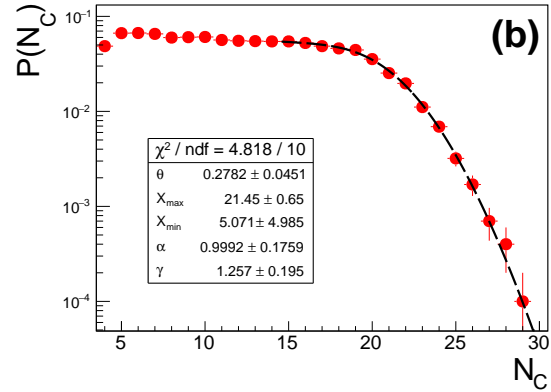
Figure B.1.1b presents the inclusive $P(N_C)$ distribution for all pseudo-events, along with the best fit which was achieved using Equations (6.2.14), (6.2.20) and (6.2.23) and starting from very different parameter values than those used to generate the events. As indicated by the dashed curve representing the fit, here we deliberately chose to exclude all but the high-multiplicity tail of the $P(N_C)$ distribution (fits to experimental data typically included a far wider range of values, down to $N_C \sim 7 - 8$ for a trigger multiplicity 4).

Nevertheless the fit converges to parameter values (shown in the figure) which are very close to the ones used to generate the events (it should be noted that if we fit the full $P(N_C)$ distribution we find exactly the initial values for all parameters within uncertainties). The main effect of limiting the fit to the high-multiplicity tail is to increase the uncertainty (and indeed the error) on the X_{min} parameter which corresponds to the low-multiplicity cut-off.

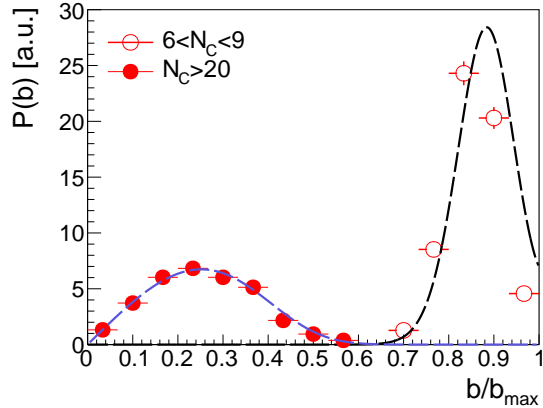
The deduced correlation between $\overline{N_C}$ and b is shown in Figure B.1.1a and can be compared



(a) Colour levels represent the joint probability distribution $P(N_C, b)$ in terms of number of events, red symbols are the mean multiplicity for each impact parameter bin and the white dashed line is $\overline{N_C}(b)$ deduced from the parameters of the fit shown in (b).



(b) red symbols: Inclusive (marginal) distribution $P(N_C)$ for all pseudo-events; dashed line: fit to $P(N_C)$ using Equations (6.2.14), (6.2.20) and (6.2.23).



(c) Impact parameter distributions for different multiplicity cuts: symbols represent the pseudo-event distributions, dashed curves are the $P(b)$ calculated using Equation (6.2.12) and the parameters found by fitting $P(N_C)$.

Figure B.1.1 – Test of the method with 10^4 pseudo-events generated using Equations (6.2.20) and (6.2.23).

directly to the values calculated from the pseudo-events themselves (red symbols). Apart from a slight deviation for the most peripheral “collisions” *i.e.* close to the low-multiplicity cut-off, the agreement is very satisfactory.

To further test the method we compare in Figure B.1.1c the impact parameter distributions of pseudo-events for multiplicity cuts corresponding to “central” or “peripheral” collisions with the $P(b)$ distributions calculated using Equation (6.2.12) and the parameters found by fitting $P(N_C)$ in Figure B.1.1b.

As can be seen, the impact parameter distributions deduced from the fit are very similar to the actual distributions of the pseudo-events selected with each cut. For the most “peripheral” cut ($6 < N_C < 9$) the deduced $P(b)$ is slightly distorted due to the low-multiplicity cut-off: the mean value and standard deviation of the distribution are slightly over-estimated using the fit parameters. The “central” cut we used corresponds to the value of $\overline{N_C}$ at $b = 0$, and corresponds to an experimental centrality $c_X = 7\%$. Using the sharp cut-off approximation of [74], Equation (6.2.8), we would therefore expect $\hat{b} < 0.26$ (and $\langle \hat{b} \rangle = 0.18$); in reality this cut selects a far wider range of impact parameters, up to $\hat{b} \approx 0.6$, with mean value $\langle \hat{b} \rangle = 0.26$ and standard deviation 0.12.

This reduced selectivity for “the most central collisions” is simply a consequence of the form of the correlation between N_C and b shown in Figure B.1.1a: due to the flattening (plateau) of the $\overline{N_C}(b)$ curve for $\hat{b} < 0.5$ the increase in $\overline{N_C}$ going towards $b = 0$ is not significant compared to the fluctuations of N_C for each impact parameter bin.

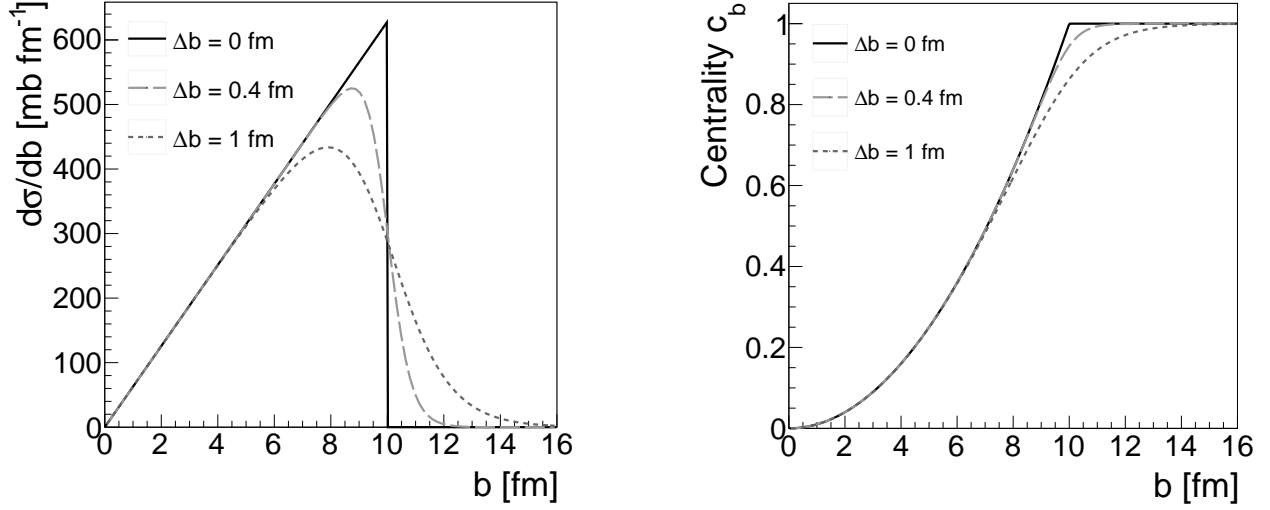
B.2 Minimum bias impact parameter distribution

Simulations with many different reaction models and different software ‘filters’ to simulate the minimum-bias acceptance of the INDRA array suggest that data has an unbiased geometrical distribution up to some trigger-multiplicity-dependent impact parameter \tilde{b} . In general the simulated minimum-bias impact parameter distributions are well described by Equation (6.2.3) with an inelastic reaction probability distribution of the form

$$P_R(b) = \frac{1}{1 + \exp\left(\frac{b-b_0}{\Delta b}\right)} \quad (\text{B.2.1})$$

with typical Δb values of 0.3-0.4 fm. Examples of such distributions are shown in Figure B.2.1a for different Δb values (including $\Delta b = 0$ fm, which is the sharp cut-off approximation) and a fixed total reaction cross-section. The b_0 values (fixed by the normalization, see B.2.1 below) change only slightly with Δb (9.97 fm for $\Delta b = 0.4$ fm, or 9.83 fm for $\Delta b = 1$ fm) and are well-approximated by the sharp cut-off value $b_{\text{max}} = b_0(\Delta b = 0) = 10$ fm. On the other hand, the upper limit of the unbiased impact parameters, \tilde{b} , decreases rapidly from ≈ 8 fm for $\Delta b = 0.4$ fm to ≈ 6 fm for $\Delta b = 1$ fm.

Also shown in Figure B.2.1b are the relationships between the centrality c_b and impact parameter for the three distributions, given by the analytic function derived in B.2.2 below. It can be seen that for all but the most peripheral reactions the parabolic sharp cut-off relationship ($\Delta b = 0$ fm) is an exact approximation to the analytic formulae with $\Delta b > 0$. The deviation from



(a) Differential cross-section distributions with different values of Δb for a fixed total reaction cross-section $\sigma_R = \pi(10\text{fm})^2$.

(b) Centrality as a function of impact parameter for the same parameter values as in (a).

Figure B.2.1 – Examples of cross-section distributions and the associated centrality calculated with Equation (B.2.1).

the parabolic form gives another estimation for \tilde{b} : for $\Delta b = 0.4$ fm the approximation holds up to $\tilde{b} \approx 9$ fm, while for $\Delta b = 1$ fm unbiased centrality holds up to $\tilde{b} \approx 7$ fm.

B.2.1 Analytic expression for total cross-section

To normalize correctly the probability distribution Equation (B.2.1) we need to know the total reaction cross-section for a given set of parameters b_0 and Δb . By definition,

$$\sigma_R = \int_0^\infty 2\pi b \left[1 + \exp\left(\frac{b - b_0}{\Delta b}\right) \right]^{-1} db$$

and making the substitutions $b = t\Delta b$ and $b_0 = x\Delta b$ we arrive at

$$\sigma_R = 2\pi(\Delta b)^2 \int_0^\infty \frac{t}{1 + \exp(t - x)} dt$$

This definite integral is related to the complete Fermi-Dirac integral

$$F_j(x) = \frac{1}{\Gamma(j+1)} \int_0^\infty \frac{t^j}{1 + \exp(t - x)} dt \quad (\text{B.2.2})$$

with $j = 1$, where $\Gamma(j+1)$ is the gamma function, $\Gamma(j+1) = j!$ for integer j . In general the value of this integral is given by a polylogarithm, $\text{Li}_s(z)$, specifically

$$F_j(x) = -\text{Li}_{j+1}(-e^x)$$

and in this particular case by the negative dilogarithm, $-\text{Li}_2(-e^x)$. Therefore we have for the final expression of the total cross-section which normalizes correctly the probability distribution of Equation (B.2.1),

$$\sigma_R = -2\pi(\Delta b)^2 \text{Li}_2 \left(-\exp \left(\frac{b_0}{\Delta b} \right) \right) \quad (\text{B.2.3})$$

This expression can be used to find b_0 for a given total cross-section and width parameter Δb , by numerical inversion [13].

B.2.2 Analytic expression for centrality

To calculate the centrality c_b we substitute Equation (B.2.1) into Equation (6.2.1), and making the same substitutions as above ($b = t\Delta b$, $b_0 = x\Delta b$) we find

$$c_b = \frac{2\pi(\Delta b)^2}{\sigma_R} \int_0^{b/\Delta b} \frac{t'}{1 + \exp(t' - x)} dt'$$

This definite integral can be calculated using the incomplete Fermi-Dirac integral

$$F_j(a, x) = \frac{1}{\Gamma(j+1)} \int_a^\infty \frac{t^j}{1 + \exp(t - x)} dt, \quad a \geq 0$$

with $a = b/\Delta b$, and the complete Fermi-Dirac integral $F_j(x)$ of Equation (B.2.2):

$$\int_0^a \frac{t^j}{1 + \exp(t - x)} dt = \Gamma(j+1) [F_j(x) - F_j(a, x)]$$

With $j = 1$, $F_1(x) = -\text{Li}_2(-e^x)$ as above, while the incomplete FD integral can be written (by integration by parts) as

$$F_1(a, x) = \frac{\pi^2}{6} - \frac{(a^2 - x^2)}{2} + a \ln(1 + e^{(a-x)}) + \text{Li}_2(-e^{(a-x)})$$

The final expression for the centrality is therefore

$$c_b = \frac{2\pi(\Delta b)^2}{\sigma_R} \left[-\text{Li}_2 \left(-\exp \left(\frac{b_0}{\Delta b} \right) \right) - \frac{\pi^2}{6} + \frac{(b^2 - b_0^2)}{2(\Delta b)^2} - \frac{b}{\Delta b} \ln(1 + \exp((b - b_0)/\Delta b)) - \text{Li}_2 \left(-e^{(b-b_0)/\Delta b} \right) \right] \quad (\text{B.2.4})$$

B.3 Fit results for all systems

B.4 “Scaling” of inclusive distributions of variables correlated with impact parameter

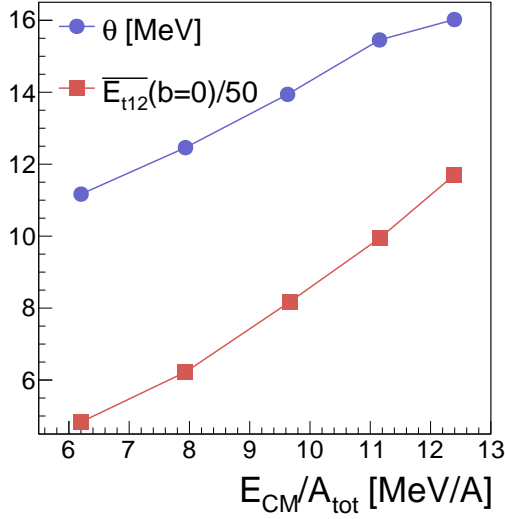
Here a long-standing misapprehension will be addressed concerning an apparent scaling of inclusive distributions of observables which are supposed to be strongly correlated with the impact

System	E_{proj} [MeV/A]	α	γ	θ	X_{max}	X_{min}	χ^2
$^{36}\text{Ar}+^{39}\text{KCl}$	32	0.95	1.25	0.20	14.1	3.7	13.2
	40	0.98	1.46	0.23	15.6	4.2	6.5
	52	0.88	1.40	0.22	17.6	4.0	8.2
	74	0.89	1.60	0.21	19.8	4.3	10.2
$^{36}\text{Ar}+^{58}\text{Ni}$	32	1.37	1.12	0.25	14.8	2.5	85.4
	40	1.23	1.14	0.27	16.8	2.6	46.4
	52	1.07	1.17	0.28	19.1	2.7	53.5
	63	0.99	1.19	0.29	20.6	2.7	28.1
	74	0.95	1.21	0.27	22.4	3.8	43.8
	84	0.96	1.24	0.27	23.2	3.8	25.8
	95	0.98	1.28	0.27	24.1	3.9	56.3
$^{58}\text{Ni}+^{58}\text{Ni}$	32	1.24	1.19	0.28	16.3	3.7	55.4
	52	0.97	1.15	0.30	21.6	3.8	14.0
	63	0.92	1.16	0.28	24.1	3.8	5.9
	74	0.81	1.17	0.27	25.8	3.7	4.2
	82	0.96	1.45	0.29	26.4	4.6	8.1
	90	0.93	1.40	0.28	27.4	4.2	38.2
$^{58}\text{Ni}+^{197}\text{Au}$	32	1.79	1.79	0.34	16.2	4.1	84.3
	52	1.63	1.66	0.37	23.0	4.2	49.5
	64	1.48	1.64	0.37	26.4	4.3	15.1
	74	1.44	1.62	0.39	28.4	4.1	45.6
	82	1.51	1.85	0.41	29.7	4.7	43.2
	90	1.06	1.43	0.37	32.2	3.9	9.5
$^{129}\text{Xe}+^{119}\text{Sn}$	25	1.26	0.95	0.32	19.6	2.8	63.5
	32	1.24	1.08	0.34	24.0	3.2	40.3
	39	1.18	1.17	0.34	28.4	3.5	55.1
	45	1.14	1.23	0.34	31.2	3.8	56.5
	50	1.14	1.35	0.34	34.1	4.0	36.6
$^{129}\text{Xe}+^{124}\text{Sn}$	65	1.09	1.40	0.36	38.4	2.9	2.0
	80	1.11	1.50	0.34	42.5	3.1	1.5
	100	1.18	1.64	0.38	45.2	3.5	2.7
$^{197}\text{Au}+^{197}\text{Au}$	40	1.23	1.27	0.42	35.5	2.1	30.1
	60	1.22	1.62	0.45	47.8	1.2	68.1
	80	1.24	1.61	0.45	54.9	2.8	16.9
	100	1.26	1.64	0.49	58.5	3.1	52.0
	150	1.38	1.52	0.49	61.8	5.2	6.0

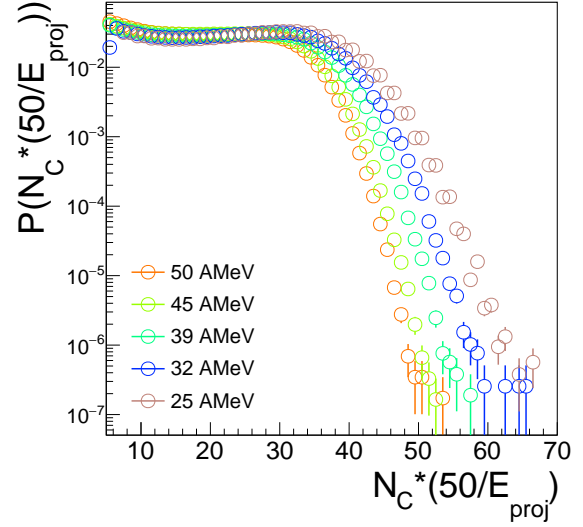
Table B.1 – Parameters of fits to total charged particle multiplicity distributions $P(N_C)$ for all datasets. See 6.2.2 for meaning of parameters. χ^2 is the reduced chi-square value of each fit.

System	E_{proj} [MeV/A]	α	γ	θ [MeV]	X_{max} [MeV]	X_{min} [MeV]	χ^2
$^{36}\text{Ar}+^{39}\text{KCl}$	32	0.35	0.76	6.1	162	3	1.2
	40	0.37	0.89	7.5	196	8	1.0
	52	0.35	1.02	8.5	269	12	1.2
	74	0.40	1.32	11.8	389	19	3.7
$^{36}\text{Ar}+^{58}\text{Ni}$	32	0.97	1.17	8.5	148	9	3.3
	40	0.83	1.17	10.0	183	11	2.5
	52	0.68	1.26	12.0	251	15	2.3
	63	0.60	1.35	13.1	328	18	1.3
	74	0.60	1.46	14.9	402	30	1.8
	84	0.60	1.52	16.1	463	32	1.7
	95	0.62	1.63	18.6	528	35	2.1
$^{58}\text{Ni}+^{58}\text{Ni}$	32	0.79	1.04	9.9	186	21	1.6
	52	0.56	1.15	13.0	340	29	2.3
	64	0.55	1.30	14.9	443	33	1.7
	74	0.52	1.40	16.7	541	37	2.8
	82	0.61	1.68	18.5	591	46	1.7
	90	0.68	1.93	20.9	629	56	1.4
$^{58}\text{Ni}+^{197}\text{Au}$	32	1.41	1.71	12.8	223	32	6.7
	52	1.08	1.45	17.2	391	36	6.1
	64	0.93	1.50	18.8	521	39	3.8
	74	0.92	1.63	21.6	630	44	4.8
	82	0.92	1.74	23.3	716	48	5.8
	90	0.74	1.68	21.8	838	49	5.0
$^{129}\text{Xe}+^{119}\text{Sn}$	25	0.74	0.68	11.1	241	6	2.2
	32	0.67	0.69	12.4	310	5	1.7
	39	0.57	0.75	13.9	408	7	2.9
	45	0.55	0.89	15.4	496	24	1.6
	50	0.57	1.06	16.0	584	34	1.3
$^{129}\text{Xe}+^{124}\text{Sn}$	65	0.59	1.32	19.9	822	34	1.5
	80	0.61	1.52	23.5	1071	41	2.0
	100	0.62	1.65	26.8	1374	44	3.6
$^{197}\text{Au}+^{197}\text{Au}$	40	1.07	1.23	24.0	521	18	24.4
	60	0.67	1.38	25.5	1089	5	24.6
	80	0.62	1.47	26.6	1648	31	3.0
	100	0.65	1.68	34.6	2054	55	4.4
	150	0.66	1.67	46.1	2831	91	2.2

Table B.2 – Results of fits to total transverse LCP energy distributions $P(E_{t12})$ for all datasets. See 6.2.2 for meaning of parameters. χ^2 is the reduced chi-square value of each fit.



(a) Evolution with available centre of mass energy per nucleon E_{CM}/A_{tot} of θ and $\overline{E}_{t12}(b=0)/50$ for $^{129}\text{Xe}+^{nat}\text{Sn}$ collisions from 25 to 50 A MeV bombarding energy.



(b) “Scaled” total multiplicity $N_C * (50/E_{proj})$ distributions for $^{129}\text{Xe}+^{nat}\text{Sn}$ collisions.

Figure B.4.1 – Scaling properties of E_{t12} and N_C variables.

parameter, in the light of the new results presented in Chapter 6. For example, the fact that $P(E_{t12})$ distributions “scale” with bombarding energy has long been presented as evidence that E_{t12} is mostly determined by the geometry of the collisions and therefore strongly correlated with impact parameter [75, 208]. By “scaling” here we mean that the probability distributions of two variables related by a linear scaling transformation, X and $Y = \gamma X$, are simply related by

$$P_Y(Y = \gamma X) = \frac{1}{\gamma} P_X(X)$$

so that the distribution of Y/γ is identical to that of X . This was demonstrated for E_{t12} for $^{129}\text{Xe}+^{nat}\text{Sn}$ collisions using $\gamma = E_{proj}/50$ in [75]¹, or, equivalently for these quasi-symmetric collisions, using $\gamma = E_{CM}$ in [208]². However, given the changes in the shape of the distributions of both N_C and E_{t12} which are clearly evident in Figure 6.3.1, such a “scaling” can only be approximate at best (in reality only the tails of the distributions superimpose well - see Figure 1 of [208]). As shown in 6.3.2, the changing shape of the $P(X)$ distributions is entirely determined by the changing shape of the $k(c_b)$ relationship of Equation (6.2.23) which basically encodes

¹Strictly speaking, in [75] the “scaling” was demonstrated by comparing the relationship between b and the scaled E_{t12} deduced using the method of [74] for bombarding energies 25 – 50 A MeV. As the shape of this relationship is basically given by the square root of the cumulative distribution function of $P(E_{t12})$, and the value of E_{t12} for any given b is given by the corresponding quantile function, this is equivalent to comparing the shapes of the $P(E_{t12})$ distributions.

²The data used in [208] correspond to the minimum bias $M \geq 1$ trigger, not the $M \geq 4$ trigger used in the present work. Although the “scaling” of the distributions presented using a logarithmic y -axis in Figure 1 of [208] appears near-perfect, the same data with a linear axis present similar differences as the distributions in Figure 6.3.1.

the physics of the collisions for any given observable. Therefore an exact scaling of the inclusive distributions would mean that, apart from scale factors such as the total available energy or the total number of nucleons, the physics of the collisions (for a given observable) would basically have to be the same for all bombarding energies.

Now let us consider the scaling properties of the gamma distribution used in $P(X|b)$. Replacing X by Y/γ in Equation (6.2.20) we find

$$\begin{aligned} P_{\theta}(Y/\gamma|c_b) &= \frac{1}{\Gamma(k)\theta^k} \frac{Y^{k-1}}{\gamma^{k-1}} e^{-Y/\gamma\theta} \\ &= \gamma \frac{1}{\Gamma(k)\vartheta^k} Y^{k-1} e^{-Y/\vartheta} = \gamma P_{\vartheta}(Y|c_b) \end{aligned} \quad (\text{B.4.1})$$

which is just the gamma distribution for a variable $Y = \gamma X$ with fluctuation parameter $\vartheta = \gamma\theta$. Hence the necessary conditions to observe scaling for distributions given by Equation (6.2.14), *i.e.* for observables which are effectively correlated with impact parameter, is not only that k *i.e.* the physics of the collisions, does not change, but also that the relative importance of the fluctuations of the observable scale in the same way as the observable itself.

As figure Figure B.4.1a shows for E_{t12} , both the mean value for the most central collisions and the fluctuation parameter θ increase approximately linearly with available (or bombarding) energy for $^{129}\text{Xe} + ^{nat}\text{Sn}$ reactions, and approximately in the same way. It is therefore to be expected that, although the overall distributions of E_{t12} do not exhibit strict scaling behaviour, nevertheless the tails of the distributions superimpose to a rather good degree, as these are dominated by the fluctuations around the values of the observable for $b = 0$ collisions. On the other hand, as shown in Figure 6.3.5a(left), the mean values of N_C for head-on collisions do not increase linearly with bombarding energy, and in addition the θ parameters for fits to N_C distributions are independent of bombarding energy for all systems listed in Table B.1. It then comes as no surprise that when trying to apply the same scaling to this observable as was done for E_{t12} in [75], not even the tails of the scaled distributions superimpose (Figure B.4.1b).

In conclusion, the correlation of observables such as N_C and E_{t12} with impact parameter is not in doubt, as demonstrated by the fact that their inclusive distributions can be well-reproduced in a self-consistent manner by supposing they have a monotonic relationship with b (including fluctuations) and integrating over all centralities. The “scaling” of their distributions (at least for E_{t12}) which was claimed in order to prove this correlation in previous works does not in fact exist, apart from an approximate scaling of the distribution tails which itself reveals something non-trivial about the way in which the fluctuations of the observable depend on bombarding energy. In general, observables which are strongly correlated with impact parameter should not exhibit scaling of their distributions with bombarding or available energy, unless their relationship with b is so trivial that it contains no information on the physics of the reactions.

Appendix C

Simulation of isotropic and anisotropic momentum distributions

To test the response of the different shape variables used in [Chapter 7](#) to momentum distributions of varying anisotropy and multiplicity, and to try to deduce the actual form of the distributions for the selected ISOMAX events, required a toy model in order to generate simulated events. This was done by drawing random kinetic energy “vectors” within an ellipsoidal volume in kinetic energy “space” according to a constant “density”. In other words, for a given multiplicity, N , and required elongation ratio a/b (where a is the radius of the major axis and b is the radius of the two transverse directions of the ellipsoid), for each product nucleus we draw values at random for the kinetic energy according to

$$P(E)dE \sim E^2dE$$

and for the polar angle (with respect to the ellipsoid major axis) according to

$$P(\theta)d\theta \sim \sin \theta d\theta$$

The kinetic energy is then checked against the maximum energy for a given polar angle (the distance of the surface of the ellipsoid from the origin)

$$E_{max} = E_0 \frac{ab}{\sqrt{a^2 \cos^2 \theta + b^2 \sin^2 \theta}}$$

If $E > E_{max}$ the draw is rejected and new values of E and θ drawn until a satisfactory value is found (*i.e.* a vector corresponding to a point inside the ellipsoid). For a successful draw the azimuthal angle for the particle is drawn uniformly between 0 and 2π .

After N particles have been successfully generated in this way, their momenta are recalculated so that they are in their centre of mass frame. The particles of each event are used to fill a super-tensor like in Equation (7.2.1) in order to calculate the “true” shape of the kinetic energy tensor without finite multiplicity distortions. The ratios used to characterise the different simulated anisotropies in momentum space in [Chapter 7](#) are then given by the square root of the ratio of the two largest eigenvectors of this tensor calculated with all events.

It has been verified that this method gives the same results for the mean values of the different shape variables as a function of multiplicity whether we draw a random partition (*i.e.* random value of Z for each nucleus) or use the same Z for all nuclei of each event: the results are therefore independent of the partitions, and do not require for example to use the real partitions of the experimental events in order to make a meaningful comparison (although that would be perfectly possible if necessary).

Bibliography

- [1] B. Borderie and J. D. Frankland, Liquid-Gas phase transition in nuclei, [Progress in Particle and Nuclear Physics](#) **105**, 82 (2019).
- [2] New Order, “Blue Monday”, [Factory Records FAC 73](#) (1983).
- [3] J. M. Lattimer and M. Prakash, Nuclear matter and its role in supernovae, neutron stars and compact object binary mergers, [Physics Reports](#) **333-334**, 121 (2000).
- [4] A. Raduta, F. Aymard, and F. Gulminelli, Clusterized nuclear matter in the (proto-)neutron star crust and the symmetry energy, [The European Physical Journal A](#) **50**, 1 (2014).
- [5] J. Margueron, R. Hoffmann Casali, and F. Gulminelli, Equation of state for dense nucleonic matter from metamodeling. II. Predictions for neutron star properties, [Physical Review C](#) **97**, 025806 (2018).
- [6] A. Chbihi, L. Manduci, J. Moisan, E. Bonnet, J. D. Frankland, R. Roy, and G. Verde, in [Journal of Physics: Conference Series](#), Vol. 420 (2013).
- [7] D. Gruyer, J. D. Frankland, E. Bonnet, A. Chbihi, G. Ademard, M. Boisjoli, B. Borderie, R. Bougault, E. Galichet, J. Gauthier, et al., Coulomb chronometry to probe the decay mechanism of hot nuclei, [Physical Review C](#) **92**, 064606 (2015).
- [8] J. D. Frankland, D. Gruyer, E. Bonnet, and A. Chbihi, Reaction mechanisms leading to 3-body exit channels in central collisions of $^{129}\text{Xe}+^{nat}\text{Sn}$ at 12 MeV/u, [Il Nuovo Cimento](#) **39 C**, 382+ (2016).
- [9] J. Pouthas, B. Borderie, R. Dayras, E. Plagnol, M. Rivet, F. Saint-Laurent, J. Steckmeyer, G. Auger, C. Bacri, S. Barbey, et al., INDRA, a 4π charged product detection array at GANIL, [Nuclear Instruments and Methods in Physics Research Section A: Accelerators, Spectrometers, Detectors and Associated Equipment](#) **357**, 418 (1995).
- [10] J. Pouthas, A. Bertaut, B. Borderie, P. Bourgault, B. Cahan, G. Carles, D. Charlet, D. Cussol, R. Dayras, M. Engrand, et al., The electronics of the INDRA 4π detection array, [Nuclear Instruments and Methods in Physics Research Section A: Accelerators, Spectrometers, Detectors and Associated Equipment](#) **369**, 222 (1996).
- [11] M. Fallot, J. A. Scarpaci, N. Frascaria, Y. Blumenfeld, A. Chbihi, P. Chomaz, P. Désesquelles, J. Frankland, E. Khan, J. L. Laville, et al., Evidence for a three-phonon giant resonance state in Ca40 nuclei, [Physical Review Letters](#) **97**, 10.1103/PhysRevLett.97.242502 (2006).

- [12] M. Morjean, D. Jacquet, J. L. Charvet, A. L'Hoir, M. Laget, M. Parlog, A. Chbihi, M. Chevallier, C. Cohen, D. Dauvergne, et al., Fission time measurements: A new probe into superheavy element stability, *Physical Review Letters* **101**, 10.1103/PhysRevLett.101.072701 (2008).
- [13] R. Brun and F. Rademakers, ROOT: An object oriented data analysis framework, *Nuclear Instruments and Methods in Physics Research Section A: Accelerators, Spectrometers, Detectors and Associated Equipment* **389**, 81 (1997).
- [14] ROOT Data Analysis Framework, <https://root.cern> .
- [15] KaliVeda Heavy-Ion Analysis Toolkit, <http://indra.in2p3.fr/kaliveda> .
- [16] R. Bougault, G. Poggi, S. Barlini, B. Borderie, G. Casini, A. Chbihi, N. Le Neindre, M. Pârlog, G. Pasquali, S. Piantelli, et al., The FAZIA project in Europe: R&D phase, *European Physical Journal A* **50**, 1 (2014).
- [17] S. Valdré, G. Casini, N. Le Neindre, M. Bini, A. Boiano, B. Borderie, P. Edelbruck, G. Poggi, F. Salomon, G. Tortone, et al., The FAZIA setup: A review on the electronics and the mechanical mounting, *Nuclear Instruments and Methods in Physics Research Section A: Accelerators, Spectrometers, Detectors and Associated Equipment* **930**, 27 (2019).
- [18] S. Piantelli, G. Casini, A. Ono, G. Poggi, G. Pastore, S. Barlini, A. Boiano, E. Bonnet, B. Borderie, R. Bougault, et al., Dynamical fission of the quasiprojectile and isospin equilibration for the system Kr 80 + Ca 48 at 35 MeV/nucleon, *Physical Review C* **101**, 034613 (2020).
- [19] A. B. McIntosh and S. J. Yennello, Interplay of neutron-proton equilibration and nuclear dynamics, *Progress in Particle and Nuclear Physics* **108**, 103707 (2019).
- [20] P. Chomaz, M. Colonna, and J. Randrup, Nuclear spinodal fragmentation, *Physics Reports* **389**, 263 (2004).
- [21] G. Sauer, H. Chandra, and U. Mosel, Thermal properties of nuclei, *Nuclear Physics A* **264**, 221 (1976).
- [22] G. Bertsch and P. J. Siemens, Nuclear fragmentation, *Physics Letters B* **126**, 9 (1983).
- [23] J. Margueron, R. Hoffmann Casali, and F. Gulminelli, Equation of state for dense nucleonic matter from metamodeling. I. Foundational aspects, *Physical Review C* **97**, 025805 (2018).
- [24] S. Typel, G. Röpke, T. Klähn, D. Blaschke, and H. H. Wolter, Composition and thermodynamics of nuclear matter with light clusters, *Physical Review C* **81**, 015803+ (2010).
- [25] G. Röpke, Nuclear matter equation of state including two-, three-, and four-nucleon correlations, *Physical Review C* **92**, 054001 (2015).
- [26] H. Pais, F. Gulminelli, C. Providência, and G. Röpke, Full distribution of clusters with universal couplings and in-medium effects, *Physical Review C* **99**, 55806 (2019).

- [27] G. Westfall, J. Yurkon, J. Van Der Plicht, Z. Koenig, B. Jacak, R. Fox, G. Crawley, M. Maier, B. Hasselquist, R. Tickle, et al., A logarithmic detection system suitable for a 4π array, *Nuclear Instruments and Methods in Physics Research Section A: Accelerators, Spectrometers, Detectors and Associated Equipment* **238**, 347 (1985).
- [28] R. T. De Souza, N. Carlin, Y. D. Kim, J. Ottarson, L. Phair, D. R. Bowman, C. K. Gelbke, W. G. Gong, W. G. Lynch, R. A. Pelak, et al., The MSU Miniball 4π fragment detection array, *Nuclear Inst. and Methods in Physics Research, A* **295**, 109 (1990).
- [29] G. Bizard, A. Drouet, F. Lefebvres, J. Patry, B. Tamain, F. Guilbault, and C. Lebrun, A plastic multidetector for light nuclei identification at GANIL, *Nuclear Instruments and Methods in Physics Research Section A: Accelerators, Spectrometers, Detectors and Associated Equipment* **244**, 483 (1986).
- [30] R. Bougault, J. Duchon, J. Gautier, A. Genoux-Lubain, C. Le Brun, J. Lecolley, F. Lefebvres, M. Louvel, P. Mosrin, and R. Regimbart, DELF, a large solid angle detection system for heavy fragments, *Nuclear Instruments and Methods in Physics Research Section A: Accelerators, Spectrometers, Detectors and Associated Equipment* **259**, 473 (1987).
- [31] J. Péter, D. Cussol, G. Bizard, R. Brou, M. Louvel, J. Patry, R. Regimbart, J. Steckmeyer, J. Sullivan, B. Tamain, et al., Global variables and impact parameter determination in nucleus-nucleus collisions below 100 MeV/u, *Nuclear Physics A* **519**, 611 (1990).
- [32] L. Phair, D. Bowman, C. Gelbke, W. Gong, Y. Kim, M. Lisa, W. Lynch, G. Peaslee, R. de Souza, M. Tsang, et al., Impact-parameter filters for $^{36}\text{Ar}+^{197}\text{Au}$ collisions at, *Nuclear Physics A* **548**, 489 (1992).
- [33] L. Phair, D. R. Bowman, N. Carlin, C. K. Gelbke, W. G. Gong, Y. D. Kim, M. A. Lisa, W. G. Lynch, G. F. Peaslee, R. T. de Souza, et al., Azimuthal correlations as a test for centrality in heavy-ion collisions, *Nuclear Physics A* **564**, 453 (1993).
- [34] J. D. Frankland, *Study of very heavy systems observed with INDRA: first evidence for a bulk effect in the nuclear multifragmentation process*, Ph.D. thesis, Université Paris Sud - Paris XI (1998).
- [35] J. D. Frankland, C. O. Bacri, B. Borderie, M. F. Rivet, and M. Squalli, Multifragmentation of a very heavy nuclear system (I): Selection of single-source events, *Nuclear Physics A* **689**, 905 (2000).
- [36] P. Danielewicz and M. Gyulassy, Jacobian free global event analysis, *Physics Letters B* **129**, 283 (1983).
- [37] J. Bondorf, C. Dasso, R. Donangelo, and G. Pollarolo, Finiteness effects in the analysis of multifragmentation events in the sphericity-coplanarity plane, *Physics Letters B* **240**, 28 (1990).
- [38] M. Gyulassy, K. A. Frankel, and H. Stöcker, Do nuclei flow at high energies?, *Physics Letters B* **110**, 185 (1982).

- [39] J. Cugnon and D. L'Hôte, Global variables and the dynamics of relativistic nucleus-nucleus collisions, *Nuclear Physics A* **397**, 519 (1983).
- [40] J. F. Lecomte, D. Durand, M. Aboufirassi, R. Bougault, J. Colin, A. Genoux-Lubain, C. Le Brun, O. Lopez, M. Louvel, C. Meslin, et al., Reaction mechanism in highly fragmented Pb + Au collisions at 29 MeV/u, *Physics Letters B* **387**, 460 (1996).
- [41] J. Wilczyński, Nuclear molecules and nuclear friction, *Physics Letters B* **47**, 484 (1973).
- [42] N. Marie, R. Laforest, R. Bougault, J. Wieleczko, D. Durand, C. Bacri, J. Lecomte, F. Saint-Laurent, G. Auger, J. Benlliure, et al., A hot expanding source in 50 A MeV Xe + Sn central reactions, *Physics Letters B* **391**, 15 (1997).
- [43] M. Rivet, C. Bacri, B. Borderie, J. D. Frankland, M. Assenard, G. Auger, F. Bocage, R. Bougault, R. Brou, P. Buchet, et al., Independence of fragment charge distributions of the size of heavy multifragmenting sources, *Physics Letters B* **430**, 217 (1998).
- [44] J. D. Frankland, B. Borderie, M. Colonna, M. Rivet, C. Bacri, P. Chomaz, D. Durand, A. Guarnera, M. Pârlog, M. Squalli, et al., Multifragmentation of a very heavy nuclear system (II): bulk properties and spinodal decomposition, *Nuclear Physics A* **689**, 940 (2001).
- [45] G. Tabacaru, M. Rivet, B. Borderie, M. Pârlog, B. Bouriquet, A. Chbihi, J. D. Frankland, J. Wieleczko, E. Bonnet, R. Bougault, et al., Multifragmentation of very heavy nuclear systems (III): Fragment velocity correlations and event topology at freeze-out, *Nuclear Physics A* **764**, 371 (2006).
- [46] E. Bonnet, B. Borderie, N. Le Neindre, M. Rivet, R. Bougault, A. Chbihi, R. Dayras, J. D. Frankland, E. Galichet, F. Gagnon-Moisan, et al., Fragment properties of fragmenting heavy nuclei produced in central and semi-peripheral collisions, *Nuclear Physics A* **816**, 1 (2009).
- [47] B. Borderie, N. Le Neindre, M. Rivet, P. Désesquelles, E. Bonnet, R. Bougault, A. Chbihi, D. Dell'Aquila, Q. Fable, J. D. Frankland, et al., Phase transition dynamics for hot nuclei, *Physics Letters B* **782**, 291 (2018).
- [48] M. D'Agostino, R. Bougault, F. Gulminelli, M. Bruno, F. Cannata, P. Chomaz, F. Gramegna, I. Iori, N. Le Neindre, G. Margagliotti, et al., On the reliability of negative heat capacity measurements, *Nuclear Physics A* **699**, 795 (2002).
- [49] N. Le Neindre, E. Bonnet, J. Wieleczko, B. Borderie, F. Gulminelli, M. Rivet, R. Bougault, A. Chbihi, R. Dayras, J. D. Frankland, et al., Yield scaling, size hierarchy and fluctuations of observables in fragmentation of excited heavy nuclei, *Nuclear Physics A* **795**, 47 (2007).
- [50] B. Borderie, S. Piantelli, E. Bonnet, R. Bougault, A. Chbihi, J. E. Ducret, J. D. Frankland, E. Galichet, D. Gruyer, M. Henri, et al., Negative heat capacity for hot nuclei using formulation from the microcanonical ensemble, *The European Physical Journal A* **56**, 101 (2020).

- [51] B. Borderie, S. Piantelli, M. F. Rivet, A. R. Raduta, G. Ademard, E. Bonnet, R. Bougault, A. Chbihi, J. D. Frankland, E. Galichet, et al., Constrained caloric curves and phase transition for hot nuclei, *Physics Letters, Section B: Nuclear, Elementary Particle and High-Energy Physics* **723**, 140 (2013).
- [52] E. Bonnet, M. Colonna, A. Chbihi, J. D. Frankland, D. Gruyer, and J. P. Wieleczko, Investigation of collective radial expansion and stopping in heavy ion collisions at Fermi energies, *Physical Review C* **89**, 034608 (2014).
- [53] M. Colonna, P. Chomaz, and A. Guarnera, Study of multifragmentation patterns induced by spinodal instabilities, *Nuclear Physics A* **613**, 165 (1997).
- [54] B. Jacquot, M. Colonna, S. Ayik, and P. Chomaz, RPA instabilities in finite nuclei at low density, *Nucl. Phys. A* **617**, 356 (1997).
- [55] L. G. Moretto, T. Rubehn, L. Phair, N. Colonna, G. J. Wozniak, D. R. Bowman, G. F. Peaslee, N. Carlin, R. T. de Souza, C. K. Gelbke, et al., Charge correlations and dynamical instabilities in the multifragment emission process, *Phys. Rev. Lett.* **77**, 2634 (1996).
- [56] P. Chomaz, M. Colonna, A. Guarnera, and J. Randrup, Brownian One-Body Dynamics in Nuclei, *Physical Review Letters* **73**, 3512 (1994).
- [57] S. Ayik, E. Suraud, M. Belkacem, and D. Boilley, The Boltzmann-Langevin model for nuclear collisions, *Nuclear Physics A* **545**, 35 (1992).
- [58] A. Bonasera, F. Gulminelli, and J. Molitoris, The Boltzmann equation at the borderline. A decade of Monte Carlo simulations of a quantum kinetic equation, *Physics Reports* **243**, 1 (1994).
- [59] A. Guarnera, P. Chomaz, M. Colonna, and J. Randrup, Multifragmentation with Brownian one-body dynamics, *Physics Letters B* **403**, 191 (1997).
- [60] D. Durand, An event generator for the study of nuclear collisions in the Fermi energy domain (I). Formalism and first applications, *Nuclear Physics A* **541**, 266 (1992).
- [61] F. G. Moisan, E. Galichet, M.-F. F. Rivet, B. Borderie, M. Colonna, R. Roy, G. Ademard, M. Boisjoli, E. Bonnet, R. Bougault, et al., New isospin effects in central heavy-ion collisions at Fermi energies, *Physical Review C - Nuclear Physics* **86**, 044617+ (2012).
- [62] P. Napolitani and M. Colonna, Bifurcations in Boltzmann-Langevin one body dynamics for fermionic systems, *Physics Letters B* **726**, 382 (2013).
- [63] H. Jaqaman, A. Mekjian, and L. Zamick, Nuclear condensation, *Physical Review C* **27**, 2782 (1983).
- [64] H. Jaqaman, A. Mekjian, and L. Zamick, Liquid-gas phase transitions in finite nuclear matter, *Physical Review C* **29**, 2067 (1984).

- [65] J. Aichelin, "Quantum" molecular dynamics—a dynamical microscopic n -body approach to investigate fragment formation and the nuclear equation of state in heavy ion collisions, *Physics Reports* **202**, 233 (1991).
- [66] R. Kumar and R. K. Puri, Using experimental data to test an n -body dynamical model coupled with an energy-based clusterization algorithm at low incident energies, *Physical Review C* **97**, 034624 (2018).
- [67] S. Hudan, A. Chbihi, J. D. Frankland, A. Mignon, J. P. Wieleczko, G. Auger, N. Bellaize, B. Borderie, A. Botvina, R. Bougault, et al., Characteristics of the fragments produced in central collisions of $^{129}\text{Xe}+\text{natSn}$ from 32A to 50A MeV, *Physical Review C* **67**, 064613 (2003).
- [68] A. Ono, S. Hudan, A. Chbihi, and J. D. Frankland, Compatibility of localized wave packets and unrestricted single particle dynamics for cluster formation in nuclear collisions, *Physical Review C - Nuclear Physics* **66**, 146031 (2002).
- [69] S. Hudan, *Experimental and theoretical study of the fragment production in the Xe+Sn collisions from 25 to 150 A.MeV*, Ph.D. thesis, Université de Caen (2001).
- [70] S. Piantelli, N. Le Neindre, E. Bonnet, B. Borderie, G. Lanzalone, M. Parlog, M. Rivet, R. Bougault, A. Chbihi, R. Dayras, et al., Estimate of average freeze-out volume in multifragmentation events, *Physics Letters B* **627**, 18 (2005).
- [71] S. Piantelli, B. Borderie, E. Bonnet, N. Le Neindre, A. Raduta, M. Rivet, R. Bougault, A. Chbihi, R. Dayras, J. D. Frankland, et al., Freeze-out properties of multifragmentation events, *Nuclear Physics A* **809**, 111 (2008).
- [72] S. E. Koonin and J. Randrup, Microcanonical simulation of nuclear disassembly, *Nuclear Physics A* **474**, 173 (1987).
- [73] A. R. Raduta, E. Bonnet, B. Borderie, N. L. Neindre, and M. F. Rivet, Break-up fragments excitation and the freeze-out volume, *Physical Review C* **72**, 057603 (2005).
- [74] C. Cavata, M. Demoulin, J. Gosset, M.-C. Lemaire, D. L'Hôte, J. Poitou, and O. Valette, Determination of the impact parameter in relativistic nucleus-nucleus collisions, *Physical Review C* **42**, 1760 (1990).
- [75] E. Plagnol, J. Łukasik, G. Auger, C. O. Bacri, N. Bellaize, F. Bocage, B. Borderie, R. Bougault, R. Brou, P. Buchet, et al., Onset of midvelocity emissions in symmetric heavy ion reactions, *Physical Review C* **61**, 014606 (1999).
- [76] J. D. Frankland, A. Chbihi, S. Hudan, A. Mignon, and A. Ono, in *XLth Int. Wint. Meet. on Nuclear Physics, Bormio (Italy)* (2002) [arXiv:0202026 \[nucl-ex\]](https://arxiv.org/abs/0202026) .
- [77] M. Colonna, A. Ono, and J. Rizzo, Fragmentation paths in dynamical models, *Physical Review C* **82**, 054613+ (2010).

- [78] R. Botet and M. Płoszajczak, Universal features of the order-parameter fluctuations : reversible and irreversible aggregation, *Physical Review E* **62**, 1825 (2000).
- [79] R. Botet, M. Płoszajczak, A. Chbihi, B. Borderie, D. Durand, and J. Frankland, Universal fluctuations in heavy-ion collisions in the Fermi energy domain, *Physical Review Letters* **86**, 3514 (2001).
- [80] J. E. Finn, S. Agarwal, A. Bujak, J. Chuang, L. J. Gutay, A. S. Hirsch, R. W. Minich, N. T. Porile, R. P. Scharenberg, B. C. Stringfellow, et al., Nuclear Fragment Mass Yields from High-Energy Proton-Nucleus Interactions, *Physical Review Letters* **49**, 1321 (1982).
- [81] J. Aichelin and J. Huefner, Fragmentation reactions on nuclei: Condensation of vapour or shattering of glass?, *Physics Letters B* **136**, 15 (1984).
- [82] J. D. Frankland, A. Chbihi, A. Mignon, M. L. Begemann-Blaich, R. Bittiger, B. Borderie, R. Bougault, J.-L. Charvet, D. Cussol, R. Dayras, et al., Model-independent tracking of criticality signals in nuclear multifragmentation data, *Physical Review C* **71**, 034607 (2005).
- [83] E. J. Gumbel, *Statistics of Extremes* (Columbia University Press, New York, 1958).
- [84] F. Gulminelli and P. Chomaz, Critical Behavior in the Coexistence Region of Finite Systems, *Physical Review Letters* **82**, 1402 (1999).
- [85] M. L. Gilkes, S. Albergo, F. Bieser, F. P. Brady, Z. Caccia, D. A. Cebra, A. D. Chacon, J. L. Chance, Y. Choi, S. Costa, et al., Determination of Critical Exponents from the Multifragmentation of Gold Nuclei, *Physical Review Letters* **73**, 1590 (1994).
- [86] W. Bauer, G. F. Bertsch, and S. Das Gupta, Fluctuations and clustering in heavy-ion collisions, *Physical Review Letters* **58**, 863 (1987).
- [87] E. Suraud, D. Cussol, C. Grégoire, D. Boilley, M. Pi, P. Schuck, B. Remaud, and F. Sébille, Explosions in Landau Vlasov dynamics, *Nuclear Physics A* **495**, 73 (1989).
- [88] M. Colonna, N. Colonna, A. Bonasera, and M. DiToro, Equilibrium features and dynamical instabilities in nuclear fragmentation, *Nuclear Physics A* **541**, 295 (1992).
- [89] H. Barz, J. Bondorf, R. Donangelo, R. Elmér, F. Hansen, B. Jakobsson, L. Karlsson, H. Nifenecker, H. Schulz, F. Schussler, et al., Flow effects in intermediate-energy nuclear collisions, *Nuclear Physics A* **531**, 453 (1991).
- [90] W. Bauer, J. P. Bondorf, R. Donangelo, R. Elmér, B. Jakobsson, H. Schulz, F. Schussler, and K. Sneppen, Large radial flow in nucleus-nucleus collisions, *Physical Review C* **47**, R1838 (1993).
- [91] S. C. Jeong, N. Herrmann, Z. G. Fan, R. Freifelder, A. Gobbi, K. D. Hildenbrand, M. Krämer, J. Randrup, W. Reisdorf, D. Schüll, et al., Collective motion in selected central collisions of Au on Au at 150 A MeV, *Physical Review Letters* **72**, 3468 (1994).

- [92] G. J. Kunde, W. C. Hsi, W. D. Kunze, A. Schüttauf, A. Wörner, M. Begemann-Blaich, T. Blaich, D. R. Bowman, R. J. Charity, A. Cosmo, et al., Fragment Flow and the Multifragmentation Phase Space, *Physical Review Letters* **74**, 38 (1995).
- [93] A. H. Raduta and A. R. Raduta, Searching for the statistically equilibrated systems formed in heavy ion collisions, *Physical Review C* **65**, 054610 (2002).
- [94] N. Le Neindre, *Aspect thermodynamique de la multifragmentation Xe + Sn 32 à 50 A.MeV*, *Theses*, Université de Caen (1999).
- [95] L. Beaulieu, T. Lefort, K. Kwiatkowski, W.-c. Hsi, G. Wang, D. S. Bracken, E. Cornell, D. S. Ginger, K. B. Morley, V. E. Viola, et al., Thermal excitation-energy deposition in 5-15 GeV/c hadron-induced reactions with ^{197}Au . II. Relation between excitation energy and reaction variables, *Physical Review C* **64**, 064604 (2001).
- [96] D. Gruyer, *Dynamic aspects of the nuclear decay : from the fission to the multifragmentation*, *Ph.D. thesis*, Université de Caen-Basse Normandie (2014).
- [97] E. Bonnet, B. Borderie, N. Le Neindre, A. R. Raduta, M. F. Rivet, R. Bougault, A. Chbihi, J. D. Frankland, E. Galichet, F. Gagnon-Moisan, et al., New Scalings in Nuclear Fragmentation, *Physical Review Letters* **105**, 142701 (2010).
- [98] N. Bellaize, O. Lopez, J. Wieleczko, D. Cussol, G. Auger, C. Bacri, F. Bocage, B. Borderie, R. Bougault, B. Bouriquet, et al., Multifragmentation process for different mass asymmetry in the entrance channel around the Fermi energy, *Nuclear Physics A* **709**, 367 (2002).
- [99] J. D. Frankland, D. Gruyer, E. Bonnet, and A. Chbihi, in *EPJ Web of Conferences*, Vol. 88 (2015) p. 00009.
- [100] J. Bondorf, A. Botvina, A. Iljinov, I. Mishustin, and K. Sneppen, Statistical multifragmentation of nuclei, *Physics Reports* **257**, 133 (1995).
- [101] A. H. Raduta and A. R. Raduta, Simulation of statistical ensembles suitable for the description of nuclear multifragmentation, *Physical Review C* **55**, 1344 (1997).
- [102] D. Gruyer, J. D. Frankland, R. Botet, M. Płoszajczak, E. Bonnet, A. Chbihi, G. Ademard, M. Boisjoli, B. Borderie, R. Bougault, et al., Nuclear Multifragmentation Time Scale and Fluctuations of the Largest Fragment Size, *Physical Review Letters* **110**, 172701 (2013).
- [103] M. v. Smoluchowski, Versuch einer mathematischen Theorie der Koagulationskinetik kolloider Lösungen (Attempt for a mathematical theory of kinetic coagulation of colloid solutions), *Zeitschrift für Physikalische Chemie* **92**, 129 (1917).
- [104] D. Stauffer and A. Aharony, *Introduction To Percolation Theory* (Taylor & Francis, 1994).
- [105] W. Reisdorf, F. Rami, B. De Schauenburg, Y. Leifels, J. P. Alard, A. Andronic, V. Barret, Z. Basrak, N. Bastid, M. L. Benabderrahmane, et al., Droplet formation in expanding nuclear matter: A system-size dependent study, *Physics Letters, Section B: Nuclear, Elementary Particle and High-Energy Physics* **595**, 118 (2004).

- [106] G. Lehaut, D. Durand, O. Lopez, E. Vient, A. Chbihi, J. D. Frankland, E. Bonnet, B. Borderie, R. Bougault, E. Galichet, et al., Study of Nuclear Stopping in Central Collisions at Intermediate Energies, *Physical Review Letters* **104**, 232701 (2010).
- [107] O. Lopez, D. Durand, G. Lehaut, B. Borderie, J. D. Frankland, M. F. Rivet, R. Bougault, A. Chbihi, E. Galichet, D. Guinet, et al., In-medium effects for nuclear matter in the Fermi-energy domain, *Physical Review C* **90**, 064602 (2014).
- [108] D. H. E. Gross, Microcanonical thermodynamics and statistical fragmentation of dissipative systems. The topological structure of the N-body phase space, *Physics Reports* **279**, 119 (1997).
- [109] P. Chomaz, V. Duflot, and F. Gulminelli, Caloric Curves and Energy Fluctuations in the Microcanonical {Liquid-Gas} Phase Transition, *Physical Review Letters* **85**, 3587 (2000).
- [110] P. Chomaz, F. Gulminelli, and V. Duflot, Topology of event distributions as a generalized definition of phase transitions in finite systems, *Physical Review E* **64**, 046114+ (2001).
- [111] E. Bonnet, D. Mercier, B. Borderie, F. Gulminelli, M. F. Rivet, B. Tamain, R. Bougault, A. Chbihi, R. Dayras, J. D. D. Frankland, et al., Bimodal behavior of the heaviest fragment distribution in projectile fragmentation, *Physical Review Letters* **103**, 072701+ (2009).
- [112] B. B. Back, H. Esbensen, C. L. Jiang, and K. E. Rehm, Recent developments in heavy-ion fusion reactions, *Reviews of Modern Physics* **86**, 317 (2014).
- [113] J. Austen, *Pride and Prejudice*, "It is a truth universally acknowledged, that a single man in possession of a good fortune must be in want of a wife." (T. Egerton, Whitehall (England), 1813).
- [114] J. P. Bondorf, M. I. Sobel, and D. Sperber, Classical dynamical theory of heavy ion fusion and scattering, *Physics Reports* **15**, 83 (1974).
- [115] J. Błocki, J. Randrup, W. J. Świąłstecki, and C. F. Tsang, Proximity forces, *Annals of Physics* **105**, 427 (1977).
- [116] G. G. Adamian, N. V. Antonenko, and W. Scheid, Model of competition between fusion and quasifission in reactions with heavy nuclei, *Nuclear Physics A* **618**, 176 (1997).
- [117] G. G. Adamian, N. V. Antonenko, W. Scheid, and V. V. Volkov, Treatment of competition between complete fusion and quasifission in collisions of heavy nuclei, *Nuclear Physics A* **627**, 361 (1997).
- [118] M. G. Itkis, Y. Oganessian, and V. I. Zagrebaev, Fission barriers of superheavy nuclei, *Physical Review C* **65**, 044602+ (2002).
- [119] M. Kowal, P. Jachimowicz, and A. Sobczewski, Fission barriers for even-even superheavy nuclei, *Physical Review C* **82**, 014303+ (2010).
- [120] M. Lefort, Nuclear fusion between heavy ions, *Reports on Progress in Physics* **39**, 129 (1976).

- [121] J. Toke, R. Bock, G. X. Dai, A. Gobbi, S. Gralla, K. D. Hildenbrand, J. Kuzminski, W. F. Müller, A. Olmi, H. Stelzer, et al., Quasi-fission - The mass-drift mode in heavy-ion reactions, *Nuclear Physics, Section A* **440**, 327 (1985).
- [122] C. Ngô, Fusion dynamics in heavy ion collisions, *Progress in Particle and Nuclear Physics* **16**, 139 (1986).
- [123] P. Laitesse, L. Nalpas, R. Dayras, M. F. Rivet, M. Pârlog, E. Bisquer, B. Borderie, R. Bougault, P. Buchet, J. L. Charvet, et al., Evolution of the fusion cross-section for light systems at intermediate energies, *The European Physical Journal A* **27**, 349 (2006).
- [124] L. Manduci, O. Lopez, A. Chbihi, M. F. Rivet, R. Bougault, J. D. Frankland, B. Borderie, E. Galichet, M. La Commara, N. Le Neindre, et al., Reaction and fusion cross sections for the near-symmetric system $^{129}\text{Xe} + ^{\text{nat}}\text{Sn}$ from 8A to 35A MeV, *Physical Review C* **94**, 044611 (2016).
- [125] P. Glässel, D. Harrach, H. J. Specht, and L. Grodzins, Observation of proximity- and non-equilibrium effects in ternary heavy ion reactions, *Zeitschrift für Physik A Atoms and Nuclei* **310**, 189 (1983).
- [126] V. E. Viola, K. Kwiatkowski, and M. Walker, Systematics of fission fragment total kinetic energy release, *Physical Review C* **31**, 1550 (1985).
- [127] D. J. Hinde, J. R. Leigh, J. J. M. Bokhorst, J. O. Newton, R. L. Walsh, and J. W. Boldeman, Mass-split dependence of the pre- and post-scission neutron multiplicities for fission of ^{251}Es , *Nuclear Physics A* **472**, 318 (1987).
- [128] G. Bizard, D. Durand, A. Genoux-Lubain, M. Louvel, R. Bougault, R. Brou, H. Dobre, Y. El-Masri, H. Fujiwara, K. Hagel, et al., Three fragment sequential decay of heavy nuclei around 3 MeV/u excitation energy, *Physics Letters B* **276**, 413 (1992).
- [129] A. Jedele, A. B. McIntosh, K. Hagel, M. Huang, L. Heilborn, Z. Kohley, L. W. May, E. McCleskey, M. Youngs, A. Zarrella, et al., Characterizing Neutron-Proton Equilibration in Nuclear Reactions with Subzeptosecond Resolution, *Physical Review Letters* **118**, 062501 (2017).
- [130] E. Williams, K. Sekizawa, D. J. Hinde, C. Simenel, M. Dasgupta, I. P. Carter, K. J. Cook, D. Y. Jeung, S. D. McNeil, C. S. Palshetkar, et al., Exploring Zeptosecond Quantum Equilibration Dynamics: From Deep-Inelastic to Fusion-Fission Outcomes in $\text{Ni}58 + \text{Ni}60$ Reactions, *Physical Review Letters* **120**, 10.1103/physrevlett.120.022501 (2018).
- [131] D. J. Hinde, D. Hilscher, and H. Rossner, Fission timescales of excited nuclei, *Nuclear Physics A* **502**, 497 (1989).
- [132] L. Tassan-Got and C. Stéphan, Deep inelastic transfers, *Nuclear Physics A* **524**, 121 (1991).
- [133] R. J. Charity, Systematic description of evaporation spectra for light and heavy compound nuclei, *Physical Review C* **82**, 014610 (2010).

- [134] D. Mancusi, R. J. Charity, and J. Cugnon, Unified description of fission in fusion and spallation reactions, *Physical Review C* **82**, 044610+ (2010).
- [135] P. Glässel, D. Harrach, L. Grodzins, and H. J. Specht, Direct Observation of Nonequilibrium Effects in Sequential Fission, *Physical Review Letters* **48**, 1089 (1982).
- [136] D. Harrach, P. Glässel, L. Grodzins, S. S. Kapoor, and H. J. Specht, Direct Observation of Proximity Effects in Ternary Heavy-Ion Reactions, *Physical Review Letters* **48**, 1093 (1982).
- [137] L. G. Moretto and R. P. Schmitt, Deep inelastic reactions: a probe of the collective properties of nuclear matter, *Reports on Progress in Physics* **44**, 533 (1981).
- [138] P. Möller, A. J. Sierk, and A. Iwamoto, Five-Dimensional Fission-Barrier Calculations from Se70 to Cf252, *Physical Review Letters* **92**, 072501+ (2004).
- [139] P. N. Nadtochy, E. G. Ryabov, A. E. Gegechkori, Yu, and G. D. Adeev, Four-dimensional Langevin dynamics of heavy-ion-induced fission, *Phys. Rev. C* **85**, 064619+ (2012).
- [140] K. Mazurek, C. Schmitt, P. N. Nadtochy, M. Kmiecik, A. Maj, P. Wasiak, and J. P. Wieleczko, Examining fine potential energy effects in high-energy fission dynamics, *Phys. Rev. C* **88**, 054614+ (2013).
- [141] D. Gruyer, K. Mazurek, J. D. Frankland, E. Bonnet, P. N. Nadtochy, A. Chbihi, and J. P. Wieleczko, *Sequential fission of highly excited compound nuclei in a 4D Langevin approach* (2017).
- [142] T. E. Lawrence, *Seven Pillars of Wisdom*, Classics of World Literature Series (Wordsworth Editions Limited, 1922).
- [143] Bob Dylan, “Stuck Inside of Mobile with the Memphis Blues Again”, *Blonde on Blonde* (1966).
- [144] S. Das Gupta and A. Z. Mekjian, The thermodynamic model for relativistic heavy ion collisions, *Physics Reports* **72**, 131 (1981).
- [145] P. Danielewicz and G. Odyniec, Transverse momentum analysis of collective motion in relativistic nuclear collisions, *Physics Letters B* **157**, 146 (1985).
- [146] S. J. Das, G. Giacalone, P.-A. Monard, and J.-Y. Ollitrault, Relating centrality to impact parameter in nucleus-nucleus collisions, *Physical Review C* **97**, 014905 (2018).
- [147] R. Rogly, G. Giacalone, and J.-Y. Ollitrault, Reconstructing the impact parameter of proton-nucleus and nucleus-nucleus collisions, *Physical Review C* **98**, 024902 (2018).
- [148] R. Nebauer, J. Aichelin, M. Assenard, G. Auger, C. Bacri, F. Bocage, R. Bougault, R. Brou, P. Buchet, J. Charvet, et al., Multifragmentation in Xe(50 AMeV) + Sn: Confrontation of theory and data, *Nuclear Physics A* **658**, 67 (1999).

- [149] K. Zbiri, A. L. Fèvre, J. Aichelin, J. Łukasik, W. Reisdorf, F. Gulminelli, U. Lynen, W. F. J. Müller, H. Orth, C. Schwarz, et al., Transition from participant to spectator fragmentation in Au+Au reactions between 60A and 150A MeV, *Physical Review C* **75**, 034612 (2007).
- [150] A. Le Fèvre, J. Aichelin, C. Hartnack, J. Lukasik, W. F. J. Müller, H. Orth, C. Schwarz, C. Sfienti, W. Trautmann, K. Turzó, et al., Bimodality: A general feature of heavy ion reactions, *Physical Review C - Nuclear Physics* **80**, 044615 (2009).
- [151] V. Métivier, B. Tamain, G. Auger, C. Bacri, J. Benlliure, F. Bocage, B. Borderie, R. Bougault, R. Brou, P. Buchet, et al., Mass scaling of reaction mechanisms in intermediate energy heavy ion collisions, *Nuclear Physics A* **672**, 357 (2000).
- [152] C. Bacri, B. Borderie, J. Charvet, D. Cussol, R. Dayras, O. Lopez, A. Ouatzerga, M. Rivet, G. Auger, A. Benkirane, et al., Onset of vaporization for the Ar+Ni system, *Physics Letters B* **353**, 27 (1995).
- [153] M. Rivet, A. Chbihi, B. Borderie, P. Eudes, M. Parlog, L. Tassan-Got, G. Auger, C. Bacri, J. Benlliure, E. Bisquer, et al., Vaporization events from binary dissipative collisions, *Physics Letters B* **388**, 219 (1996).
- [154] D. Cussol, T. Lefort, J. Péter, G. Auger, C. O. Bacri, F. Bocage, B. Borderie, R. Bougault, R. Brou, P. Buchet, et al., Measurements of sideward flow around the balance energy, *Physical Review C* **65**, 044604 (2002).
- [155] E. Galichet, M. F. Rivet, B. Borderie, M. Colonna, R. Bougault, A. Chbihi, R. Dayras, D. Durand, J. D. Frankland, D. C. R. Guinet, et al., Isospin diffusion in Ni58-induced reactions at intermediate energies. I. Experimental results, *Physical Review C* **79**, 064614+ (2009).
- [156] J. Łukasik, G. Auger, M. Begemann-Blaich, N. Bellaize, R. Bittiger, F. Bocage, B. Borderie, R. Bougault, B. Bouriquet, J. Charvet, et al., Directed and elliptic flow in 197Au + 197Au at intermediate energies, *Physics Letters B* **608**, 223 (2005).
- [157] E. Vient, L. Manduci, E. Legouée, L. Augey, E. Bonnet, B. Borderie, R. Bougault, A. Chbihi, D. Dell'Aquila, Q. Fable, et al., Validation of a new 3D calorimetry of hot nuclei with the HIPSE event generator, *Physical Review C* **98**, 044612 (2018).
- [158] R. Bougault, E. Bonnet, B. Borderie, A. Chbihi, D. Dell'Aquila, Q. Fable, L. Francalanza, J. D. Frankland, E. Galichet, D. Gruyer, et al., Light charged clusters emitted in 32 MeV/nucleon $^{136,124}\text{Xe} + ^{124,112}\text{Sn}$ reactions: Chemical equilibrium and production of ^3He and ^6He , *Physical Review C* **97**, 024612 (2018).
- [159] J. Xu, L.-W. Chen, M. B. Tsang, H. Wolter, Y.-X. Zhang, J. Aichelin, M. Colonna, D. Cozma, P. Danielewicz, Z.-Q. Feng, et al., Understanding transport simulations of heavy-ion collisions at 100A and 400A MeV: Comparison of heavy-ion transport codes under controlled conditions, *Physical Review C* **93**, 044609 (2016).

- [160] Y.-X. Zhang, Y.-J. Wang, M. Colonna, P. Danielewicz, A. Ono, M. B. Tsang, H. Wolter, J. Xu, L.-W. Chen, D. Cozma, et al., Comparison of heavy-ion transport simulations: Collision integral in a box, *Physical Review C* **97**, 034625 (2018).
- [161] G. Q. Zhang, Y. G. Ma, X. G. Cao, C. L. Zhou, X. Z. Cai, D. Q. Fang, W. D. Tian, and H. W. Wang, Unified description of nuclear stopping in central heavy-ion collisions from 10A MeV to 1.2A GeV, *Physical Review C* **84**, 034612 (2011).
- [162] C. Grégoire, B. Remaud, F. Sébille, L. Vinet, and Y. Raffray, Semi-classical dynamics of heavy-ion reactions, *Nuclear Physics A* **465**, 317 (1987).
- [163] G. F. Bertsch and S. Das Gupta, A guide to microscopic models for intermediate energy heavy ion collisions, *Physics Reports* **160**, 189 (1988).
- [164] S. Ayik and C. Grégoire, Transport theory of fluctuation phenomena in nuclear collisions, *Nuclear Physics A* **513**, 187 (1990).
- [165] C. Simenel, Nuclear quantum many-body dynamics, *The European Physical Journal A* **48**, 152 (2012), [arXiv:1209.3375](https://arxiv.org/abs/1209.3375) .
- [166] A. Ono, Dynamics of clusters and fragments in heavy-ion collisions, *Progress in Particle and Nuclear Physics* **105**, 139 (2019).
- [167] O. Buss, T. Gaitanos, K. Gallmeister, H. van Hees, M. Kaskulov, O. Lalakulich, A. B. Larionov, T. Leitner, J. Weil, and U. Mosel, Transport-theoretical description of nuclear reactions, *Physics Reports* **512**, 1 (2012).
- [168] O. Juillet and P. Chomaz, Exact Stochastic Mean-Field Approach to the Fermionic Many-Body Problem, *Physical Review Letters* **88**, 142503 (2002), [arXiv:0104085 \[nucl-th\]](https://arxiv.org/abs/0104085) .
- [169] D. Lacroix, Exact and approximate many-body dynamics with stochastic one-body density matrix evolution, *Physical Review C* **71**, 064322 (2005).
- [170] B. Jouault, F. Sébille, and V. de la Mota, Wavelet representation of the nuclear dynamics, *Nuclear Physics A* **628**, 119 (1998).
- [171] G. Besse, V. de la Mota, E. Bonnet, P. Eudes, P. Napolitani, and Z. Basrak, Reexamining an extended-mean-field approach in heavy-ion collisions near the Fermi energy, *Physical Review C* **101**, 054608 (2020).
- [172] E. A. Uehling and G. E. Uhlenbeck, Transport Phenomena in Einstein-Bose and Fermi-Dirac Gases. I, *Physical Review* **43**, 552 (1933).
- [173] C.-Y. Wong, Dynamics of nuclear fluid. VIII. Time-dependent Hartree-Fock approximation from a classical point of view, *Physical Review C* **25**, 1460 (1982).
- [174] S. Ayik and C. Gregoire, Fluctuations of single-particle density in nuclear collisions, *Physics Letters B* **212**, 269 (1988).

- [175] M. Colonna, M. Di Toro, A. Guarnera, S. Maccarone, M. Zielinska-Pfabé, and H. Wolter, Fluctuations and dynamical instabilities in heavy-ion reactions, *Nuclear Physics A* **642**, 449 (1998).
- [176] M. Colonna, G. Fabbri, M. Di Toro, F. Matera, and H. Wolter, Fragmentation path of excited nuclear systems, *Nuclear Physics A* **742**, 337 (2004).
- [177] H. Lin and P. Danielewicz, One-body Langevin dynamics in heavy-ion collisions at intermediate energies, *Physical Review C* **99**, 1 (2019).
- [178] M. Papa, T. Maruyama, and A. Bonasera, Constrained molecular dynamics approach to fermionic systems, *Physical Review C* **64**, 024612 (2001).
- [179] A. Ono and H. Horiuchi, Antisymmetrized molecular dynamics for heavy ion collisions, *Progress in Particle and Nuclear Physics* **53**, 501 (2004).
- [180] J. Schnack and H. Feldmeier, The nuclear liquid-gas phase transition within fermionic molecular dynamics, *Physics Letters B* **409**, 6 (1997).
- [181] J.-Y. Liu, W.-J. Guo, S.-J. Wang, W. Zuo, Q. Zhao, and Y.-F. Yang, Nuclear Stopping as a Probe for In-Medium Nucleon-Nucleon Cross Sections in Intermediate Energy Heavy Ion Collisions, *Physical Review Letters* **86**, 975 (2001).
- [182] J. Su and F.-S. Zhang, Non-equilibrium and residual memory in momentum space of fragmenting sources in central heavy-ion collisions, *Physical Review C* **87**, 10.1103/physrevc.87.017602 (2013).
- [183] J. Rizzo, M. Colonna, and A. Ono, Comparison of multifragmentation dynamical models, *Physical Review C* **76**, 024611+ (2007).
- [184] R. Machleidt, High-precision, charge-dependent bonn nucleon-nucleon potential, *Phys. Rev. C* **63**, 024001 (2001).
- [185] Z. Li, U. Lombardo, H. J. Schulze, W. Zuo, L. Chen, and H. Ma, Nuclear matter saturation point and symmetry energy with modern nucleon-nucleon potentials, *Physical Review C* **74**, 047304+ (2006).
- [186] E. van Dalen, C. Fuchs, and A. Faessler, The relativistic dirac-brueckner approach to asymmetric nuclear matter, *Nuclear Physics A* **744**, 227 (2004).
- [187] T. Skyrme, The effective nuclear potential, *Nuclear Physics* **9**, 615 (1958).
- [188] D. Vautherin and D. M. Brink, Hartree-Fock Calculations with Skyrme's Interaction. I. Spherical Nuclei, *Physical Review C* **5**, 626 (1972).
- [189] J. R. Stone and P. G. Reinhard, The Skyrme interaction in finite nuclei and nuclear matter, *Progress in Particle and Nuclear Physics* **58**, 587 (2007).

- [190] M. Dutra, O. Lourenço, J. S. Sá Martins, A. Delfino, J. R. Stone, and P. D. Stevenson, Skyrme interaction and nuclear matter constraints, *Physical Review C - Nuclear Physics* **85**, 10.1103/PhysRevC.85.035201 (2012).
- [191] J. Dechargé and D. Gogny, Hartree-Fock-Bogolyubov calculations with the D 1 effective interaction on spherical nuclei, *Physical Review C* **21**, 1568 (1980).
- [192] F. Sebillé, G. Royer, C. Grégoire, B. Remaud, and P. Schuck, Nuclear dynamics with the (finite-range) Gogny force: Flow effects, *Nuclear Physics A* **501**, 137 (1989).
- [193] C. B. Das, S. Das Gupta, C. Gale, and B.-A. Li, Momentum dependence of symmetry potential in asymmetric nuclear matter for transport model calculations, *Physical Review C* **67**, 034611 (2003).
- [194] M. Baldo and G. F. Burgio, The nuclear symmetry energy, *Progress in Particle and Nuclear Physics* **91**, 203 (2016).
- [195] J. Randrup and S. E. Koonin, The disassembly of nuclear matter, *Nuclear Physics A* **356**, 223 (1981).
- [196] D. H. E. Gross, Statistical decay of very hot nuclei-the production of large clusters, *Reports on Progress in Physics* **53**, 605 (1990).
- [197] A. S. Botvina and I. N. Mishustin, Statistical description of nuclear break-up, *European Physical Journal A* **30**, 121 (2006).
- [198] J. Bondorf, R. Donangelo, I. Mishustin, C. Pethick, H. Schulz, and K. Sneppen, Statistical multifragmentation of nuclei, *Nuclear Physics A* **443**, 321 (1985).
- [199] J. Bondorf, R. Donangelo, I. Mishustin, and H. Schulz, Statistical multifragmentation of nuclei, *Nuclear Physics A* **444**, 460 (1985).
- [200] K. Sneppen, Partitioning of a two component particle system and the isotope distribution in nuclear fragmentation, *Nuclear Physics A* **470**, 213 (1987).
- [201] A. S. Botvina, A. D. Jackson, and I. N. Mishustin, Partitioning composite finite systems, *Physical Review E* **62**, R64 (2000).
- [202] A. S. Botvina and I. N. Mishustin, Statistical evolution of isotope composition of nuclear fragments, *Physical Review C* **63**, 061601+ (2001).
- [203] X.-Z. Zhang, D. H. E. Gross, S.-Y. Xu, and Y.-M. Zheng, On the decay of very hot nuclei (I). Canonical metropolis sampling of multifragmentation, *Nuclear Physics A* **461**, 641 (1987).
- [204] X.-Z. Zhang, D. H. E. Gross, S.-Y. Xu, and Y.-M. Zheng, On the decay of very hot nuclei (II). Microcanonical metropolis sampling of multifragmentation, *Nuclear Physics A* **461**, 668 (1987).

- [205] A. Le Fèvre, M. Płoszajczak, and V. D. Toneev, Multifragmentation of nonspherical nuclei, *Physical Review C - Nuclear Physics* **60**, 5 (1999).
- [206] A. Le Fèvre, M. Płoszajczak, V. D. Toneev, G. Auger, M. L. Begemann-Blaich, N. Bellaize, R. Bittiger, F. Bocage, B. Borderie, R. Bougault, et al., Statistical multifragmentation of non-spherical expanding sources in central heavy-ion collisions, *Nuclear Physics A* **735**, 219 (2004).
- [207] J. Randrup and S. E. Koonin, Microcanonical simulation of nuclear multifragmentation, *Nuclear Physics A* **471**, 355 (1987).
- [208] F. Bocage, J. Colin, M. Louvel, G. Auger, C. Bacri, N. Bellaize, B. Borderie, R. Bougault, R. Brou, P. Buchet, et al., Dynamical effects in nuclear collisions in the Fermi energy range: aligned breakup of heavy projectiles, *Nuclear Physics A* **676**, 391 (2000).